Republic of Iraq
Ministry of Higher Education
and Scientific Research
University of Babylon
College of Materials Engineering
Department of Metallurgical Engineering

Failure Analysis and Prevention of Centrifugal Heavy Fuel Oil Separator Pump Used in Power Plant

A Dissertation
Submitted to the Council of the College of Materials Engineering /
University of Babylon in Partial Fulfillment of the Requirements for
the Degree of Doctor of Philosophy in Materials Engineering/
Metallurgical.
by

Hassan Hadi Masallb Abid Zaid

Al-ghazali

B.Sc. In Mechanical Engineering (2002)

H.D.In Metallurgical Engineering (2017)

M.Sc. Metallurgical Engineering (2020)

Supervised by

Prof. Abdul Raheem. K. Abid Ali (Ph.D.)

2023A.D **1445A .H**

وزارة التعليم العالي والبحث العلمي
جامعة بابل
كلية هندسة المواد
قسم هندسة المعادن

تحليل ومنع الفشل في فواصل مضخات الطرد المركزي التي تعمل بالوقود الثقيل المستخدمة في محطات الطاقة

اطروحة

مقدمة إلى قسم هندسة المعادن في كلية هندسة المواد/ جامعة بابل
وهي جزء من متطلبات نيل درجة الدكتوراه فلسفة

في هندسة المواد/ المعادن

من قبل

حسن هادي مسلب عبد زيد

الغزالي

بكلوريوس هندسة ميكانيك(٢٠٠٢)

دبلوم عالي هندسة مواد معادن(٢٠١٧)

ماجستير هندسة مواد معادن(٢٠٢٠)

بإشراف

أ. د. عبد الرحيم كاظم عبدعلي

٢٠٢٣م　　　　**١٤٤٥ هـ**

النور الآية (٣٥)

Supervisor Certificate

I certify that this thesis entitled (**Failure Analysis and Prevention of Centrifugal Heavy Fuel Oil Separator Pump Used in Power Plant)** was prepared by (**Hassan Hadi Masallab**) had been carried out under our supervision at the department of Metallurgical Engineering / College of Materials Engineering / university of Babylon in partial fulfillment of the requirements for the degree of Philosophy-Doctorate in Materials Engineering / Metallurgical Engineering.

Signature:

Name: Prof. Dr. Abdulraheem K.AbidAli

Date: / / 2023

Dedication

To….

My Father

My Mother

My Brothers

My Wife

My Daughter

My sons

Hassan

2023

Acknowledgments

First of all, praise be to Allah, profusely all thanks be to **Allah** who enables me to achieve this work.

I would like to express my gratitude to my supervisor**, Prof.Dr.Abdul-Raheem Kadhim** for all guidance, knowledge and support they have presented to me in difficult times that have been essential for completing this research. Also, I am very grateful to all the people whose professional help and personal support have made it possible for me to overcome all the obstacles that faced me till I finished this humble research.

Last but not least, I would like to thank **Iraqi Cement State Company; especially Kufa Cement Factory- Kufa Power Plant** represented by its manager and their enginerring staff.

Finally I am grateful to my family , especially to my wife, and also to my brothers and my sisters for their assistance, encouragement and support during the period of preparing this work.

Abstract

. Separator is the most important part in power plant that used heavy fuel oil in operation system. Separator works on purification the crude oil from particles, mud, mineral elements, water, and any contaminations by centrifuge force. In this study, investigation on reasons of failure in heavy fuel separator and suggestions four baths of electroless plating to prevent it have been studied Three types of specimens are used in this study. The first type is presented by taken several specimens from damage disc to analyze the failure.The second type is several specimens from shaft of SS316L in 15mm diameters ×10mm thickness for electroless plating have been taken.The last type is U-bend sheets from SS316L at different dimensions are used in test of stress corrosion cracking and numerical modeling. For analysis the failure, material characterizations ;chemical composition, hardness, light optical microscope, X-ray diffraction, scanning electron microscope, X-ray fluorescence, heavy fuel analysis and numerical modeling of stress corrosion cracking by ANSYS15.07 have been studied. Electroless nickel plating has been done in four different baths (Ni-P),(Ni-Cu-P), (Ni-Zn-P) and (Ni-SiC-P) nano composite coating at (1and 2 hours) respectively have been studied. Micro-hardness, surface roughness have been carried out. Corrosion with Tafel extrapolation and cyclic polarization in 3.5%NaCl solution have been accomplished. The erosion-corrosion has also been carried out in one active environment (heavy crude oil)at nine different periods:15, 30, 45,60,75,90,105,120and 135 minutes). Also stress corrosion cracking test for four U-bend specimens in the same media at three different times(480,960and1440 hours) has been taken.

From the failure analysis results, the chemical composition of disc separator material is identical with 316SS alloy, the hardness of failed disc separator has been

decreased from 331HV_{300} at far away damage position to 220HV_{300} near the damage position. From visual test , SEM images ,reduction in hardness , disc weight loss, decreasing toughness of disc and presence of several micro cracks so the most important causes to failure are erosion-corrosion and stress corrosion cracking. Intergranular stress corrosion cracking(IGSCC) can be seen by SEM images. The best results of electroless plating tests for heat treated specimens which coating by (Ni-SiC-P),(Ni-Zn-P),(Ni-Cu-P)and(Ni -P) at (2 hours' time of coating) showed that (erosion-corrosion rate at 90 minutes in heavy crude oil) have been decreased by (47.5%,42.4%, 13%and 12.5) respectively. On the other hand after heat treated the Vickers hardness has been increased by (70%,64.7%,65% and 64%) for coated specimens by (Ni-SiC-P),(Ni-Zn-P),(Ni-Cu-P)and(Ni-P) at (2 hours' time of coating) respectively. From results of polarization tests; the corrosion rate after heat treated for coated specimens by (Ni-SiC-P),(Ni-Zn-P),(Ni-Cu-P)and(Ni-P) at (2 hours' time of coating) have been decreased by 91.6%,96% ,87% and 81% respectively.In cyclic polarization examinations the difference between pitting potential and protect potential for(Ni-SiC-P),(Ni-Cu-P), (Ni-Zn-P), and(Ni-P) at (2 hours' time of coating) have been improved by 63%,39.1%,36 and 21.7%respectively. However the average surface roughness of all four coating layers in(2 hours' time of coating) have been increased after heat treated than them in (1 hour time of coating) as(73%,36.5%,60%and65%)respectively. The results of SEM images for stress corrosion cracking test in U-bend specimens in heavy crude oil at 480,960 and 1440 hours show that stress corrosion cracking take the intergranular form especially for bare specimens. The stress corrosion cracking don’t appear in all four coating layers which have high thickness.Finally the results of finite elements analysis give clear picture about the regions which subjected to high and low stresses and strains.Minimum equivalent stress and strain in all four samples were 0.0310Pa and 2.5657×10^{-10} respectively.

List of Content

Chapter one: Introduction

Chapter Two: Theoretical Part & Literature Review

Chapter Three: Experimental Part

Chapter Four: Results & Discussion

Chapter Five: Conclusions & Recommendations

List of Latin Symbols

Symbol	Meaning	Units
A	Specimens Surface Area	mm^2
E	Elastic modulus	GPa
n_1	Agitation Factor	
s	second	
Tm	Melting Temperature	^{o}C
t	Time	Hour
T	Temperature	^{o}C
Wt	Percentage of Weight	%

List of Greek Symbols

Symbol	Meaning	Units
α	Ferrite Phase	-
γ	Austenite Phase	-
σ	Stress	MPa
μ	Micro-	
ρ	Density	g/cm^3
Δ	Difference in Temperature	
ε	Strain Rate	
ω	Angular Velocity	rad/s
Ω	Ohms	
π	Constant Ratio	3.14

List of Subscripts & Superscripts

Symbol	Meaning	Units
A_3	Temperature Above Phase	^{o}C
A_4	Temperature Above δ Phase	^{o}C
BF_s	Bamboo fibers	
C_{Ni2+}	Concentration of Nickel in The Solution	

C_{Red}	Concentration of Reducing Agent	
E_{corr}	Corrosion Potential	mV
$E_{pit.}$	Pitting Potential	mV
$E_{prot.}$	Protection Potential	mV
$I_{corr.}$	Corrosion current	μ A
$i_{corr.}$	Corrosion Current Density	$\mu A/cm^2$
R_a	Surface Roughness	μm

List of Abbreviations

Symbol	Meaning
AFM	Atomic Force Microscope
AISI	American Iron and steel Institute
API	American Petroleum Institute
AS	As-Plated
ASTM	American Society for Testing and Materials
CFD	Computational Fluid Dynamic
C&W	Corrosion and Wear
C.R	Corrosion Rate
DES	Deep Eutectic Solvent
EBSD	Electron-Backscatter-Diffraction
EDAX	Energy Dispersive Analysis of X-Ray
EDS	Energy Dispersive Spectroscopy
EN	Electroless Nickel
EPMA	Electron Probe Micro Analyzer
FEA	Finite Elements Analysis
FSEM	Field Emission Scanning Electron Microscope
HAZ	Heat Affected Zone
HV	Vickers Hardness
IGSCC	Intergranular Stress Corrosion Cracking

LOM	Light-Optical-Microscope
m.p	Melting Point
mpy	Mils Per Year
MPa	Mega Pascal
MW	Mega-Watt
MOF	Metal-Organic Framework
NiP	Nickel-Phosphorus
OM	Optical-Microscope
OPC	Open Circuit Potential
PH	Precipitation-Hardenable
PVC	Polyvinyl Chloride
RMS	Root Mean Square
RS	Surface Roughness
SCC	Stress Corrosion Cracking
SS	Stainless Steel
SEM	Scanning Electron Microscope
SEC	Saturated Electrode Calomel
TEM	Transmission Electron Microscope
TGSCC	Transgranular Stress Corrosion Cracking
TG-FTIR	Thermo-Gravimetric- Fourier- Transform- Infrared
USA	United State of America
XRD	X-Ray Diffraction
XRF	X-Ray-Fluorescence
XPS	X-ray Photoelectron Spectroscopy

Chapter1

Introduction

Introduction

1.1. General View

The term separator in oilfield terminology designates a pressure vessel used for separating well fluids produced from oil and gas wells into gaseous and liquid components. A separator for petroleum production is a large vessel designed to separate production fluids into their constituent components oil, gas and water. All electric stations that work in heavy fuel have separators. These separators work to purify heavy fuel from clay, particulates and mineral impurities. The separators can be classified into three or some time more types. The most famous types are vertical, horizontal and spherical or centrifugal separators**[1].** Separators of Kufa power plant are lied in the last specie . Figure (1.1) shows Kufa cement factory and its power plant which consists of five units with 30MW.

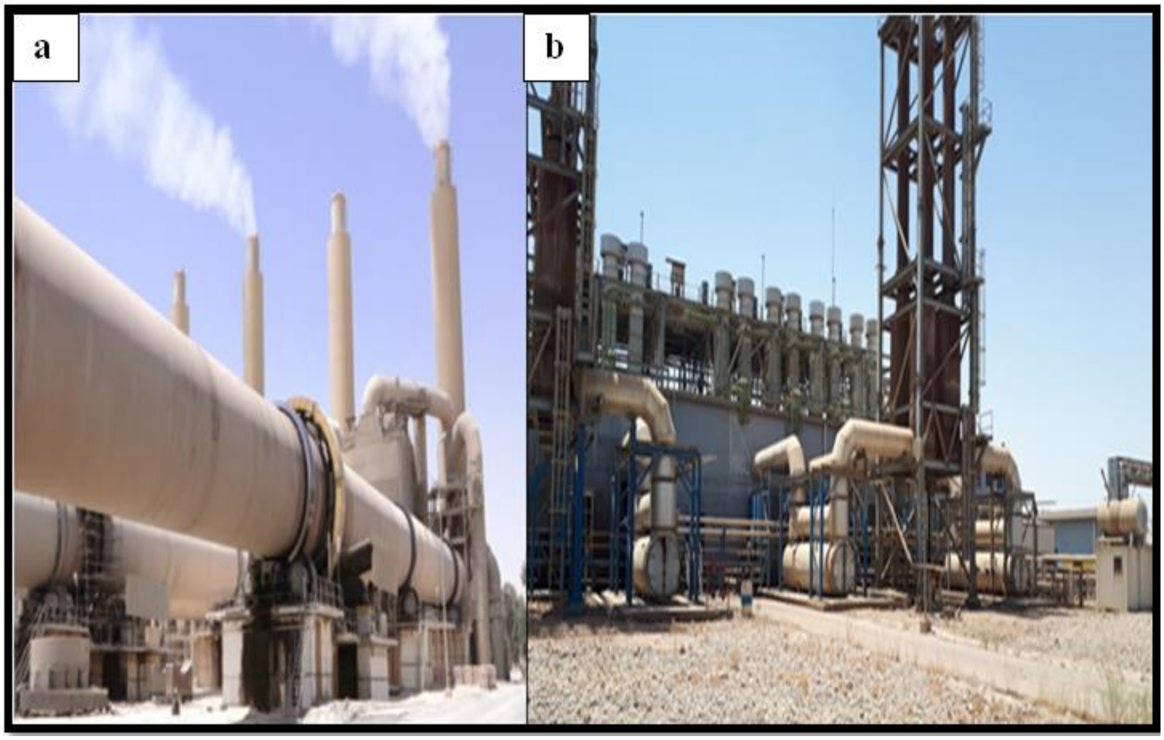

Figure (1.1):(a) Kufa Cement Factory (b): Kufa Power Plant.

Each unit has one oil separator for purification lubrication oil engine but all units are participated in two large heavy fuel oil separators. All types of separators are shown in Figure (1.2). Each main basic part in separator consists of several components. The most important component in separator is bowel disc or called disc stack**[1]**.

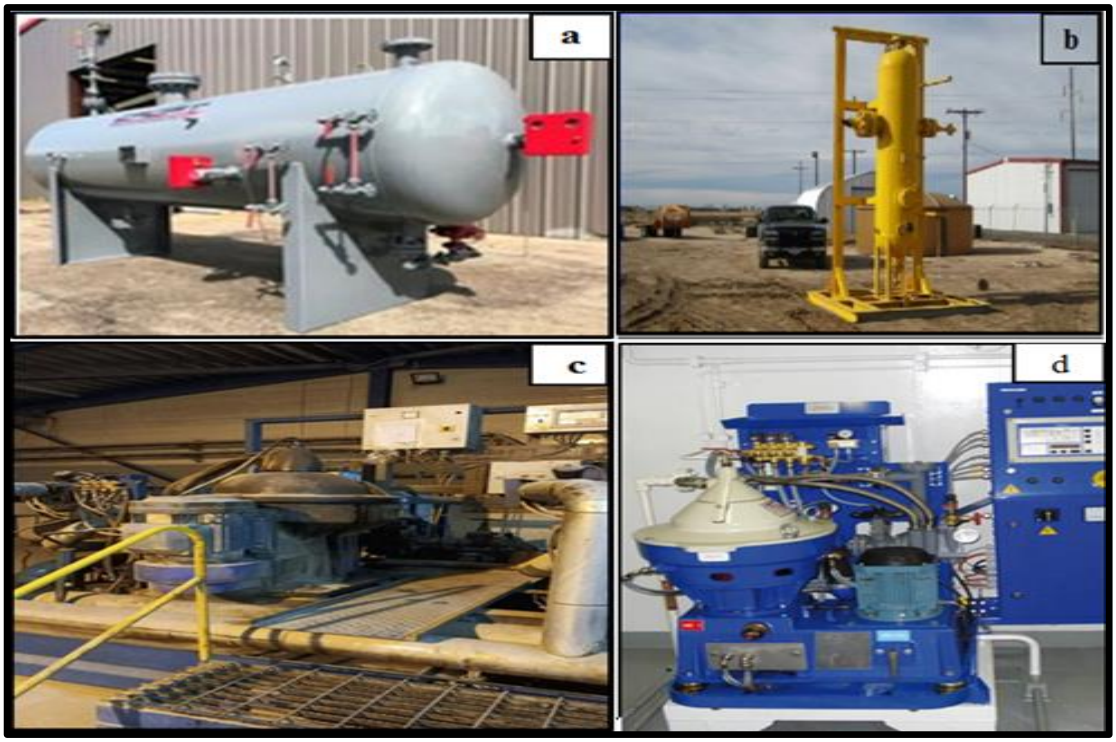

Figure (1.2):Types of Separators (a): Horizontal (b): Vertical (c) and (d)Spherical Centrifugal Separator Kufa Power Plant.

Disc stack is a small part made from stainless steel or special alloy called superalloy. The main function of disc stack is to scatter metal particles and clays at a high speed aside and thus exit them away from the fuel.**[2]** .The disc stack centrifuge uses a tremendously high centrifugal force to separate two liquid phases from one another or to remove solids (typically impurities) from liquids. When subjected to these forces, the less dense fluids move toward the center, while the denser solids or liquids move outward toward the rotating bowl wall. However heavy fuel contains harmful contents such as sediment, clay, mineral particles, sulfur, vanadium, chlorides. All these inclusions create an effective corrosive environment **[2-5].**Figure (1.3) shows the discs stack of Kufa power plant which number 68 piece, so they are chosen in this study to analyze the failure on it and then attempting to reduce or prevent this failure in this part.

Figure (1.3):Discs Separator.

1.2. Service Conditions and Main Problem

Separator spins at a very high speed, up to 7000 r.p.m. It consists of large spherical tank which involves on heavy crude oil with temperature about 85-100°C, and an entry pressure about 1 bar. This particular type gives a production of 9m^3/hr..Failure may occur quickly or slowly, but it is not sudden, depending on the purity of the fuel used and the operating conditions. Precipitates, clay ,mineral particles, high pressure and high speed all these lead to failure**.** All these circumstances conditions and centrifugal forces from high speeds may encourage the occurrence of environmental failure**[6]**. Due to the complex shape of separator discs and high velocity of separator a turbulent flow is occurred. Turbulent flow is the most effective factor which encourages on erosion corrosion. Materials selection for engineering parts which are subjected to erosive-corrosive environments is a continuous challenge in the mining industry**[6,7].** Through the SEM images and the virtual inspection cracks, corrosion products and pitting are noticed on surface separator discs surface. The type of failure is proven by the current study and identifies ways to treat it.However the most important way to reduce failure in most parts that they operate in high or low temperature like gas turbine, compressor, separators and blades of nozzle ring is surface treatment or called surface engineering**[8,9]**.

1.3. Surface Treatments

These processes are sometimes referred to as post-processing. They play a very important role in the appearance, function and life of the product. Broadly, these are processes that affect either a thin layer on the surface of the part itself, or add a thin layer on top of the surface of the part. There are different coatings and surface treatments processes, with different applications, uses, etc. The important uses include: improving the hardness , improving the wear resistance, controlling friction, improving the lubrication, improving corrosion resistance,improving aesthetics**[10].** The surface engineering is presented by treatment of the surface and near –surface region of material to allow the surface to perform functions that are distinct from those functions demanded from the bulk of the material**[11]** .There are several way of surface treatment that can be used to protect the surfaces from corrosion, stress corrosion cracking ,erosion corrosion, wear and oxidation, the most important ways that are used in centrifugal pumps ,turbocharger, gas turbine and impeller are **:**thermal spraying ,vapor deposition, anodizing, painting, cladding, electroplating and electroless plating**[12,13]** . In this study, the electroless plating by binary , ternary alloy and composite coating are chosen to prevent the failure.

1.3.1.Electroless Plating by Binary Alloys (Ni-P)

Preventive strategies to reduce the high cost of corrosion have attracted enormous interests in the world. Advanced technologies have been utilized to control this phenomenon. For instance, creation of the stable and protective layer between the metal and its corrosive environment through coating processes enables us inhibit or reduce the corrosion rate **[14-16].** Deposition of binary Ni–P coatings by electroless method has been extensively developed as a simple, low-cost, and easy technique in the commercial processes. ElectrolessNi–P (EN) deposit is useful in many practical applications due to their unique properties such as high corrosion, wear and abrasion resistance, good ductility, hardness and surface uniformity **[17].**

1.3.2. Electroless Plating by Ternary Alloys

In this study, two types of ternary alloys are used as follows:

1.3.2.1. Electroless Plating by (Ni-Cu-P)

Interest in electroless plating of nickel-based ternary alloys has increased because of their excellent corrosion, wear, thermal and electrical resistance. They also possess good magnetic properties. Many metal elements, such as copper, zinc, iron, cobalt, tungsten, molybdenum, and rhenium can be codeposited in an Ni-P matrix to improve some properties. The choice of these elements depends on the applications sought after**[18].**Copper content in electroless Ni-Cu-P alloy coatings depends mainly on pH, temperature, and Cu^{2+} concentration in electrolyte composition and has a significant effect on the corrosion resistance of the coatings. In addition, it was reported that the inclusion of Cu in electroless Ni-P coatings improves their smoothness, brightness, anti-corrosion and also increases the deposit rate and surface hardness **[19].**

1.3.2.2. Electroless Plating by (Ni-Zn-P)

Ternary Ni-Zn-P alloy thin films are considered a replacement for cadmium sacrificial coatings for anticorrosive protection of steel parts working in highly corrosive media. Also, cadmium plating presents major disadvantages due to metal toxicity and utilized salts as well as simultaneous discharge of hydrogen ions during the cadmium plating process, making cadmium plating parts to be susceptible of acid provoked brittleness**[20].** For these reasons, in the last decades, intense studies and researches were accomplished for finding replacements for cadmium based anticorrosive protection coatings**[20].** The most common sacrificial layer replacements for cadmium are zinc and its alloys. Zinc presents a more negative electrode standard potential (E=-0.76 V, measured vs. hydrogen normal electrode), thus being capable of acting as a sacrificial coating for plated steel parts .The dissolution rate of the protective coating was considerably reduced by alloying zinc with other elements (Ni, Co, Fe, etc.) that shifted the standard electrode potential of the alloy to values closer to those of the substrate**[21]**. The incorporation of Zn into Ni–P matrix has great impact on its microstructure, mechanical and electrochemical properties. The electrochemical properties of Ni–Zn–P alloy have revealed that these coatings possess more noble character compared to other ternary alloys **[22].**

1.3.3. Electroless Plating by Nano-Composite Coating(Ni-P-SiC)

Electroless nickel-phosphorus matrix deposition method received widespread acceptance in various industries. Adding second-phase hard particles have improved several properties of composite coatings such as mechanical, tribological, anti-corrosion and anti-oxidation properties. Hard particles such as oxides or carbides embedded in a metal matrix aim to increase its mechanical and wear properties of the coatings**[23].** The use of particles in nano scale could also change the microstructure of the electrodeposits and electroless plating leading to a more compact structure and thus to improved corrosion resistance. Further the engineering materials can be strengthened and protected from corrosion and abrasion phenomenon, by plating them with the micro/nano composite of non metallic/metallic particles such as ZrO_2, SiC, WC, TiO_2, Si_3N_4 and Al_2O_3 etc **[24,25].**

1.4. Aim of This Work

The main objective of this work includes the analysis of failure in separator heavy fuel power plant and attempts to prevent this failure by using electroless nickel phosphorus coatings (EN).The real objectives for this study can be presented as follow:

1-Analysis the failure parts, fuel analysis ,products and their chemical compositions.

2-Applying four types of coating baths (Ni-P) , (Ni-Cu-P)(Ni-Zn-P)and (Ni-P-SiC) nano composite coating based up on Ni electroless plating at two different time (60,120 minutes).

3-Reducing corrosion, erosion-corrosion and stress corrosion cracking(SCC) by electroless plating.

4-Simulate stress corrosion cracking (SCC)by using ANSYS software(15.07) based on U-bend specimens types.

Chapter2

Theoretical Part and Literature Review

Chapter Two

Theoretical Part and Literature Review

2.1.Introduction

This chapter deals with the definition of failure analysis, types of failure, heavy fuel oil and its components. Electroless plating by binary,tenrary and composite coating, types of solutions, baths, electroless plating mechanism and factors affecting on electroless plating are presented in this chapter as a way suggested for reducing the failure. Finally this chapter deals with industrial alloys which the discs separator made from it and they have special applications.

2.2.Failure Analysis

Failure analysis is a critical process in determining the physical root causes of problems. The process is complex, draws upon many different technical disciplines, and uses a variety of observation, inspection, and laboratory techniques and its important process of finding the root causes by collecting enough information for the part to be analyzed. This process is not limited to collecting information, but rather exceeds the expectation of failures in structures, equipment, buildings, etc., as well as through the process of finding solutions or correct treatment of problems .The engineering importance of failure analysis is evident in minimizing material and human losses as all the engineering parts are designed to work under certain conditions and for a certain age cannot be exceeded unless the development of these parts **[26]**. In the current study, the failure is analyzed by visual inspection, LOM, SEM, EDS, AFM and hardness test. Not only this current study is presented in the failure analysis, but also the attempting to prevent or reduce it by suggested surface treatment.

2.3.Types of Failures

The failure of engineering materials is almost an undesirable event for several reasons; these include putting human lives in jeopardy, causing economic losses, and interfering with the availability of products and services. Several failures types can be presented in this chapter as follow **[26]:**

2.3.1. Mechanical Failure

The mechanism of mechanical failure has several sorts as follow:

2.3.1.1. Fracture

Simple fracture is the separation of a body into two or more pieces in response to an imposed stress that is static (i.e., constant or slowly changing with time) and at temperatures that are low relative to the melting temperature of the material. For metals, two fracture modes are possible: ductile and brittle. Classification is based on the ability of a material to experience plastic deformation. Ductile metals typically exhibit substantial plastic deformation with high energy absorption before fracture. However, there is normally little or no plastic deformation with low energy absorption accompanying a brittle fracture. Ductile and brittle are relative terms; whether a particular fracture is one mode or the other depends on the situation**[27]**. Ductile fracture is almost always preferred to brittle fracture for two reasons: First, brittle fracture occurs suddenly and catastrophically without any warning; this is a consequence of the spontaneous and rapid crack propagation. However, for ductile fracture, the presence of plastic deformation gives warning that failure is imminent, allowing preventive measures to be taken. Second, more strain energy is required to induce ductile fracture inasmuch as these materials are generally tougher**[27,28]**.

2.3.1.2. Fatigue

Fatigue is a form of failure that occurs in structures subjected to dynamic and fluctuating stresses (e.g., bridges, aircraft, machine components). Under these circumstances, it is possible for failure to occur at a stress level considerably lower than the tensile or yield strength for a static load. The term fatigue is used because this type of failure normally occurs after a lengthy period of repeated stress or strain cycling. Fatigue is important inasmuch as it is the single largest cause of failure in metals, estimated to be involved in approximately 90% of all metallic failures; polymers and ceramics (except for glasses) are also susceptible to this type of failure**[27,29]**.

2.3.1.3. Thermal Fatigue

Thermal Fatigue is normally induced at elevated temperatures by fluctuating thermal stresses; mechanical stresses from an external source need not be present. The origin of these thermal stresses is the restraint to the dimensional expansion and/or contraction that would normally occur in a structural member with variations in temperature **[30]**.

Furthermore, a cyclical temperature change encourages failure by thermal fatigue; when the material heats in a non-uniform manner, some parts of the structure expand more than others. This non uniform expansion introduces a stress within the material, and when the structure later cools and contracts, stresses of the opposite sign are imposed. As a consequence of the thermally induced stresses and strains, fatigue may eventually occur. The magnitude of a thermal stress developed by a temperature change ΔT depends on the coefficient of thermal expansion $\propto, l$ and the modulus of elasticity E

according to this equation **[30,31]:**

$$\sigma_{th} = \propto lE\,\Delta T \quad \ldots\ldots 2.1$$

Where: σ_{th}:thermal stress

$\propto$:thermal expansion

l :length of specimens

E:young modulus

ΔT:the difference between temerature

2.3.1.4. Creep

Materials are frequently used at high temperatures and subjected to static mechanical stresses (e.g., turbine rotors in jet engines and steam generators subjected to centrifugal stresses; high-pressure steam lines). Deformation under such circumstances is termed creep. Creep, defined as the time-dependent and permanent deformation of materials when subjected to a continuous load or stress, is typically an undesired phenomena that is frequently the limiting factor in a part's lifetime. It is observed in all sorts of materials; for metals, it becomes significant only at temperatures above around 0.4Tm, where Tm is the absolute melting point. **[27,32]**.

2.3.1.5. Wear

It is known that loaded contacts in relative movement give rise to wear phenomenon, which depends on several parameters such as: roughness of rubbing surfaces, nature and microstructure of materials **[33].**

Wear is progressive in that it increases with usage or increasing amounts of motion, and it ultimately results in the loss of material from a surface or the transfer of material between surfaces. Wear failures occur because of the sensitivity of a material or system to the surface changes caused by wear . The wear process can be examined in three stages. The first stage is concerned with debris generation and deals with various mechanisms of material removal from sliding surfaces. The second one is devoted to the evolution of debris inside contact (i.e. mechanical physical and chemical changes). The third stage refers to own behavior of debris, which can be either eliminated out of the contact, or accumulated between sliding surfaces**[34]**.

2.3.2. Mechanical Environmental

In the following several mechanical environmental are presented as follow:

2.3.2.1. Stress Corrosion Cracking

Stress corrosion cracking (SCC) is the formation and growth of crack through materials subjected to tensile stress and a specific corrosive medium. The stress in the form of tensile (not compressive) plays a key role in the SCC fracture processes. In fact, SCC would never have occurred in the absence of stress. The required tensile stresses may be in the form of directly applied stresses, thermal, in the form of residual stresses, or a combination of all. SCC can lead to unexpected sudden failure of normally ductile metals. Metal-environment combinations susceptible to cracking are specific. This means that all environments do not cause SCC on all of the alloys. Additionally, the environments that cause this kind of cracking have little corrosion effect on the alloy in normal conditions**[35-37].**

In certain states, unwanted environmental and metallurgical changes have occurred and provide the metal-environment combination sensitive to SCC.

The SCC sites on the metal surfaces may not be visible by visual inspection, while metal parts are being filled with microscopic cracks. These invisible cracks progress rapidly and lead the component and structures to catastrophic failures. SCC is classified as either intergranular stress corrosion cracking (IGSCC) or transgranular stress corrosion cracking (TGSCC), depending upon the primary crack morphology **[35-37].** SCC can be shown in Figure (2.1).

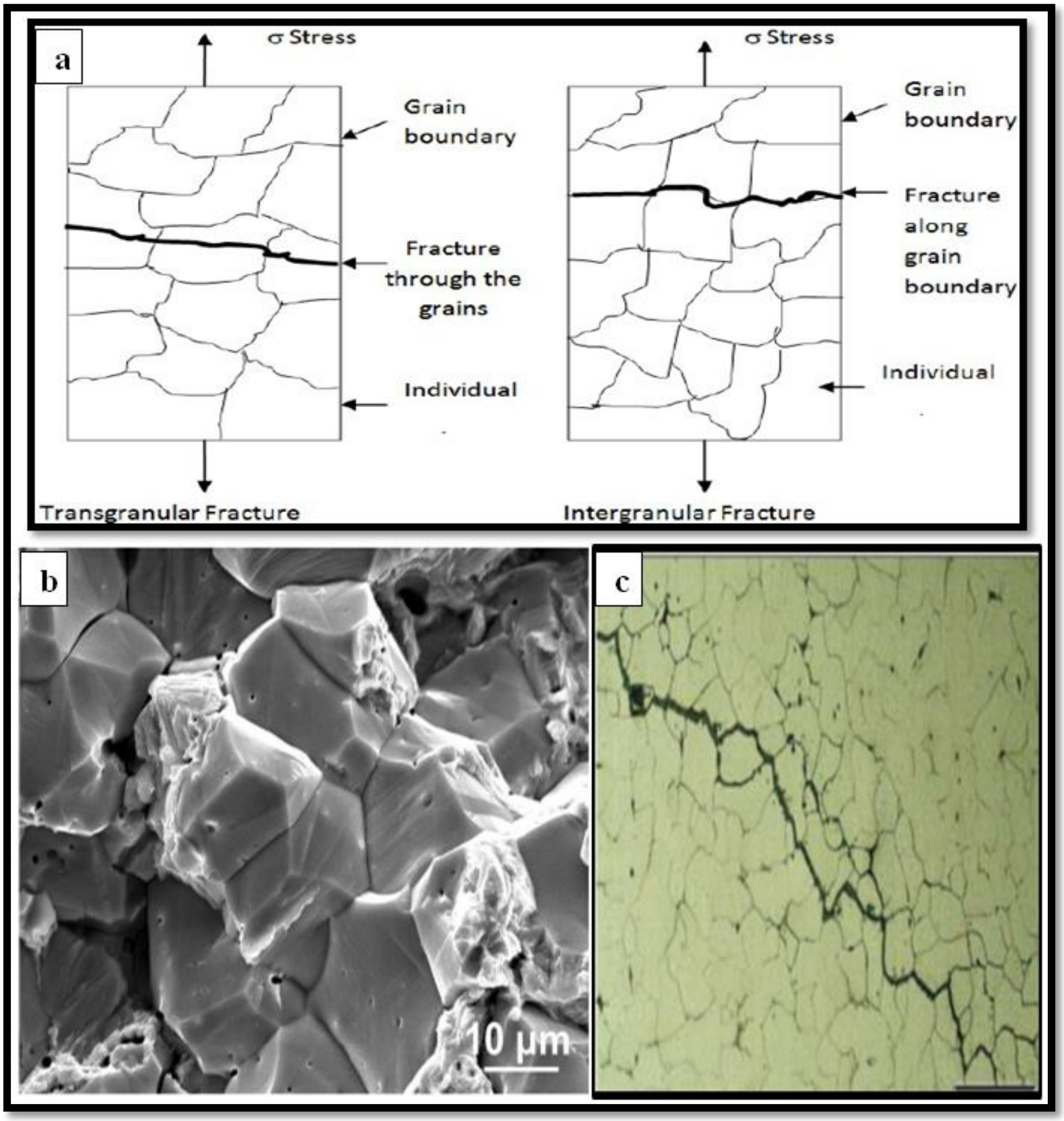

Figure(2.1): (a):Sketch of TGSCC and IGSCC(b):SEM Image of TGSCC(c):SEM Image of IGSCC **[35,36]**.

To facilitate the study and knowledge of SCC, it has been classified into four concepts that include influencing factors, conditions , Major types of stress-corrosion cracking, alloys with high sensitivity to SCC, and the mechanism of its occurrence.

Factors affecting SCC:

The factors affecting SCC involve the tensile stress ,corrosive environments and sensitive materials. Factors affecting SCC can be presented in Figure (2.2).

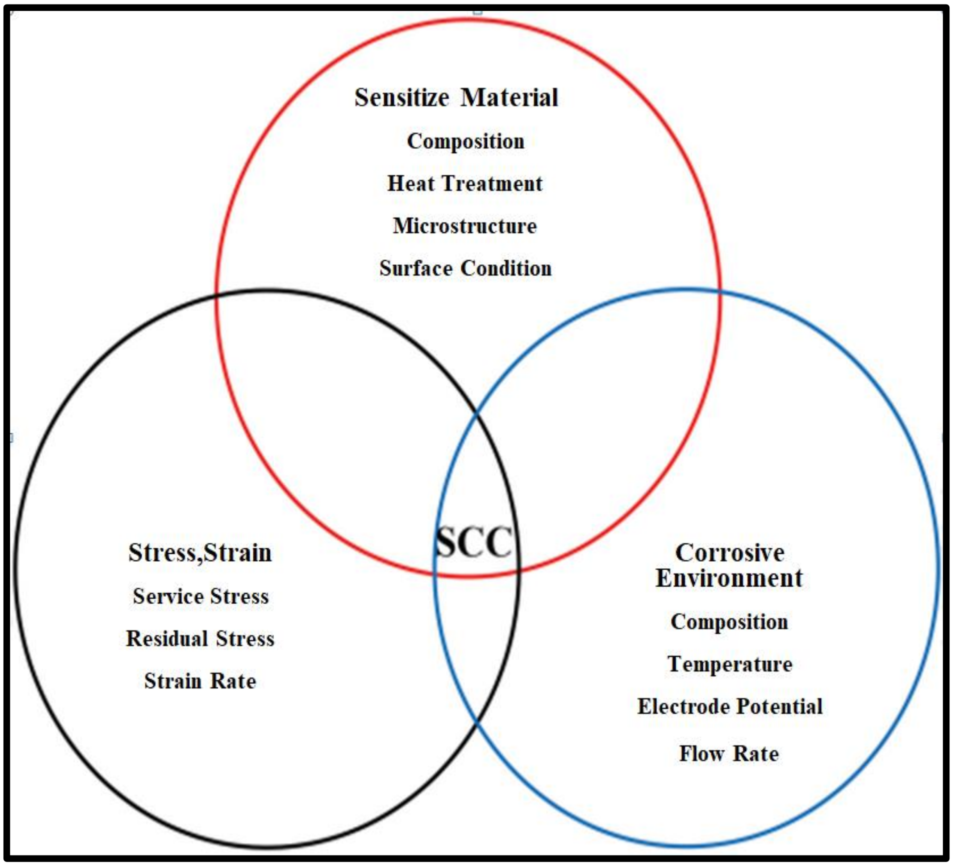

Figure(2.2): Factors Affecting Stress Corrosion Cracking**[35]**.

Pure metals are typically resistant to stress corrosion cracking, but metallic alloys such as stainless steel and aluminum alloys are susceptible due to the large amount of alloying elements in the matrix. Typically, alloys rely on intermetallic formation at the grain boundaries to increase strength and ductility**[38].**

Consequently, the intermetallics cause an anodic condition at the grain boundaries, which in turn causes preferential intergranular corrosion in aluminum alloys**.** Macroscopically, SCC fractures have a brittle appearance**[38].**

- **Major types of stress-corrosion cracking [38-41]**:

(a) Chloride stress corrosion cracking. It occurs in austenitic steels under tensile stress in the presence of oxygen, chloride ion and high temperature.

(b) Caustic stress corrosion cracking. Cracking of steels in caustic environments where the hydrogen concentration is high, for instance, cracking of Inconel tubes in alkaline solutions.

(c) Sulfide stress corrosion cracking. Cracking of steels in hydrogen sulfide environment as encountered in oil drilling industry.

(d) Seasonal cracking. The term is now obsolete. It had a historical significance only. It refers only to SCC of brass in ammoniacal environment, but still occasionally occurs in refrigeration plant using ammonia refrigerant.

- **SCC sites**

(a) Surface discontinuities. Cracks may initiate at surface irregularities, such as grooves.

(b) Corrosion pits. SCC can also initiate at the pits which are formed on the surface due to breakdown of passivity by chloride ions.

(c) Grain boundaries. Intergranular corrosion resulting from the sensitization by impurities, such as sulfur, at the grain boundary which makes the grain boundaries very reactive to SCC.

Table (2.1) shows most environments with sensitive materials to SCC.

Table (2.1): Metals and Alloys with Environments that Produce SCC[43].

Metals, Alloys	Environments
Aluminum alloys	$NaCl–H_2O_2$ solutions ,NaCl solutions, Seawater ,Air or water vapor
Copper alloys	Ammonia vapor and solutions Amines, Water or water vapor
Titanium alloys	Red fuming nitric acid ,Seawater, Methanol–HCl
Stainless steels	Acidic chloride solutions, $NaCl–H_2O_2$ solutions, Seawater ,H_2S $NaOH–H_2S$ solutions ,Condensing steam from chloride waters
Steel	NaOH solutions ,$NaOH–Na_2SiO_4$ solutions, Calcium, ammonium, and sodium nitrite solutions ,Mixed acids (H_2SO4–HNO3) ,Acidic H_2S solutions, Seawater, Carbonate–bicarbonate solutions
Magnesium alloys	$NaCl–Na_2CrO4$ solutions, Rural and coastal atmospheres ,Seawater, Distilled water
Nickel	Fused caustic soda
Lead	Lead acetate solutions
Inconel	Caustic soda solutions
Gold alloys	$FeCl_3$ solutions ,Acetic acid–salt solutions

❖ Mechanisms of Stress Corrosion Cracking

In past,the mechanisms of SCC are not completely understood. There has been disagreement as to the mechanism of cracking in any given system and there is confusion as to whether the mechanism varies from one system to another. Four basic categories of mechanisms have been proposed**[44,45]**:

(a) Mechano-electrochemical model.

This suggests that there are pre-existing paths in an alloy which become intrinsically susceptible to anodic dissolution. For instance, a grain boundary precipitated anodic to the grain boundary would provide an active path for localized corrosion to proceed. Similarly, if a more noble constituent is precipitated along a grain boundary, the impoverished zone adjacent to the precipitate would provide an active path for localized corrosion. Also, the removal of the protective film at the crack tip by plastic deformation would facilitate the onset of localized corrosion.

(b) Film rupture model. This is based on a repetitive cycle comprising: localized film disruption, localized attack at the point of disruption and film repair. Plastic strain plays a major role. This mechanism has several variations.

(c) Embrittlement model. This is based on the postulate that an electrochemical process embrittles the materials in the vicinity of a corroding surface. This mechanism was based on a study of high strength martensitic steels in chloride media.

(d) Adsorption model . Adsorption of damaging species causes weakening of cohesive bonds between surface metal atoms by specific damaging species. The surface energy associated with crack formation is lowered by adsorption of species and the probability of a metal forming a crack under tensile stress is increased. A universal theory does not exist and several theories have to be examined for results and analyzed to reach a plausible explanation.

2.3.2.2. Embrittlement

Various metal alloys, specifically some steels, experience a significant reduction in ductility and tensile strength when atomic hydrogen (H) penetrates into the material. This phenomenon is aptly referred to as hydrogen embrittlement; the terms hydrogen induced cracking and hydrogen stress cracking are sometimes also used. Strictly speaking, hydrogen embrittlement is a type of failure; in response to applied or residual tensile stresses, brittle fracture occurs catastrophically as cracks grow and rapidly propagate.

Hydrogen in its atomic form (H as opposed to the molecular form, H_2) diffuses interstitially through the crystal lattice, and concentrations as low as several parts per million can lead to cracking**[36,46]**.

As for SCC, three different conditions must be present at the same time (see Figure (2.3)**[47].**

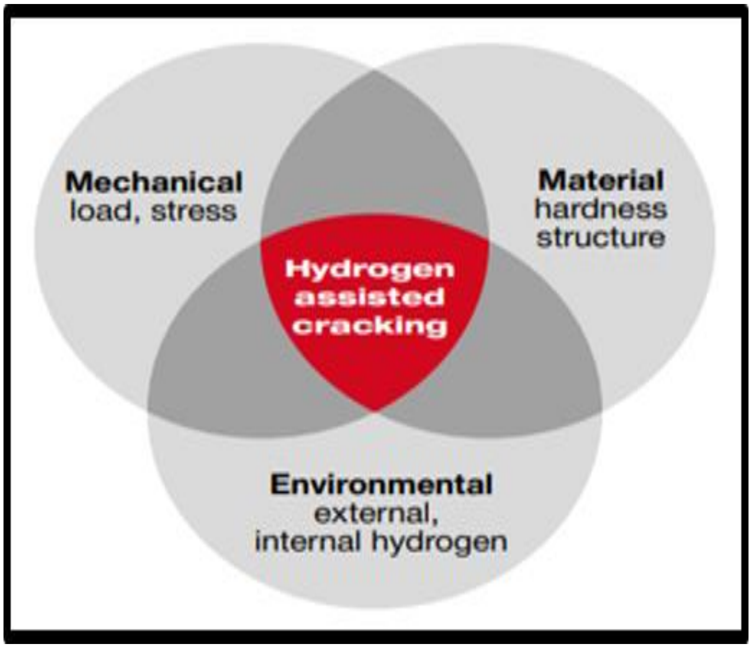

Figure(2.3): Factors Required for The Occurrence of Hydrogen-Assisted Cracking**[47].**

2.3.3. Environmental Failure

2.3.3.1. Corrosion Damage

Corrosion is the destructive attack of a metal by chemical or electrochemical reaction with its environment. Deterioration by physical causes is not called corrosion, but is described as erosion, galling, or wear. In some instances, chemical attack accompanies physical deterioration, as described by the following terms: corrosion–erosion, corrosive wear, or fretting corrosion. Rusting applies to the corrosion of iron or iron-base alloys with formation of corrosion products consisting largely of hydrous ferric oxides. Nonferrous metals, therefore, corrode, but do not rust. However, corrosion is beneficial or desirable in some cases. For example, chemical machining or chemical milling is widely used in aircraft and other applications. Unmasked areas are exposed to acid and excess metal is dissolved. This process is adopted when it is more economical or when the parts are hard and difficult to machine by more conventional methods. Anodizing of aluminum is another beneficial corrosion process used to obtain better and more uniform appearance in addition to a protective corrosion product on the surface**[48-50]**.

2.3.3.2. Erosion-Corrosion

Erosion-corrosion has many definitions. Erosion-corrosion is the acceleration of corrosive attack due to the simultaneous action of corrosion and erosion. The attack is more severe than if just corrosion or erosion alone were acting. The erosive action removes metal from the surface as dissolved ions, as particles of solid corrosion products, or as elemental metal. Erosion corrosion can be primarily erosive attack or primarily chemical attack, or somewhere in between. Both gases and liquids can cause attack **[51,52]**.

Nearly all turbulent corrosive media can cause erosion-corrosion .Erosion-corrosion is characterized in appearance by grooves, waves, rounded holes, and/or shaped grooves. Affected areas are usually free of deposits and corrosion products, although corrosion products can sometimes be found if erosion-corrosion occurs intermittently and/or the liquid flow rate is relatively low **[52].**

Several parameters are effected on erosion corrosion**[53]**:

- Impact angle

- Hardness of material
- Particle size
- Shape of particle
- Type of material
- Protective layer
- Flow rate velocity
- Temperature of fluid .

The mechanism of corrosion-erosion can be presented in Figure(2.4). The way in which this corrosion mechanism manifests itself can vary but typically it has two basic features:

- The liquid flow removes diffusion limitations and increases the supply of corrosive reagents
- The metal is exposed through mechanical removal of the passivized protective film.

A passive film on a metal is a non-active chemically protective barrier layer between the corrosive substance and the metal substrate, the protective layer typically has low mechanical strength. When this layer is broken off by high velocity fluid flow, or some other impinging material, the metal beneath begins form another passive layer. When pits are formed this can accelerate the degradation even further by the disruption of the flow this can cause eddy current which then speed up the removal the protective layer**[54]**.

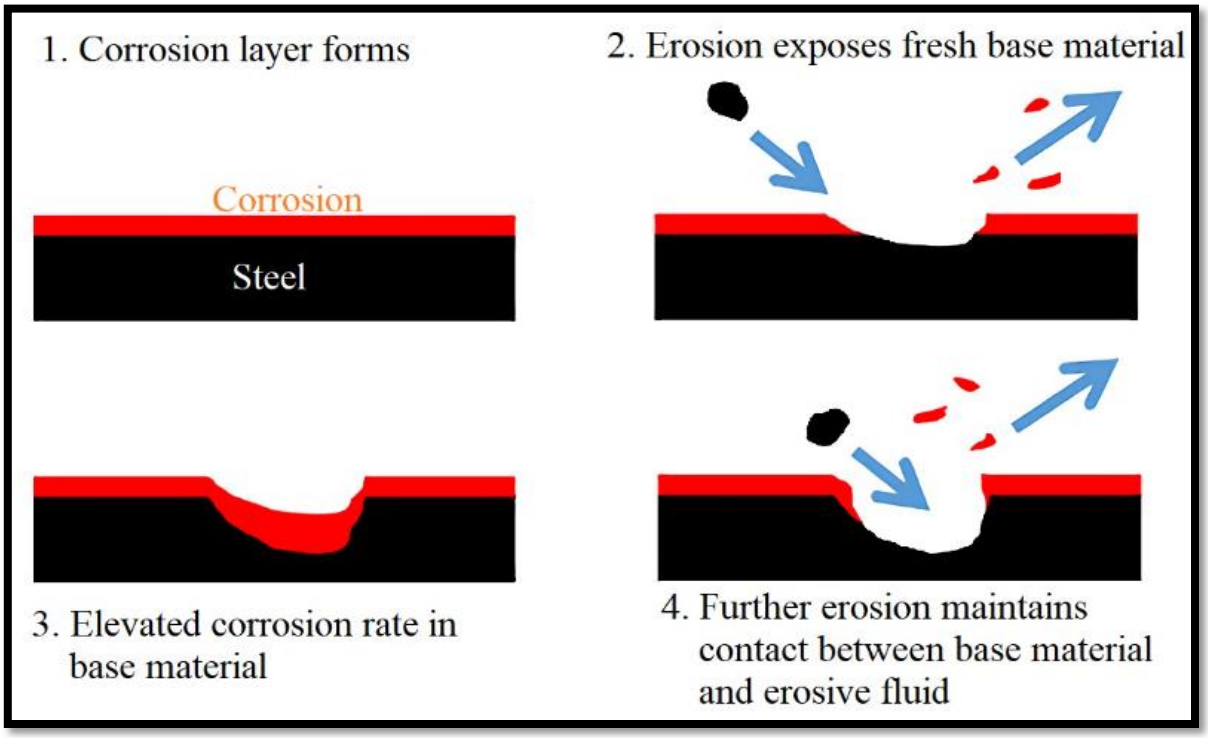

Figure(2.4):Sketch of Mechanism Corrosion-Erosion**[54]**.

2.4. Protection Methods of Corrosion ,Erosion-Corrosion and Stress Crack Corrosion

2.4.1. Methods of Corrosion and Erosion Corrosion Control

1- Barrier protection: Provided by a protective coating that acts as a barrier between corrosive elements and the metal substrate like paint, powder, coatings and galvanizing.

2- Cathodic protection: Employs protecting one metal by connecting it to another metal that is more anodic, according to the galvanic series like impressed current ,galvanic sacrificial anode

3- Corrosion resistant materials: Materials inherently resistant to corrosion in certain environments.

4- Design factors, for example, for copper tubing carrying potable water, are the control of the velocity and the minimization of abrupt changes in the flow system geometry reduce erosion corrosion.

5- Inhibitors are used in recirculating cooling water systems and steam condensate return lines but find limited application in once-through production systems because of the cost. A notable exception is the extensive use of inhibitors in oil/gas production**[55,56]**.

2.4.2. Methods of Stress Crack Corrosion Control

1-Lowering the stress levels. This may be done by annealing treatment in the case of residual stress. Stress relief temperature for plain carbon steels are at a range of 1100–1200^{o}F(594-649^{o}C) and for austenitic stainless steels are frequently at temperatures ranging from 1500 to 1700°F(816-927^{o}C).

2-Eliminating aggressive species in the environment. For instance, in case of austenitic stainless steels, reduction of chloride under 10 ppm reduces significantly the probability of the stress corrosion cracking to occur.

3-Changing the material in one plane if neither environment condition nor stress level can be changed. For example, in case of AISI304, stainless steel utilizing a high nickel alloy content (e.g., Inconel) can be useful.

4-Applying cathodic protection by impressed current or sacrificial anode. In cathodic protection, note that the failure is due to SCC, not hydrogen embrittlement. In cathodic protection, the released hydrogen due to cathodic reaction can accelerate the hydrogen embrittlement.

5-Generally,in galvanic corrosion (a)select metals, close together, as far as possible, in the galvanic series.

(b) Do not have the area of the more active metal smaller than the area of the less active metal.

(c) If dissimilar metals are to be used, insulate them.

6-Adding inhibitors such as phosphate and other organic and inorganic to the system can reduce the stress corrosion cracking effects in mildly corrosive media.

7-Shot-peening generates residual compressive stress in surface of the component and prevent the stress corrosion cracking to be occurred.

8-Coating by hot dipping ,chemical vapour deposition,thermal barrier coating and electrodepostion or electrolessplating by binary ,ternary and compsite coating is sometimes effective**[57]**.

In this study electrolessplating by binary,ternary alloy and nano compsite coating are used to reduce the failure.

2.5. Electroless Plating

The electroless coating technology was invented by A. Brenner and G. Riddell in 1946. Electroless nickel coating, which was used under the idiom (autocatalytic nickel coating), which is produced nickel ions by the catalytic reduction doesn’t use electric current **[58].**

Electroless nickel plating is a process for depositing a nickel alloy from aqueous solutions onto a substrate without the use of electric current. It differs from electroplating which depends on an external source of direct current to reduce nickel ions in the electrolyte to nickel metal on the substrate **[59].** Electroless nickel plating is a chemical process which reduces nickel ions in solution to nickel metal by chemical reduction. The most common reducing agent used is sodium hypophosphite. It is estimated that sodium hypophosphite is used in more than 99% of all electroless nickel plating. There are three types of EN (Electroless of Nickel), coatings available based on the weight percentage of phosphorus: (i) low phosphorus (2-5) %, (ii) medium phosphorus (6-9) % and (iii) high phosphorus (10-13)% **[60].**

Consequently, once the performance requirements for the coating have been defined, it is essential that the appropriate type of electroless nickel be specified. For instance, there are distinct differences in the corrosion resistance and hardness properties of low and high phosphorus deposits**[59,61].**

Based on the presence of phosphorus content the structure may be microcrystalline, amorphous or a combination of both. Only electroless Ni-high P coating is effective in offering an excellent protection whereas electroless Ni-low P and Ni-medium P coatings are not recommended for severe corrosive environment **[62].**

The structure of electroless nickel is responsible for some of its unique properties. It differs greatly from the crystalline structure of electrodeposited nickel and it can normally be described as having an amorphous structure or one consisting of ultra-fine crystallites. The amorphous nature of the deposits becomes more dominant with increasing phosphorus content and above 10.5%, deposits are considered truly amorphous. The absence of a well-defined crystal structure eliminates the possibility of intergranular corrosion that can be a problem with crystalline deposits, such as electrolytic nickel. Electroless nickel, therefore, provides a more effective barrier coating in protecting a substrate from corrosive attack **[59,63].**

A feature of great importance in all applications for electroless nickel is the ability to produce deposits with a very high degree of thickness uniformity. It is obviously beneficial when coating complex parts with critical dimensions, such as ball valves or threaded components. This huge advantage over electrodeposited nickel is due to the fact that no current is involved and the associated problems of current distribution do not exist. Uniform thickness of electrodeposits is not easy to obtain and becomes more difficult with increasing complexity of the part. Improved current distribution can be obtained by a suitable choice of electrolyte, the use of auxiliary anodes and shields and by optimizing rack design. However, it is almost certain that the thickness uniformity available by electroless plating will not be achieved on complex parts by electroplating. In electroless nickel plating the rate of nickel deposition on all areas should be equal, provided uniform solution conditions are maintained**[64,65]**. The wide acceptance and growth of electroless nickel plating can be attributed in part to this outstanding feature of deposit uniformity, even on complex components **[59,65].** Figure (2.5) provides an example of the difference in thickness uniformity of nickel deposited electrolytically and by the electroless process.

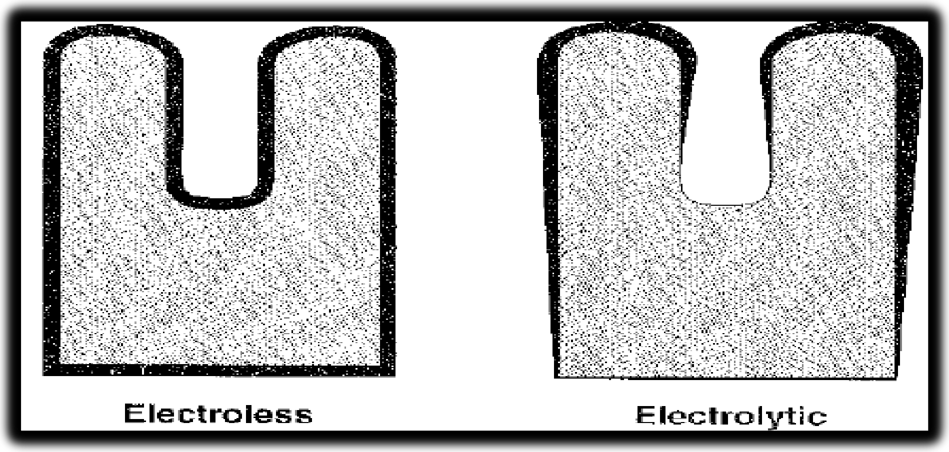

Figure (2.5): Comparison of Deposit Uniformity **[59]**.

2.5.1 Typology of Electroless Baths

Most applications of the electroless coating are based on their wear and corrosion resistance. However, characteristic like luminescence has a great potential in defense and aerospace applications **[66].**

Electroless coatings can be divided, essentially, into three main categories:

- Alloy coatings
- Composite coatings
- Metallic coatings

In particular NiP with or without particles is considered alloy or composite coating **[66].**

2.5.2. Types of Electroless Baths

Electroless nickel plating is carried out by the immersion of objects, with a surface wetted and activated by a catalyst, in a solution containing nickel ions and suitable reducing agents, which may include hypophosphite, borohydride, aminoboranes, hydrazine, etc. at temperatures above 85 °C. Further, some organic complexing agents for nickel ions, buffers, stabilizers, accelerators, etc. are also present**.** Mainly two types of baths have been used for depositing alloys, These also include acidic and alkaline baths **[67]**.

2.5.2.1.Acidic Baths

Firstly acidic baths, that represents almost the whole of the process used nowadays, are described. Once the substrate is immersed into the bath, the reaction proceeds forward due to the following factors: reduction in nickel ion concentration, conversion of the hypophosphite to phosphate, then the consequence is the increase in hydrogen ion concentration, and adsorption of this gas by the deposit**[67]**. Aminoboranes are also used as reductants instead of hypophosphite in electroless nickel deposition from acid solutions. The coatings obtained from this formulation have a better quality **[68].**

2.5.2.2.Alkaline Baths

The second and less used type of electroless nickel baths consists in solutions with alkaline features. The reduction of nickel in these solutions follows the same pattern as in acid ones unfortunately they have some problems**[68]**.

The main disadvantage of the alkaline solutions are their high instability at higher temperature, in particular greater than 90°C, due to the loss of ammonia, which is useful to raise the bath pH at that temperature. Another difference from the previous solutions is that the nickel's rate of deposition increases with hypophosphite concentrations; unfortunately very high concentrations of this element make the bath unstable due to homogeneous deposition in the bulk. Also temperature influences the rate of deposition in the same way as in acid solutions. The control of pH is very difficult due to higher temperature than 90°C. Borohydrides are used as reducing agents in alkaline electroless nickel-plating baths. **[69]**.

2.6. Components of Ni Bath

Firstly the most important component is represented by the metal ions which constitutes the source of metal are deposited. Metal ions(source of nickel ions): nickel chloride, nickel sulfate, nickel acetates . The reducing agents are another fundamental element because they reduce metal ions and allow them to deposit on the substrate **.** Complexant agents are used in order to prevent excess of free nickel ions concentration, so they stabilize the nickel phosphate precipitation and act also like pH buffers. Exultant, known as accelerators, are useful to increase the deposition rate and are the exact opposite of complexants and stabilizers. These last prevent the breakdown of the solution by shielding catalytically eventual active nuclei**.** Buffers are used for long-term pH control instead pH regulators are used for subsequent pH adjustment. Finally wetting agents increase the wettability of the surfaces that has to be coated **[70]**.

It follows a list where are described the components, seen before, and some of physical properties are shown in Table (2.2):

Table (2.2): Physical Properties of Ni-P Matrix Coating**[71]**:

Property	**Value**
Organization of the Coating	Amorphous in precipitation state, crystallized when heat treated
Melting Temperature	890^{o}C
Electrical Resistance	60 μΩ /cm^{2}/cm at 15 °C
Thermal Conductivity	0.0105- 0.0135cal/cm.sec.°C
Wear Resistance	Superior to electroplating. Superior to industrial plating when heat treated
Thermal expansion	13* 10^{-6}m/m·K
Uniformity	Excellent.
Adhesion	Excellent.
Heat Resistance	Withstands high temperature oxidation
Corrosion Resistance	Equivalent to pure nickel
Hardness	Precipitation state: 500~550Hv, Heat treated at 400°C:800~1000Hv

2.7. Theory of Electroless Plating

Electroless nickel plating is different from most of the plating techniques. EN solutions contain a reducing agent such as sodium hypophosphite to drive the reaction that reduces nickel ions to their metallic state. Hypophosphite baths are the most common types of commercially used EN baths.

The mechanism of the electroless Ni-P deposition reactions taking place in the hypophosphite bath is not well understood, but it has been postulated that it occurs in microcells of alternating anodic/cathodic polarity on the surface of the substrate. The chemical reactions that occur when using sodium hypophosphite as the reducing agent in electroless nickel plating are as follows **[72]**:

$3NaH_2PO_3 + 3H_2O + NiSO_4 \leftrightarrow 3NaH_2PO_3 + H_2SO_4 + 2H_2 + Ni$ . ...…. .2.2

$H_2PO_2^- + H_2O \leftrightarrow H^+ + HPO_3^{-2} + 2H$ .... ………………..2.3

$2HPO_2^- + Ni^{++} + 2H_2O \leftrightarrow 2H_2PO_3^- + H + 2H^+ + Ni$......………. ….......2.4

$Ni^{2+} + 2H \leftrightarrow Ni + 2H^+$ ………………………………………….........2.5

$H_2PO_2^- + H \leftrightarrow P + OH^- + H_2O$ ……………………..……………… ……. 2.6

Reactions (2.4) to (2.6) are responsible for the formation of the Ni-P alloy coating. Also the reactions of electroless plating by Ni-Cu-P are presented:

$\mathrm{Cu(II)} + 2H_2PO_2^- + 2H_2O \rightarrow Cu + 2H_2PO_3^- + H_2 + 2H^+$ …...............2.7

$2\mathrm{Cu(II)} + 2H_2PO_2^- + 2H_2O \rightarrow 2\mathrm{Cu(I)} + 2H_2PO_3^- + H_2 + 2H^+$ …..............2.8

These reactions resulted in reduction of Zn, Ni, and P on the metal surface as follows :$Ni^{+2} + H_2PO_2 + 2H_2O \rightarrow Ni + H_2PO_3^- + 2H^+$……………………... 2.9

$2H_2PO_2 \rightarrow H_2PO_3^- + P + OH^- + ½ H_2$………………..……………2.10

$Zn^{+2} + 2e \rightarrow Zn$……………………………………………………..2.11

Thus in the EN plating process, the driving force for the reduction of nickel metal ions and their deposition is supplied by a chemical reducing agent in solution. This driving potential is essentially constant at all points of the surface of the component, provided the agitation is sufficient to ensure a uniform concentration of metal ions and reducing agents **[72].**

2.7.1 Phase Diagram of Nickel-Phosphor Alloys

The phase diagram for nickel-phosphorus alloys was originally developed by Konstantinov in 1908, many years before electroless nickel was discovered. It was modified by Hansen in 1943 and by Koeneman and Metcalfe in 1958**[73]**.

Phase or constitution diagrams are representations of the structures present in equilibrium in an alloy at different compositions and temperatures. They are used by metallurgists as road maps for alloy design, heat treatment, performance prediction, failure analysis, and the like. Most are binary, consisting of mixtures of only two elements. Phase diagrams are normally developed by combining pure elements, melting the mixture at high temperature to homogenize it, then slowly cooling the alloy to room temperature. The formation of phases is then normally detected by thermal analysis, by X-ray diffraction, or by microscopic observation **[73]**.

At temperatures below the melting point, the conventional diagram shows only two phases for alloys containing less than 15 percent phosphorus. There is a very small solid solution region called alpha (α), and the nickel phosphide, Ni_3P. The alpha phase consists of less than 0.17 percent phosphorus dissolved in nickel. Ni_3P is an intermetallic compound containing 15 percent phosphorus. The region between these two phases consists of a mixture of α and Ni_3P. This diagram has frequently been used to try to explain the structure of electroless nickel coatings. Different authors have theorized that Ni_3P and other phosphides were present in the as-deposited coating, and that the deposit consisted of a mixture of these intermetallic compounds with a nickel. Figure (2.6) illustrates the phase diagram of nickel –phosphor alloy **[73].**

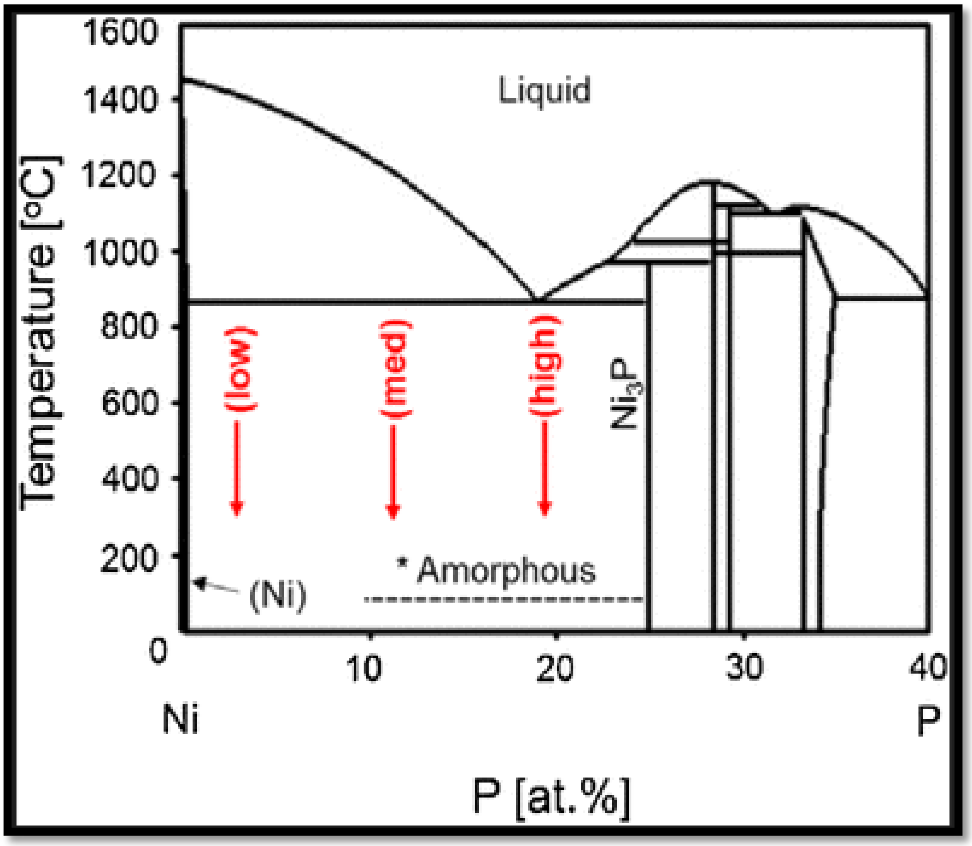

Figure (2.6): Phase Diagram of Nickel - Phosphor Alloys **[73]**

2.7.2 Effective Parameters

There are numerous parameters affecting the EN process. The following function, describes the deposition rate as a function of effective parameters of the EN method **[72,74]:**

$D = f\ (T, pH, C_{Ni}^{2+}, Red, C_{Red}, n_1)$ .... ……………………………………..2.12

Where: D= Deposition rate

T= Temperature

pH= solution pH

C_{Ni}^{2+} = Concentration of nickel in the solution

Red= Type of the reducing agent

C_{Red} = Concentration of reducing agent

n_1 = Agitation factor

2.7.2.1 Effect of Temperature

Temperature is the most important parameter affecting the EN deposition rate. Most of the reactions involved in the deposition process are endothermic. As a result, by increasing the temperature the deposition rate increases. The increasing in temperature of solution bath increased the chemical reaction due to increase of motion of ions, molecules and electrons.

Figure (2.7) illustrates the effect of temperature on the deposition rate .As the Figure shows, the deposition rate increases with increasing bath temperature. Most of the acidic baths are operated at 80-90°C while the alkaline baths can be operated at lower temperatures (as low as 40°C). This is why alkaline baths are used for coating plastic substrates **[72,74].**

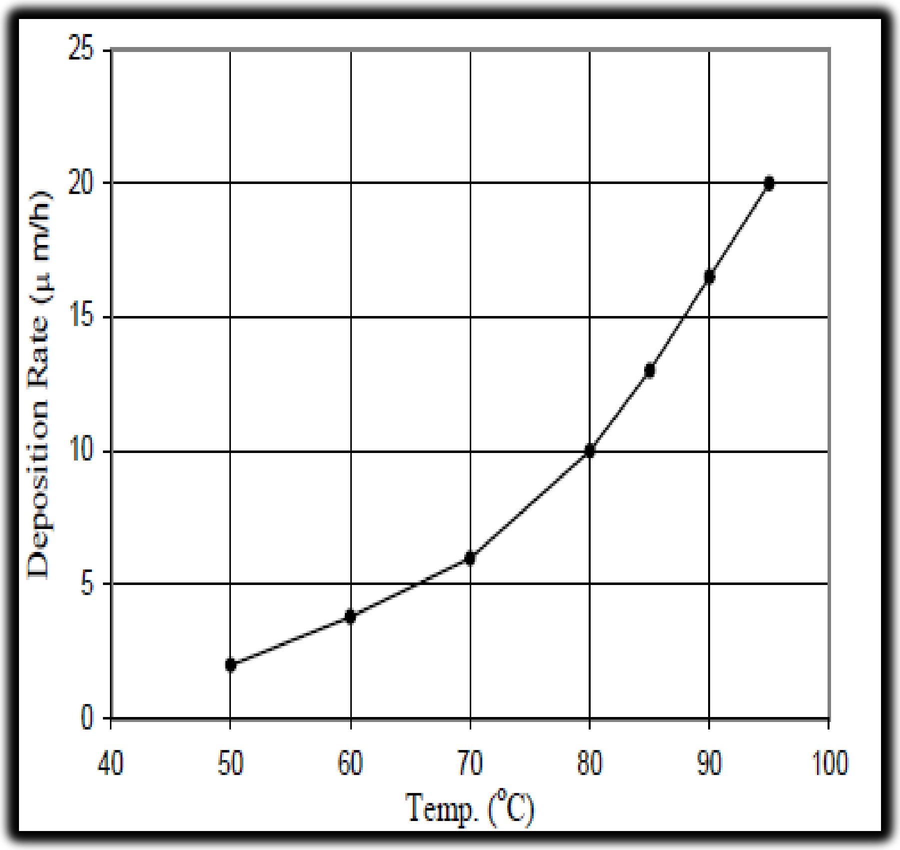

Figure (2.7): Effect of Temperature on the Deposition Rate **[72].**

2.7.2.2. Effect of pH

Many of the reactions involved in the EN process are sensitive to changes in the pH of the solution. By increasing the pH the nickel-reduction reaction is accelerated. On the contrary, by increasing the pH of the solution, the phosphorus reduction is retarded. This is due to the production of hydroxide ions as a result of the phosphorus reduction reaction. Therefore, increasing the pH of the solution decreases the phosphorus content of the coating. Also, since the nickel reduction reaction predominantly controls the deposition rate, increasing the pH of the solution increases the deposition rate. Figure (2.8) illustrates the effect of pH of the solution on both deposition rate and phosphorus content **[74].**

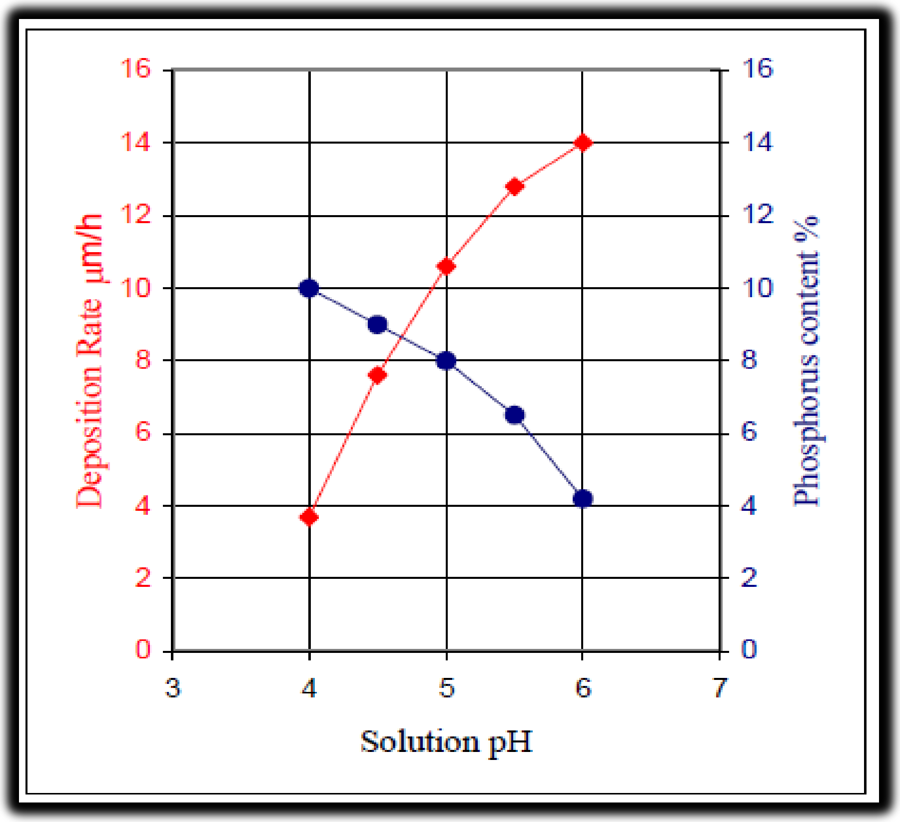

Figure (2.8): Effect of pH on Deposition Rate and Phosphorus Content **[72]**.

2.7.2.3 Effect of Bath Composition

The Ni concentration as well as the Ni^{++}/H_2PO_2 ratio are two important parameters affecting deposition rate. If the Ni^{++}/H_2PO_2 ratio is too low, the lack of Ni ions in the solution causes a brownish coating on the specimen. Also, the lower the value of the Ni^{++}/H_2PO_2 ratio, the higher is the concentration of the hypophosphite ions and the danger of solution decomposition increases **[72,74].**

On the other hand, if the Ni^{++}/H_2PO_2 ratio is too high, the phosphorus content of the deposition decreases **[72,74].**

2.7.2.4 Effect of Agitation Factor

Good dispersion and uniform coating of the particles in the solution of bath of the coating required suitable solution agitation. To achieve an effective bath agitation different ways are used such as vibration of the ultrasonic and dynamic agitation. Also to that, used of surfactants in combination by agitation of the bath to maintain particles of powder in suspension **[75].**

2.8 Applications With Matrix of Nickel-Phosphor Coating

There are many applications for nickel-phosphor coating as a result of its high resistance to corrosion, wear, erosion and carry to high temperatures. These applications include chemical, medical, industrial and food. Most applications of electroless and electrodeposition nickel- phosphorus matrix used to protect the metallurgical materials, none metal material from wear, erosion. Not only these plating were used to enhance surface properties but also may be used to improve magnetic and some of mechanical properties **[72,76]**.

Table (2.3) shows a lot of applications of EN and Figure (2.9) depicted some of applications of Nickel –Phosphorus.

Table (2.3): Applications of Ni-P Matrix Coatings **[72]**.

Application	**Components**	**Thickness (µm)**
Automotive	Heat sinks, carburetor components, fuel injection, ball studs, disk brake pistons ,transmission thrust washers, pins, exhaust manifolds pipes, and gear	2-38
Air craft/ aerospace	Compressor blades, hot zone hardware, pistons heads, engine main shafts and propellers, seal snaps, oil nozzle components.	10-50
Chemical & petroleum	Pressure vessels, reactors, pumps and impellers, heat exchangers, turbine blades, compressor blades and impellers, spray nozzle	25-125
Electronic	Head sinks, computer drive mechanisms, chassis memory drums and discs, diode and transistor	2-25
Material &handling	Hydraulic cylinders and shafts, extruders, link drive belts, gears and clutches	12-75
Medical	Disposable surgical instruments and equipment, pill sorters and feed screws	12-25

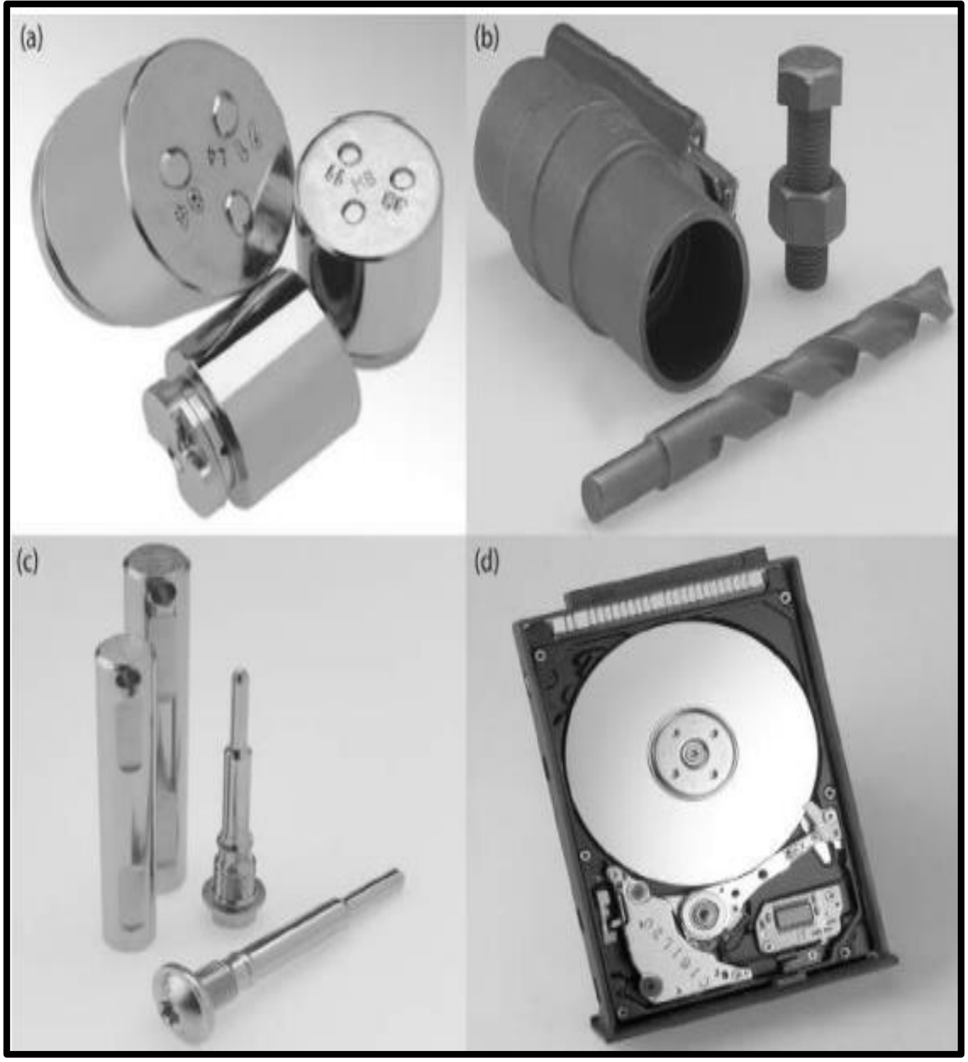

Figure (2.9): Electroless Ni-P-Plated Components (a) Machine Components, (b) Fittings with Nut and Bolt, (c) Special Screws and Pins and (d) Computer Hard Disk. **[73]**.

2.9. Heavy Fuel

Oil and natural gas were formed hundred years ago from the prehistoric plant and animals. It is believed that hydrocarbon formed by the thermal maturation of organic matter buried deep in earth. Over the millions of years under extreme pressure and high temperature these organic matter converted to hydrocarbons consisting of oil and gas. Hydrocarbons are present in the variety of forms: koregen, asphalt, crude oil, natural gas, condensates, and coal in solid form. Petroleum or crude oil is a complex mixture of hydrocarbons and other chemicals **[77].**

The composition varies widely depending on where and how the petroleum was formed. In fact, chemical analysis can be used to fingerprint the source of petroleum **[77]**.

Heavy fuel oil is a residual fuel incurred during the distillation of crude oil. The quality of the residual fuel depends on the quality of the crude oil used in the refinery. To achieve various specifications and quality levels, these residual fuels are blended with lighter fuels such as marine gasoil or marine diesel oil. **[78]**.

2.10. Stainless Steel

Stainless steel which alloy with good properties such as high corrosion resistance, oxidation resistance and possess excellent mechanical properties such as high tensile strength and high durability**.** They exhibit a combination of mechanical strength and resistance to surface degradation. Stainless steels have been used in aircraft,cars, industrial, gas turbines, nuclear reactors, aircraft skins, spacecraft structures, petrochemical production, orthopedic and environmental protection applications **[79]**.

Historically, stainless steels have been classified by microstructure and are described as austenitic, martensitic, ferritic, or duplex (austenitic plus ferritic). In addition, a fifth family, the precipitation-hardenable (PH) stainless steels, is based on the type of heat treatment used rather than the microstructure**[80]**.

2.10.1. Austenitic Stainless Steels

Constitute the largest stainless steel family in terms of alloys and usage. They include these grades:

- Iron-chromium-nickel grades corresponding to both standard AISI 300-series alloys and modified versions of these alloys. Such alloys, which are based on type 304 (18-8) stainless steel, generally contain 16 to 26% Cr, 10 to 22% Ni, and small amounts of other alloying elements such as molybdenum, titanium, niobium, and nitrogen.

- Iron-chromium-manganese-nickel grades corresponding to both standard AISI 200-series alloys and modified versions of these alloys. In these alloys, manganese (5 to 18%) replaces some of the nickel. Nitrogen alloying is also common with these alloys.
- Highly alloyed iron-nickel-chromium stainless steels for more severe corrosive environments. Nickel contents in these alloys can be as high as 35%. Molybdenum and copper additions are also common.
- Superaustenitic grades containing 6% Mo as well as liberal amounts of chromium, nickel, and nitrogen for improved corrosion resistance**[80]**.

2.10.2. Ferritic Stainless Steels

Ferritic stainless steels are non hardenable iron-chromium alloys. They include the following:

- Standard 400-series alloys as well as modified versions of these alloys containing 11 to 27% Cr, 0.08 to 20% C, and small amounts of ferrite stabilizers, such as aluminum, niobium, and titanium.
- More recently developed low-interstitial content (low carbon/nitrogen) grades containing higher chromium (up to 30%), molybdenum (up to 4%), and nickel (up to 2%). Such grades, which exhibit excellent resistance to stress-corrosion cracking (SCC), are referred to as super ferritics**[80]**.

2.10.3. Martensitic Stainless Steels

Martensitic stainless steels are similar in composition to the ferritic group but contain higher carbon and lower chromium to permit hardening by heat treatment. They include the following:

- Standard 400-series containing 11 to 18.0% Cr, up to 1.20% C, and small amounts of manganese and nickel.
- Nonstandard grades, including free-machining grades, heat-resistant grades, and grades for gears and bearings**[80]**.

2.10.4. Duplex Stainless Steels

Duplex stainless steels are supplied with a microstructure of approximately equal amounts of austenite and ferrite. These alloys contain roughly 22 to 25% Cr, 5 to 7% Ni, up to 4% Mo, as well as additions of copper and nitrogen. Some of the more highly alloyed, corrosion-resistant grades are referred to as super-duplex stainless steels. Duplex stainless steels are not covered by the standard AISI 200, 300, or 400 groups.

While most have UNS numbers, some are also referred to by their chromium and nickel contents. For example, alloy 2205 contains 22% Cr and 5% Ni**[80,81]**.

2.10.5. Precipitation-Hardenable Stainless Steels

Precipitation-hardenable stainless steels are chromium-nickel alloys containing alloy elements such as aluminum, copper, or titanium, which allow them to be hardened by a solution and aging heat treatment. They are further classified into subgroups as martensitic, semi-austenitic, and austenitic PH stainless steels**[80].**

They are used in the oil and gas, nuclear and aerospace industries where a combination of high strength, corrosion resistance and a generally low but acceptable degree of toughness is required. Precipitation hardening is achieved by the addition of copper, molybdenum, aluminium and titanium either singly or in combination **[80,81]**.

Table (2.4) shows nominal compositions of austenitic stainless steel alloys.

Table (2.4): Nominal Compositions of Austenitic Stainless Steel Alloys **[81]**.

Composition %						
Designation	**C**	**Cr**	**Ni**	**Mo**	**Fe**	**Others**
316	0.04	17.2	10.1	2.1	Bal.	
316L	0.02	17.2	10.1	2.1	Bal.	
304	0.04	18.1	8.1	-	Bal.	
304L	0.02	18.1	8.1	-	Bal	
321	0.04	17.3	9.1	-	Bal.	Ti
347	0.05	17.5	9.5	-	Bal.	Nb
303	0.05	17.3	8.2	-	Bal.	S
305	0.04	17.7	12.5	-	Bal.	
301	0.01	17	7	-	Bal.	
201	0.05	17	4	-	Bal.	7Mn

2.11. Mechanical Properties of Austenitic Stainless Steel Alloys

Austenitic stainless steels generally have a relatively low proof strength and are characterized by strong work hardening. The strength of the austenitic steels increases with increasing levels of carbon, nitrogen and, to a certain extent, also molybdenum. It should however be noted that carbon increases the risk of sensitization, which has a detrimental effect on corrosion resistance. Austenitic steels exhibit very high ductility; they have a high elongation to fracture and are very tough, also at low temperatures**[81].**

Some of ASS with a low total content of alloying elements; e.g. 4301, 4310, 4318 and 4372 can be meta- stable and may form martensite either due to cooling below ambient temperature or through plastic deformation or a combination of both. This formation of martensite will cause a considerable increase in strength and will also influence the magnetic properties**[81].**

The mechanical properties of stainless steels are strongly affected by the degree of cold work. In particular the work hardening of the austenitic steels causes considerable changes in properties after, e.g. cold forming operations. The general effect of cold work is an increased proof and ultimate tensile strength and at the same time a decrease in the elongation to fracture**[81].**

Table (2.5) displays some of mechanical and physical properties of austenitic stainless steel 316L which is chosen the base metal in this study.

Table (2.5): Physical and Mechanical Properties of Austenitic Stainless Steel**[81]**.

Physical Properties	
Density	7.9-8.1 g/cm^3
Electrical Resistivity	0.8 µΩm
Mean Coefficient of Thermal Expansion	(17-18)*10^{-6} /^{o}C
Thermal Conductivity	15 W/m^{o}C
Melting Range	1450-1530 ^{o}C
Mechanical Properties	
Tensile Strength	560-580 MPa
Vickers Hardness	300-330 HV
Ultimate Tensile Strength	580-620 MPa
Yield Strength	255-280 MPa
Poisson's Ratio	0.28-0.3
Modulus of Elasticity	195-215GPa
Fracture Toughness	110-130MPa m$^{0.5}$

2.12. Review of Literatures

Firstly, several researchers had been studied the failure analysis in stainless steel alloys at multiple places, especially in,oil and petrolium industral, the blades of gas turbines, steam turbines , heavy fuel turbine,seperators that work by heavy fuel.

Finally, some researchers were studied the reduction of the failure by electroless plating these alloys and others in other ways. In this work, the reduction of failure by electroless plating with binary alloys ,ternary alloys and compsite coating are studied .

2.12.1 Studies Related to Failure Analysis

In 2020, Xiaojia et.al[82] studied the failure analysis in 304 stainless steel (304 SS) tube used as a steam heater in a liquid sulfur recovery unit.The failure was investigated by using various characterizing techniques(XRF , XRD,SEM with EDX and visual tests). The investigation revealed the outer wall of the heat exchanger underwent severe pitting corrosion, and the formation of cracks was initiated from the outer wall pits. The cracks were branched and propagated mainly in a transgranular mode. Pitting, intergranular corrosion and corrosion thinning due to the external medium led to the failure of the heat exchanger by SCC. XRD and EDX analyses showed that the corrosive medium mainly contains sulfur compounds and some chloride ions. The resulted in this study suggest that the failure of the 304 SS tube occurred due to pitting, intergranular corrosion and SCC caused by sulfuric acid and chloride ions.

In 2021, Zhou et.al [83] studied the failure analysis in four-way flange. The failures were analyzed by reading spectrometer, Rockwell hardness tester, optical microscope, scanning electron microscope, energy dispersion spectrometer and numerical simulation method. The results show that the chemical composition, hardness and grain size of the four-way flange and connecting gate valve meet the standard requirements; By microstructural characterization and energy spectrum analysis, it is confirmed that a large number of corrosion products are attached to the inner wall of the four-way valve and gate valve. At the same time, a large numbers of eddy current are formed at the intersection of the four-way and the gate valve flows channel. Rockwell hardness test results for four gate(A,B,C and D) were225 HB-HLD 219 HB-HLD 218 HB-HLD and 221 HB-HLD respectively. Also measurement results of connecting gate valve were 212 HB-HLD 218 HB-HLD 214 HB-HLD 205 HB-HLD.

In 2021, Yan et.al [84] studied the causes of failure in the stainless-steel bend pipe is used to transport the media that contains H_2S and NH_3 in sewage stripping unit.The failure analysis is carried out by using traditional characterization techniques and computational fluid dynamics. Results demonstrate that the high risk area obtained from CFD simulation coincides with the practical breakage area. Not only the corrosive medium dissolving in sewage contributes to the failure of the elbow, but also the inserted thermocouple leads to the uneven distribution of flow velocity inside the pipe which aggravates the local erosion-corrosion of the elbow. The failure morphology of the elbow provides a series of information for failure analysis. Hardnes Vickers for six position were 1-228.1HV , 2-217.1HV, 3-211.9HV, 4 226.2HV, 5-228.1HV and 6 - 226.9HV.

In 2022, Peng et.al [85] studied the causes of failure in the 316L stainless steel steam tube. Optical microscope, energy dispersive spectrometer,scanning electronic microscopy and numerical simulation were used to analysis the failure reason of the failed bellows. Through the investigation of the operating environment, analysis of the chemical compositions of bellows material and corrosion products, micromorphology and metallographic test of specimens with cracks, the cracking mode can be described as the stress corrosion cracking of austenitic stainless steel. The simulation analysis results further proved that there exists high level tensile stress zone on the inner surface. Based on the analysis results, failure causes can be drawn: under the combine action of working stress and corrosion medium (caustic Na and chloride), stress cracks came into being at the inner wall of the bellows.

In 2022, **Rivaz et.al [86]** studied the causes of failure in turbine blade made of 410 stainless steel was under operation for 72,000 h. As well, mechanical properties evaluation was performed using hardness testing. Results showed that the existence of foreign particles in the environment of the turbine has led to the initiation of damage in the blade through the erosion mechanism. Alternatively, such a damage was intensified by corrosion attack due to the presence of the fuel impurities. Such damages eventually led to the formation of fatigue cracks on the trailing edge of the blade. The latest phenomenon substantially reduced the fatigue strength of the blade.

In 2022, Wang et.al [87] studied the failure analysis pump casing and wear ring of an S32760 duplex stainless steel fire pump assembled on an offshore platform. The failure mechanism of the cracked wear ring was analyzed, and results showed that the chemical composition of the wear ring corresponds to the standard S32760.

However, metallographic test results showed that the wear ring has many harmful σ-phases and inclusions in the matrix, which led to the decrease of corrosion resistance of the material and induced crevice corrosion at the bolt joint and the wear ring. Besides, chloride, sulfide, sodium and potassium have been found at corrosion products and pump casing fragments through energy dispersive X-ray spectrometry.

In 2022, Mohapatra et.al [88] studied the causes of failure in the skirt plate used in the reduction shaft of Corex plant at areal gas distribution that failed after seven years of service. The analysis involved composition, hardness, mechanical properties, impact toughness, microstructure and phase analysis in the failed plate, and after solution annealing the plate for different lengths of time. It was found that the plate completely embrittled due to formation of massive $Cr_{23}C_6$ type carbides and σ-phase (FeCr) for prolonged service at high temperature (~ 850°C), observed through microstructure and EDS analysis). The fracture surface showed intergranular brittle failure. After solution annealing treatment, the massive carbides and phases were mostly dissolved resulting in the restoration of the property.

In 2022, Gokhale et.al [89] studied the causes of failure in the reheater tube made of stainless-steel SS 304 in power plant. Optical and electron microscopy was used in the analysis in the vicinity of the attachment weld on the reheater tubes. Even though microstructural investigation showed no sign of sensitization, the presence of chloride (Cl), identified through SEM-EDS scan, and localized strain, identified through EBSD scans near the failed region, confirmed stress corrosion cracking in the material.

The results obtained during the investigation have clearly brought out the cause of stress corrosion cracking in reheater tube. Further, it was observed that the weld bead size played an important role in inducing residual stress in the material and the bead size was modified to address the localized stresses at the weld; this helped in solving the problem.

In 2023, Wang et.al [90] studied the failure of the circumferential weld (C-Weld) of the inner tank. The failure was analyzed by optical microscopy, scanning electron microscopy, energy dispersive spectrometer, and microhardness test.

Results show that the fracture of the C-Weld was induced by stress corrosion cracking (SCC). The corrosion and crack propagation resistance of the C-Weld are worsened by the presence of coarse grains in HAZ. The high axial stress component generated by the superposition of welding residual stress and working stress is the main driving force of crack expansion. The presence of the root gap of the C-Weld leads to stress concentration, which is more likely to cause scaling and accumulation of chloride ions, resulting in crevice corrosion.

2.12.2. Studies Related to Electroless Plating of (Ni-P)

In 2016, Smoljan et.al [91] focused on comparison of testing methods of adhesivity of electroless nickel-phosphorous coatings and analyses of influence of heat treatment on adhesivity of electroless nickel-phosphorous on SS316L.The results show that adhesivity of electroless nickel-phosphorous coatings can be successfully characterized by Vickers hardness tester.Based on experimental results it was found out that heat treated nickel-phosphorous coatings have higher microhardness than non-heat treated electroless nickel-phosphorous coatings. High microhardness of heat treated nickel-phosphorous coating is connected with formation of Ni_3P phase.

Moreover, better adhesivity can be achieved by application of proper activation process before electroless coating. The obtained microhardness of the non-heat treated electroless Ni-P coating on austenitic stainless steel AISI 316 substrate was 429±17 HV, while the hardness of the heat treated electroless Ni-P coating was 853±26 HV**.**

In 2017, JEKLA et.al [92] studied the properties of electroless deposited nickel-phosphorous coatings on an austenitic stainless-steel 316L substrate. The main study was focused on the influence of heat treatment on the microhardness and microstructure analysis of electroless Ni-P coatings. A nickel-phosphorous coating was deposited without nickel-strike pre-coating treatment. An electroless Ni-P layer was deposited on a stainless-steel substrate. Sodium hypophosphite was used as the reducing agent. The microstructure and morphology of heat-treated electroless specimens were analyzed with optical and scanning electron microscopy. Adhesivity was estimated with a Vickers indenter.

Based on the experimental results, it can be concluded that heat-treated electroless nickel-phosphorous coatings have a higher microhardness than non-heat-treated electroless nickel-phosphorous coatings. An analysis of the Vickers indentation results showed that the proposed electroless process gives satisfactory results.

In 2018, Fayyad et.al [93] studied the Coatings can be carried through various routes (e.g., mechanical and electrochemical plating techniques). Electroless nickel coatings present unparalleled properties and a unique combination of corrosion and wear resistance features. Recently, the use and development of electroless nickel-phosphorus (ENP) coatings has attracted broad attention from many industries (e.g., oil and gas) due to their superior corrosion and wear resistance properties. In the present review article, mechanisms of ENP and preparation methods are briefly outlined. The review sheds light on properties of electroless Ni-P coatings and of their nanocomposites with an emphasis on new products and on their future development.

In 2018, Fayyad et.al [94] studied the electroless plating of Ni-P on carbon steel specimens .The bath composition of electroless plating was nickel sulfate 15g/L, sodium hypophosphite 30g/L, lactic acid 20g/Land citric acid 20 g/L .Several tests were carried out in this study , micro-hardness, XRD,SEM, surface roughness, thickness of coating and Tafel analysis. The results showed that the micro-hardness increased from 160HV_{200} for substrate to 406 HV_{200} after plating. XRD analysis showed the presence of Ni_3P on surface of coated specimens. In Tafel analysis the corrosion current density in 3.5%NaCl were 21.4,1.84$\mu A/cm^2$ for substrate and coating specimens by Ni-P respectively.

In 2019, Kazimierczak et.al [95] studied the electroless plating of Ni-P on copper substrate. The study included certain effect parameters on deposition rate such as temperature and pH. Several examinations were carried out to know the phases that appeared and the morphology of surface coating. XRD was stated that alloy coating containing 5.5%wt phosphorus displayed completely crystalline microstructure and it showed that coating consist of Ni_3P. SEM showed that the surface of specimens was bright and smooth. The results showed that surface morphology depends on the deposition rate of alloy.

In 2022, Rajabalizadeh et.al [96] investigated in electroless Ni-P-MOF nanocomposite coating on AM60B magnesium alloy**.**The results show that SEM images captured with two various zooming scales from the surface of the plain and MOF containing electroless layers showed cauliflower-like morphology with even distribution of nodule size. Also, the sub-grains of the plain coating disappeared after incorporation of the MOF. Although, both the normal and nanostructure-containing electroless layers have crystalline-amorphous structure, but the nanocomposite coating showed less crystallinity. The average surface roughness of the plain electroless coating was about 309 nm, which decreased to about 222 nm after incorporation of the MOF. The XRD patterns showed that the characteristic peak of Ni broadened after incorporation of the MOF, probably due to the decreasing of the crystallinity. For the heat-treated normal and MOF containing coatings at 200 °C no phase transition takes place, but new peaks appeared for heat-treated coatings at 400 °C due to the crystallization and second-phase precipitation.

In 2022, Fu et.al [97] worked on 16Mn steel plate as the base substrate for electroless plating by Ni-P/Ni-Mo-P duplex coating with Ni-P coating as the inner layer and Ni-Mo-P coating as the outer layer. The results show that the porosity of Ni-P/Ni-Mo-P duplex coating is only 1.2 spot/cm^2 for the best corrosion resistance, and its surface density is better than that of the Ni-P single-layer coating and Ni-Mo-P single-layer coating. Compared with the substrate, the corrosion current density of Ni-P/Ni-Mo-P duplex coating is reduced by nearly two orders of magnitude, and the protection efficiency reaches 98.5%, which can play a better role in corrosion protection and significantly improve corrosion resistance of 16Mn steel in seawater.

In 2022, Kumar[98] investigated on electrolessplating by Ni-P with or without B_4C particles on steel substrate . It was seen that a remarkable increase in corrosion resistance and hardness value achieve because of presence of B_4C nanoparticles in the electroless bath coating. Also wear resistance was improved. Basically the heat treatment at 400°C for 1 hour may responsible for enhancement of wear and hardness performance. The reason behind the improvement of corrosion resistance of substrate when incorporation B_4C particles was done , because of reduction of porosity of Ni-P coating and its increasing coherence as well as the development of the surface with a high chemical resistance mechanism against corrosive environment. resulted in the improvement of the corrosion resistance of Ni–P–B_4C composite coatings

In 2022, Kumar et.al [99] studied the electroless plating of Ni-P matrix contains strapping ZnO nanoparticles as white globules. The electroless platings of thickness 6–10 μm were deposited on mild steel substrates (grade AISI1040). The as-deposited platings show mostly amorphous structures. On the other hand, heat treatment of platings (200 °C to 600 °C in steps of 200 °C in argon atmosphere for 1 h duration) transform the structure from amorphous to crystalline state. The well-developed Ni-P/Ni-P-ZnO deposits have also been tested for microhardness and wear resistance by microhardness and wear testers. The results of the micro-hardness and wear tests on well-developed Ni-P/Ni-P-ZnO platings showed that good insertion of ZnO nanoparticles into the Ni-P matrix and had a significant effect on microhardness and wear resistance. The phase changes of the Ni-P-ZnO nanocomposite plating at 400 °C further enhanced the microhardness as well as wear resistance.

In 2022, Fayyad et.al [100] studied the electroless plating of Ni-P matrix on carbon steel. Halloysite nanotubes and their modifications with either NH_2 (HNT-NH_2) or NH_2/Polypyrrole were electroless-deposited into the NiP matrix for the first time to form NiP/HNT, NiP/HNT-NH_2 and NiP/HNT–NH_2–PPy nano-composite coatings. The as-prepared nanocomposite coatings were heat-treated at 400 °C for 1 h. The transformation in microstructure, nano-indentation, Vicker's microhardness, surface morphology, and anti-corrosive properties of all prepared composite coatings were compared to the HNT-free (NiP) coating. Incorporating HNTs in the NiP coating made an appreciable enhancement in the hardness and corrosion resistance. Using the electrochemical impedance spectroscopy technique (EIS), the NiP/HNT-NH_2 and NiP/HNT–NH_2–PPy coatings showed more significant levels of enhancement in anticorrosion performance, offering about 16.5% and 25.4%, respectively, an increase in the inhibition efficiency of unmodified one (NiP/HNT), reached to 73 and 82%.

Moreover, the modified HNT coatings revealed slightly high levels of betterment in microhardness, about 9% and 5.4% for HNT modification with NH_2 and NH_2-PPy, respectively. In addition, the heat treatment extra improved the hardness and the corrosion resistance of all HNTs nanocomposite coatings compared to HNT-free coating. Furthermore, the heat-treated NiP/HNT has the highest protection efficiency reached to about 95%, based on the polarization measurements.

In 2023, Li et.al [101] studied the electroless plating of Ni-P was deposited on a low carbon steel substrate.Heat treatment with a range from 200 ◦C to 500 ◦C for 1 h. Anodic electrochemical behavior was investigated by potentiostatic methods in a 3.5 wt% NaCl solution.

The experimental results indicate that the diffusion, dissolution, and enrichment of the component elements in the Ni-P alloy are essential during crystallization because the various corrosion behaviors corresponding to Ni and P are directly affected. More importantly, under the 400 ◦C treatment, H_2PO_2 was enriched in the alloy, which effectively hinders the anodic dissolution of nickel and forms a complete adsorption layer on the surface of the alloy.

The results demonstrate that P can effectively block the anodic dissolution of Ni during the corrosion process, and the crystallization process can effectively promote the surface enrichment of P to improve the corrosion resistance of the coating. The results show that P alone cannot form a passivation film at high polarization potentials.

In 2023, Khaira et.al [102] in this study the electroless Ni composite coatings are fabricated on low carbon steel (AISI1020) specimens. X-ray diffraction (XRD) confirms the crystalline nature of as deposited Ni–P alloy coating which transforms to a structure with short-range order in presence of hBN particles in the electroless bath. Ni–P-hBN (H0.5) composite coating fabricated in addition of DES in the electroless bath shows a significant difference in wear mechanism and reduction of friction coefficient from 0.4 to 0.3 as compared to coating deposited from conventional electroless bath.

Microhardness evaluation of the coatings presents the dependence of hardness of the coating upon the content of phosphorus in the composite. The results shows the average thickness of the deposited layer being maintained at or near 40 μm. Scratch hardness and fracture toughness from scratch response confirm an increased scratch hardness value ranging from 7.50 to 8.51 GPa and fracture toughness value from 7.83 to 8.54 MPa-m$^{0.5}$respectively with addition of DES compared to conventional electroless Ni–P-hBN composite coating from bath containing 0.5 gm/l of Hbn**.**

2.12.3 Studies Related to Electroless Plating of (Ni-Cu-P)

In 2022, Davoodi et.al [103] studied the effect of copper content in electroless plating of Ni-Cu-P on substrate L80 steel substrates. Heat treatment at 200 and 400 °C are conducated on as-plated specimens. The results of Tafel polarization and electrochemical impedance spectroscopy tests in 3.5% NaCl solution indicated that for non-treated samples treatment, the corrosion resistance was improved by increasing the thickness of the coating due to the filling of the micropores. Furthermore, the corrosion resistance was highly increased for the sample treated at 400 °C for 1 h because of the increase in the $Ni_{3.8}Cu$ phase in the electroless $Ni\text{-}Cu_m\text{-}P$ coating. In addition, it was observed that at thicknesses above 50 μm, the corrosion resistance of the samples treated at 400 °C was reduced due to the formation of microcracks. Nevertheless, the highest corrosion resistance was attributed to the electroless $Ni\text{-}Cu_m\text{-}P$ coating with a thickness of 25 μm and the Ni–P coating with a thickness of 50 μm the resulted coatings were heat treated.

In 2022, Biswas et.al [104] investigated on electrolessplating by duplex Ni-P/Ni-Cu-P on mild steel substrates. Coatings are developed on substrates with Ni-Cu-P as the outer layer and Ni-P as the inner layer. The coated samples are heat treated at temperatures ranging between 200 to 800 °C during 1 and 4 h. The results show that the duplex coatings can provide substantial protection to the mild steel substrates.

Heat treatment is also found to have a significant influence on the corrosion behavior of duplex coatings. The results of corrosion study show that the duplex coatings are able to provide significant protection to the mild steel substrates. Heat treatment results in an increase in the corrosion resistance of the coatings. Corrosion resistance is severely compromised for higher heat treatment conditions, viz. 800 °C This is due to the formation of microcracks and oxides at these conditions. Overall, it can be said that 400 °C and a time duration of 1 h is the optimal condition of heat treatment for the present duplex coatings.

In 2022, Biswas et.al [105] investigated on electrolessplating by duplex

Ni-P/Ni-Cu-P on mild steel substrates. Heat treatment is carried out at temperatures between 200 and 800°C. Heat treatment is found to significantly affect the coatings. The hardness is increased by about 43 % after heat treatment whereas friction and wear rate are reduced by about 50 % and 40 % respectively.

Heat treatment at 400°C is found to be the best for tribological performance of the coatings. The microstructural tests show the formation of nickel phosphide which are responsible for improved hardness of the coatings after heat treatment. However, heat treatment at higher temperature lead to grain coarsening and oxide formation which affect the tribological performance of the coatings negatively. The coating with Ni-Cu-P as the outer layer shows better corrosion resistance ability due to the presence of copper which promotes the formation of passive layer.

In 2022, Biswas et.al [106]studied the duplex electroless Ni-P/Ni-Cu-P and Ni-P/Ni–W-P coatings on mild steel substrate. Heat treatment is carried out at a temperature range between 200 °C and 800 °C. The results show that surface morphology of the as-deposited coatings is nodular. Grain growth and grain boundaries are clearly visible in heat treated coatings. The EDX of Ni-P/Ni-Cu-P and Ni-P/Ni–W-P coating showed the phosphorus content as 12% and 9% respectively indicating high-P deposits.

The copper and tungsten content of the coatings are 10% and 3% respectively.XRD analysis of both the as-deposited coatings indicate amorphous phase while heat-treated ones have crystalline phase structure. The crystalline structure increases the hardness of coating along with its wear resistance. The friction and wear behavior are assessed by a pin on disc tribometer. Overall, it can be seen that Ni-P/Ni–W-P system performs better compared to Ni-P/Ni-Cu-P in terms of wear.

In 2022, Davoodi et.al [107] studied the effect of copper content in electroless plating of Ni-Cu-P on substrate L80 steel substrates. The microstructure study by XRD showed that the Ni-Cu-P coating has an amorphous structure. The heat treatment at 400 °C transformed the structure from amorphous to crystalline and formed Niα, Ni_3P, and $Ni_{3.8Cu}$ phases. The amount of copper nanoparticles in the coating 4.58 wt% was measured. The deposition rate of the Ni-Cu-P coating was 11 µm/h. Furthermore, the hardness of the coating increased from 738HV to 1300HV by performing heat treatment.

In 2022, Mukhopadhyay et.al [108] investigated in electroless plating of ternary alloys Ni-Cu-P on rebars structure of Fe-600 grade steel. Investigation of electrochemical corrosion phenomenon (potentiodynamic polarization) was carried out in 3.5% NaCl to simulate saline coastal environment. Ni-P coatings with Cu and W inclusion were considered due to their proven corrosion resistance. The bath constituents such as nickel sulphate (Ni source), sodium hypophosphite (reducing agent and source of P) and the tungsten / copper concentration were varied to get various elemental composition following a sequential experimental design. The optimized coatings exhibited initiation of passivation which could prove to be beneficial for the health of the structure in the long-run. A noble corrosion potential and lower corrosion current density could be obtained in the coated rebars. The best results in Ni-Cu-P coatings were the E_{corr} and i_{corr} equel to -350 mV and 0.4 µA/cm^2 respectively. This was significantly lower compared to the bare rebars (E_{corr} = -653 mV and i_{corr} = 11.7 µA/cm^2.

In 2023, Bhattacharyya, [109] studied the electroless Ni-P-Cu coating on mild steel (AISI-1040) for improving its hardness, corrosion and wear resistance properties. The experiments are carried out varying the Cu concentration at 0 g/l, 0.2 g/l, 0.4 g/l, 0.6 g/l, 0.8 g/l, 1 g/l and 1.2 g/l in the electroless solution bath. Both corrosion and tribological analysis proved the sample Ni-P-Cu-1 with a copper concentration 1 g/l to be the best-optimised concentration for the experiment. Moreover, Vickers's microhardness of the coating with respect to mild steel specimen shows an increment of 40–70 %. The study can be readily scaled up by analysing the application on an industrial shell and tube heat exchangers; thus will be helpful for engineers and industrialists of the related field.

In 2023, Zhang et.al [110] studied the electroless plating by Ni-Cu-P on L360 steel substrate and knowing the effect of Cu concentration on coating. The experimental results show that the introduction of Cu can inhibit the growth of cellular structures on the surface of the coating, increase the number of nucleation points, and improve the microstructure of the coating during the deposition of Ni–Cu–P films. In addition, copper enables the composite coating to have passivation and a uniform and dense coating structure, which is the main reason for the improvement of the corrosion protection performance of the composite coating. The protective effect of the coating can effectively improve the electrochemical resistance and erosion resistance of L360. The Ni–P/Ni–Cu–P bilayer composite film reduces the electrochemical corrosion rate of the substrate from 0.417mpy to 0.025mpy, and the scouring weight loss rate of the film decreases to 0.05% of the substrate.

2.12.4 .Studies Related to Electroless Plating of (Ni-Zn-P)

In 2020, Fayomi et.al[111] investigated in electrolessplating by ternary alloys Ni-Zn-P on mild steel for advanced application. The coating was produced in an aqueous nickel electrolyte solution with zinc at a temperature of 90 ^oC and varying time conditions between 20 and 50 min. The corrosion characteristics of the coatings examined in 0.5 M H_2SO_4 and 3.5% NaCl were analyzed using linear potentiodynamic polarization technique.

The best results revealed that the microstructure constituent deposited on the steel.Also the microstructure revealed that the constituent deposited on the steel. A more uniformly distributed crystallite with minimal pores was observed at 20 min of Ni–P–Zn coating, while the tiniest film was observed at 50 min of the coating without crack. There was also a fully compact grain within the intermetallic matrix of the coating due to the synergetic effect of the electrolyte constituent with the strengthening phase of $Zn_7Ni_4P_2$, Zn_2Ni_5P, and Zn_3Ni.

In 2020, Kilanko et.al[112]studied the electroless depostion of Ni-Zn-P on mild steel substrate. Silicon nitrides and zirconium diboride as additives at a constant time was studied. The electrochemical corrosion analysis of the deposited mild steel with and without composite additives was analyzed using linear polarization resistance and open circuit potential in both H_2SO_4 and NaCl solution.

The results revealed that the structural evolution shows proper homogeneous crystal formation and stable packed additive concentrated at the lattices with EDS showing the presence of induced peak. From the corrosion assessment result, electroless deposited mild steel with Ni–P–Zn–10$ZrBr_2$ and Ni–P–Zn–10Si_3N_4 with optimum particle concentration shows better corrosion resistance performance with a corrosion rate of 0.5048 mm/year, and 5.1347 mm/year, as against the unadditive deposition with 11.393 mm/year in

NaCl solution.

In 2021, Fu et.al[113] investigated in electrolessplating by multilayer ternary and binary alloys Ni-Zn-P/Ni-P on Q235 low-carbon steel substrate. The results show when compared the low-phosphorus Ni-P coating with the high-phosphorus Ni-P coating, the three-layer Ni-P/Ni-Zn-P composite coating has uniform cell size, and the cells are dense and smooth.

The thickness of the inner layer of low phosphorus Ni-P coating is about 14.5 μm, the mass fraction of nickel is about 96.5%, and the mass fraction of phosphorus is 3.5%. The section thickness of the middle layer high phosphorus Ni-P coating is about 17.6 μm, the mass fraction of nickel is about 90.2%, and the mass fraction of phosphorus is about 9.8%.

The total section thickness of Ni-P/Ni-Zn-P composite coating is about 40 μm, the mass fraction of nickel is about 80.7%, the mass fraction of zinc and phosphorus are 7.6% and 11.7%, respectively. In Tafel polarization curve, the corrosion current density of Ni-P/Ni-Zn-P composite coating is the smallest, which is 3.815×10^{-6} A/cm^2 and has better corrosion resistance. After 220 h corrosion in simulated seawater 5%NaCl solution, the inner layer and middle layer were corroded into pieces, with holes and pitting corrosion.

In 2022, Kao et.al [114] investigated in electrolessplating by ternary alloys Ni-Zn-P on low-carbon steel substrate. The surface morphology, hardness, and corrosion characteristic of the Ni-Zn-P film coatings were measured. The results were that the X-ray diffraction patterns for all Ni-Zn-P films at 2θ～44.5° and~65.2° respectively correspond to Ni (111) and FeNi (200). Also The results show that the coating parameters and process performance of the films are controllable and stable.

Furthermore, increasing the external magnetic field strength increases the film thickness and improves the mechanical properties, and enhances the intensity of the diffraction peaks suggesting an improvement in the crystalline quality of the Ni-Zn-P film.

In 2022, Abdalla et.al [115] investigated in Ni-Zn-P electroless deposited on mild steel specimens substrate with dimension of 10×15×1.5 mm. The coatings were electroless formed at 85ºC for various deposition time (10, 30, 60 and 90 min). The results revealed that the weight loss of bare steel sample after 24 and 168 h of immersion time was 3.25 and 16.93 g/m^2 respectively, whilst it was 0.55 and 5.39 g/m^2 for the coating deposited with 90 min of process time.

It was also noticed that, as the process time increased the corrosion performance of coated substrates was improved indicating a remarkable effect of process time in the coating deposition and corrosion resistance. These results clearly revealed that the Ni-Zn-P coating provided an excellent corrosion protection to the mild steel surface and the best corrosion resistance obtained with deposition time of 90 min.

In 2023, Li et.al [116] studied the electroless plating by Ni–Zn–P onto a low carbon steel substrate (AISI 1005 steel). The substrates pretreated using the proposed roughening (15 % H_2SO_4, 20 min) and activation (10 % H_2SO_4, 1 min) produce good Ni-Zn-P film deposition.

The results show that when the annealing temperature reaches 400 °C, the Ni–P-Zn films contain crystalline Ni, Fe Ni and a precipitation Ni_3P structures phase. Applied magnetic field improves the film growth rate, mechanical properties and corrosion resistance. The mechanical properties, resistance to corrosion and fatigue life of Ni-Zn-P ternary alloys are enhanced if a relatively long roughening time is used.

2.12.5. Studies Related to Electroless Plating of Compsite Coating (Ni-P-SiC)

In 2019, Dhakal et.al [117] studied the electroless compsite coating by Ni-SiC-P onto Cu-plates of size(20 mm × 15 mm × 2 mm)substrate. Heat treatment for coated specimens at 400 °C for 1h are carried out. After the heat treatment, the matrix phase transformation was not altered due to the incorporation of SiC or TiC into the Ni-P coating; however, a slight increase in residual stress was identified from the XRD analysis. In addition, the content of carbon deposition was found to be higher in the matrix of Ni-P-SiC composite coating than that in the NiP-TiC coating. The agglomeration of SiC particles was higher than TiC particles in the coating matrix. Heat treatment improved wear and coefficient of friction in the Ni-P-SiC and Ni-P-TiC composite coatings. Compared to Ni-P-SiC coating, Ni-P-TiC coating revealed the enhanced tribological and scratch resistance performance after the heat treatment.

In 2020, Ram et.al [118] investigated on electroless Ni-P-SiC/Ni-P-TiO_2-ZrO_2 nano-composite platings have been deposited upon mild steel substrate (AISI 1040). A homogeneous and consistent allocation of SiC, TiO_2 and ZrO_2 nano-particles into EL Ni-P matrix is recognized in as plated and heated (400°C) coupons respectively through SEM and EDAX methods. The investigated coupons exhibited resistance against corrosion in order as: 254SMO > SS2205 > Ni-P-TiO_2-ZrO_2 as-plated > Ni-P-TiO_2-ZrO_2 heat treated > Ni-P-SiC as-plated > Ni-P-SiC heat treated > SS316L.

In 2020, Fu et.al [119] studied the electroless compsite coating by Ni-SiC-P onto AZ31 alloy substrate. Various amounts of nano -SiC particles were used to enhance the hardness, corrosion and wear resistance of the coatings.

Polarization tests were carried out for investigating the corrosion resistance of the coatings. Pin on disk test s were used to study wear behavior of the coatings. The effect of heat treatment temperature s on the coatings structure, hardness and corrosion behavior were studied .The results were that hardness of the substrate decreased due to the growth of Mg grains at high temperatures.

As a result, the temperature of 300 ºC was chosen as the optimum temperature. Results also indicated that 1 g L^{-1} nano -SiC in plating bath provided a uniform composite Ni - P electroless coating with high hardness (795 HV) and corrosion resistance . Adding more nano -particles to the bath resulted in agglomeration of the particles and did not have positive effect on properties. The wear behavior of coatings were investigated using steel pin (AISI 52100) as the counterpart in pin -on -disk wear test. The optimum as - plated composite coating (Ni -P/1SiC) produced the best wear resistance at a rate of 4 .2 × 10^{-5} mm^{3} N^{1} m^{-1} wear rate and the highest corrosion resistance belonged to Ni -P/1SiC after annealing at temperature 300 ºC .

In 2021,Parthiban et.al[120] investigated of addition SiC particles to electroless plating with matrix Ni-P on aluminium alloy LM6 substrate.The results refered to thin composite coatings in the range of 25 to 32 µm was deposited on surface of sub substrate.The applied force and hold time in microhardness was 100g ,15s respectively. The hardnes was ranged between(500-680 HV) according the variation in pH.

In 2022, Chintada et.al [121] studied the effect of surfactants of electroless nickel silicon (Ni–P–SiC) coatings on steel substrates. The presence of the three surfactants at a 0.6 g/L concentration significantly influences the characteristics of the coatings. The maximum number of SiC nanoparticles was homogeneously distributed in the Ni alloy in the presence of a cationic surfactant. The coating developed from the cationic surfactant bath exhibited the highest microhardness, corrosion resistance, deposition rate, and smooth surface identified in the coating developed from the cationic surfactant bath.

In 2022, Uppada et.al [122] studied the effect of surfacants of electroless nickel silicon (Ni–P–SiC) coatings on mild steel substrates. To improve the surface properties of mild steel, such as microhardness and resistance to corrosion, Al_2O_3 and SiC nanoparticle-reinforced multilayer Ni-P coatings were fabricated using an electroless surface coating technique. Scanning electron microscopy with energy-dispersive spectrometry and X-ray diffraction were used to examine the morphology, elemental composition, and coating structure.

The microhardness of the deposits was examined using a Vickers hardness tester. The corrosion protection ability of the coatings was analyzed by performing potentiodynamic polarization studies in a 3.5% NaCl solution. The experimental results showed that the samples coating with Ni-P-SiC as the external layer provided the highest microhardness. The Ni-P-Al_2O_3 outer layered duplex coating offers the maximum resistance to corrosion owing to the higher electrochemical resistivity of the Al_2O_3 particles. The thermal process performed at the optimized temperature of 400 °C enhanced the coating properties owing to crystallization.

In 2022, Kumar et.al [123] studied the effect of surfacants of electroless nickel silicon (Ni–P–SiC) coatings on SS 304 steel sample substrates. Taguchi L16 orthogonal array, ANOVA, and regression analysis have been used to obtain experiment layout, significant process parameters, and linear relationship between input and output variables, respectively, under the experiment of design and validate with confirmatory test. Combination of operating parameters which minimize both coefficient of friction and wear is generated using multi-objective optimization.

Experiments are carried out according to L16 orthogonal array and the significant parameters among the chosen, which influence wear and coefficient of friction of Ni-P-SiC electroless coated SS 304 under dry conditions are determined. Relations between the output variable and input variable is established by linear regression equations of the friction coefficient between interacting components and wear under the dry condition in terms of load, speed, and temperature. 10 N, 100 rpm, and 90°C are found to be an optimum set of operating parameters among selected levels which minimize both wear and coefficient of friction of sample.

2.13. Summary

There are many studies on failure analysis and electrolessplating, but they may be non-existent or very little on an effective and important part in power stations, which is the separator. The previous studies were similar to this work had been divided into three parts. In the first part, studies of failure analysis in heavy fuel oil centrifugal separator of different power plants was studied. Whereas the electroless plating is the second where the studies are discussed. These studies about electroless plating were classified into three types which they suggested as a way to reduce the environmental failure. Table (2.6) showed the nearest studies that consists of most important data, operations condition and parameters were studied by several researchers.

For more explicating in Table(2.6), six colors have been presented as follow: (1):full similarity in failure causes and prevention it by plating presented by the red color 🟥, (2) :large similarity in failure causes and prevention it by plating presented by the green color 🟩,(3) :full similarity in media presented by the blue color 🟪,(4) : large similarity in media presented by the brown color 🟫(5): full similarity in base metal presented by yellow color 🟨 and (6) large similarity in base metal presented by the pink color ■ .

Table (2.6): The Nearest Previous Studies about Failure Analysis and Electroless plating

Failure Analysis Studies					
No.	**Years**	**Researchers**	**Substrate**	**Environment conditions**	**Failure causes**
1	2020	Xiaojia Yang	304SS	corrosive medium mainly contains sulfur compounds and some chloride ions.	pitting, intergranular corrosion and SCC caused by sulfuric acid and chloride ions.
2	2022	Yi Peng&TaoYang	316SS	corrosion medium (caustic Na and chloride),	SCC
3	2022	Aditya Gokhale	304SS	chloride (Cl)	SCC

Electroless Plating (Nickel-Phosphorus) Studies				
No.	**Years**	**Researchers**	**Substrate**	**Advantage of plating**
1	2016	Smoljan	316SS	Increasing of corrosion resistance and hardness
2	2017	JEKLA	316SS	Improving wear and corrosion resistance
3	2023	Zhizhen Li	Low carbon steel	Increasing of corrosion resistance,erosion and hardness

Electroless Plating(Nickel- Copper-Phosphorus) Studies				
No.	**Years**	**Researchers**	**Substrate**	**Advantage of plating**
1	2022	Davoodi	L80 steel	Improving of corrosion resistance,erosion resistance and hardness,
2	2022	Mukhopadhyay	Fe 600-grade steel	Corrosion resistance

Electroless Plating(Nickel- Zinc-Phosphorus) Studies				
No.	**Years**	**Researchers**	**Substrate**	**Advantage of plating**

1	2021	Fu.Chuanqi	Q235 low-carbon steel	Corrosion resistance
2	2023	Li	AISI 1005 steel	Corrosion resistance

Electroless Plating(Nickel- Phosphorus-SiC) Studies

No.	Years	Researchers	Substrate	Advantage of plating
1	2020	Chintada	Mild steel	Wear,corrosion and erosion resistance
2	2022	Uppada	Mild steel	Microhardness,corrosion resistance
3	2022	Kumar	304SS	Wear,corrosion,friction and erosion resistance

Chapter3

Experimental Work

Chapter Three
Experimental Work

3.1 Introduction

The first part of this chapter describes the materials and devices used in the process of failure analysis in discs of heavy fuel oil seperators. In this part several investigation tests are carried out: chemical composition analysis, optical microscope analysis, XRF, SEM, EDS, hardness measurement and fuel analysis.

The second part describes specimens preparation, electroless plating method and the bath composition (Ni-P), (Ni-Cu-P), (Ni-Zn-P)and(Ni-SiC-P)nano-compsite coating which are used in the electroless plating methods.

The third part also includes some important test such as adhesion force, Tafel extrapolation,cyclic polarization, erosion-corrosion and stress crack corrosion(SCC) tests of coated and uncoated specimens.

The examinations are carried out during the practical part after completion of the electroless plating include physical and mechanical tests such as XRD,SEM, EDS ,AFM as well as hardness test.

Finally the last part involves numerical modeling of stress residuial cracking by using ANSYS workbench(15.07).Not only anaylsis stress corrosion cracking but also calcalution of centrifugal force and checking if the cracks will be propagate or not.

3.2. Program of the Present Study

Figure (3.1) shows the experimental program of the overall procedure employed in the current work.In this diagram there is a brief explanation for the most and more important processes that are carried out during this study.

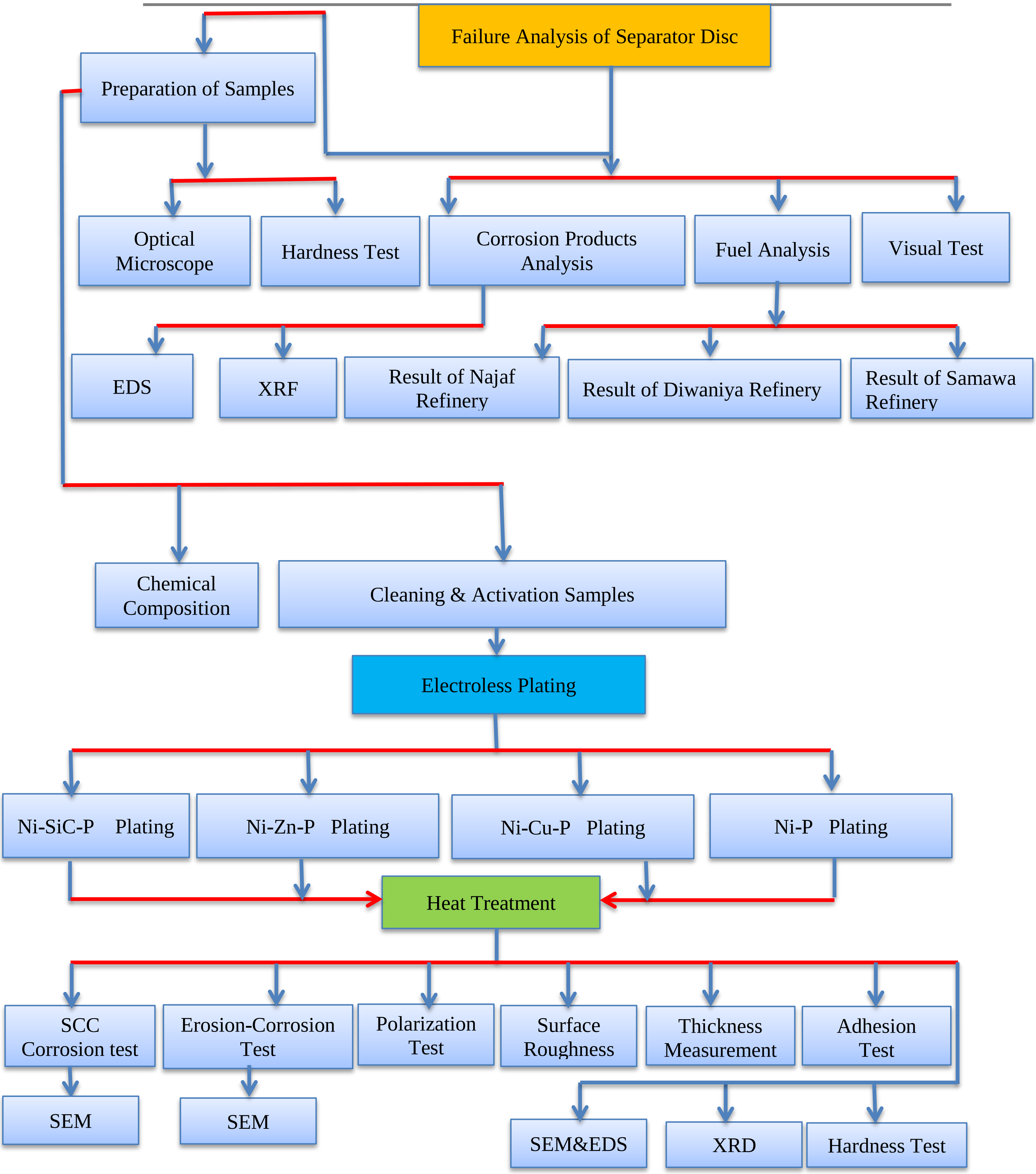

Figure (3.1): Flow Chart of the Present Work.

3.3. Failure Analysis of Seperator Disc

It is carried out by knowledgement visual inspection, fuel analysis, chemical composition of seperatator disc , corrosion product analysis, hardness measurement and microstructure of seperator disc material.

3.3.1. Visual Inspection

Through visual inspection, the effects of failure, such as corrosion products, erosion effect are observed .Figure (3.2) illustrates the failure in seperataor disc.This failure gives clear pictures about the severe environment ,where the disc is subjected to it , so that the stress corrosion cracking and erosion-corrosion may be occured.

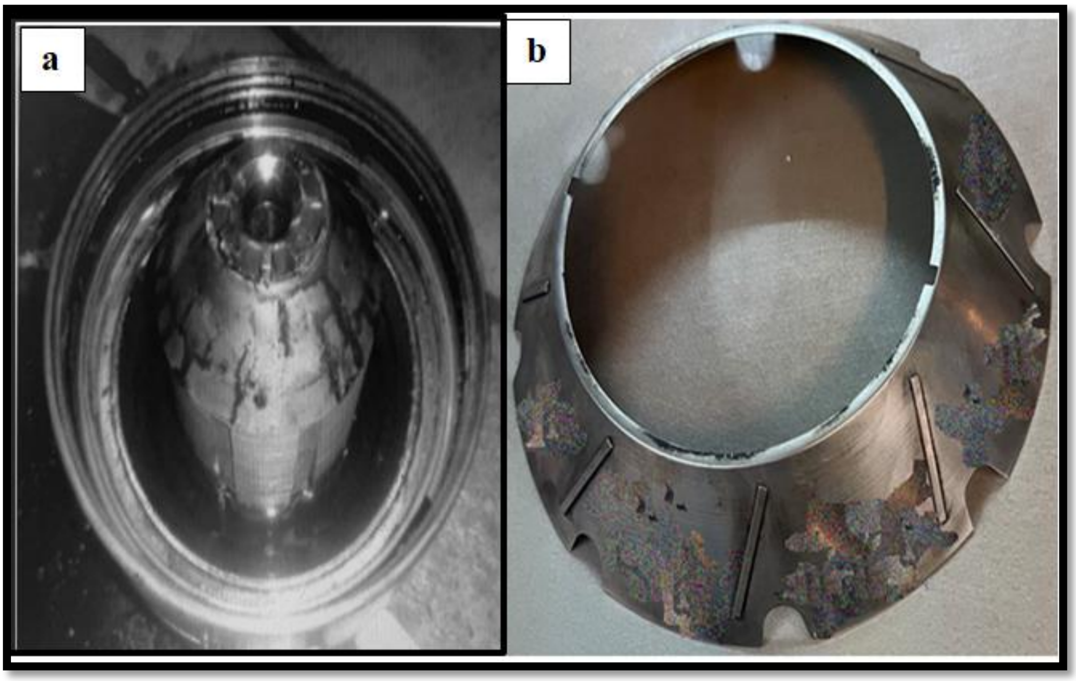

Figure (3.2) : Failure in Separator(a):Discs in Bowel System(b):Damage Disc.

3.3.2. Samples Preparation

Three types of specimens have been taken.The first type is shaft sample from stainless steel 316L have been cut into some circular specimens with (15 x10 mm) and with side hole (2mm) by wire cutting machine (ACRA-W-A430)which locates in Ministry of Science and Technology that shown in Figure (3.3).The second type of specimen is small part from damage disc is taken to analyze the failure.This specimen with dimension 20x 20x1.5mm.The third type of specimens is cutting from four different thickness SS316L sheets to examine the stress corrosion cracking.All three specimens types are shown in Figure(3.4).

Figure(3.3):Wire Cutting Machine Model (ACRA-W-A430).

These specimens are flattened by using SiC grinding papers (100,120,150,180, 220, 320, 400, 600, 800, 1000, 1200, 1500, 2000, 2500,grit size).Figure (3.4)displays sketch and perperation specimens. This last process is achieved in (the Lab of Metallurgical Engineering Department / College of Materials Engineering - University of Babylon) by using polishing machine model (MP-2B grinder- polisher) .

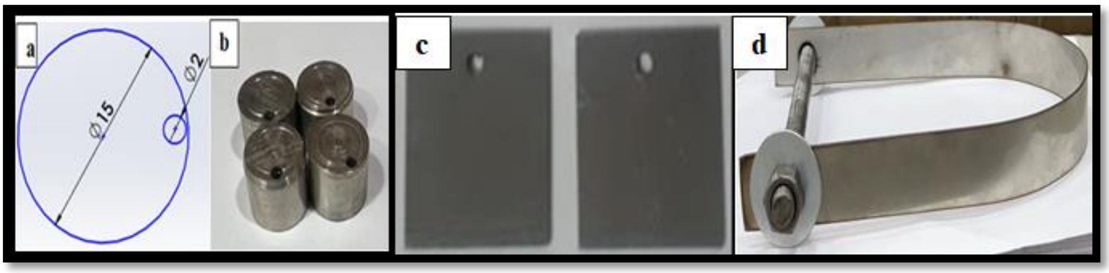

Figure (3.4): (a)and(b)Sketch and Perpetration Specimens for Electroless Plating(c) Specimens Image for Failure Analysis(d) Perpetration Specimens Image for SCC Test.

3.3.3. Heavy Fuel Analysis

The fuel used in Kufa power plant is provided from three source: Diwaniya Refinery, Samawa Refinery, Najaf Refinery. The fuel is analyzed by (SPECTROIL M,USA Made) Analyzer in Midland Refineries Company (Doraa Refineries) which shown in Figure(3.5) below:

Figure(3.5):Spectroil Analyzer.

3.3.4. Chemical Composition

Chemical composition of disc separator and shaft samples is carried out by SPECTRO model (SPECTROMAXx) at General Company for Inspectionand Engineering Rehabilitation-Baghdad. Figure(3.6)dislpays this instrument.

Figure(3.6): Spectro Analyzer.

3.3.5 Corrosion Products Analysis

Corrosion products on the surface of disc seperataor are removed and milled to put at small cups. (XRF) examination is carried out by (Thermo Scientific Niton XRF Analyzer) to know the chemical composition of corrosion products and corrosion oxides. XRF instrument which shown in Figure(3.7) locates in University of Babylon- Science College .

```
NAV Tools
Time 8.5 sec
+Alloy 500   0.5

Ele    %     2σ
Al   2.73  0.55
Si   0.138 0.089
Ti   0.536 0.149
Mn   0.759 0.074
Fe   0.080 0.064
Ni  63.66  0.55
Cu  31.02  0.39
LEC  0.125 0.011
```

Figure (3.7): Thermo Scientific Niton XRF Analyzer.

3.3.6. Hardness Measurement

Hardness testing for failure analysis is carried out on cross section disc separator specimens to evaluate the mechanical properties of disc separator failed in 18 points.This cross section area for damaged disc stack is taken from length (L) by thickness of of disc ickers technique is carried out with load 300g and hold time for 15 seconds. The applied load on cross section of disc stack is largely different from applied load of electroless plating specimens.The low thickness of electroless plating which reach to several microns is the effective factor in chossing the applied load.

After completion of electroless plating and heat treatment, hardness measurement is carried out by 30-50g load and 15s hold time. The hardness measurement is applied on several specimens with different parameters. These different parameters are four bath composition ,time of coating and heat treatment. This test is achieved by machine type (HVS-1000) Tester which made in China. The Vickers hardness tester in (the Lab of Metallurgical Engineering Department / College of Materials Engineering - University of Babylon).

3.3.7.Optical Microscopic Examination

This test is carried out to display base metal microstructure. Specimens are prepared as mentioned earlier but polishing process is added to produce a scratch free surface. Finally etching process is applied on the specimens. Etchings are accomplished by submerged the specimen in (10 g CrO_3+100 ml water) electrolytic solution at 6volt for 30-65s according to ASTM- E407. This work is achieved by using optical microscope with magnification 80X type (BEL PHOTONICS) at the Lab of Metallurgical Engineering Department / College of Materials Engineering - University of Babylon.

3.4. Electroless Plating

This method has been used to reduce failure in separator disc and include high preparation of specimens, activation of the surface specimens, the types of bath used and coating process.

3.4.1 Specimens Preparation for Electroless Plating

After the processes of grinding and polishing that mentioned above the specimens need high preparation as follow:

1- Cleaning by acetone in ultrasonic device for 30 minutes to remove finishing compound, dust and any contaminations according to ASTM-B 254 – 92 (Reapproved 2004).The ultrasonic device locates in (the Lab of Metallurgical Engineering Department / College of Materials Engineering - University of Babylon) which is shown in Figure (3.8). After that the specimen is raining by distilled water and then drying by electrical dryer.

2-Alkaline cleaning solution (60g/L NaOH+38 g/L Sodium Phosphate+38g/L Sodium Carbonate) is used to remove last traces of grease,oil or any contaminations at 65-70°C with 3volt DC power supply.

3-Special activation is carried on specimen's surface to break the oxide thin metal film and to rise the adhesion force between the bare surface and the thin plating. This method is applied by unusual nickel strike in electro-chemical process contains [240g/L nickel chloride($NiCl_2$) +126ml/L hydraulic acid (HCl)] where the specimens connected to power supply as anode with voltage 3volt for 2-4 minutes at room temperature.

On the other hand the cathode is nickel pole.After this ,the polarity is reverse for 5 minutes and then the specimens are raining by distilled water and drying by electrical dryer.

Figure (3.8): Ultrasonic Cleaner.

3.4.2 Bath Composition

In this work four bath composition of electroless nickel plating are used, (Ni-P), (Ni-Cu-P),(Ni-Zn-P)and(Ni-SiC-P) nano compsite coating. Table (3.1) refers to the base source of these four bath composition as well as indicate to the baths composition and its operating conditions of all fourth elecrtoless plating that used in this work.All chosen baths were according to concepts of the electoless plating procedure through the controlling of the operations conditions such as pH,temperature and magntic stirring.Not only these concepts were taken into consideration but also some of important components bath such as metal ions,reducing agent,complexant,accelator,buffer and stabilizer. The right side of Table(3.2)in the yellow color is presented the current baths study.On the other hand the left side which has blue color from Table(3.1)is presented the reference baths in this study.

Table (3.1): Operating Conditions and Bath Composition of Main Reference Fourth Composition **[70,110,115,124]** As Well As The Baths of Current Study.

Reference Baths		**Current Study Baths**	
Ni-P Bath[70]		**Ni-P Bath**	
Chemical Composition	**Concentration (g/L)**	**Chemical Composition**	**Concentration (g/L)**
Nickel Chloride	20-30	Nickel Chloride	25
Sodium Hypophosphite	8-10	Sodium Hypophosphite	9
Sodium Citrate	90-100	Sodium Citrate	95
Operating Conditions		**Operating Conditions**	
pH	8 -9	pH	8.5
Temperature	85-90 °C	Temperature	88
Magnetic Stirring (rpm)	200 ± 20	Magnetic Stirring (rpm)	200
Ni-Cu-P Bath[110]		**Ni-Cu-P Bath**	
Chemical Composition	**Concentration (g/L)**	**Chemical Composition**	**Concentration (g/L)**
Nickel Sulphate	22-30	Nickel Sulphate	25
Sodium Hypophosphite	15-20	Sodium Hypophosphite	18
Sodium Citrate	12-15	Sodium Citrate	13
Copper Sulphate	0.3-0.8	Copper Sulphate	0.7
Operating Conditions		**Operating Conditions**	
pH	8 -9	pH	8.5
Temperature	85 °C±2	Temperature	87
Magnetic Stirring (rpm)	250 ± 20	Magnetic Stirring (rpm)	260
Ni-Zn-P Bath[115]		**Ni-Zn-P Bath**	
Chemical Composition	**Concentration (g/L)**	**Chemical Composition**	**Concentration (g/L)**
Nickel Sulphate	20-26	Nickel Sulphate	25
Sodium Hypophosphite	15-17.5	Sodium Hypophosphite	16
Zinc Chloride	3	Zinc Chloride	3
Ammonium Chloride	22-25	Ammonium Chloride	23
Sodium Citrate	35-41	Sodium Citrate	35
Operating Conditions		**Operating Conditions**	
pH	8.5	pH	8
Temperature	85°C±2	Temperature	86
Magnetic Stirring (rpm)	300± 25	Magnetic Stirring (rpm)	310
Ni-SiC-P Bath[124]		**Ni-SiC-P Bath**	
Chemical Composition	**Concentration (g/L)**	**Chemical Composition**	**Concentration (g/L)**
Nickel Sulphate	20-25	Nickel Sulphate	23
Sodium Hypophosphite	20-25	Sodium Hypophosphite	22
Superfine SiC Particles	5-15	Superfine SiC Particles	7-9
Lactic Acid (ml/L)	30-33	Lactic Acid (ml/L)	32
Operating Conditions		**Operating Conditions**	
pH	4-6	pH	5.5
Temperature	90 °C±2	Temperature	89
Magnetic Stirring (rpm)	350 ± 20	Magnetic Stirring (rpm)	320

3.4.3 Coating Operations

After finishing of grinding, cleaning, polishing, and activation surface processes the solution is prepared according to the concentration in Tables(3.1) for coating Ni-P , Ni-Cu-P, Ni-Zn-P and Ni-SiC-P nano-compsite coating respectively. The specimen is hanged from the side hole inside the solution. The solution is homogenized by magnetic stirrer. The bath temperature is different from bath to other coating. pH of solution is controlled between 8-10, in Ni-P , Ni-Cu-P and Ni-Zn-P coating respectively but it range between4-6 in Ni-SiC-P nano-compsite coating. About 8-12 µm/h was the average deposition rate for composite coatings containing (30-50nm) SiC particles which are lied on the standard range of nano particles(90-100nm). Drops of sodium hydroxide or hydrochloric acid are added to regulate solution pH during the operation of coating. Sodium hydroxide is added to increase pH but hydrochloric acid is added to decrease pH .The time of coating is chosen 1 and 2 hrs.. The process of coating is illustrated in Figure (3.9). After the completion of the process of coating, specimens are placed inside a vacuum oven, to dry for 30 minutes, at temperature 50 ºC. Figure (3.10) shows several specimens before and after coating process.

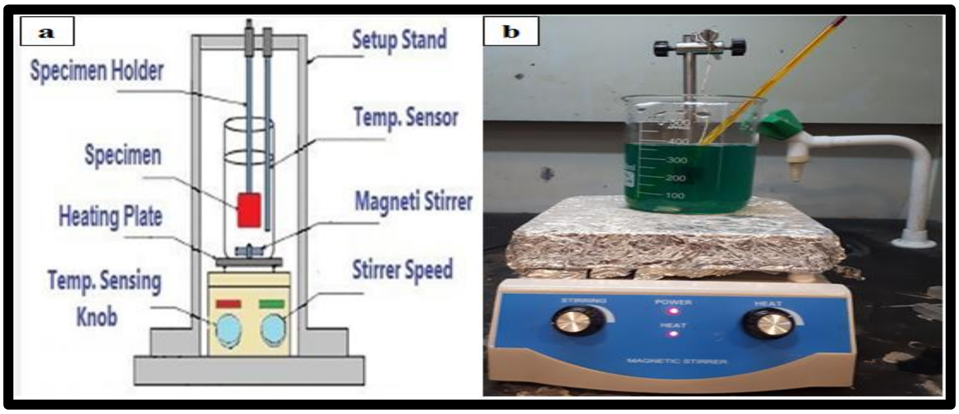

Figure (3.9): (a):Sketch of Electroless Plating Apparatus(b): Actual Electroless Plating.

Figure (3.10): Specimens: (a) Before Coating (b) After Coating.

3.4.4 Heat Treatment

After the completion of coating process all the specimens are put in small cup in vacuum furnace (Electrical Tube Furnace Type MTI-(GSL1600X)) at 400^{o}C for one hour to Ni-P , Ni-Cu-P and Ni-Zn-P but at 600^{o}C for hour to Ni-SiC-P nano-compisite coating. This process is carried out in (the Lab of Metallurgical Engineering Department / College of Materials Engineering - University of Babylon). Figure (3.11) shows the electrical tube furnace.

Figure (3.11): Electrical Tube Furnace Type MTI-(GSL1600X).

3.5. Physical and Mechanical Examinations

Some of physical and mechanical examinations are carried out after completely electroless plating such as hardness test, SEM, EDS ,XRD and AFM.

3.5.1. Thickness Measurements of Coating

A digital gage Type (TT260), is used to determine the thickness of coating for different coating specimens at two different time of coating. Figure (3.12) a view the digital gage which is located at (the Lab of Metallurgical Engineering Department / College of Materials Engineering - University of Babylon).The device accuracy ± 0.1 μm. In this way measurement is taken in three or four places to obtain averaged thickness but this device in some times gives non accurate readings, so that, the optical microscope and SEM are used to know the thickness in most times.

Figure :(3.12) Digital Coating Thickness-TT260.

3.5.2. Adhesion Test

Coating adhesion to the surfaces of coating specimense plays an important role in industrial applications. To measure the adhesion strength between the coating and the alloy substrate, pull-off test was conducted according to the ASTM-D4541 standard**[125]** as shown in Figure (3.13) located in the Metallurgical laboratory in the Laboratories of the Department of Metallurgical Engineering - University of Babylon.

Figure (3.13): Pull-off Device.

3.5.3. X-Ray Diffraction to Electroless Plating Specimens

Coated circuler specimens with (15mm diameter x10mm thickness) are prepared for XRD analysis. The analysis has been done in two different places.One of them is chosen for all as-plated specimens and the other for all heat treated specimens. The first place is the device in the Lab of Ceramic Engineering Department / College of Materials Engineering - University of Babylon).

The second place where the heat treated coated specimens is BuAli Institute in Mashad city-Iran.The operation conditions for analysis are (Target: Cu, wave length 1.54056 , current and voltage are 15 mA and 40 KV respectively, speed of scanning 2 deg/min, scanning range of (30^o-80^o).The X-ray diffraction is used in order to know phases of the matrix and then compare it with the standard charts.

3.5.4.Scanning Electron Microscopy (SEM) and Energy Dispersive Spectroscopy (EDS)

Specimens are prepared to accommodate the catcher of SEM device. The analysis has been done in two different places one of them (BuAli Institute in Mashad city-Iran)and the other in Lab of Ceramic Engineering Department / College of Materials Engineering - University of Babylon) This test is used to determine the percentage of coating elements. On the other hand, it uses to know the morphology of coating surface.

3.5.5. Atomic Force Microscope (AFM)

Surface molecular analysis is possible with atomic force microscopes (AFM)model Aa 3000 Scanning Probe Microscope. Topography data is gathered as opposed to photographs. The size and other characteristics of produced nanoparticles are examined using AFM. The AFM is operating as shown in Figure (3.14). It located in University of Babylon-College of Education for Pure Sciences.

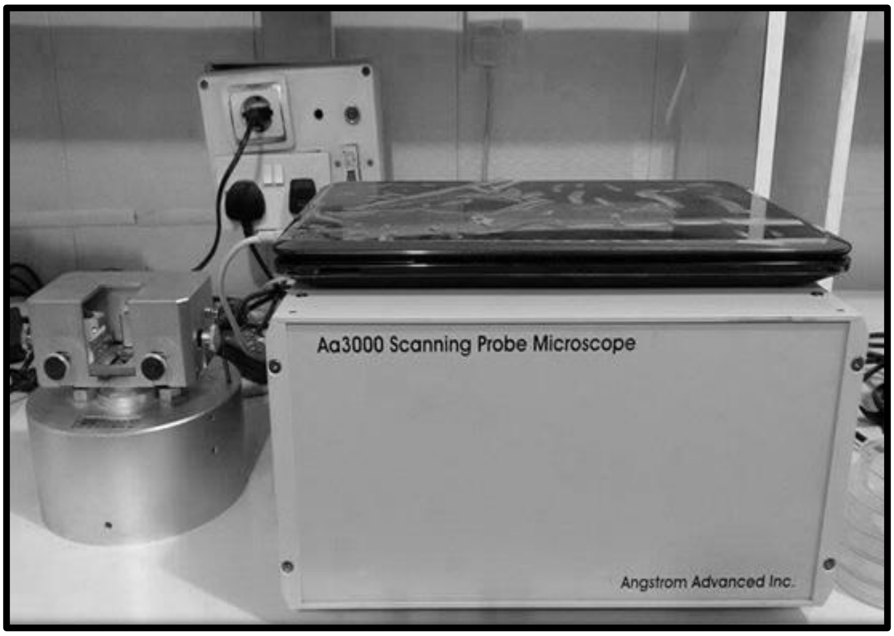

Figure (3.14): Atomic Force Microscopes.

3.6. Corrosion Tests

The essential tests to be performed are electrochemical test, erosion corrosion and stress crack corrosion(SCC).

3.6.1. Electrochemical Tests

Three electrochemical tests have been conducted in this study to know the ability of bare and coated specimens on electrochemical corrosion resistance.These three electrochemical tests can be classified as:

3.6.1.1. Open Circuit Potential Test (O.C.P)

Open-Circuit Potential (O.C.P) also known as equilibrium potential is the potential of an electrode measured with respect to a reference electrode in the absence of current (under open-circuit conditions). It is simply a valuable technique that determines that potential difference between the working (specimen) and a reference electrode. The O.C.P. (voltage versus time) is recorded at period time in the corrosion solution 3.5%NaCl. The period of time from (0 up to 80 minutes) with time interval 5 minutes are potentially reported. The voltage are measured of open circuit potential (O.C.P) as a function of time till steady-state potentials. Figure (3.15) shows open circuit system.

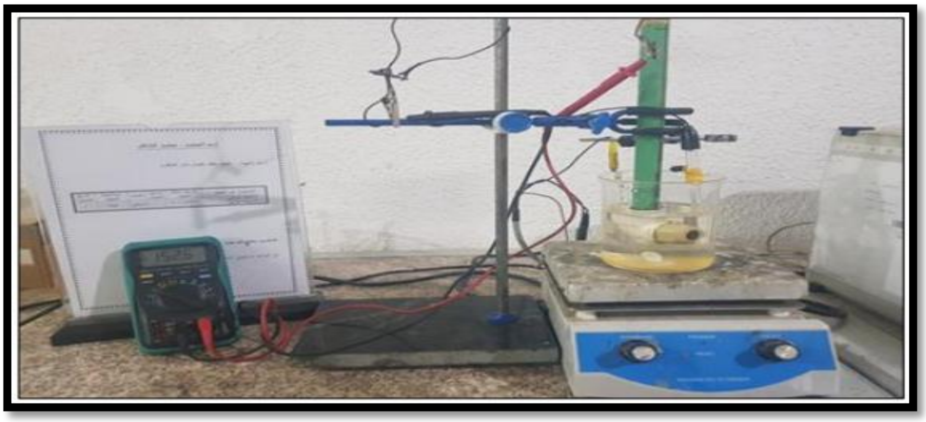

Figure (3.15): Open Circuit System**.**

3.6.1.2. Polarization Test

Specimens are used after insulation one face by polymer material and install conduction wire in the same insulation face .The polarization test is done by using a potentiostate instrument. This method is used to calculate current and potential of corrosion. Three electrodes and an electrochemical cell are the contents of the tester apparatus. The three electrode are working electrode (SS316L), auxiliary electrode (Pt. electrode) and saturated calomel electrode (SEC).Several cases for working electrode are bare metal, coating with Ni-P , Ni-Cu-P, Ni-Zn-P and Ni-SiC-P for(1and 2 hrs.). The process is carried out in 3.5%NaCl. This process is done by a computer program through which an account is calculated current (μA) and potential (mV) to determine density of corrosion current through the intersection tangents of the polarization two curves. This examination was carried out at the Lab in College of Materials Engineering - Department of Metallurgical -University of Babylon. The equation is applied for calculations corrosion rate during electrochemical reaction according to ASTM G102-89 is **[126]**:

Corrosionrate (mpy)=(0.13 $I_{corr} *$E.W)/(A. ρ) … ..………………..3.1

Where:

0.13 = metric and time conversion factor.

I_{corr} : Total corrosion current μA

E.W= equivalent weight of bare metal (for SS316L =25.5) calculated.

E.W= equivalent weight of coated metal (for Ni_3P=17.25 and for Ni_5P_2=14.74, 14.465 for NiSi ,20.42 for Ni_3Si and for NiZn=31.022) calculated according to ASTM G102 .

ρ: Density of bare metal (for SS316L =7.98g/ cm^3)

ρ : Density of coated metal (7.8g/ cm^3 for Ni_3P,7.71 g/ $cm^3$for Ni_5P_2, 5.97g/cm^3 for NiSi,7.85g/cm^3 forNi_3Si)calculated according to ASTM G102 where these phases (Ni_3P, Ni_5P_2, NiSi,Ni_3Si and NiZn) are the dominates phase in coating layers

A= exposed specimen area (cm^2)

mpy = Corrosion rate (mils per year).

3.6.1.3. Cyclic Potentiodynamic Polarization(CPDP) Test

The cyclic potentiodynamic polarization technique is a method for evaluating the susceptibility of a metal to localized corrosion such as pitting and crevice corrosion. It is widely used to determine resistance to localized corrosion or degradation rate in a short time.Thus this technique is applicable as a method for prediction of localized corrosion also beneficial for alloys that are passivized spontaneously and underwent localized corrosion.Also this way is similar to Tafel test in connection the specimens by electrochemical computerized system but different in calcaluted the pitting potential (E_{pit}) and the protection potential (E_{prot}).Three different electrode can be found in this test.Work specimen,platinuim (Pt)electrode for electrical conduction and reference electrode(saturated calomel electrode) (SEC) for comparsion.

3.6.2. Erosion-Corrosion Test

The erosion-corrosion device was manufactured locally agreeing to (G 73-10) ASTM**[127]**. Figure (3.16) a view the device of erosion-corrosion. The erosion-corrosion device consists of a cylindrical plastic tank is used as a chamber. The tank has a dimensions of 30cm in diameter ,and 50 cm in height . The different media are delivered directly at high pressure and the vertical direction of the sample face through jet nozzle d=2 mm by a pump sucking the different media from plastic tank (chamber) with 1 horse power, single phase electric motor made from teflon (chemical pump) while the distance between sample and nozzle= 10mm.The chemical pump is resistant to the slurry and chemical solution .

The pipe joints and valves connected to the chamber with chemical pump are made from PVC plastic.The impact angle between chemical solution and surface specimen is 90^0 .There is one type of chemical solution is used in this work,which is heavy fuel oil.Several specimens are tested in this work, these specimens are bare, coated with fourth different coatings at two different coating time (1, 2hrs.). The times of erosion test are (15, 30, 45, 60, 75, 90 ,105,120 and135 minutes) respectively.

The erosion rate can be determined in the equation below **[71]**:

The losses in weight=original weight-weight after test ……………3.2

Erosion rate=the losses in weight/exposure time (g/min)…… …….3.3

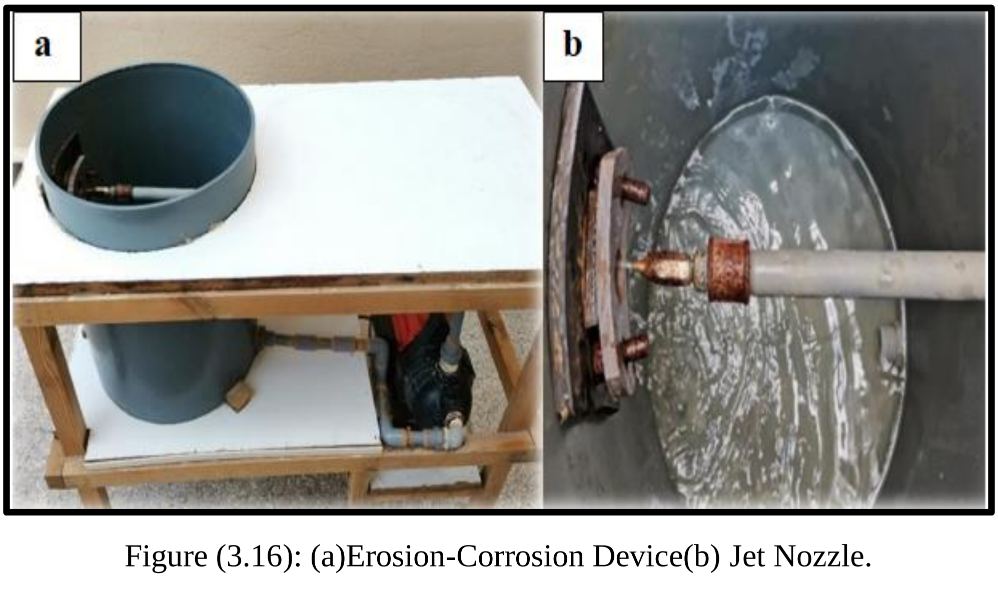

Figure (3.16): (a)Erosion-Corrosion Device(b) Jet Nozzle.

3.6.3. Stress Corrosion Cracking Test

This test involves the stressing of a specimen bent to a U shape. The applied strain is estimated from the bend conditions. The stressed specimens are then exposed to the test environment and the time required for developing cracks is determined. This cracking time is used as an estimate of the stress corrosion resistance of the material in the test environment.

The U-bend specimen may be used for any metal alloy sufficiently ductile to be formed into the U-shape without mechanically cracking. The specimen is most easily made from strip or sheet but can be machined from plate, bar, castings, or weldments; wire specimens may be used also. Figure (3.17) shows sketch of U-bend samples .To know the stress crack corrosion, four samples were taken according to ASTM G-30-97(2015).Table(3.2) displays the dimensions of stress crack corrosion samples which exposure to the bending.

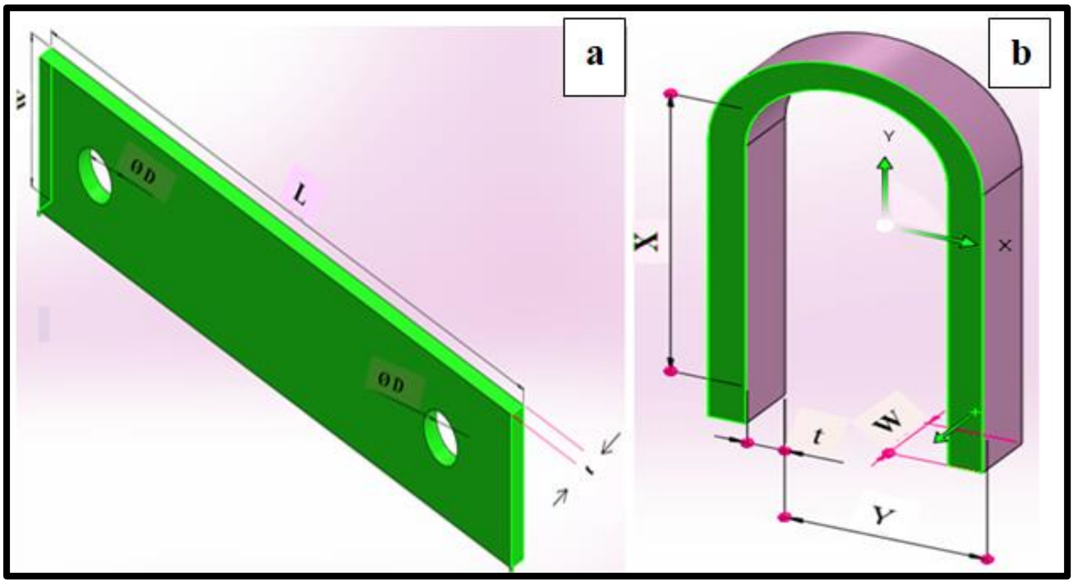

Figure (3.17): 3-D Sketch of SCC Samples(a)Before Bending (b) After Bending .

Table(3.2) : Dimensions of Stress Crack Corrosion Specimens(U-Bend).

Specimens	L,mm	M,mm	W,mm	T,mm	D,mm	X,mm	Y,mm	R,mm
A	150	140	15	0.8	3	61	20	9
B	130	100	15	3	6	45	32	13
C	120	20	90	1.5	8	35	35	16
D	102	38	19	3	9	40	16	5

The test environment is heavy fuel oil and the time of test is 480,960 and 1440hours respectively.The specimens are immersed in heavy fuel oil at each these period of time.This test is done according to G30-97-2015 standard**[128]**.Figure(3.19)displays the specimens before and after putting them in heavy fuel oil.

After completion this process, the specimens are cleaned in two stage:

(1): by light fuel to remove all oils,oxides,mud and another particles

(2) : by acetone in ultrasonic device which shown in Figure (3.8) for 20 min. to remove residual particles

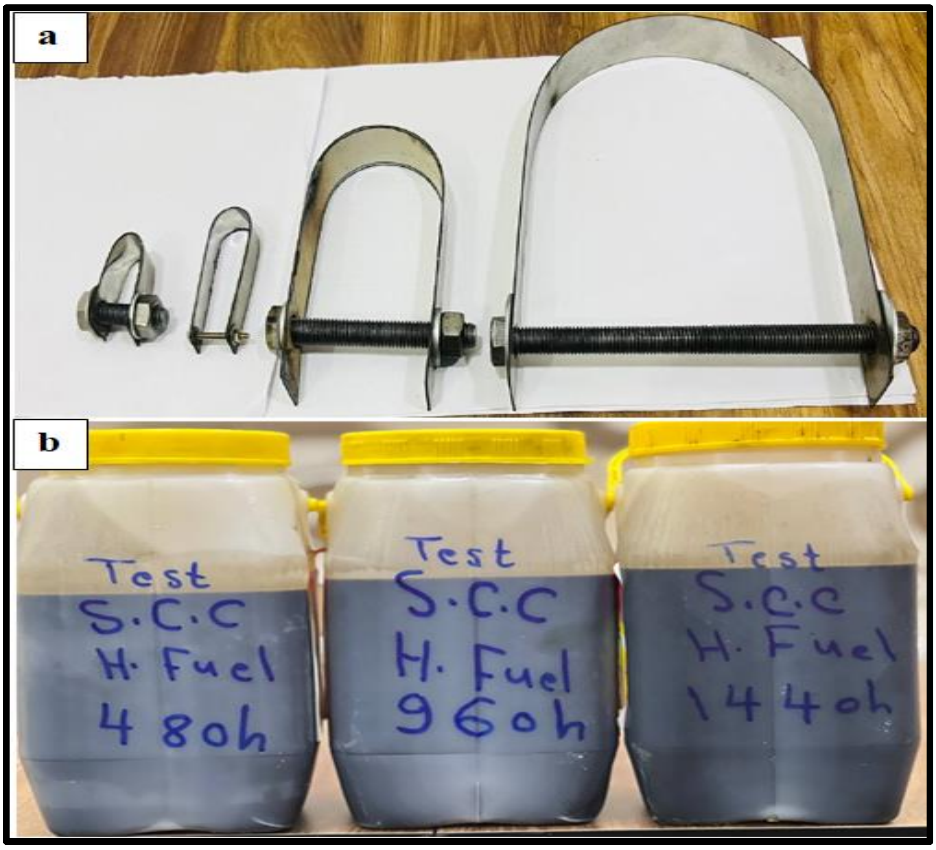

Figure(3.17):SCC Test Specimens(a)Outside Environment(b)Inside Environment.

After finishing the process of cleaning ,SEM examination is carried out to recognize the presence of stress corrosion cracking which may be ccurred. Coating specimens are also subjected to SEM examination.

3.7.Numerical Modeling of Stress Corrosion Cracking by Using ANSYS Workbench 15.07 Software

Finite Element Analysis (FEA), as it is known to in most sources.It is a numerical way of solving a boundary value issue in a mathematical procedure using a computing package to complete the work; this method provides us with an estimated solution. The finite element method has seen the most widespread application in solid and structural mechanics.The mechanical loads have been examined in this study**.**

3.7.1.Geometry of Specimens

All nodes, their positions, and element connectivity are limited by the paragon geometry. The connection information allows the software to group the component stiffness matrix and the component equivalent force vector in order to arrive at the global equilibrium equation. There are two approaches to generate the model: manually creating a mesh and using solid meshing, then meshing the solid to get the node and element dispensing. It means drawing the part to be analyzed for thermal or mechanical stresses with the required dimensions.

If the geometry needs to be U-bend, the pattern of bend,the type of load, the place of load have been selected.Figure(3.19) depicts geometry of U-bend specimen.The dimensions of each U-bend plate are different from specimens to other according to Table(3.2).

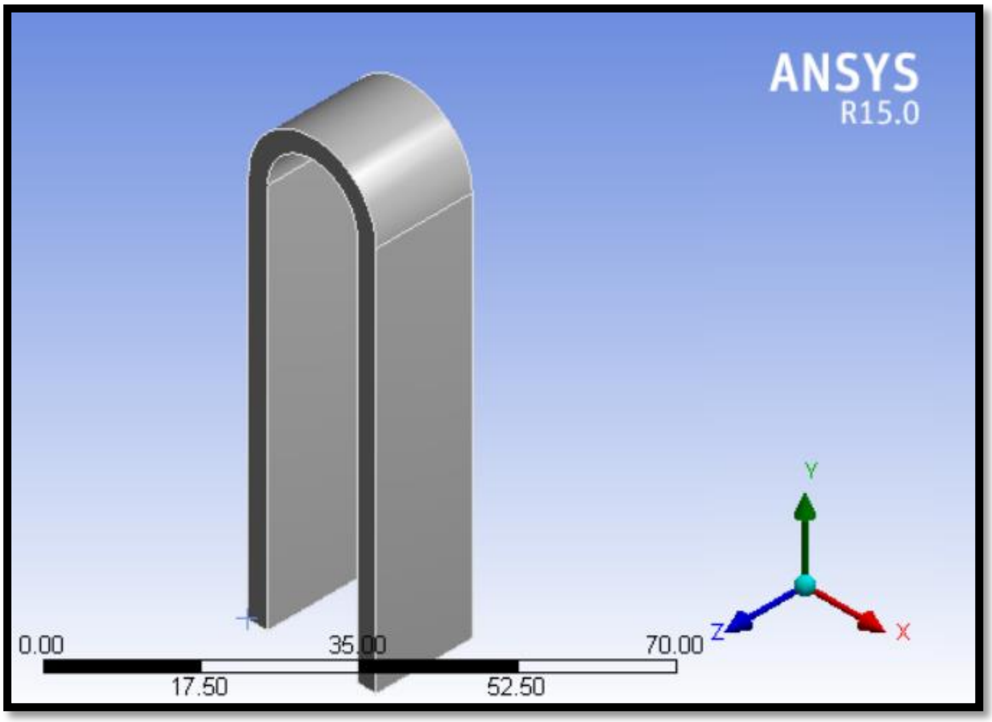

Figure(3.19):Geometry of Stress Corrosion Cracking Specimen.

3.7.2.Element Type and Meshing

The software backage FEA uses meshing technology to divide the part into multiple elements and nodes, and the solution is completed by applying boundary conditions that simplify the equations.The element types depicted in the diagram below:

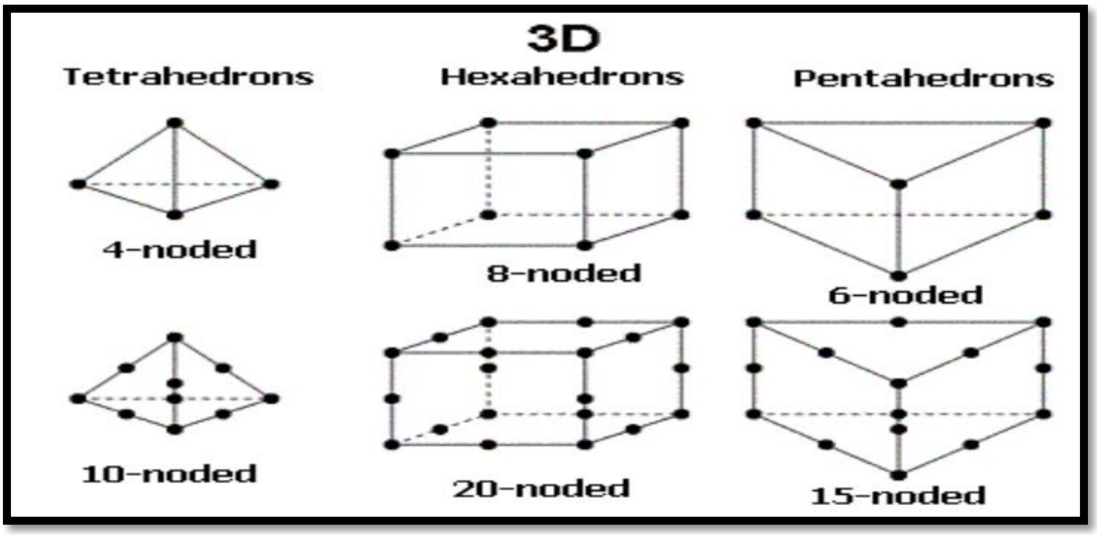

Figure(3.20):Types of Elements Used in ANSYS**[129]**.

The graphic above explains the types of elements chosen: the 10 nods tetra for Autodesk Inventor Pro and the 20 node and 15 node for ANSYS.To simplify the task, commercial programs have been developed to do the task and reduce the time to finish, and these programs show very good progress in finishing tasks and representing the result and recommendation, such as Autodesk Inventor, ANSYS, ABAQUS, Nastran. In this study, the ANSYS15.07 will be used.

In solving problems, the ANSYS program relies on the method of the finite elements (FEM)in the solution, which is known as the mesh.The meshing method divides the geometry diagram after drawing it into small areas, which means that form a network of elements from the solid or liquid body.This network connects points and straights, and in turn forms the mesh necessary for the program to move in the solution starts from the first point to the first line to the first element, and so on the program performs tens, hundreds, or even thousands of mathematical operations, checking each element to give more accurate solutions.

The accuracy of the solution varies depending on the accuracy of the mesh. Therefore, great care must be taken in choosing the mesh based on scientific concepts such as the specific shape and type of material.

The ANSYS program suggests forming a mesh according to its vision of the body in the mesh window, and the mesh is usually correct in very simple shapes, unlike most complex things.Figure(3.21)shows mesh of specimen.

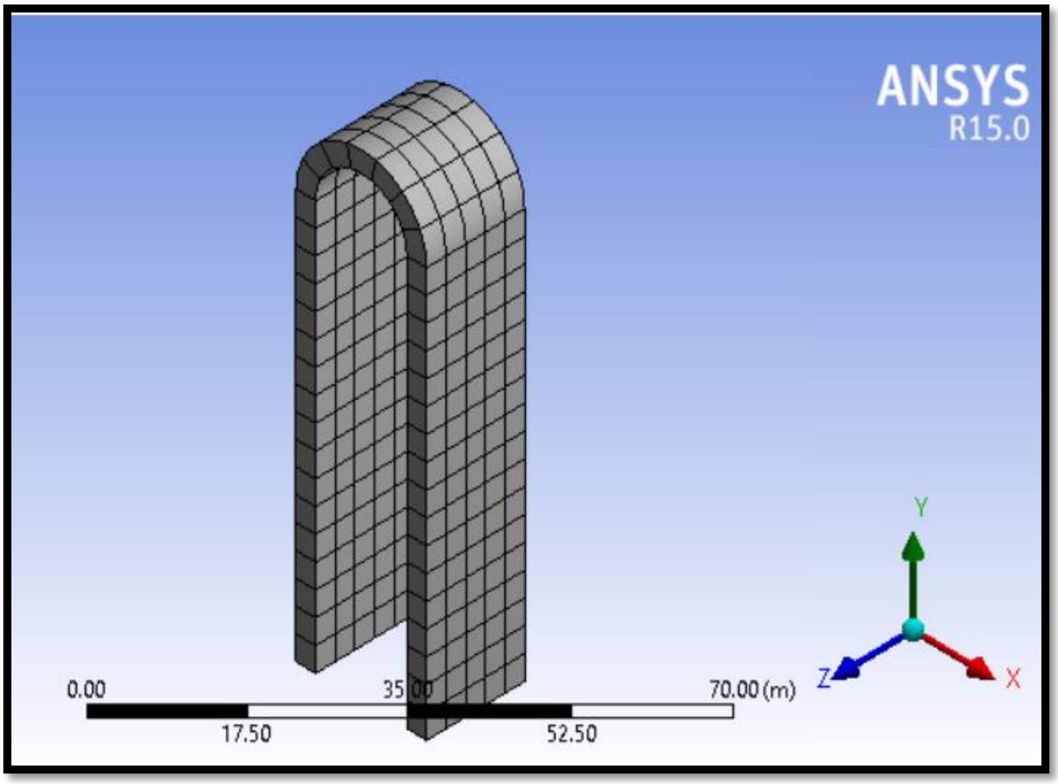

Figure(3.21):Meshing of U-Bend Specimen.

3.7.3.Boundary Counditions and Assumptions

In this study, 3-D FEM (Finite Element Method) analysis model is designed about SS316L U-bend plate, and performed stress corrosion cracking analysis. For stress analysis, stress corrosion cracking variation is expected regarding to mechanical properties depending on load and geometrical constraints, using geometrical variation obtained load analysis boundary conditions.All boundary conditions for all specimens are equal in all properties but in the applied load are different.Each types of four U-bend specimens have the same mechanical and thermal properties due to same material are used.Stainless steel 316 is the material is used for all these four specimens.

Every mechanical and thermal properties for stainless steel 316 found in the library of all new vergion ANSYS program.However the assumptions depend on some founditions such as type of specimens(flat, bend,helical), the postion of applied load and the side which is suggested to fixed.

3.7.4. ANSYS and Theoretical Calculations of Stress Corrosion Cracking (SCC)

In the following ANSYS Calculation**s** have been presented as follows:

3.7.4.1.Centrifugal Force of Disc Separator

Centrifugal force is the force that appears to be pushing outward when an object is rotated**[130]**.

$$F = \frac{mv^2}{r} \qquad \text{3.4}$$

where:

F: is centrifugal force in(N),

V: is the velocity of the moving body in (m/s),

r :is the distance of the moving body from the center in (m)

and :m is the mass of the moving body in (Kg).

Figure (3.22)displays sketch of direction particles speed and centrifugal force.

$$v = \omega \times r \qquad \text{3.5}$$

where: ω is the angular velocity in (rad/s).

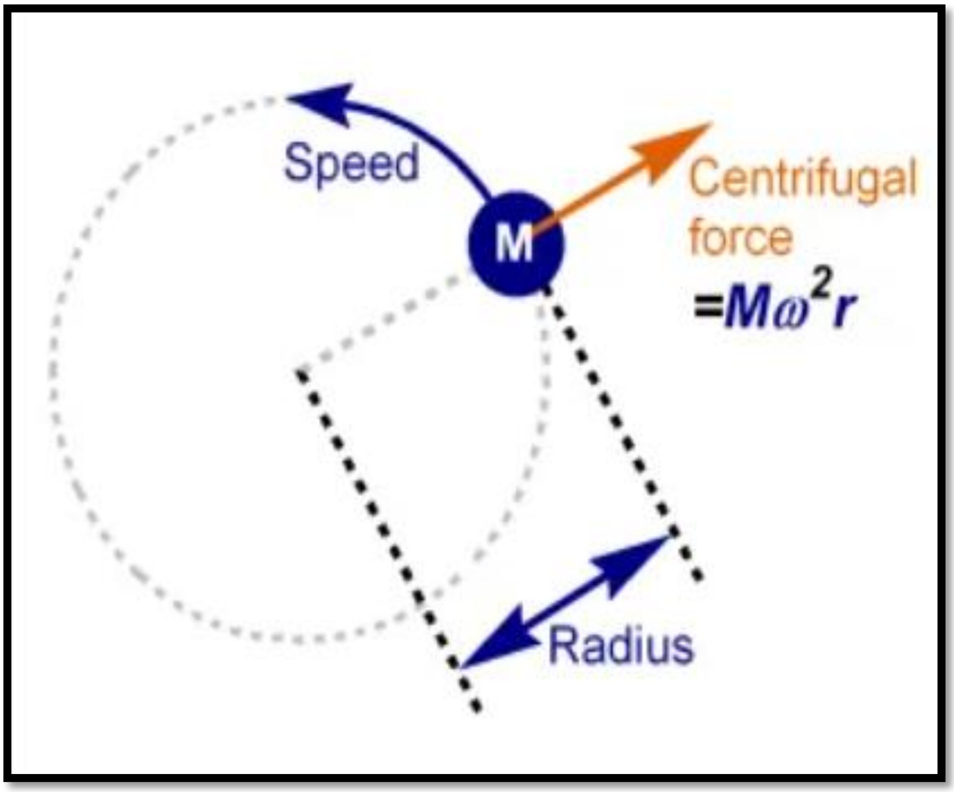

Figure (3.22):Sketch of Direction Particles Speed and Centrifugal Force.

Separator has high velocity(N) ranging between(6000-7100) r.p.m.The disc stack has truncated(frustrated) cone shape that shown in Figure (3.23.a).

Also the disc stack separator has lower(R) and upper (r)radii 80,50mm respectively and total weight 115g. The vertical height of disc separator(truncated cone) equals to 25mm.The disc stack has nine semi-circle with radius 5mm which are located at the lower surrounding diameter as shown in Figure (3.24.b).

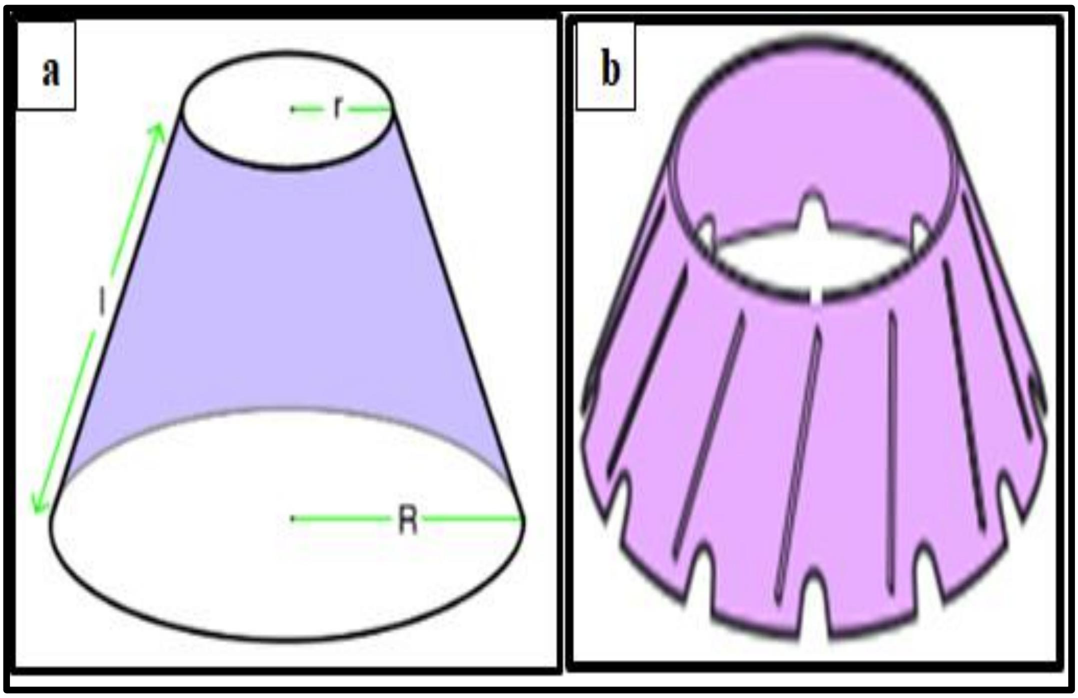

Figure (3.23):(a)Sketch of Truncated Cone(b)Disc Separator.

$\omega=\frac{2\pi N}{60}$ ……………………..……………………………….3.6

$= \frac{2*3.14*6500}{60} = 680.33\text{rad/s}$

$v = \omega \times r \quad =680.33\times0.08=54.4\text{m/s}$

Area of circle= πr^2……………………..……………………………3.7

Area of semi- circle=$\frac{\pi r^2}{2}$

Area of nine semi-circle=$\frac{9\pi r^2}{2}$

Area of truncated cone= $\pi(R+r)\sqrt[2]{h^2+(R-r)^2}$ …………………..3.8

Area of disc stack (truncated cone)=$\pi(R+r)\sqrt[2]{h^2+(R-r)^2} - \frac{9\pi r^2}{2}$

$=\pi(0.08+0.05)\sqrt[2]{0.025^2+(0.08-0.03)^2} - \frac{9\pi 0.005^2}{2}$

$=0.000621m^2 \quad =62.1 \times 10^{-5}\ m^2$

$$F = \frac{mv^2}{r} = \frac{0.115 \times 54.4^2}{0.08}$$
$$= 4254.08\text{N}$$

Cross section area of disc separator

L×t=40mm×1.5mm= 0.04×0.0015

$=0.00006m^2 \quad 6\times10^{-5}m^2$ $\quad σ= \frac{F}{A}$ ……………….………3.9

$σ= \frac{4.25\times1000}{62\times10^{-5}}$ =6.85MPa

The actual affected stress is $σ= \frac{4.25\times1000}{6\times10-5}$ =70.9MPa

According to ASTM G-30-97(2015) that is mentioned in this chapter in Table (3.2) and Figure (3.19), The stress corrosion cracking can be calculated from equation:

$$б = \in \times E \text{ ………………………………………………………………..} 3.10$$

Where : σ=theoretical stress corrosion cracking

$\in$: $strain\ rate$

*E:*moduls of elasticity for stainless steel 316L=210MPa

$$\in\ = \frac{T}{2R} \text{ ……………………………..…………………………………….} 3.11$$

Where T:thickness of specimen in meters or millimeters

R:radius curvature of U bend specimens in meters or millimeters

- For specimen (A):

From Table(3.2):

L=150mm,T=0.8mm,R=9mm

$$\epsilon = \frac{T}{2R} = \frac{0.8}{2 \times 9}$$
$$= 0.044$$

$$б = \epsilon \times E = 0.044 \times 210$$
$$= 9.24MPa$$

Cross section area of specimen (A)=T×w=0.8×15=0.0008×0.015=

0.000012m^2,so б= $\frac{F}{A}$ =9.24×10^6=$\frac{F}{0.000012}$ F$_A$=110.88N

- For specimen (B):

From Table(3.2):L=130mm,T=3mm,R=13mm

$$\epsilon = \frac{T}{2R} = \frac{3}{2 \times 13} = 0.115$$

$$б = \epsilon \times E = 0.115 \times 210$$
$$= 24.15MPa$$

Cross section area of specimen (B)=T×w=3×15

0.003×0.015

=0.000045 m^2 б= $\frac{F}{A}$ = 24.15×10^6=$\frac{F}{0.000045}$ F$_B$=1086.75N

- For specimen (C):

From Table(3.2):L=120mm,T=1.5mm,R=16mm

$\in= \frac{T}{2R} = \frac{1.5}{2\times16}$ =0.04687

$=\in \times E$ = $0.04687 \times 210 =$

9.828MPa

Cross section area of specimen (C)

=T×w=1.5×20

0.0015×0.02=0.00003 m^2

Ϭ= $\frac{F}{A}$ = 9.828 ×10^6 = $\frac{F}{0.00003}$ F_C=294.84N

- For specimen (D):

From Table(3.2):L=102mm,T=3mm,R=5mm

$$\in= \frac{T}{2R} = \frac{3}{2\times5}$$
$$= 0.3$$

$6 =\in \times E =\ 0.3 \times 210 = 63$MPa

Cross section area of specimen (D)=T×w

=3×19

0.003×0.019

=0.000057 m^2

Ϭ= $\frac{F}{A}$ = 63 ×10^6

= $\frac{F}{0.000057}$

F_D=3591N

3.7.4.2. The Modeling and Method of Stress Procedure Analysis

The commercial code ANSYS 15.07 was used for stress analysis. Figure (3.24) shows 3-D FEM meshed model of sample (A) U-bend plate. The number of node sample(A) is 1668, and the number of elements is 205. Total applied force was 110.88N,so the force in the end of each side of U-bend plate was 55.44N but these forces were in the opposite side.

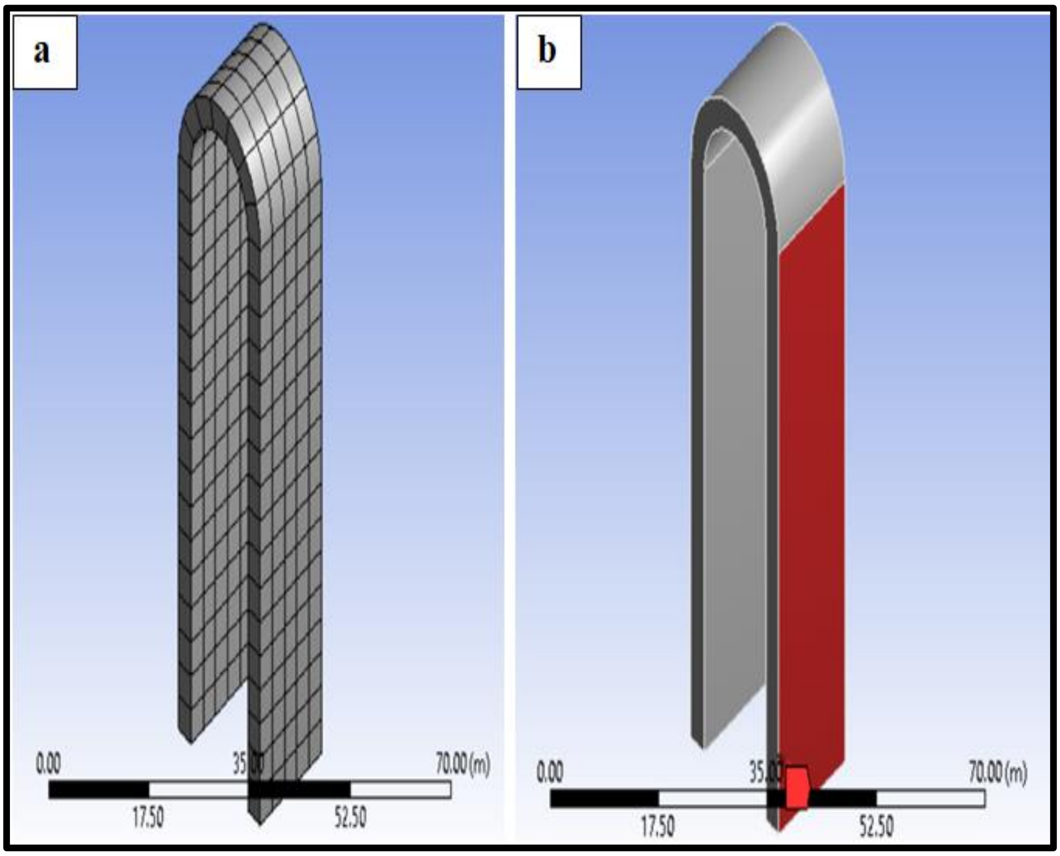

Figure(3.24): U-Bend of Sample (A) (a): Meshed Model (b)Applying Force.

Figure(3.25) shows 3-D FEM meshed model of sample (B) U-bend plate. The number of node sample(B) is 1628, and the number of elements is 200. Total applied force was 1086.75N,so the force in the end of each side of U-bend plate was 543.375N but these forces were in the opposite side.

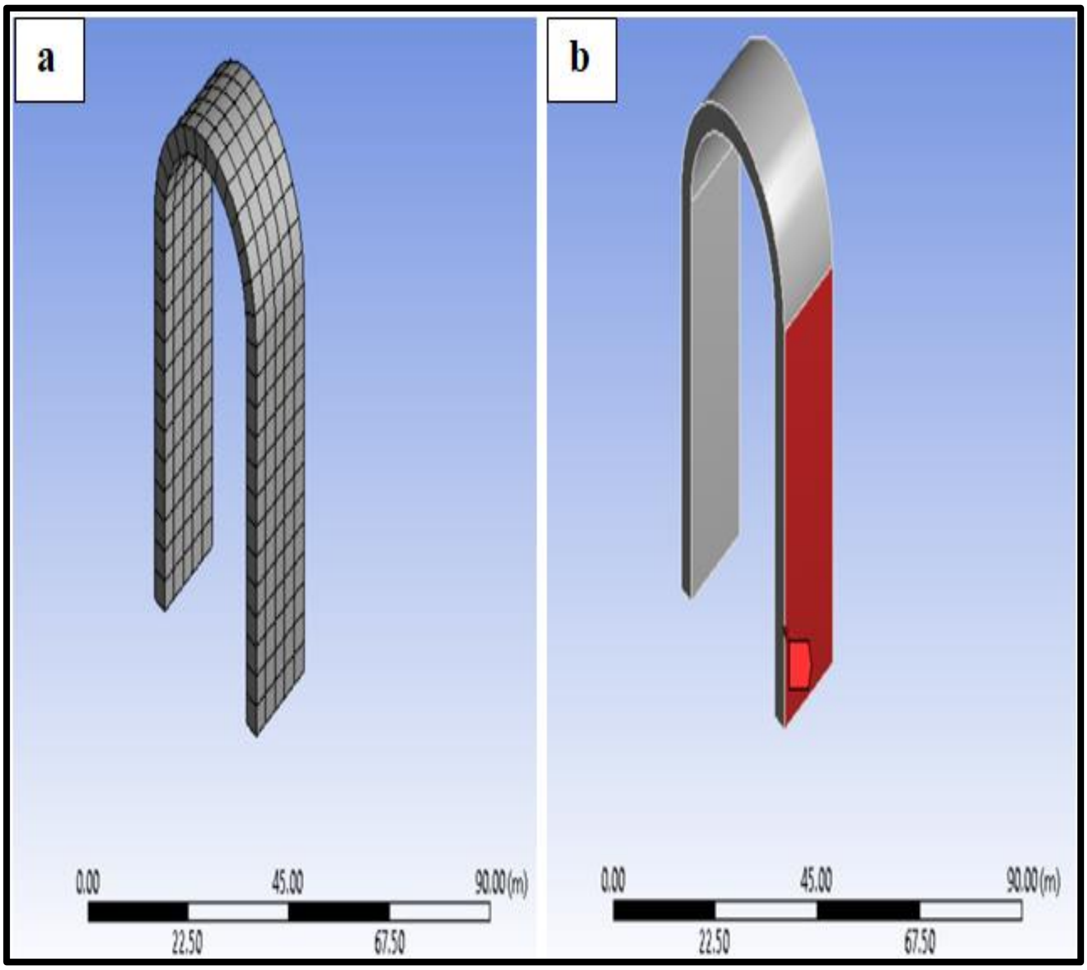

Figure(3.25): U-Bend of Sample (B) (a): Meshed Model (b)Applying Force.

Figure(3.26) shows 3-D FEM meshed model of sample (C) U-bend plate The number of node sample(C) is 4304, and the number of elements is 553. Total applied force was 294.84N,so the force in the end of each side of U-bend plate was 147.42N but these forces were in the opposite side.

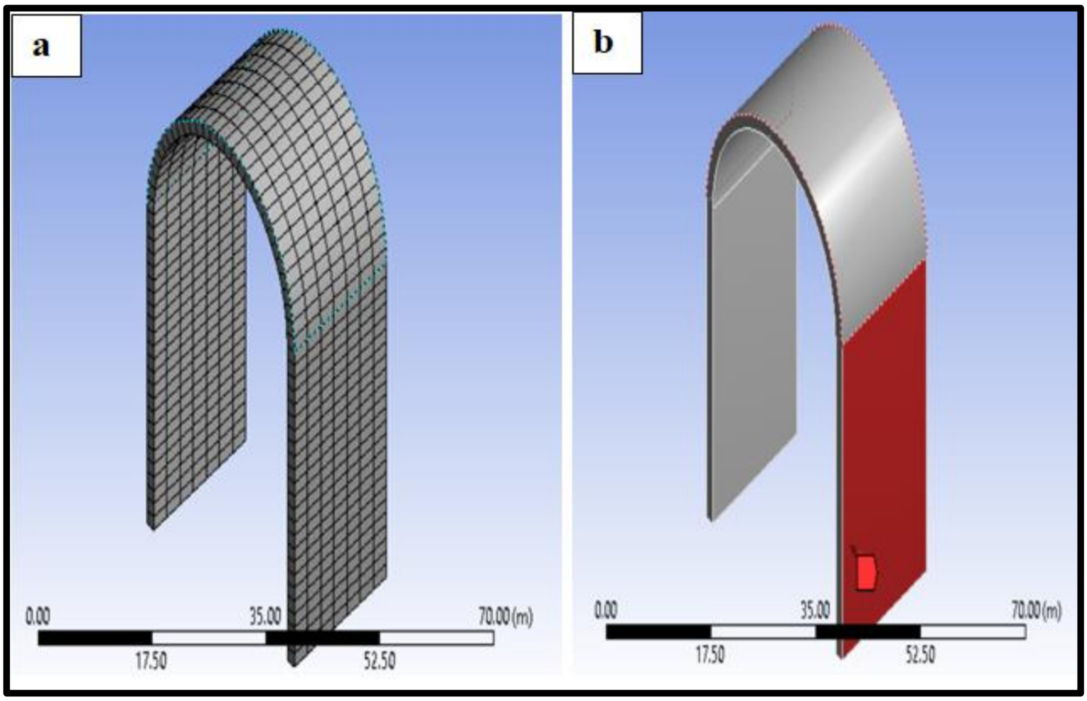

Figure(3.26): U-Bend of Sample (C) (a): Meshed Model (b)Applying Force.

Figure(3.27) shows 3-D FEM meshed model of sample (D) U-bend plate The number of node sample(D) is 4304, and the number of elements is 553. Total applied force was 3591N,so the force in the end of each side of U-bend plate was 1795.5N but these forces were in the opposite side.

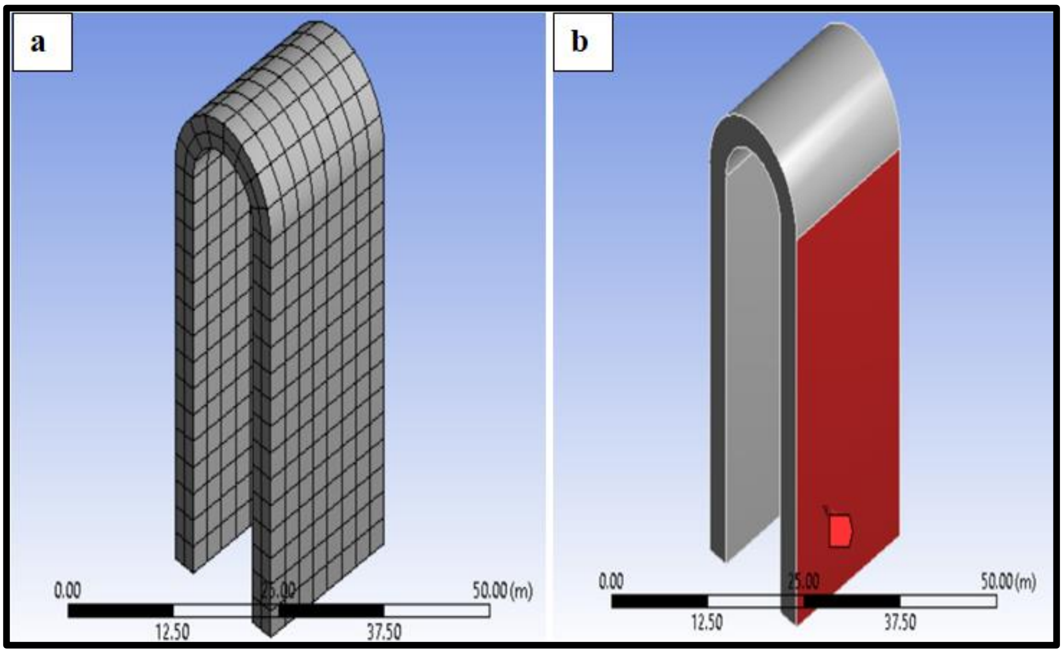

Figure(3.27)-Bend of Sample (D) (a): Meshed Model (b)Applying Force.

Chapter4

Results & Discussion

Chapter Four

Results & Discussion

4.1. Introduction

Firstly, the results of the failure analysis; visual test, fuel analysis, corrosion product analysis, and hardness measurement are discussed. Secondly this chapter deals with analyzing the force and stress, equivalent stress , strain, directional deformation and total deformation due to mechanical force are calculated by ANSYS workbench(15.07). Finally this chapter shows and discusses all results of mechanical, physical tests after electroless plating. Several various aspects are chosen in the discussion of results; time of coating, examination time in erosion-corrosion test ,time and force effect on stress crack corrosion test.

4.2. Failure Analysis

In the following failure analysis results have been presented as follows:

4.2.1. Chemical Composition of Disc Stack Separator

The result of quantitative examination of the disc separator material is found as in Table (4.1)

Material of Disc Separator							
Element	**%**	**Element**	**%**	**Element**	**%**	**Element**	**%**
C	0.0416	Ni	9.14	Al	0.0428	Mn	1.13
Si	0.283	Cr	17.66	Cu	0.411	Fe	Bal.
Mo	1.9						

It was similar to stainless steel 316. From the result of chemical composition, it is clear that the disc separator is manufactured from alloys has high corrosion resistance. The presence of Ni and Cr in high percentage in alloy of bowel disc has high corrosion resistance .

4.2.2. Microstructural of Disc Separator

Optical microscopy is used to evaluate the microstructural of disc stack . In this easy test, samples were taken from an undamaged disc to find out the microstructure and compare it with the microstructure of a damaged disc .From disc microstructure; grains of γ (Austenite) and carbide particles shown to be precipitated in the matrix.

Substances that have a tendency to strengthen austenite γ are copper, manganese, and nickel are prominent elements in chemical composition analysis.(Cu)Copper Similar to (C)carbon, these elements change the critical points of iron by raising the A_4 point and reducing the A_3 point, expanding the range in which austenite is stable. Figure (4.1) displays the microstructure of damaged and undamaged discs.

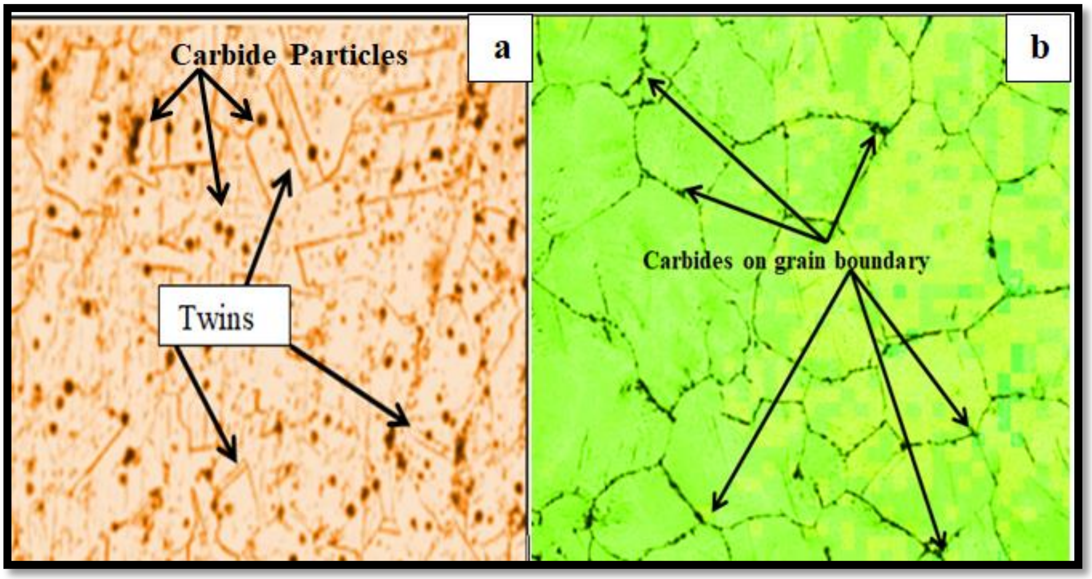

Figure (4.1): Microstructure of(a): Undamaged Disc (80x) and(b): damaged Disc (80x).

4.2.3. Crack Evaluation

The damaged of disc stack separator consists of many different cracks located at different regions and has different lengths. Figure (4.2) shows three different region which subjected to the stresses. The lower region III of damage bowel disc has more micro-crack, because it consists of high concentration stresses in addition to the high tensile load from centrifugal force which coming from high rotational speed. Figure (4.3) shows in SEM image of failure disc separator, several cracks have been observed which propagate along grain boundary. In the cases the cracks propagate along the grain boundary, the fracture that obtained is called intergranular fracture. All cracks are considered as stress concentrations which raise the induced stresses and lead to fracture.

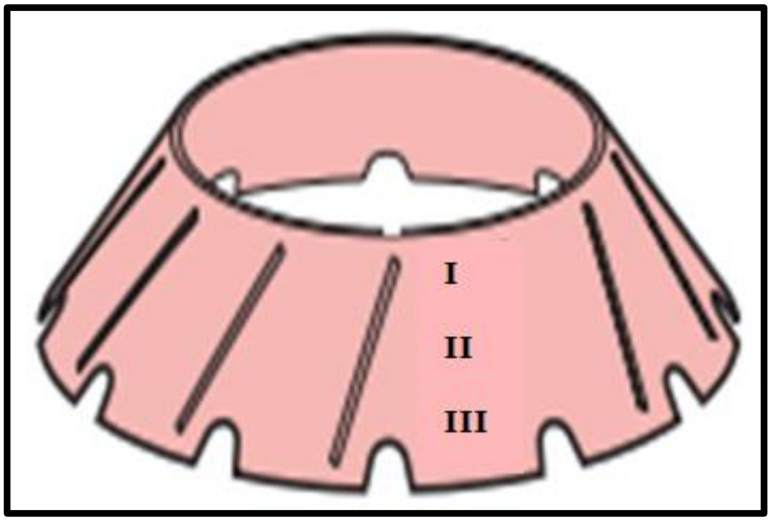

Figure (4.2):Sketch of Damage Disc Separator Consists of Three Different Regions.

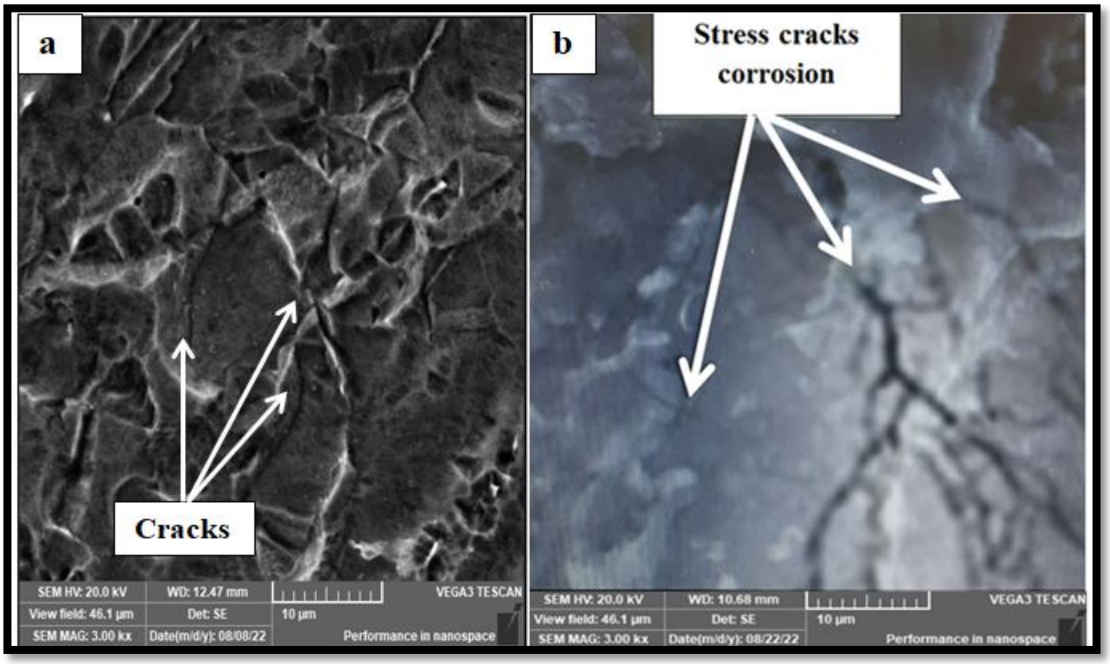

Figure (4.3):SEM Images Cracks Propagate in:(a): RegionII(b)RegionIII.

4.2.4. Evaluation of Corrosion Products Analysis

Samples for evaluation corrosion product analysis are taken from the surface of disc stack where the corrosion products deposited on the surface. The chemical composition of corrosion product is obtained by X-ray-fluorescence as illustrated in Table (4.2) that consists of many effective contaminants. Some of these contaminations with high percentage in high speed rotational more than 6000 r.p.m may be considered the most causes to occur erosion –corrosion. Most of contaminations such as sodium, calcium, chlorine may be found combine with other elements.

Mostly compounds and oxides such as sodium chloride found in fuel or sodium carbonate or other compounds contain one of the halide radicals. Halides such as chlorine, iodine, and bromine are among the most important causes of stress corrosion cracking (SCC).

Table (4.2):Analysis Elements of Corrosion Products.

Elements	**Percentage%**	**±σ**	**Elements**	**Percentage%**	**±σ**
Ca	8.1	0.05	Mo	0.02	0.00
Sc	0.012	0.005	W	0.035	0.011
Ti	0.03	0.033	Au	0.001	0.000
V	3.1	0.02	Hg	0.000	0.002
Cr	0.509	0.008	Pb	0.006	0.001
Mn	0.013	0.008	Th	0.000	0.000
Fe	0.697	0.011	U	0.001	0.000
Co	0.017	0.005	S	9.00	0.17
Ni	3.00	0.02	Ash	residual	
Cu	0.01	0.004			
Zn	0.14	0.003			
As	0.002	0.000			
Na	0.501	0.001			
Rb	0.000	0.000			
Sr	0.04	0.001			
Zr	0.000	0.000			

4.2.5. Evaluation of Heavy Fuel

Samples for evaluation the used fuel in Kufa power plant are taken from three different sources; Najaf Refinery, Samawa Refinery and Diwanya Refinery. Table (4.3)shows the harmful elements in heavy crude oil which are provided from three refineries. From the results, the contaminations in fuel providing from Najaf refinery and Diwanya refinery are higher than the fuel which providing from Samawa refinery. The results of analysis and the information's of database are taken from the planning unit at the power plant refer to the life failure of disc stack depending on type of fuel used. When the power plant works on fuel supplied from Samawa refinery, the life of disc stack ranges between (5760-6480) hrs. On the other hand when the power plants works on fuel supplied from Diwanya refinery ranges between (4320-5760) hrs. operating with fuel supplied from the Najaf refinery gives a short life ranging from(4320hrs to 3600hrs).Chart(4.4) displays the life of disc stack according to the used fuel.

Table (4.3): Analysis of Heavy Fuel

Results of Samawa Refinery		**Results of Diwaniya Refinery**	
Type	**wt. %& (ppm)**	**Type**	**wt. %& (ppm)**
C%	8.0	C%	10.2
Asphaltaene%	2.82	Asphaltaene%	4.216
Na(ppm)	32.93	Na(ppm)	44.4
Zn(ppm)	0.13	Zn(ppm)	0.066
S%	4.63	S%	5.18
Al &Si(ppm)	3.67	Al &Si(ppm)	5.03
Ca (ppm)	24.46	Ca (ppm)	10.09
V(ppm)	70.27	V(ppm)	99.47

Results of Najaf Refinery	
Type	**wt. %& (ppm)**
C%	10.2
Asphaltaene%	3.864
Na(ppm)	52.17
Zn(ppm)	0.06
S%	5.15
Al &Si(ppm)	4.55
Ca (ppm)	4.76
V(ppm)	104.91

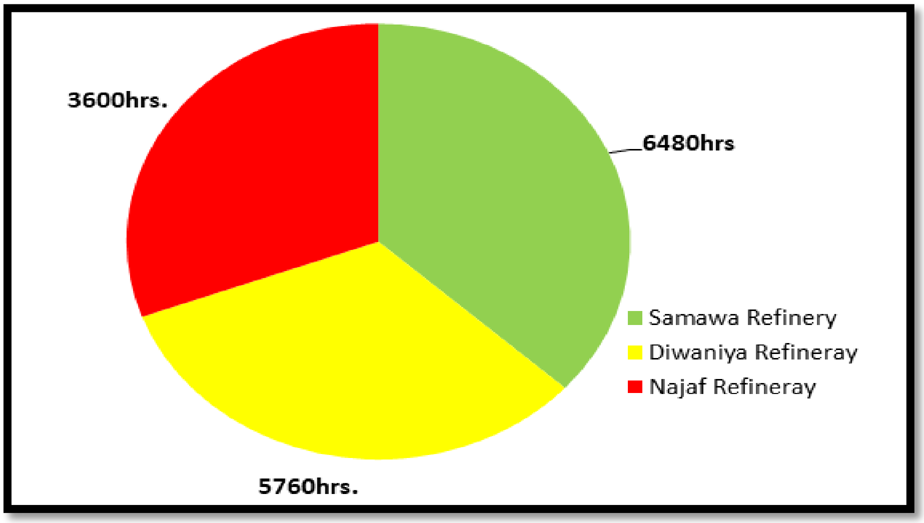

Figure(4.4):Life of Disc Bowel According to Source of Heavy Fuel Used.

4.2.6.Evaluation of Hardness Test

The hardness was taken for a cross-section along 40 mm(length of all three regions) of the disc bowel to the upper, middle and lower three regions, as these regions are shown in Figure (4.2)above. Figure (4.5.a) below shows the hardness values for the three regions of the damage disc bowel. On the other hand ,Figures (4.5.b) and (4.5.c) display the traces of diamond pyramid in the damage disc. The hardness values in the three regions showed a clear and remarkable gradient between the first and the third regions. The hardness in the first region ranged from 330HV to 316HV, which is almost identical to the hardness of the undamaged base metal. In the second region, the hardness was slightly affected and almost did not differ much from the first region, and the hardness values ranged between 312HV to 265HV. Finally, the third region witnessed a clear decline in the hardness values, reaching approximately 220HV. This gradation and decline in hardness values is due to the influence of this region by erosion factors, as well as being an area of high stress concentration, in addition to the surrounding conditions. All these may help in formation of stress corrosion cracking and a decrease in hardness.

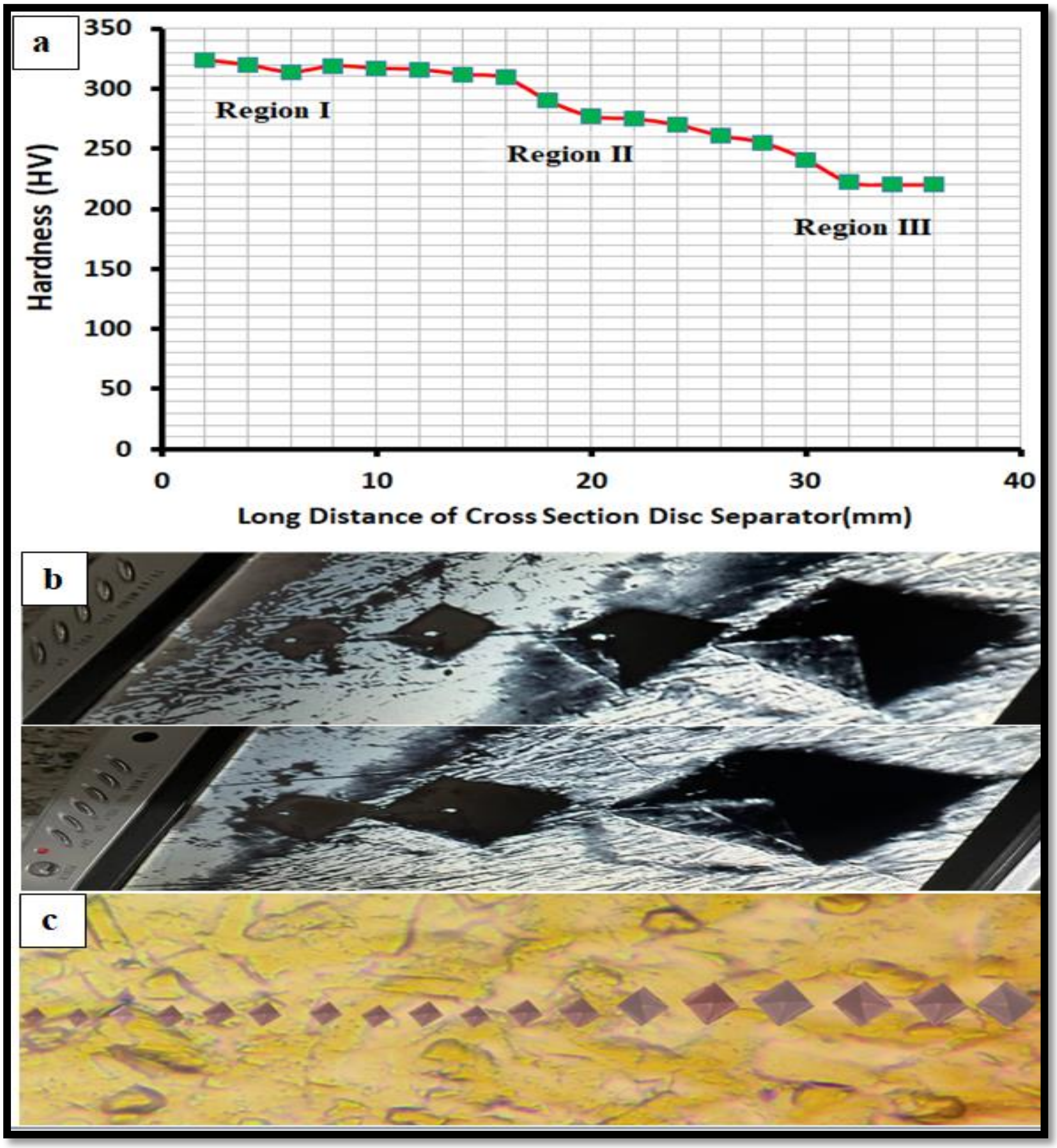

Figure (4.5): (a)Hardness of Disc Bowel in Three Different Regions(b)and(c)Pyramid Diamond Traces of Hardness.

4.2.7. XRD Analysis of Disc Bowel Material

To examine the produced phases, the X-ray diffraction (XRD) was performed for the prepared alloy standard SS316L. In this alloy that was examined, the austenitic stainless steel peaks were obtained at (111), (200), and (220) with face center cubic structure, as shown in Figure (4.6). The diffraction patterns contain large peak at 43.6^{o} and relatively small peaks at 51.2^{o} and74.3^{o}. These peaks are close to the austenite phase's (200) and

(220) peaks in the substrate, but they are wider, indicating the existence of a different phase with smaller crystallite size. Due to their low weight percentage, the other phases, such as molybdenum-carbide, may not be visible during XRD analysis.

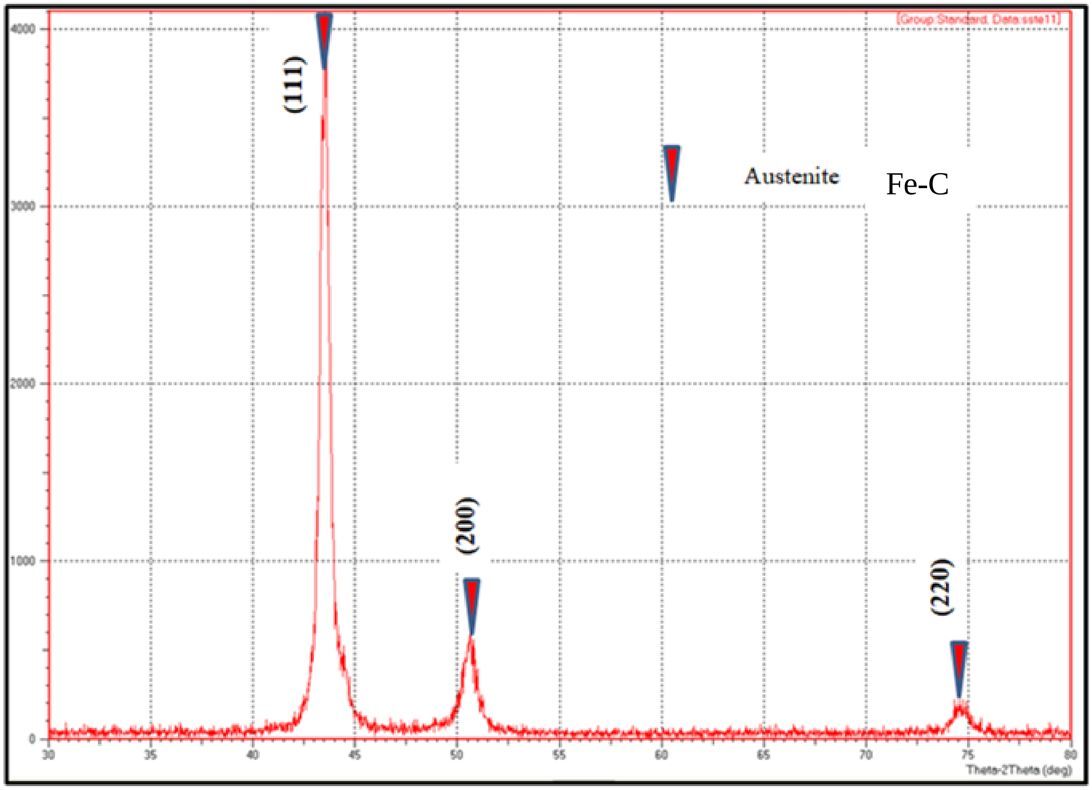

Figure (4.6):XRD-Pattern for Disc Stack Material.

4.3.Electroless Plating

After discussion failure analysis , the results of mechanical, physical, stress corrosion cracking, erosion corrosion, and microscopic properties of EN coatings are discussed.

4.3.1. Chemical Composition of Material Used

The material that used for electroless-plating by four different coatings in two different coating time approximately similar to the material of failed disc separator. Table(4.4) displays the most important elements in this alloy.The material is identical to SS316L.

Table(4.4): Chemical Composition of Material Used,Disc Separator and Standard Material.

Material Used							
Element	**%**	**Element**	**%**	**Element**	**%**	**Element**	**%**
C	0.0258	S	0.0005	Al	0.0428	P	0.0409
Si	0.509	Cr	17.61	Cu	0.261	Fe	Bal.
Mn	1.04	Mo	2.35	Ni	11.55		
Disc Separator							
Element	**%**	**Element**	**%**	**Element**	**%**	**Element**	**%**
C	0.0416	Ni	9.14	Al	0.0428	Mn	1.13
Standard Material[81]							
Element	**%**	**Element**	**%**	**Element**	**%**	**Element**	**%**
C	0.02	Cr	17.2	Ni	10.1	Mo	2.1

4.3.2. Coating Thickness

Several different range of coating thickness that are obtained; (10-70), (7-50)and(7-30) µm. This different depends on several parameters (time of coating, temperature of solution, type of bath, degree of agitations, the presence of another particle). In this study, two different time(60,120min.) are used. Figure (4.7) shows the thickness of coating by SEM image for cross section of coated specimens by(Ni-Zn-P).

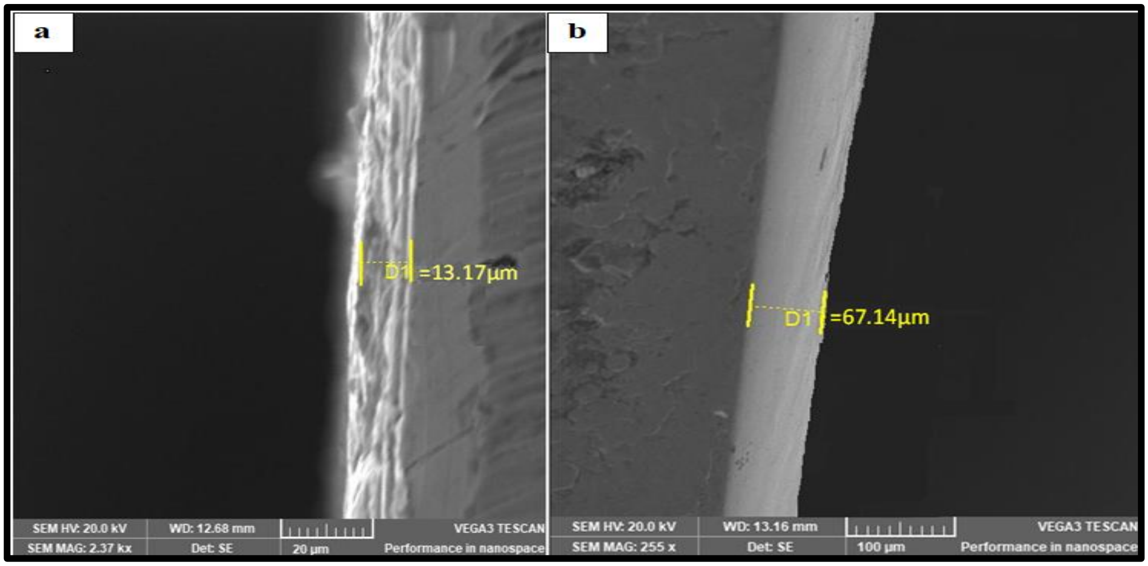

Figure (4.7):SEM Images of Coating Specimens by (Ni-Zn-P)at: (a): 1-hr. Time of Coating (b): 2-hrs time of Coating.

Figure(4.7b) has a significant difference in some properties such as magnitude of thickness, good compaction, and apparent cohesion rather than Figure(4.7.a). Figure (4.8) shows the thickness of coating by SEM image for cross section of coated specimens by(Ni -P). In this figure, clusters or balls of nickel-phosphorous phases are clear, in addition to the increase in the size of the balls in Figure(4.8b) in comparison with Figure(4.8.a) as a result of the increase in the thickness of the coating through the change in time between 60 and 120 minutes. From the pictures of SEM, there are no visible cracks.

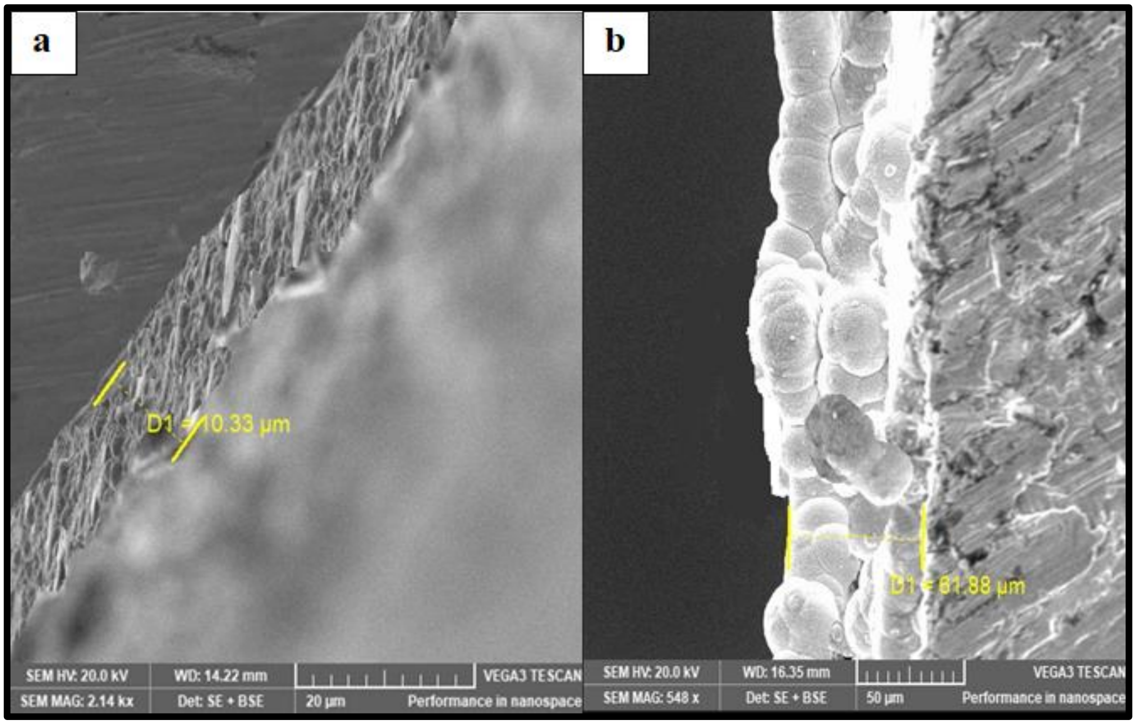

Figure (4.8):SEM Images of Coating Specimens by (Ni -P)at (a): 1-hr. Time of Coating(Side Image) (b): 2-hrs. Time of Coating(Cross Section Image).

Figure (4.9) shows the thickness of coating by SEM image for cross section of coated specimens by(Ni-Cu-P). There is no significant difference in thickness or morphology between the (Ni-Cu-P) plate and (Ni-P). Perhaps the change will be in the surface properties between them as a result of the presence of copper.

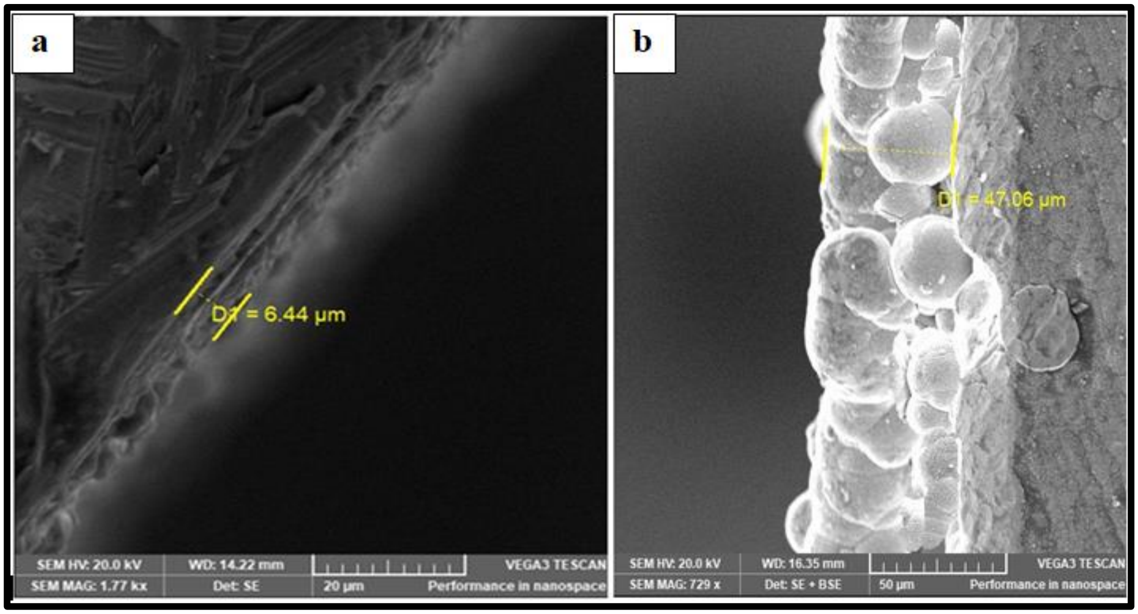

Figure (4.9):SEM Images of Coating Specimens by (Ni-Cu -P)at: (a): 1-hr. Time of Coating (Side Image) (b): 2-hrs. Time of Coating(Cross Section Image).

Figure (4.10) shows the thickness of coating by SEM image for cross section of coated specimens by(Ni-SiC-P). There is significant difference in thickness of (Ni-SiC-P) plate from other three plating. The obvious difference in thickness is due to the presence of nanoparticles. These particles improve the surface properties of the samples, but they make the sedimentation process difficult and require high control.

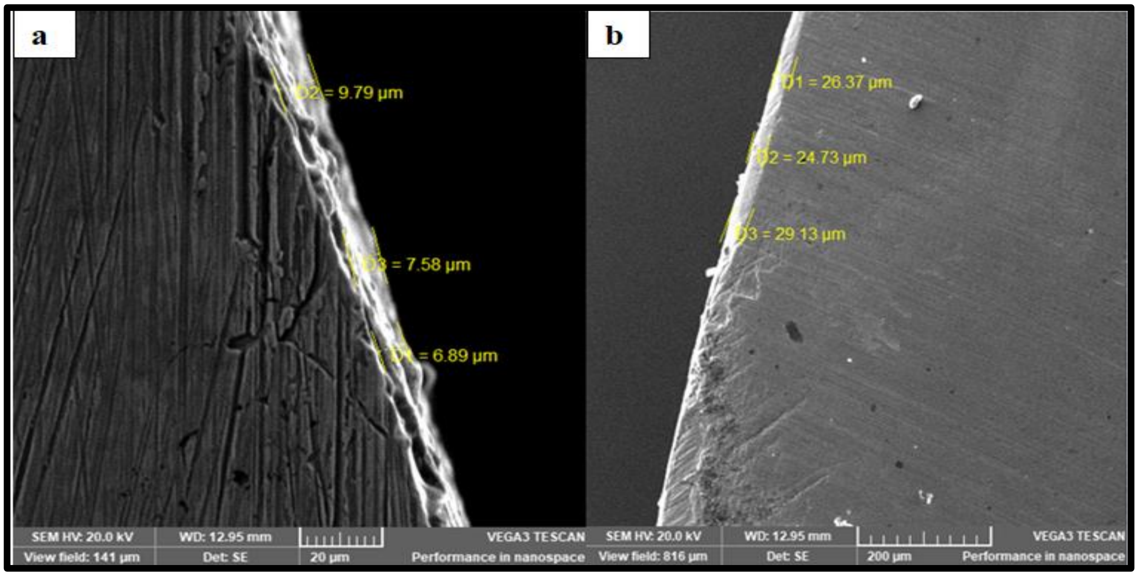

Figure (4.10):SEM Images of Coating Specimens by (Ni-SiC-P)at: (a): 1-hr. Time of(Side Image) Coating (b): 2-hrs. Time of Coating(Side Image).

4.3.3. Coating Adhesion Strength

The adhesion strength of the coating layers for (Ni-P,Ni-Cu-P,Ni-Zn-P, and Ni-SiC-P) was tested before and after heat treatment for two parameters(1, 2-hrs.) time of coating by using the pull-off test (ASTM-D4541) **[125]**, as shown in Table (4.5). It is noticed that increasing in adhesion strength after heat treated samples than as plated samples ,this explanition is agreed with **[131].**

Table (4.5)Adhesion Strength of Four Electroless Plating.

Type of Electroless Plating	Adhesion Strength(MPa)			
	As-Plated (1-hr.)	Heat-Treated (1-hr.)	As-Plated (2-hrs.)	Heat-Treated (2-hrs.)
Ni-Zn-P	28.6	49.3	25.7	45.6
Ni-P	31.6	56.6	27.8	50.11
Ni-Cu-P	33.9	64.2	31.4	58.8
Ni-SiC-P	39.2	71.5	35.3	63.4

4.3.4. Heat Treatment Effect on Hardness

Hardness test is carried out after plating the specimens(as-plated and heat treated) to study the effect of heat treatment on the hardness electroless plating. SS316L circle specimens are coated by Ni-P as a matrix with thickness ranged(7-70µm) for four types of electroless plating. Figure (4.11) shows the temperature effects of heat treatment and coating time on electroless plating hardness measurement. Also this figure significantly displays the hardness of the heat treated specimens is much higher than the hardness of the specimens as-plated only. The sharp increasing in hardness is obtained from good distribution of fine crystallites of nickel and phosphorus in matrix after the heat treatment. The presence of SiC nanoparticles which have a hardness of more than 2000 HV, in Ni-P matrix, contributes to increasing the hardness of the nickel-phosphorus coating several times compared to the coating that does not contain it. The heat treatment forms intermetallic compounds like (NiSi,Ni_3Si,Ni_5P_2,Ni_3P, NiZn,$Ni_{12}P_5$ and NiP),all these intermetallic compound contributed by increasing the hardness and improving surface properties. Finally through the curves in the Figure (4.11) show that there is an increase in hardness values of the (Ni-Cu-P),(Ni-Zn-P)and(Ni-SiC-P) electroless plating which containing a percentage of copper, zinc and SiC compared with the other (Ni-P)alone, this increasing in hardness values of electroless plating that due to the presence copper and zinc content which give more compactness and high smoothness to the coating layer as well as reduce porosity in coating layer.The aim from this process (heat treatment) is given a high crystalline and uniform distribution , also to improve some of mechanical properties such as hardness and corrosion resistance.

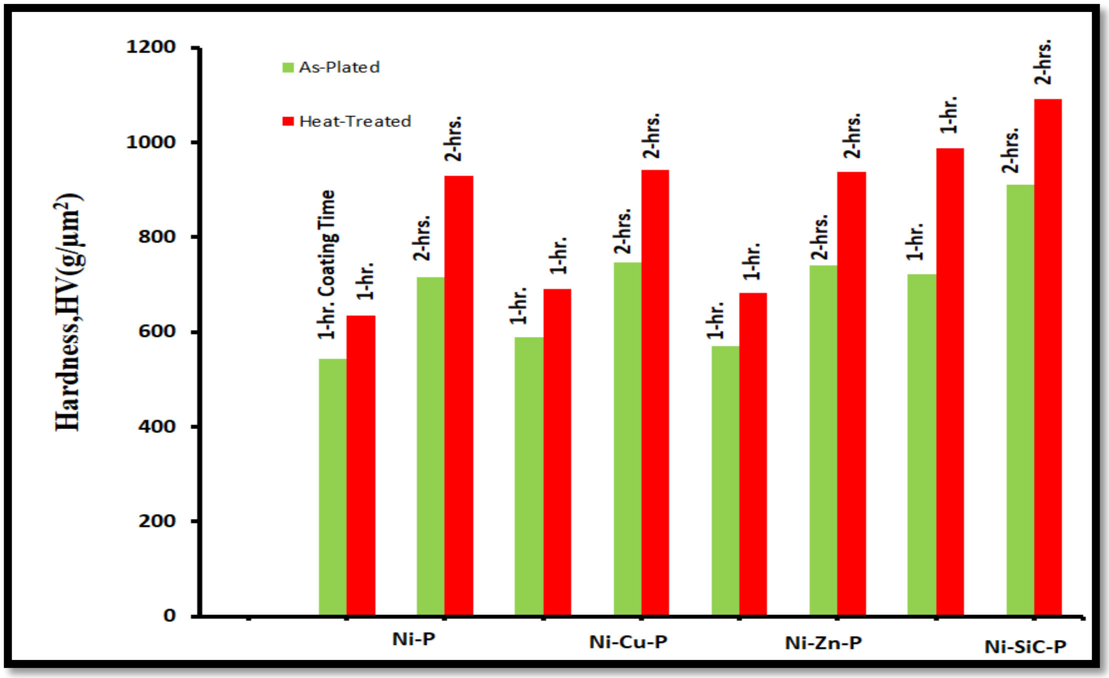

Figure (4.11): Hardness Variation with Coating Time for As Plated & Heat Treated Specimens

Through the two Figures(4.12)and(4.13), the state of the distribution of the coating elements before and after the heat treatment for specimens with 2-hrs. coating time can be seen, where Figure(4.12) shows the agglomerations of coating elements for (Ni-P)plating(As-Plated), while Figure(4.13) shows the correct diffusion and actual distribution after the heat treatment.

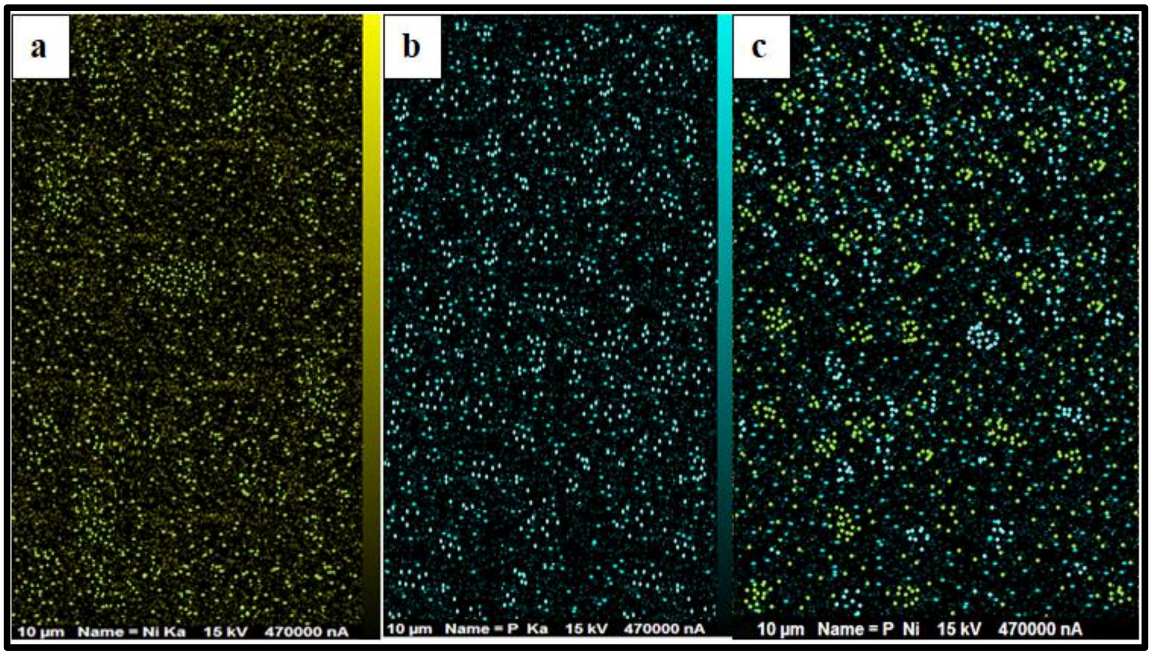

Figure (4. 12): EDS Mapping Displays Distribution of Coating Layer Elements by Ni – P(As Plated-2hrs.): (a) Ni- Element(b): P-Element(c)Ni&P elements.

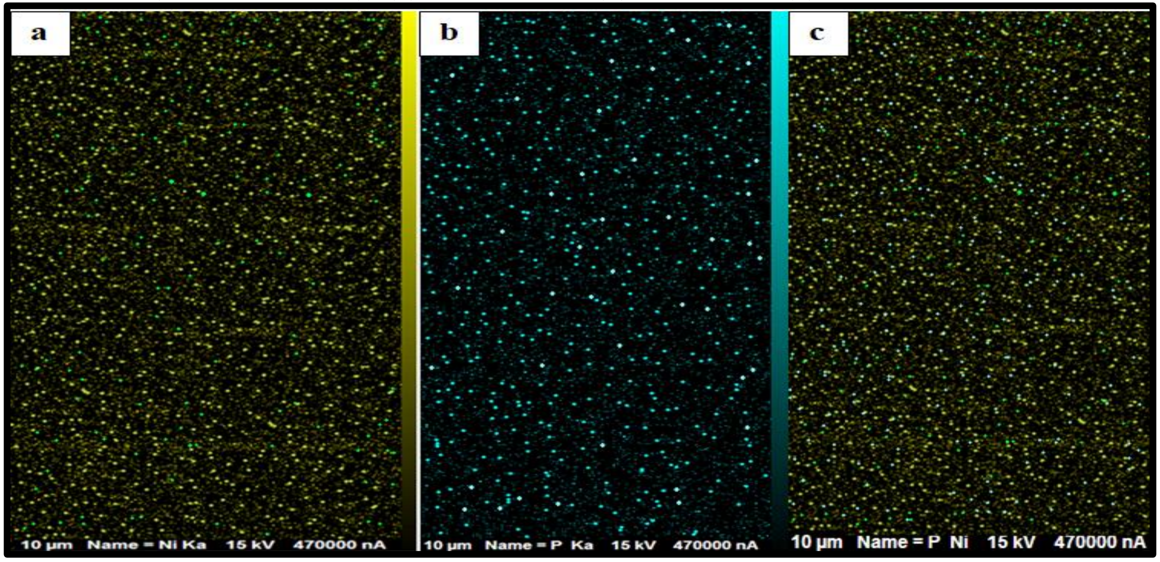

Figure (4. 13): EDS Mapping Displays Distribution of Coating Layer Elements by Ni – P(After Heat-Treated-2hrs): (a) Ni- Element(b): P-Element(c)Ni&P elements.

Figure(4.14) displays the random distribution of coating layer(Ni-Cu-P) (As-Plated),where Figure(4.14.a) shows the random agglomerations of Ni which the main coating elements. Figure(4.14.b) shows the presence of copper which is another coating element in a matrix. Copper adds good surface properties to the matrix of coating layer. Figure(4.14.c) shows the random distribution of phosphorus element in the matrix .

After heat treatment in high temperature(400^{o}C) for 1-hour,all elements of coating layer tend to re-disribution them in matrix.This heat treated process give high improvement to the most surface properties. Hardness, corrosion resistance,erosin resistance and wear resistance can be increased due to formation the intermeatallic compound (Ni_xP_y).Figure(4.15) shows the re-distribution coating elements after heat treated.

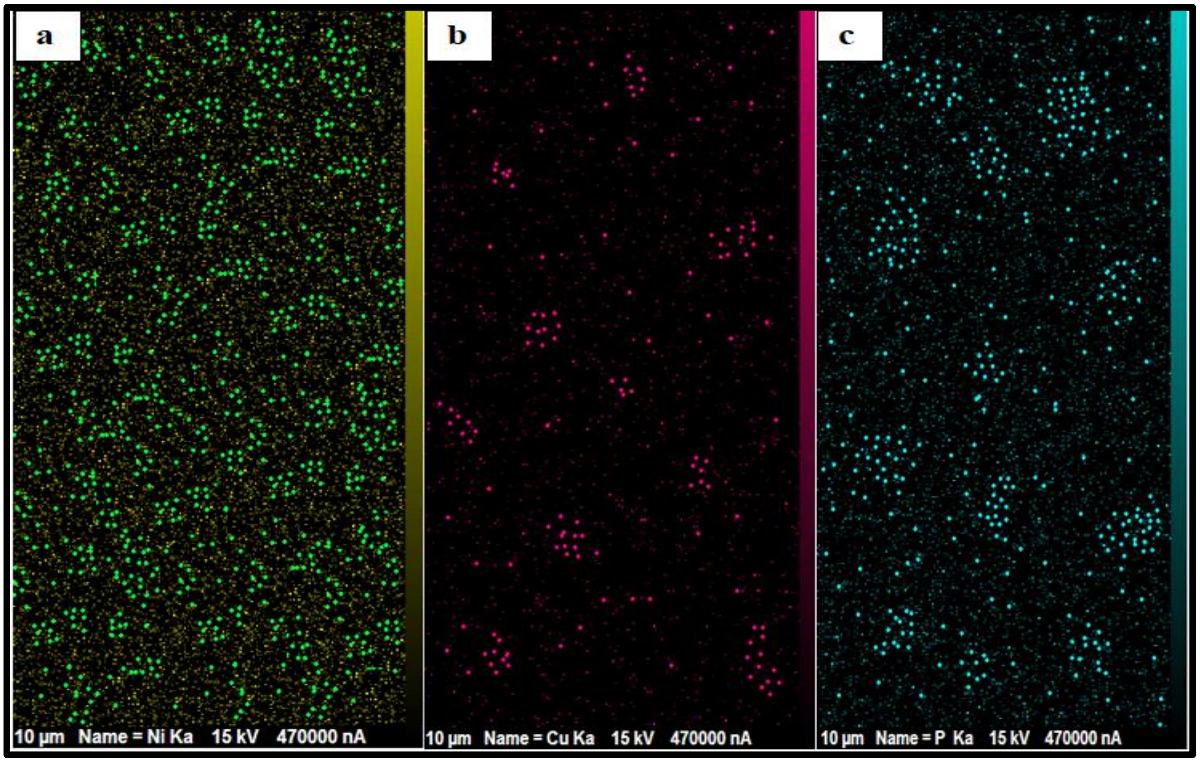

Figure (4. 14): EDS Mapping Displays Distribution of Coating Layer Elements by Ni-Cu-P(As-Plated-2-hrs.): (a) Ni- Element(b)Cu-Element(c)P-Element.

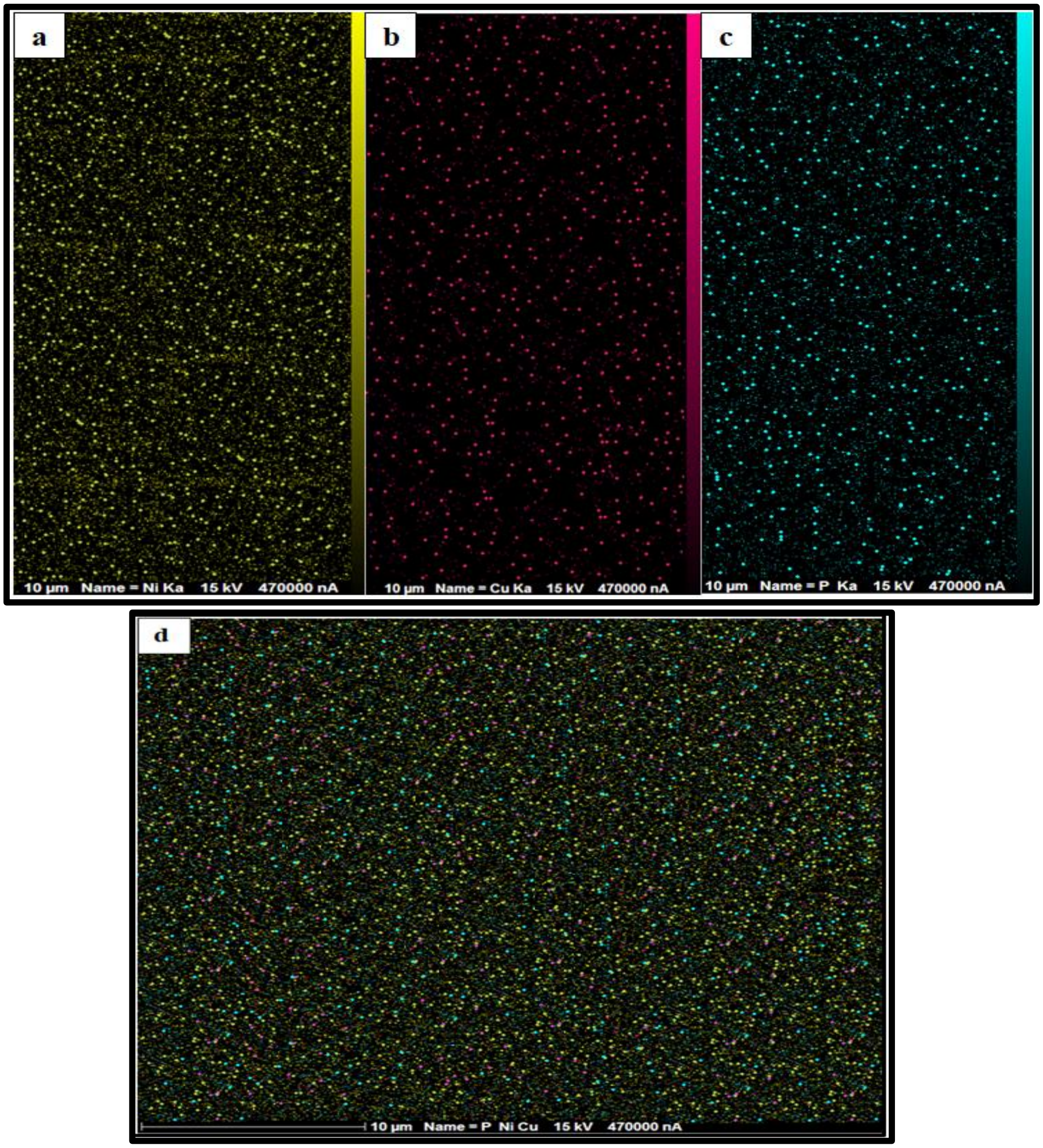

Figure (4. 15): EDS Mapping Displays Distribution of Coating Layer Elements by Ni-Cu-P(Heat-Treated-2-hrs.): (a) Ni- Element(b)Cu-Element(c)P-Element(d)All elements.

Figure(4.16) displays the random distribution of coating layer(Ni-Zn-P) (As-Plated),where Figure(4.16.a) shows the random agglomerations of Ni which the main coating elements. Figure(4.16.b) shows the presence of zinc which is another coating element in a matrix. Zinc enhances surface properties of coating layer. Figure(4.16.c) shows the random distribution of phosphorus element in the matrix .

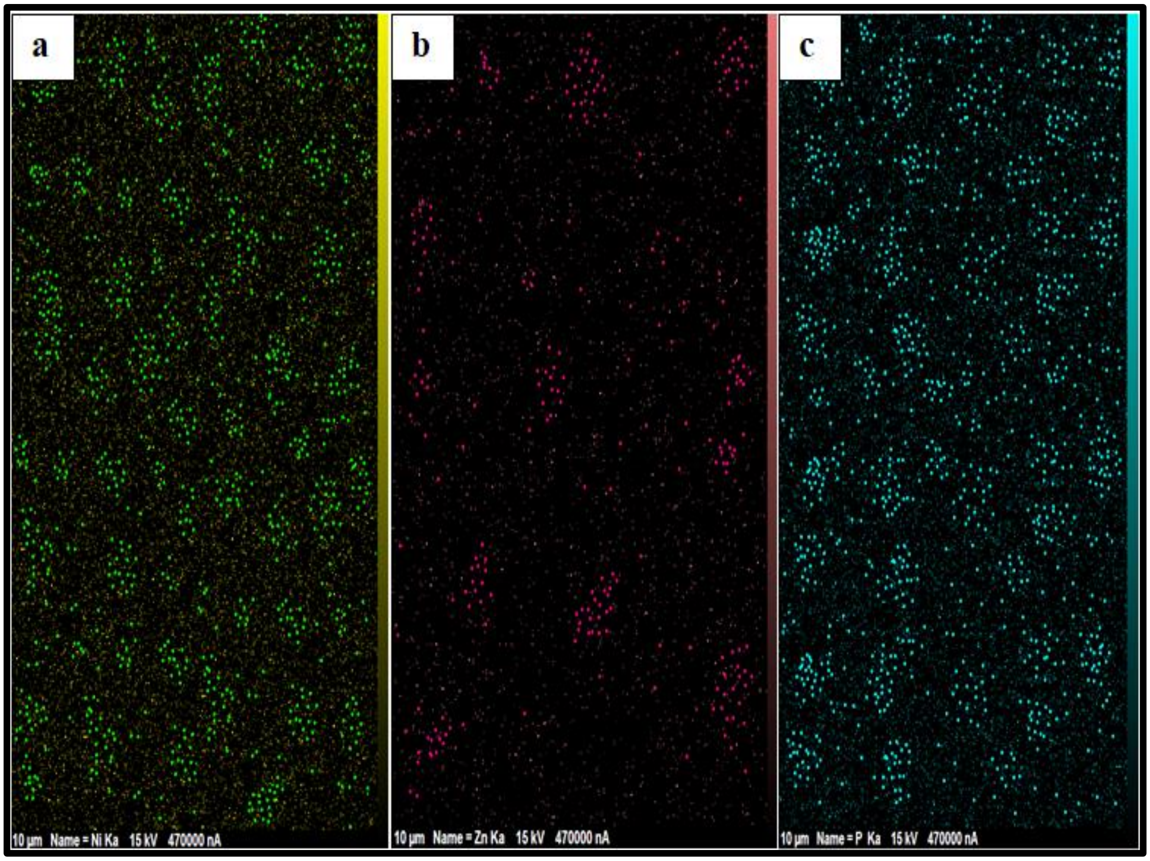

Figure (4. 16): EDS Mapping Displays Distribution of Coating Layer Elements by Ni-Zn-P(As-Plated-2-hrs.): (a) Ni- Element(b)Zn-Element(c)P-Element

All coating layer elements have a tendency to redistribute themselves in the matrix after being heated at a high temperature (400^{o}C) for one hour.The majority of surface qualities are significantly improved by this heat treatment procedure. Due to the development of the intermetallic compound, hardness, corrosion resistance, erosion resistance, and wear resistance can all be increased. The elements with re-distribution coating following heat treatment are shown in Figure (4.17).

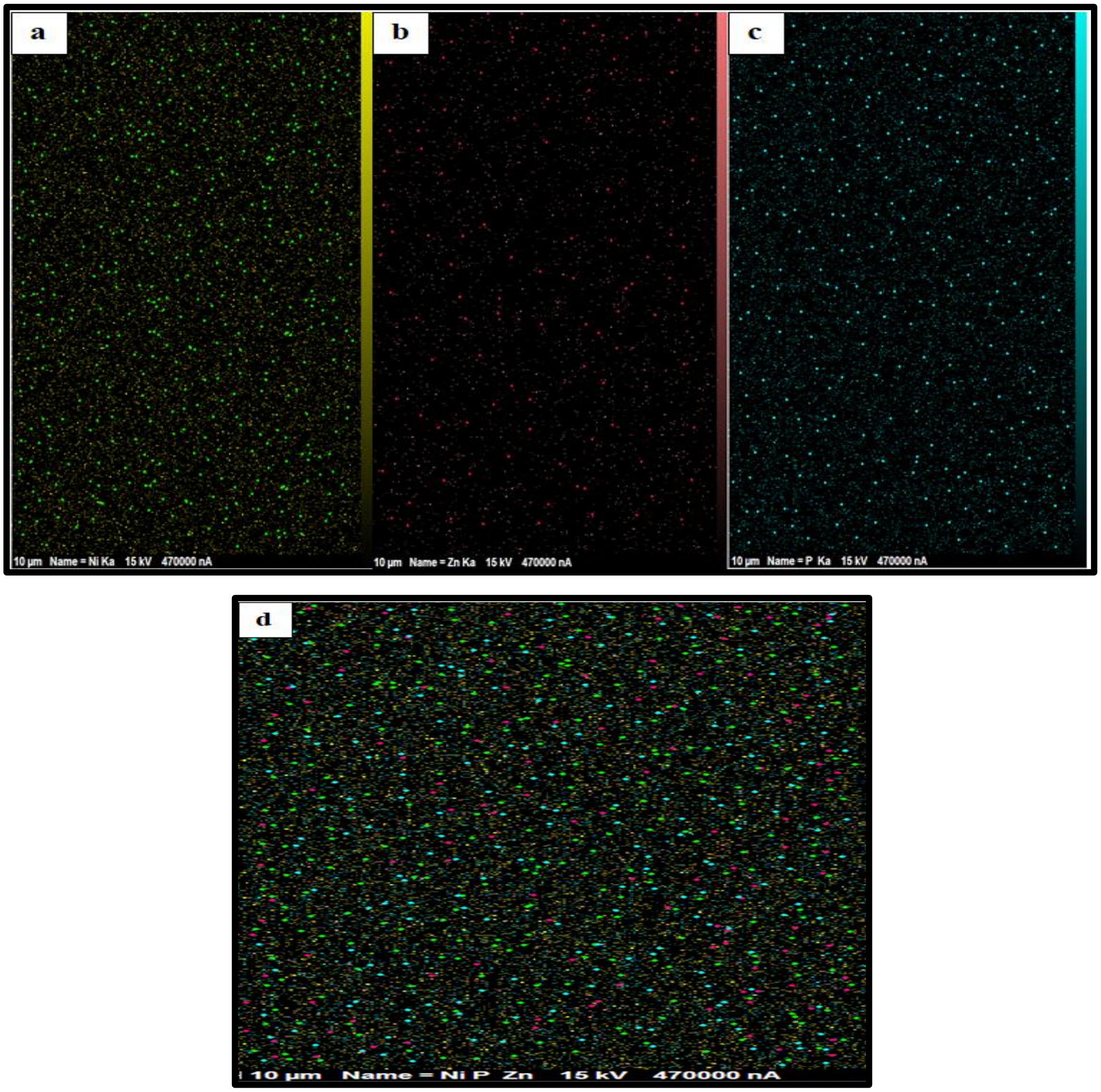

Figure (4. 17): EDS Mapping Displays Distribution of Coating Layer Elements by Ni-Zn-P(Heat-Treated-2-hrs.): (a) Ni- Element(b)Zn-Element(c)P-Element(d)All Elements

Figure(4.18) illustrates the random distribution of the coating layer (Ni-SiC-P) (As-Plated), and Figure (4.18.a) depicts the random clusters of Ni, which make up the majority of the coating. Silicon another coating element, is depicted in Figure (4.18.b) as being present in a matrix. The coating layer's surface characteristics are improved by silicon. The random distribution of the element phosphorus in the matrix is depicted in Figure (4.26.c).While Figure(4.18.d)depicts the random distribution of carbon element in the matrix.

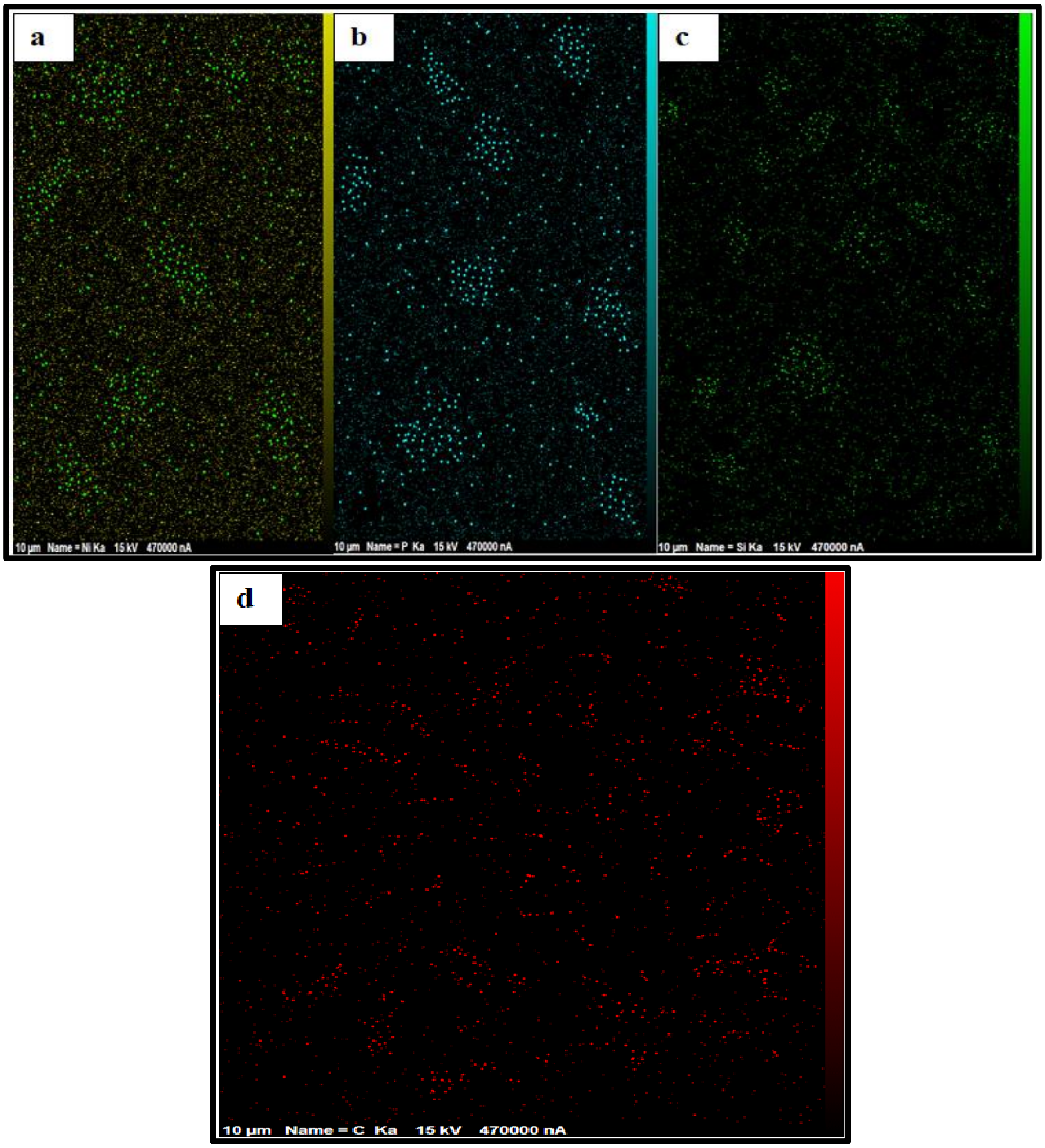

Figure (4. 18): EDS Mapping Displays Distribution of Coating Layer Elements by Ni-SiC-P(As-Plated-2hrs.): (a) Ni- Element(b)P-Element(c)Si-Element(d)C-Element.

After being heated at a high temperature (600^{o}C) for one hour, all coating layer elements have a tendency to redistribute themselves in the matrix. This heat treatment procedure significantly improves the majority of surface qualities by increasing hardness, corrosion resistance, erosion resistance, and wear resistance by developing the intermetallic compound. The elements with re-distribution coating after heat treatment are shown in Figure(4.19).

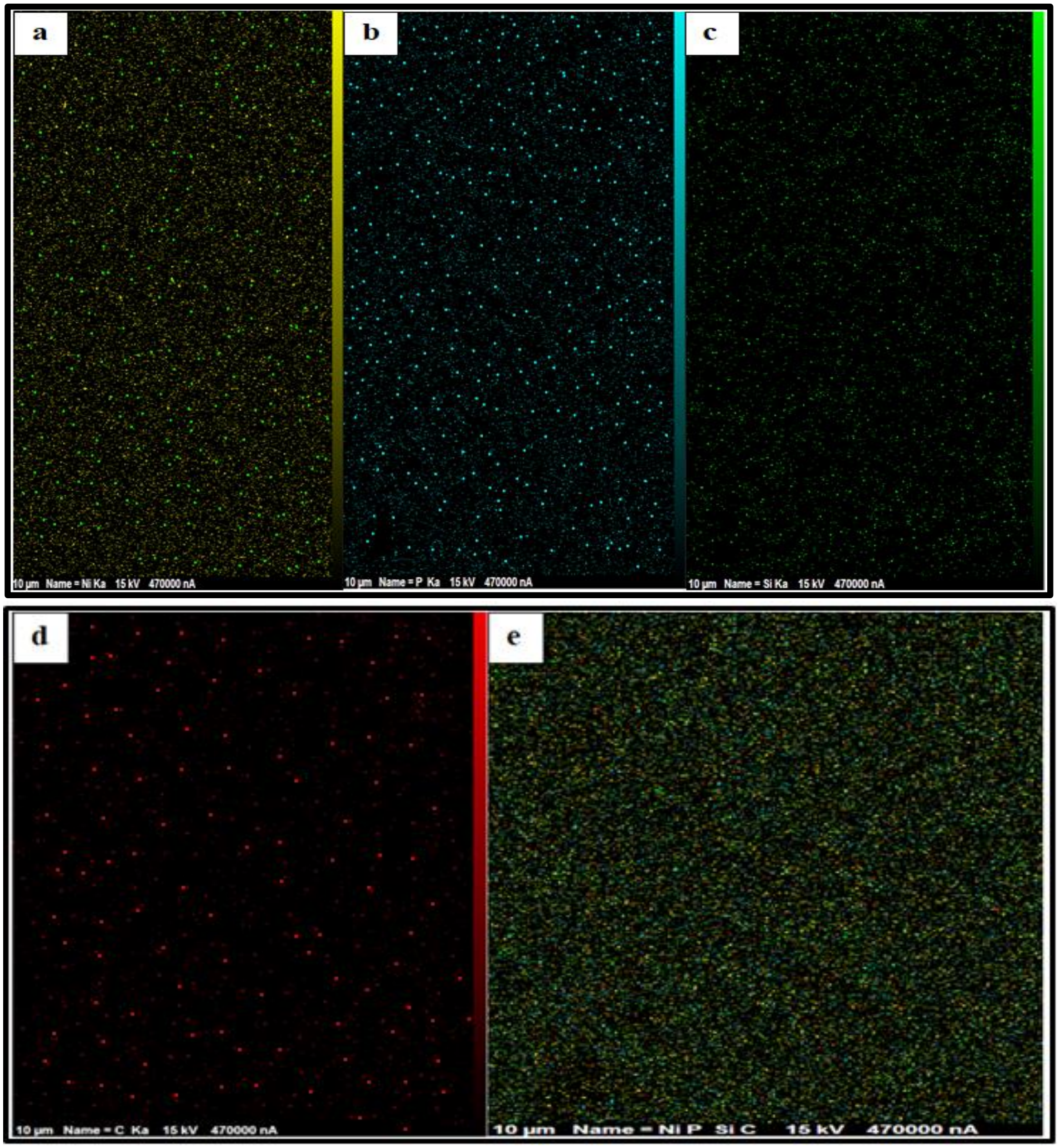

Figure (4. 19): EDS Mapping Displays Distribution of Coating Layer Elements by Ni-SiC-P(Heat-Treated-2hrs.): (a) Ni- Element(b)P-Element(c)Si-Element(d)C-Element(e)All Elements

4.3.5. Evaluation of (P,Cu,Zn,SiC) Content Effect

Incorporating mineral elements into electroless-plating techniques is of utmost importance in enhancing surface and mechanical properties. The most significant characteristics that are impacted by (P,Cu,Zn,SiC) content change are hardness, wear resistance, and corrosion resistance. Figure (4.20.a) shows the EDS chart of Ni-P in 1-hr.time coating. In this chart some important element appear in the surface of coating such as Ni, P. The percentage of phosphorus element results from coating at 1-hr. approximately equal to 3.12%,but this percentage increased to the twice at 2-hrs. time of coating and reached to 6.87% as in Figure(4.20.b).

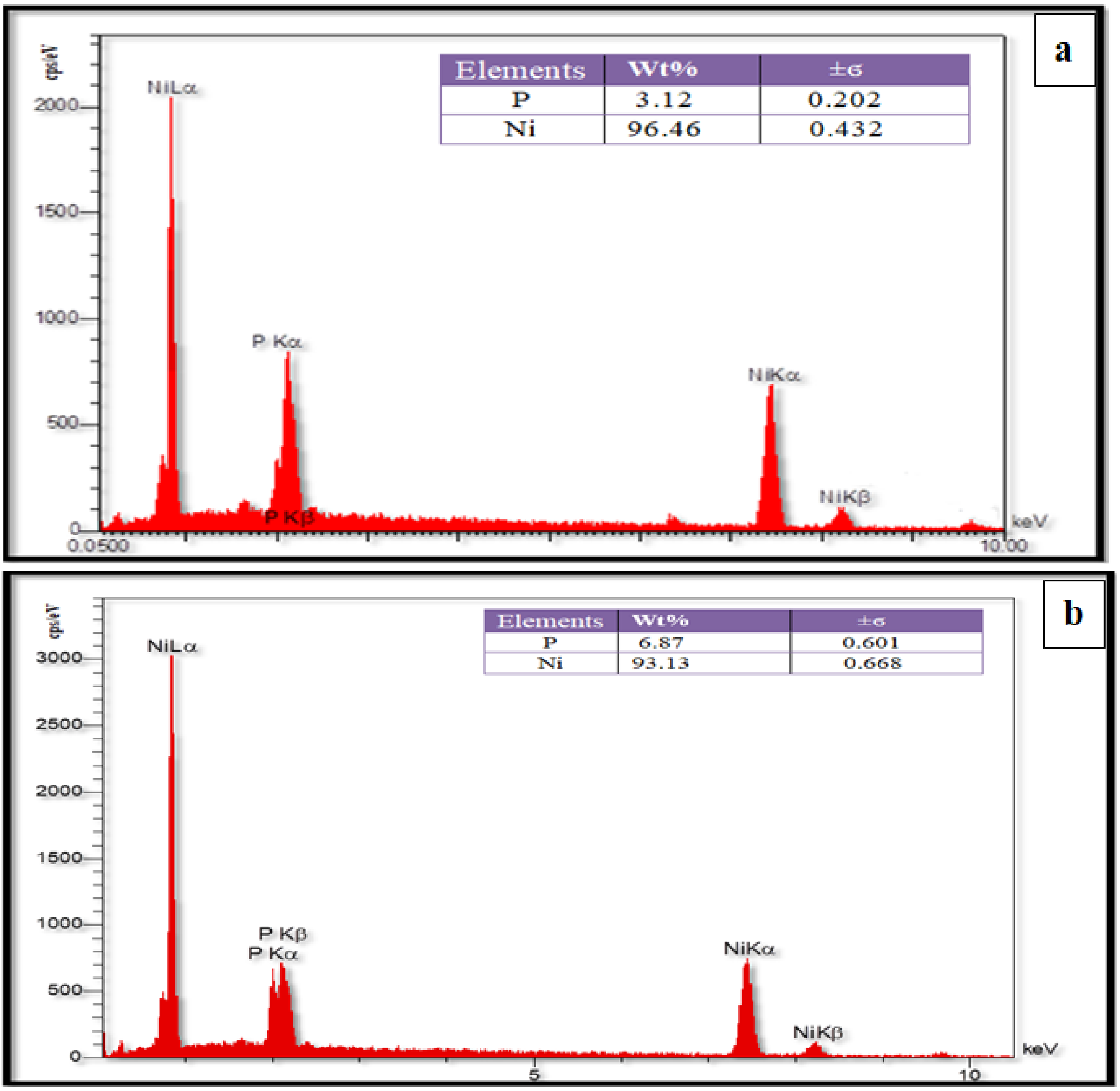

Elements	Wt%	±σ
P	3.12	0.202
Ni	96.46	0.432

Elements	Wt%	±σ
P	6.87	0.601
Ni	93.13	0.668

Figure (4.20): EDS Chart of Coated Specimen by Ni-P at Coating Time:(a):1-hr.:(b):2-hrs.

The EDS chart of Ni-Cu-P in a 1-hour time coating is displayed in Figure (4.21.a). This graph illustrates various significant elements that can be found on coating surfaces, such as Ni, P and Cu. In Figure (4.21.a) the percentage of copper that results from coating at one hour is equivalent to 2.55%; however, at 2-hrs., this proportion reaches to 3.92% as in Figure(4.21.b). The increase in the copper content was at the expense of the decrease in the phosphorous content.

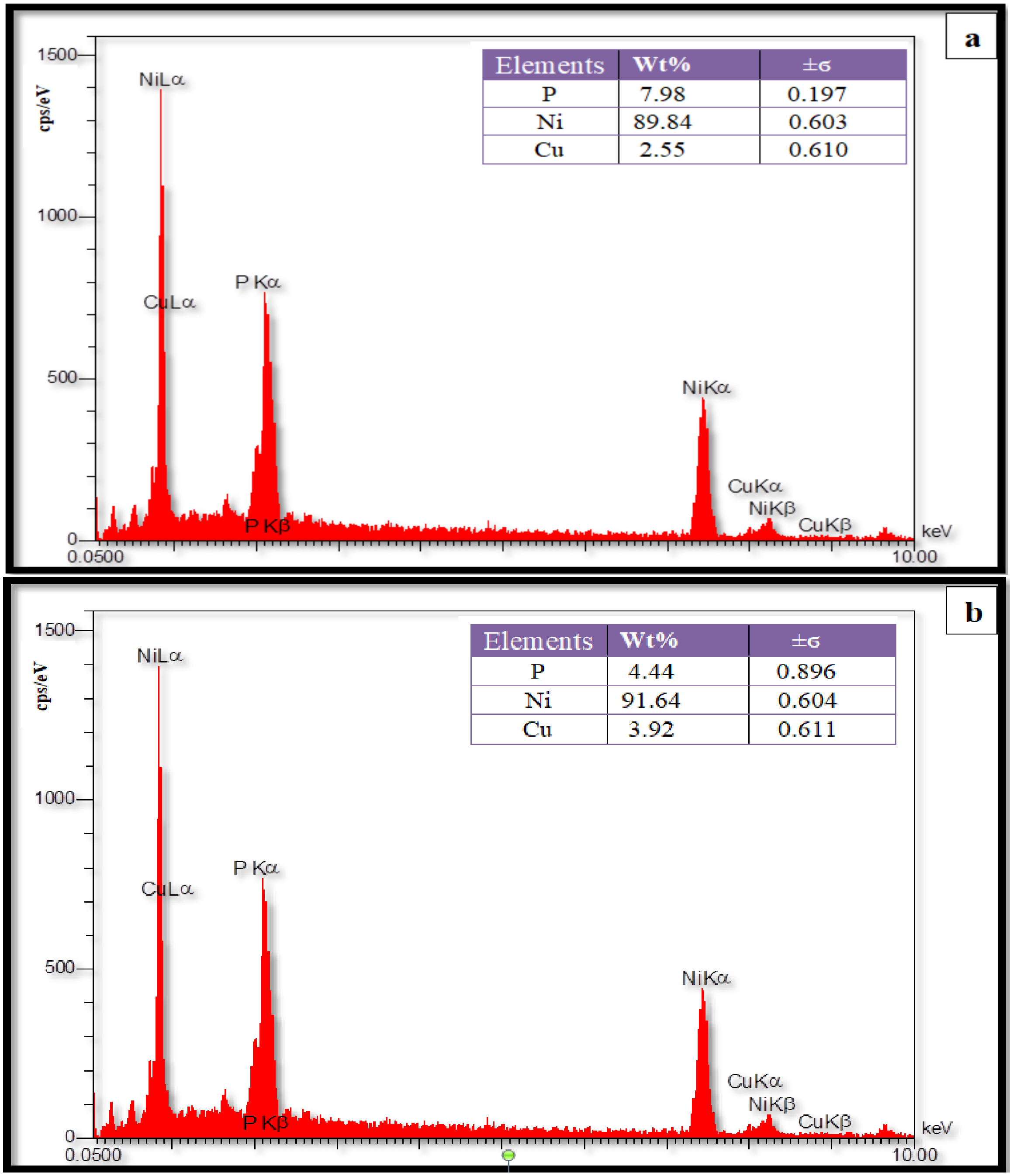

Elements	Wt%	±σ
P	7.98	0.197
Ni	89.84	0.603
Cu	2.55	0.610

Elements	Wt%	±σ
P	4.44	0.896
Ni	91.64	0.604
Cu	3.92	0.611

Figure (4.21): EDS Chart of Coated Specimen by Ni-Cu-P at Coating Time:(a):1-hr.:(b):2-hrs.

Figure (4.22.a) shows the (Ni-Zn-P)EDS chart for a one-hour time coating. This graph shows different important substances that are present on coating surfaces, including Ni, P, and Zn. Figure (4.22.a) shows the percentage of zinc produced by coating after one hour, which is equal to 15.77%; whereas, Figure (4.22.b) shows the percentage after two hours, which is equal to 18.77%.

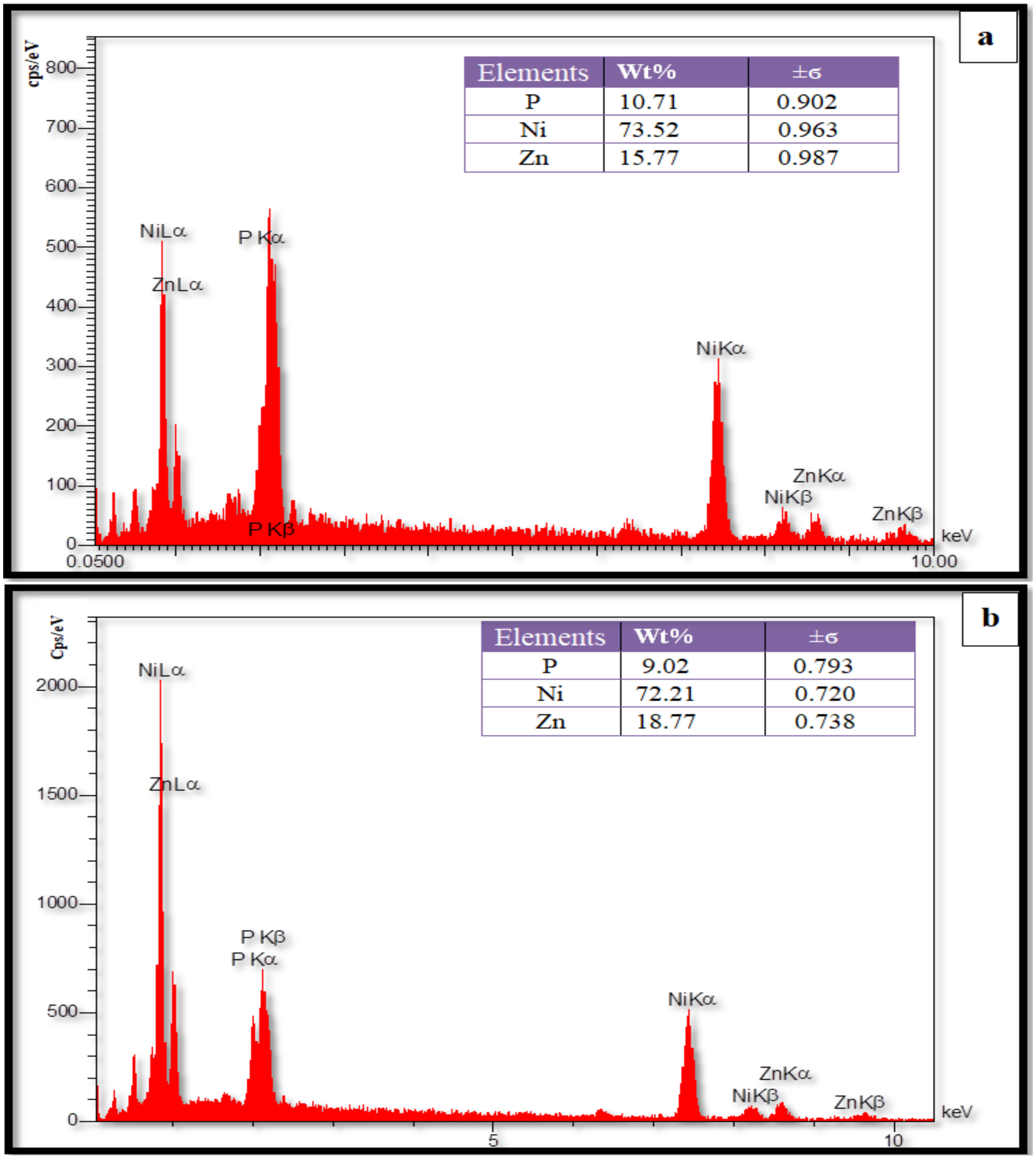

Elements	Wt%	±σ
P	10.71	0.902
Ni	73.52	0.963
Zn	15.77	0.987

Elements	Wt%	±σ
P	9.02	0.793
Ni	72.21	0.720
Zn	18.77	0.738

Figure (4.22): EDS Chart of Coated Specimen by Ni-Zn-P at Coating Time:(a):1-hr.:(b):2-hrs.

Phosphorus and nickel have their clear and well-known effect in electroless plating processes, but what concerns us in this section and this Figure(4.23) is knowing the proportions and presence of the elements silicon and carbon.

The Ni-SiC-P EDS chart for a 1-hour coating is shown in Figure (4.23.a). This diagram displays some significant elements that can be found on coating surface. There are approximately four important and influential elements in the surface properties. These elements are Ni, Si, P and C where they are found in varying proportions according to the type of coating solution used, as well as depending on the period time coating, in addition to other factors such as temperature and pH.

In Figure (4.23.a), the presence of phosphorus in 7.57%, nickel in 80.63%, carbon in 11.24 % and silicon in 0.57% have more affection on intermetallic compound.The presence of nano particles of silicon in low or medium percentage gives good surface properties.

Figure (4.23.b) shows the effect of time on the proportions of the presence of elements, the presence of elements such as silicon and carbon in proportions of 1.85 % and 10.89 % respectively give an important and clear character to the surface properties, especially hardness and resistance to erosion, but the rise of these ratios to high values affects negatively.

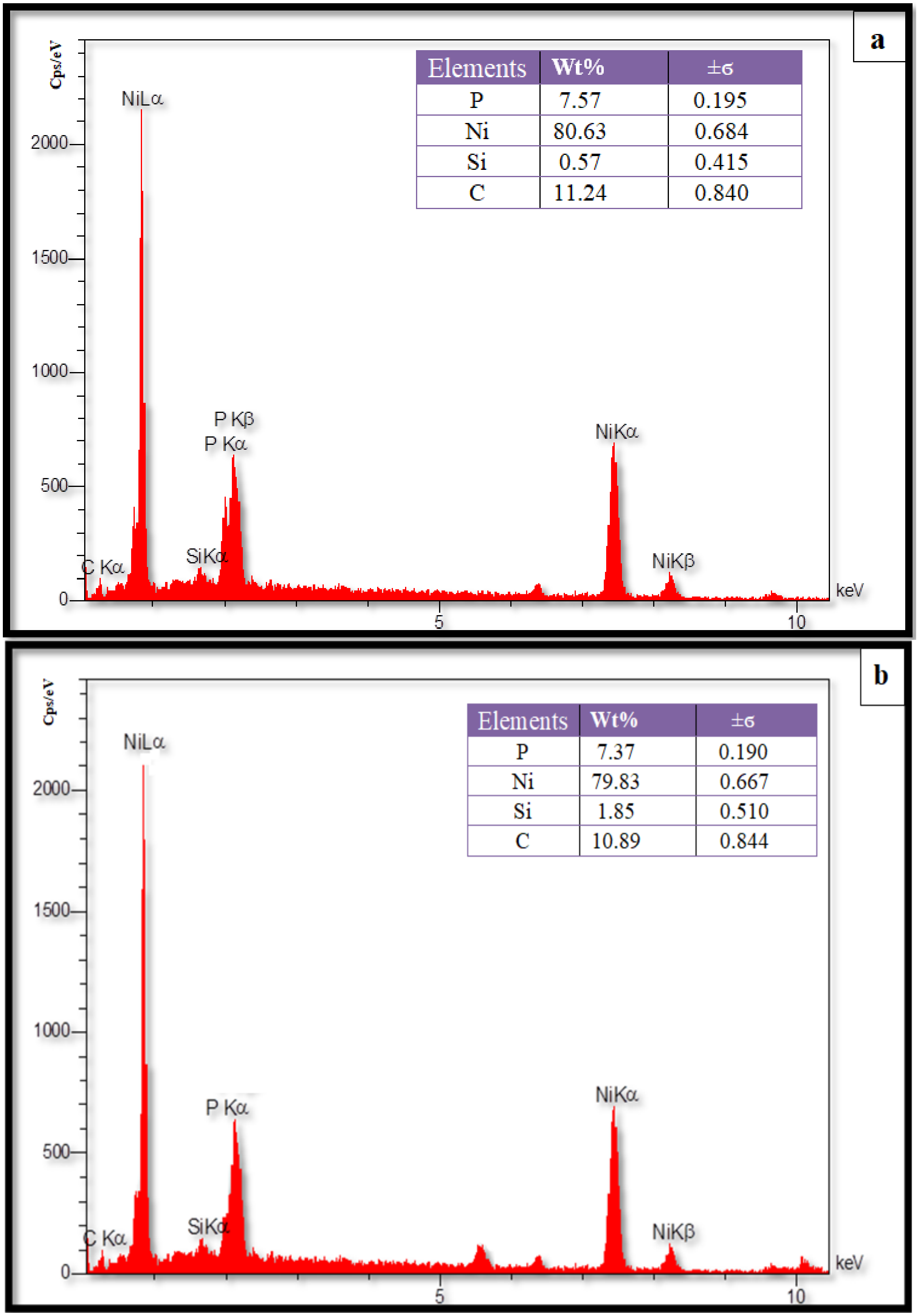

a

Elements	Wt%	±σ
P	7.57	0.195
Ni	80.63	0.684
Si	0.57	0.415
C	11.24	0.840

b

Elements	Wt%	±σ
P	7.37	0.190
Ni	79.83	0.667
Si	1.85	0.510
C	10.89	0.844

Figure (4.23): EDS Chart of Coated Specimen by Ni-SiC-P at Coating Time:(a):1-hr.:(b):2-hrs.

4.3.6. Tribological Properties for Matrix(Ni-P) Plating

There are important considerations made by the electroless plating for various applications such as super-corrosion resistance and wear resistance. Hardness is one of the important criteria that serve to increase wear resistance. Moreover, the roughness of the contact surfaces has a significant role in resisting wear and corrosion resistance,porosity of electroless plating of Ni-P and Ni-Zn-P ,Ni-Cu-P and Ni-SiC-P has been established to rely on the surface roughness and on the surface morphology.

4.3.6.1.Evaluation of Surface Morphology Characterization

All the coatings of (Ni–P) ,(Ni-Zn-P),(Ni-Cu-P) and (Ni-SiC-P) are obtained in this study exhibit a silvery, dark, grayish, smooth and luster surface by bare-eye glance. These appearances results are depend on several factors such as concentration of nickel ions, temperature, pH, copper, zinc ,and phosphorus contents.This explanation is agreed with **[91].**

SEM clarifications in Figures (4.24-4.27) show the surface morphology of all these four coating layers at as-plated and heat-treated statement . They involve nodular or spherical structure, distinctive for electroless nickel alloys. The observed coating layer in Figure (4.24.a) has finer grains and more number than Figure (4.24.b).The heat treatment in 400^{o}C for 1-hr. encourages to develops the size of grains and supports formation of intermetallic compound. The presence of intermetallic compound in electroless plating and electroplating is very important as they improve surface properties such as hardness, erosion and corrosion resistance. In Ni-P electoless plating the surface color specimens tends to silver and brightness but this depends on some of factors which mentioned early.

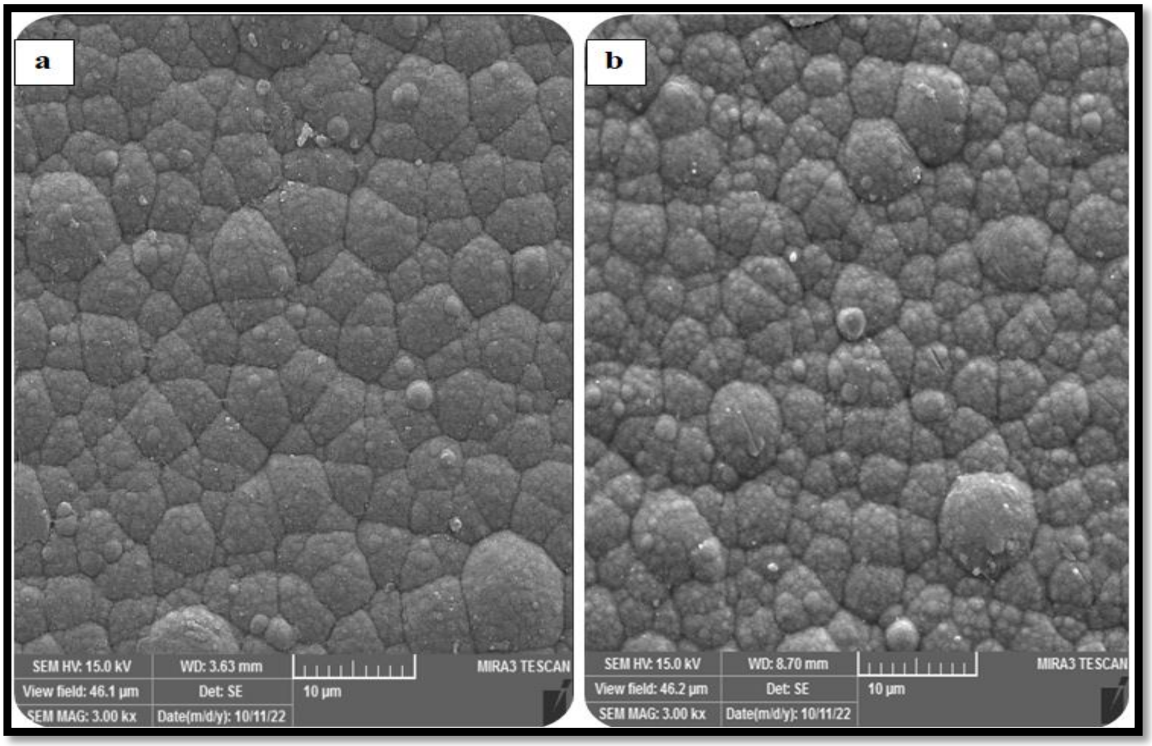

Figure (4.24): Surface Morphology SEM Images of Ni -P Plating (a):As-Plated(b):Heat Treated(400^{o}C 1-hr.)

Figure (4.25.a) shows the surface morphology of electroless plating by(Ni-Cu-P) as-plated. On the other hand Figure (4.25.b)shows the surface morphology after heat treated. The grains in heat treated state appear in a relatively larger size than as plated state, and the intermetallic compounds are re-formed and distributed, and they have more clearness. Small agglomerations indicate to Ni_3P phase, and large agglomerations indicate to Ni_5P_2 phase.From these figures the compactness and the good adhesion were noticed in this coating. This explanation is agreed with **[92]**. No cracks ,cavities and pores also can be seen. Although the difficulty of coating all types of stainless steel and superalloys due to possess these alloy to high passive layers but they can plated by electodepsition or electrolessplating.

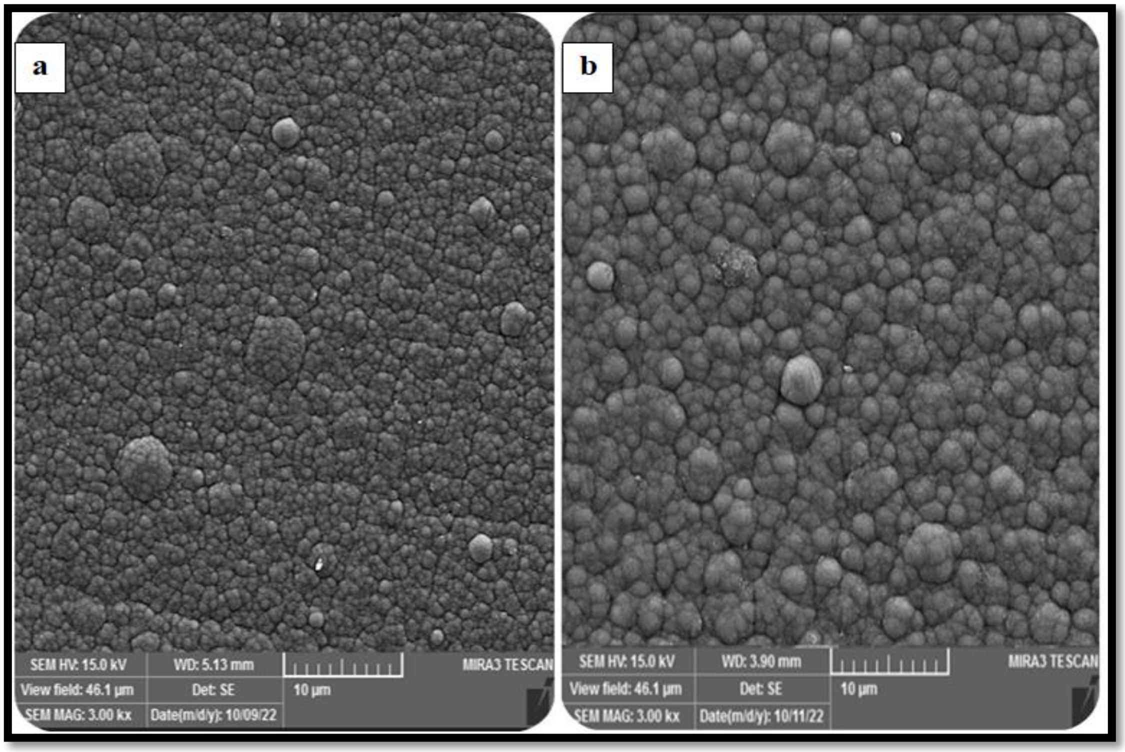

Figure (4.25: Surface Morphology SEM Images of Ni-Cu-P Plating (a):As-Plated(b):Heat Treated (400^{o}C 1-hr.)**.**

The surface morphology of (Ni-Zn-P) as-plated is depicted in Figure (4.26.a). In contrast, Figure (4.26.b) displays the surface morphology following heat treatment. The intermetallic compounds are reformed and dispersed, and the grains are clearer when they are in a heat-treated state as opposed to when they are as plated. Ni_5P_2 ,$Ni_{12}P_5$phase are indicated by small agglomerations, while NiZn phase is indicated by huge agglomerations.The formation of intermetallic compounds in the formula Ni_xP_y or Ni_xY after heat treated the coating specimens give the plated surface good mechanical,magntic and surface properties. The phases Ni_5P_2,$Ni_{12}P_5$ and NiZn are formed after the heat treatment at 400^{o}C for 1-hour.High increasing in hardness and electrochemical properties such as drop in corrosion current density and corrosion current after formed these phases . This explanation is agreed with **[113].**

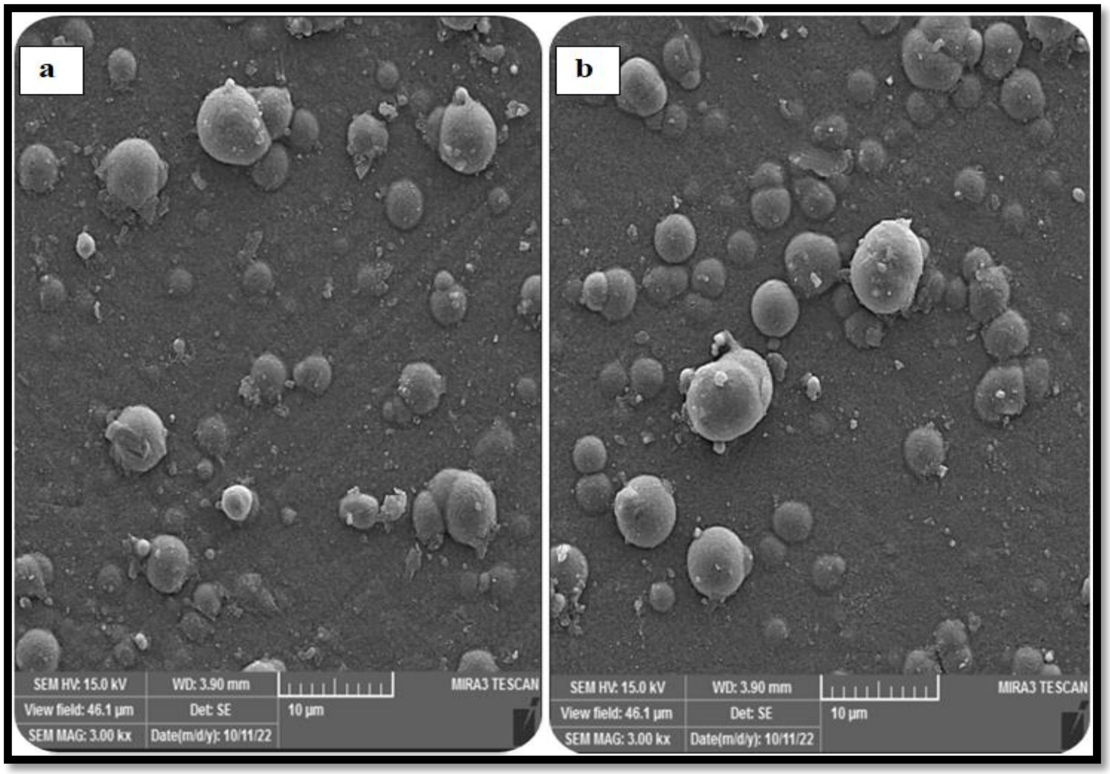

Figure (4.26): Surface Morphology SEM Images of Ni-Zn-P Plating (a):As-Plated(b):Heat Treated (400^{o}C 1-hr.)

Figure (4.27.a) shows the surface morphology after electroless plating with (Ni-SiC-P).On the other hand, Figure (4.27.b) depicts the surface morphology following heat treatment in(600^{o}C-1-hr.), where the intermetallic compounds are reformed and redistributed and appear to be clearer. Large agglomerations signify the NiSi,andNi_3Si phase, while small agglomerations signify the Ni_3Pphase.Most heat treated of electrolessplatings were carried out in 400^{o}C for one hour but the heat treated for electrplessplating with high solid particles such as nano SiC particles need to more temperature than that may be reached to 600^{o}C.Most previous studies refer to used 600^{o}C to obtain on the necessary intermetallic compounds which give good surface properties for electrolessplating with nano composite coating.All these exlanisions are agreed with**[132].**

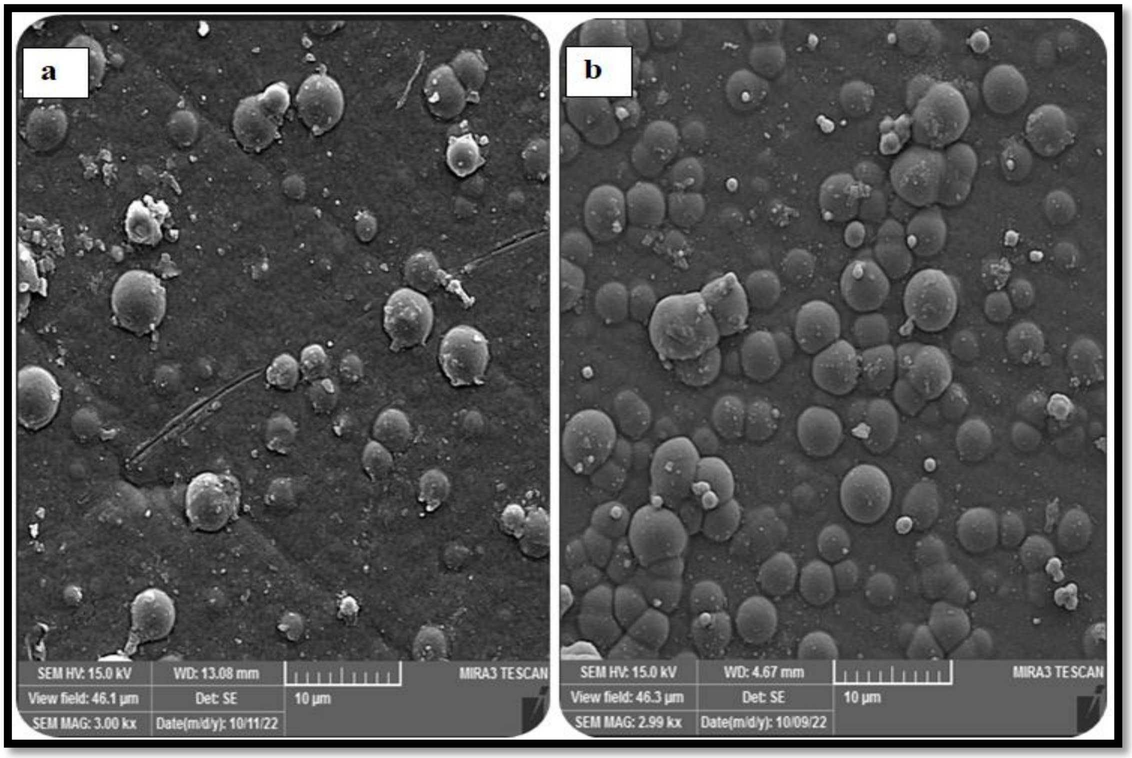

Figure (4.27): Surface Morphology SEM Images of Ni-SiC-P Plating (a):As-Plated(b):Heat Treated (600^{o}C 1-hr.)

4.3.6.2.Phases Analysis of Electroless Plating

X-ray-diffraction analysis has been used to identify all phases present in the specimens, as well as crystalline planes and their orientation for the phases are also analyzed. Figure (4.28.a) shows the X-ray-diffraction pattern for Ni-P plating bath as plated. Randomness and lack of crystallization are observed, but at certain angles and intensity, crystallization may be observed, and the phase is weak or critical. On the other hand the Figure (4.28.b) shows the X-ray diffraction pattern for Ni-P plating bath after heat treated. It is clear that the presence of Ni_3P in the coating layer which considers the major phase, so it more scattering of X-ray through this phase in the planes of (013) and(112).

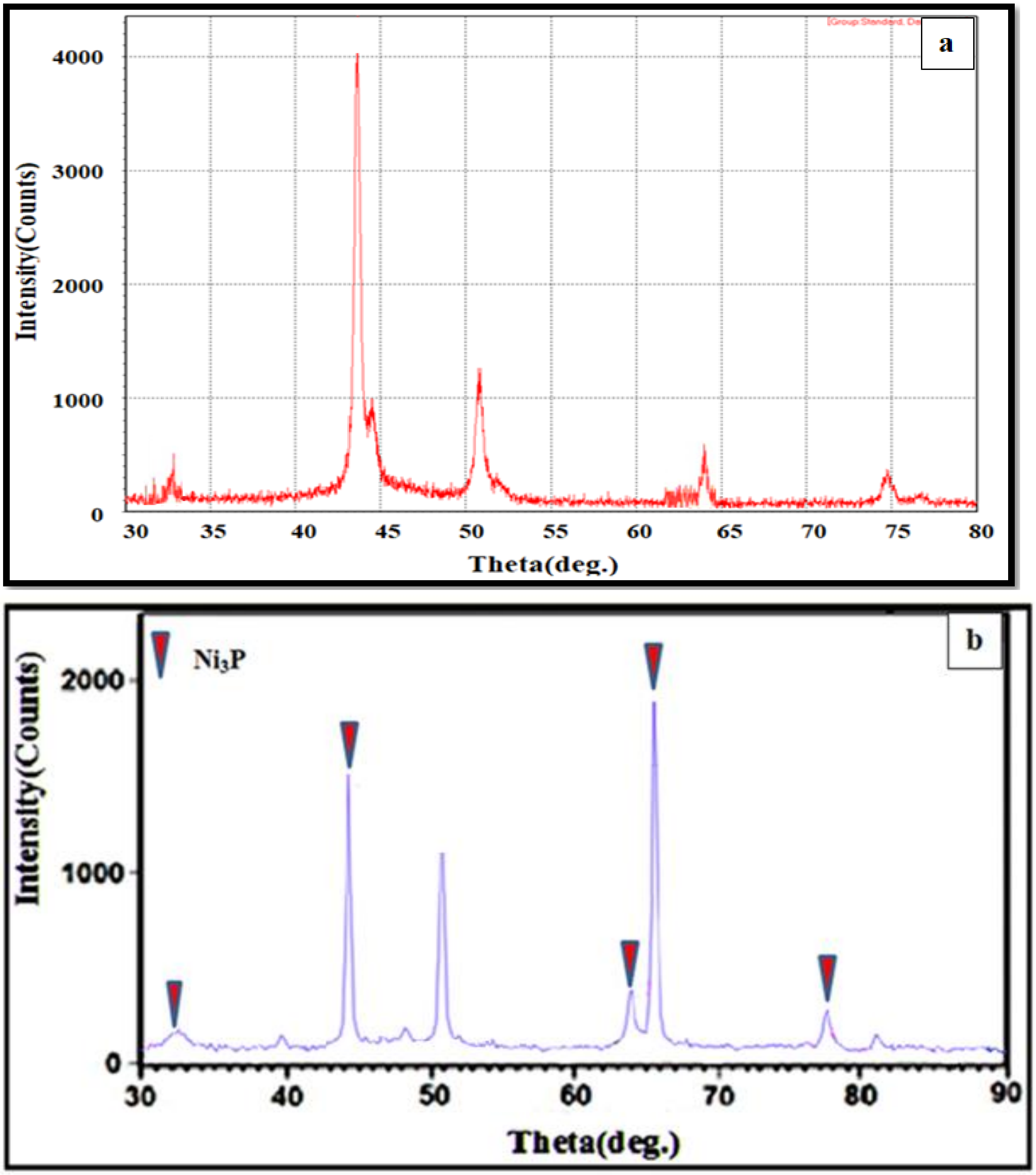

Figure (4.28): XRD Pattern of (Ni-P) :(a):As Plated(b):Heat-Treated.

The X-ray diffraction pattern for the Ni-Cu-P plating bath as it was plated is shown in Figure (4.29.a). Randomness and a lack of crystallization are evident, however under specific conditions and with a certain amount of intensity, crystallization may be seen, and the phase may be weak or crucial. On the other hand, the X-ray diffraction pattern for Ni-Cu-P plating bath following heat treatment is shown in Figure (4.29.b). The major phases are Ni_3P and Ni_5P_2 due to more scattering of X-ray through these phases in the plane (231) with 100 percent and in plane(608) with 35 percent respectively.

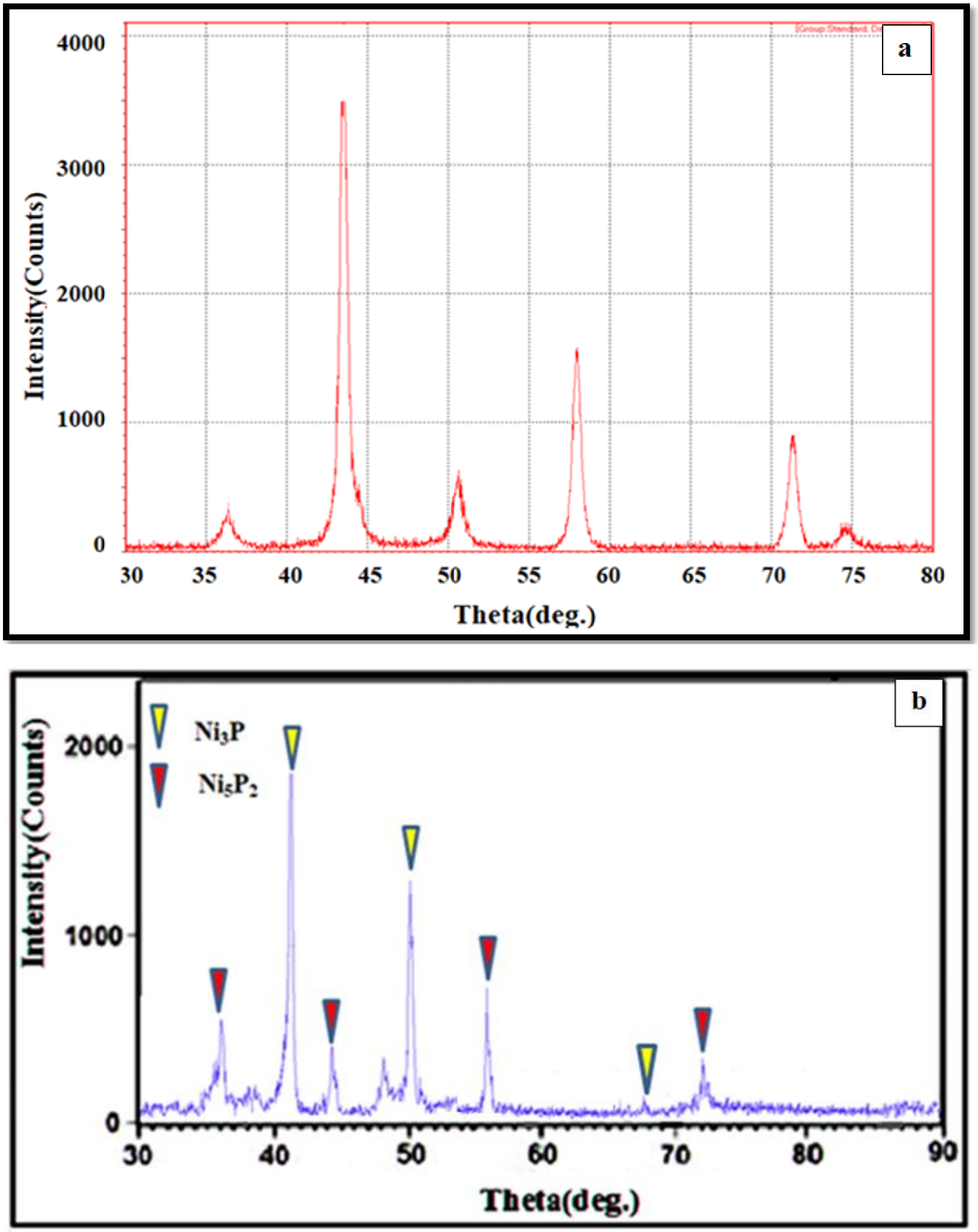

Figure (4.29): XRD Pattern of (Ni-Cu-P) :(a):As Plated(b):Heat-Treated

Figure (4.30.a) depicts the Ni-Zn-P plating bath's X-ray diffraction pattern as it was being plated. Randomness and the absence of crystallization are obvious, however under some circumstances and with a certain level of intensity, crystallization may be observed, and the phase may be weak. On the other hand, Figure (4.30.b) depicts the X-ray diffraction pattern for the Ni-Zn-P plating bath after heat treatment. The predominant phases are $Ni_{12}P_5$,NiZn and Ni_5P_2 due to increased X-ray scattering. These phases appear in the planes (400) with 100%, (101) with 45%and(428) with 55% respectively.

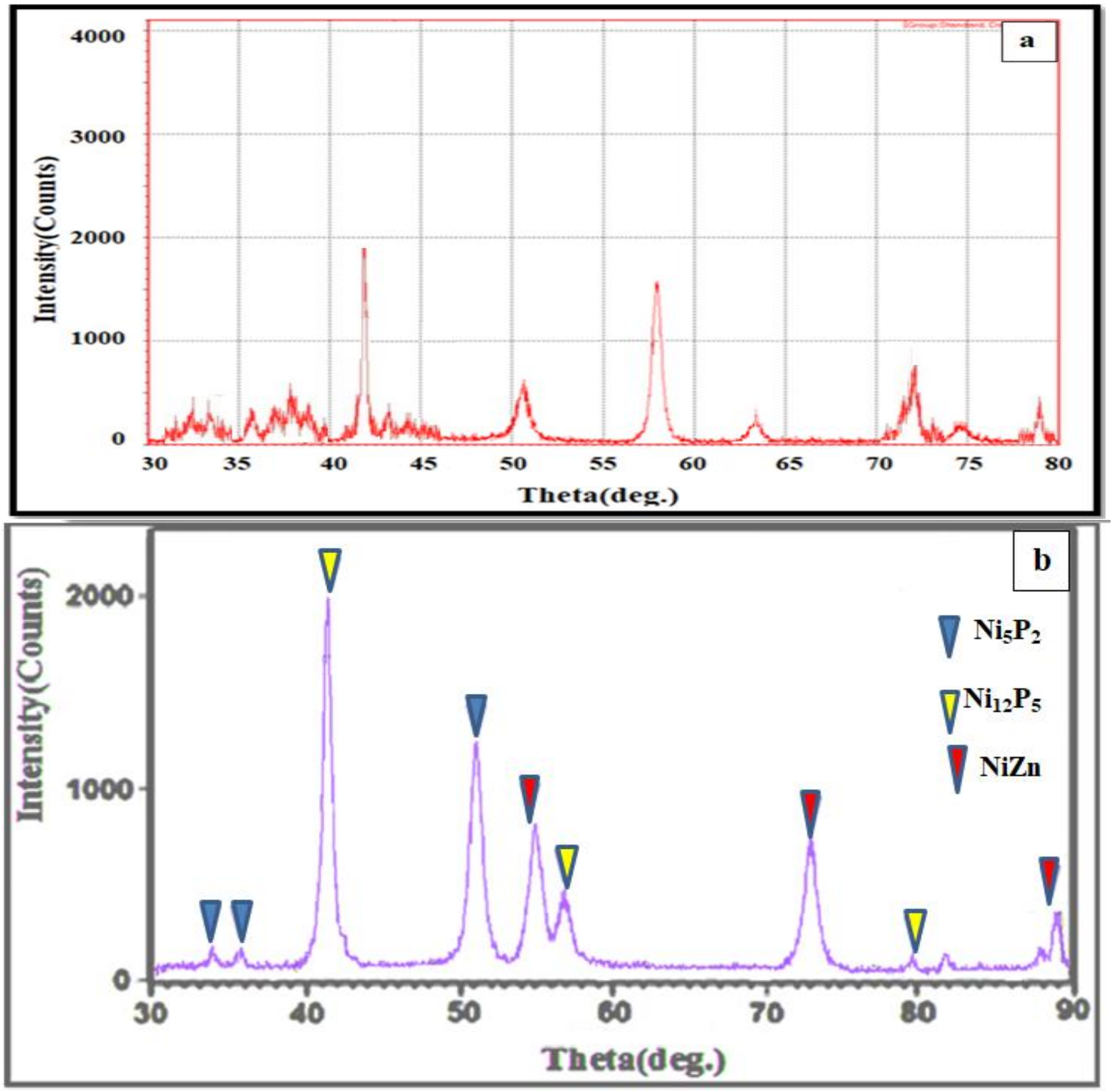

Figure (4.30): XRD Pattern of (Ni-Zn-P) :(a):As Plated(b):Heat-Treated.

Figure (4.31.a) depicts the X-ray diffraction pattern for the Ni-SiC-P plating bath as it was being plated. Randomness and the absence of crystallization are obvious, but under certain conditions and with a certain level of intensity, crystallization may be observed, and the phase may be weak. Figure (4.31.b) depicts the X-ray diffraction pattern for the Ni-SiC-P plating bath after heat treatment. Because of the increased X-ray scattering, the dominating phases are Ni_3P, Ni_3Si, and NiSi. These phases can be seen in the planes (222) with 100%, (220) with 45%, and (112) with 80%.The charts of all phases (Ni_3P,Ni_5P_2,$Ni_{12}P_5$, NiZn ,NiSi and Ni_3Si) are placed in appendix D.

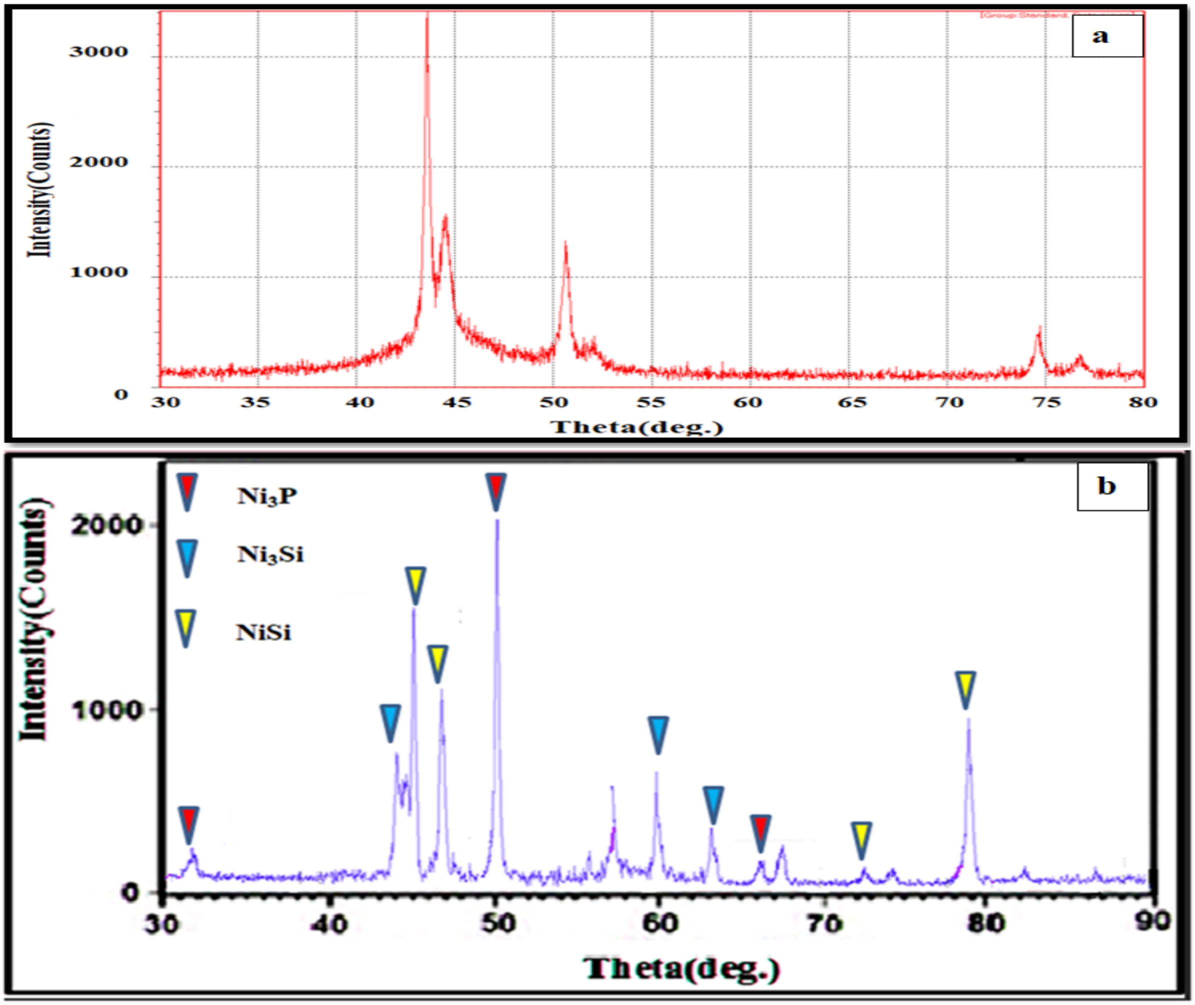

Figure (4.31): XRD Pattern of (Ni-SiC-P) :(a):As Plated(b):Heat-Treated.

4.3.6.3. Analysis of Topographic Surface by Atomic Force Microscope (AFM)

The atomic force microscopy (AFM) technique is effective for analyzing thin film surface topography. Figures (4.32) displays three dimensional AFM images of all four coating layers at 1-hrs. time of coating deposited on a stainless steel 316L that show the variation of surface roughness with type of coating.This test is carried out after heat treatment in(400^{o}C-1hr.)for (Ni-P),(Ni-Zn-P)and (Ni-Cu-P)but in(600^{o}C-1hr.) for(Ni-SiC-P).The nanoparticles SiC thin films have a high degree of homogeneity, as indicated in the image, and the small grains are spread uniformly on the substrate.

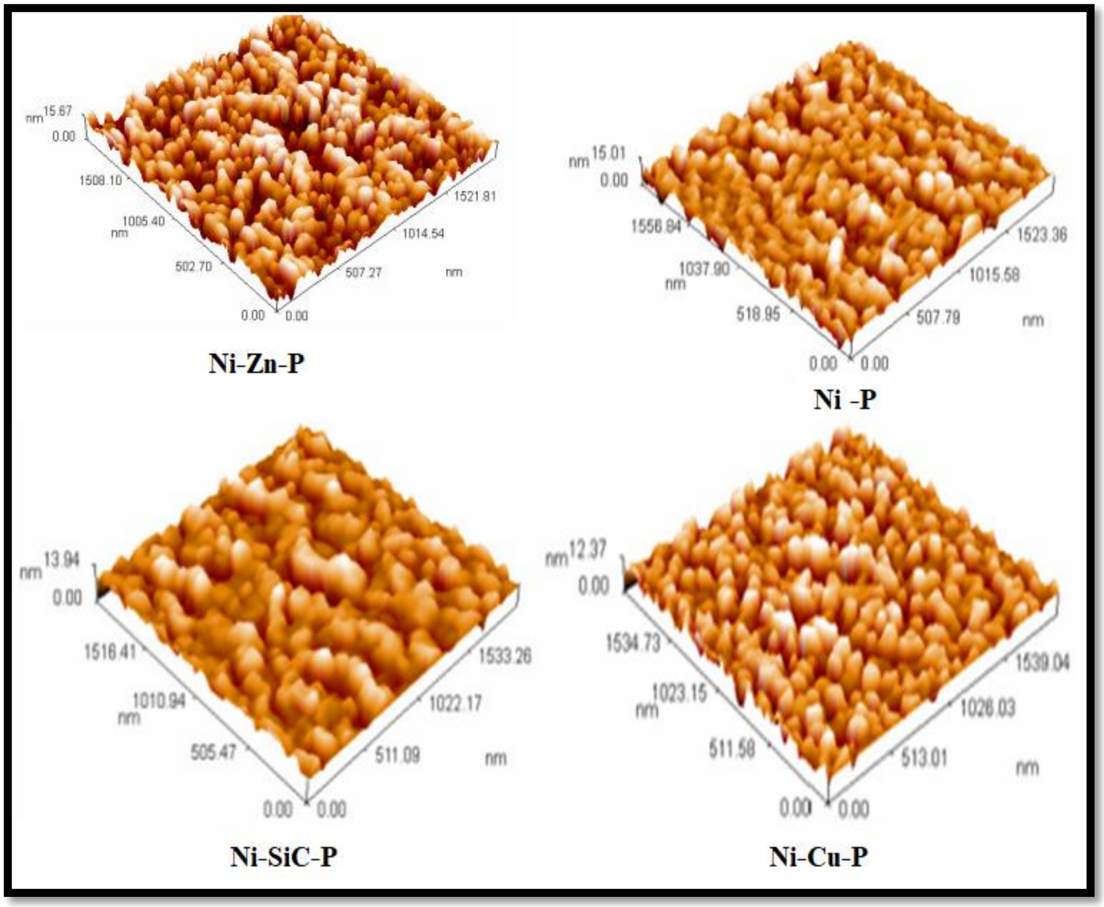

Ni-Zn-P **Ni -P**

Ni-SiC-P **Ni-Cu-P**

Figure(4.32):3-D AFM Images For Four Heat Treated Electroless Plating at (1-hr. Coating Time).

From Figure(4.32) electroless plating by (Ni-Zn-P)displays the highest surface roughness than all other three platings. On the other hand the electroless plating by (Ni-SiC-P) nano composite coating displays the lowest surface roughness than all other three plating. All electroplating or electroless plating processes, or in general, most metal surface coating processes, give surfaces a higher roughness compared to bare metal.The corresponding root mean square (RMS) values to four elctroless plating (Ni-Zn-P, Ni-P, Ni-Cu-P and Ni-SiC-P) are (4.17 ,2.53, 2.34 and 2.03nm) respectively. The AFM test revealed that the root mean square (RMS) and surface roughness (RS) average and maximum height of thin coating increase with increasing thickness, as shown in Table (4.6). The surface roughness appeared uneven from one coating to another depending on several variables such as the temperature of the solution, the concentration of the solution, pH, the degree of agitations and the presence or absence of other particles. A very important factor that has a great influence on the surface roughness is the heat treatment of the coating surfaces.Not insignificant, the effect of heat treatment appears on the coating surfaces. Most of the coated surface properties are witnessing a clear increase, and this includes the surface roughness.

Table (4.6):AFM Data For Coating Layers(Heat-Treated) at 1-hr.Time of Plated.

Type of Electroless Plating	Coating Thickness (µm)	Roughness Average Sa(nm)	Root Mean Square Sq(nm)
Ni-Zn-P	13.17	3.58	4.17
Ni-P	10.33	1.98	2.53
Ni-Cu-P	6.44	1.89	2.34
Ni-SiC-P	7.58	1.57	2.03

Figure (4.33) displays three dimensional AFM images of all four coating layers at 2-hrs. time of coating deposited on substrate. It clearly refers to the films are homogeneous and densely packed. It demonstrates that the morphology of these films is homogeneously dispersed, indicating that the films are crystalline.

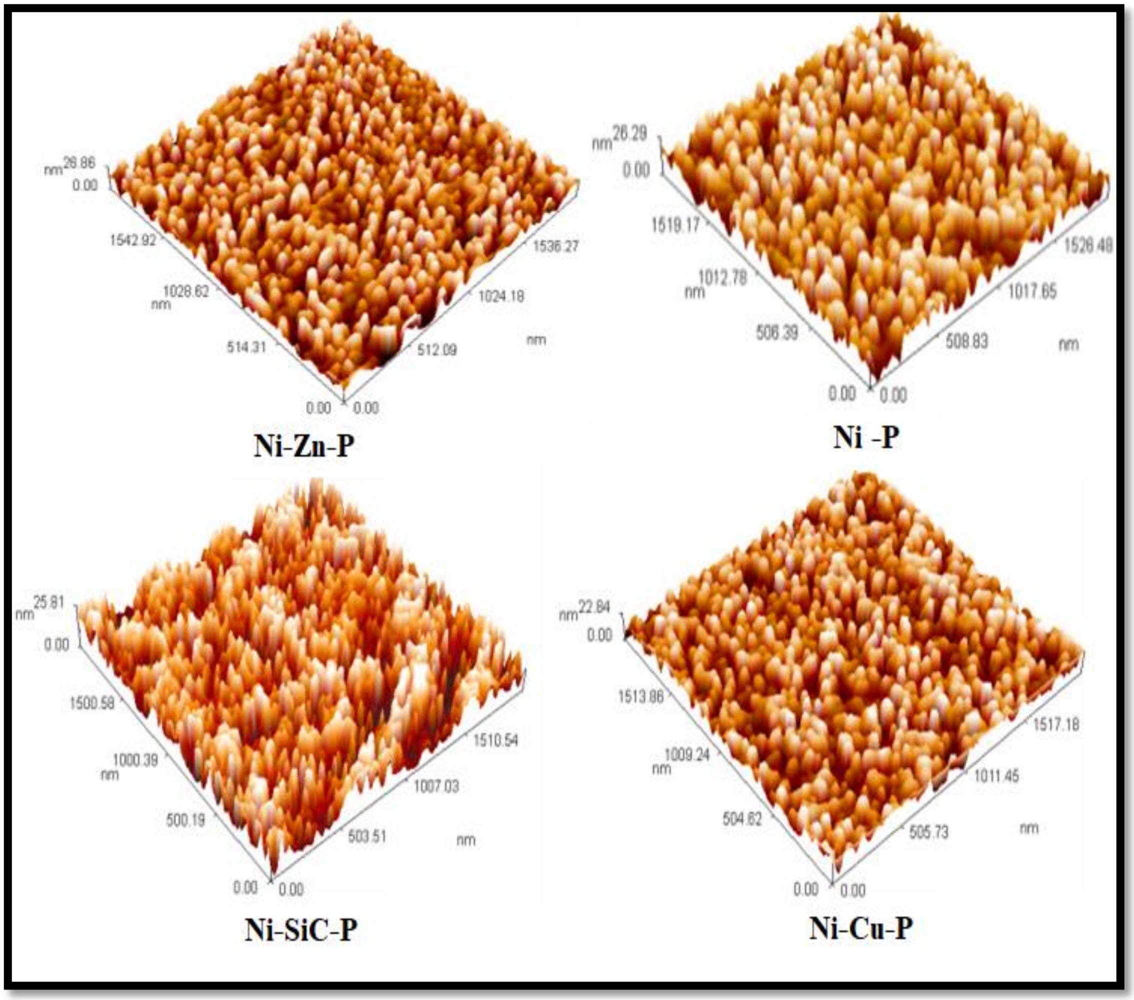

Ni-Zn-P **Ni -P**

Ni-SiC-P **Ni-Cu-P**

Figure(4.33):3-D AFM Images For Four Heat Treated Electroless Plating at (2-hrs. Coating Time).

The corresponding root mean square (RMS) values for four electroless platings (Ni-Zn-P, Ni-P, Ni-Cu-P, and Ni-SiC-P) are (6.71, 6.68, 5.75, and 5.71nm) respectively.Average roughness and root mean square magnitudes are refered in Table(4.7).The effect of heat treatment and the increasing in thickness of coating give noticeable increasing in surface roughness.

Table (4.7):AFM Data For Coating Layers(Heat-Treated) at 2-hrs.Time of Plated .

Type of Electroless Plating	Coating Thickness (μm)	Roughness Average Sa(nm)	Root Mean Square Sq(nm)
Ni-Zn-P	67.14	5.64	6.71
Ni-P	61.88	5.61	6.68
Ni-Cu-P	47.06	4.83	5.75
Ni-SiC-P	29.13	4.69	5.71

4.4. Corrosion

The results of three important tests: electrochemical, erosion corrosion and stress corrosion cracking results are discussed in this section.

4.4.1. Electrochemical Evaluation

In the following results of electrochemical tests(open circuit potential , polarization and cyclic polarization) have been presented as follows:

4.4.1.1. Open Circuit Potential

Before polarization process, the potential of open circuit for working electrode is measured as function of time up to the equilibrium and the quasi-stability gotten. This test carries out in one solution(3.5%NaCl) at 30^{o}C. The main aim for this process is identified the domain which potential corrosion is occurred. Figures (4.34-4.38) show the potential curves plot as opposed to immersion time, that display clearly the potential dropped to a reasonable for steady value. From all the figures below that can be noticed the voltage decreases this means, that equilibrium of positive charge carries (metal ions) have the same charge of electron, so that the tendency of corrosion is decreased.This explanation is agreed with**[71].**

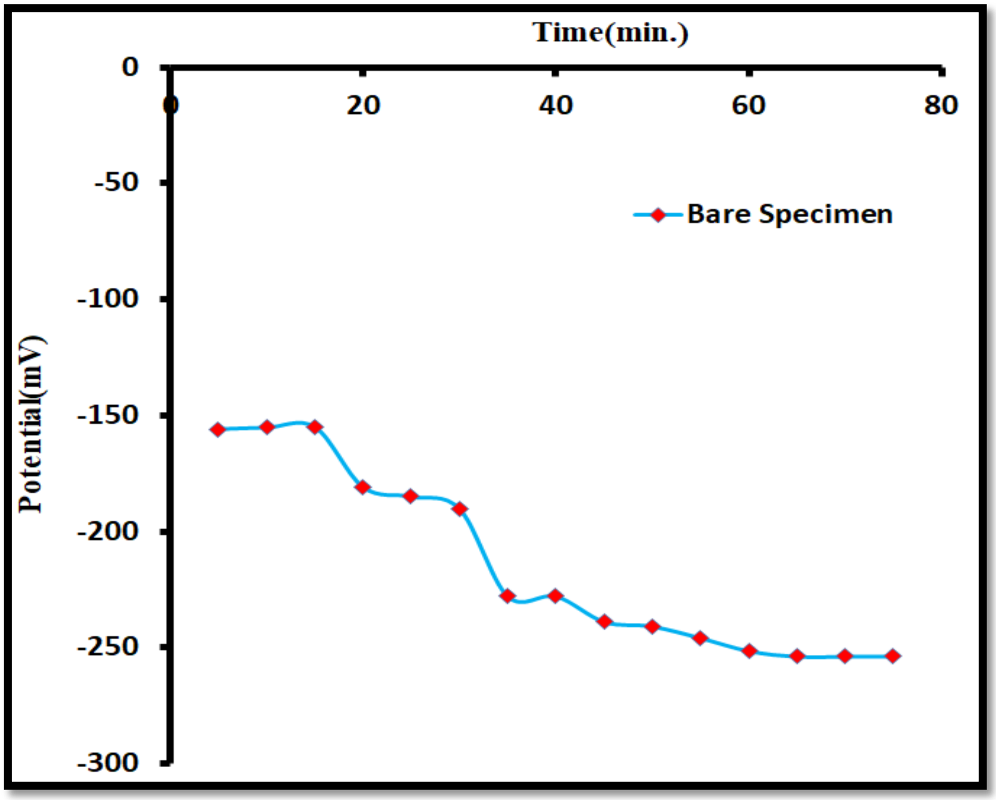

Figure (4.34): Open Circuit Potential for Bare Specimen in 3.5%NaCl Solution.

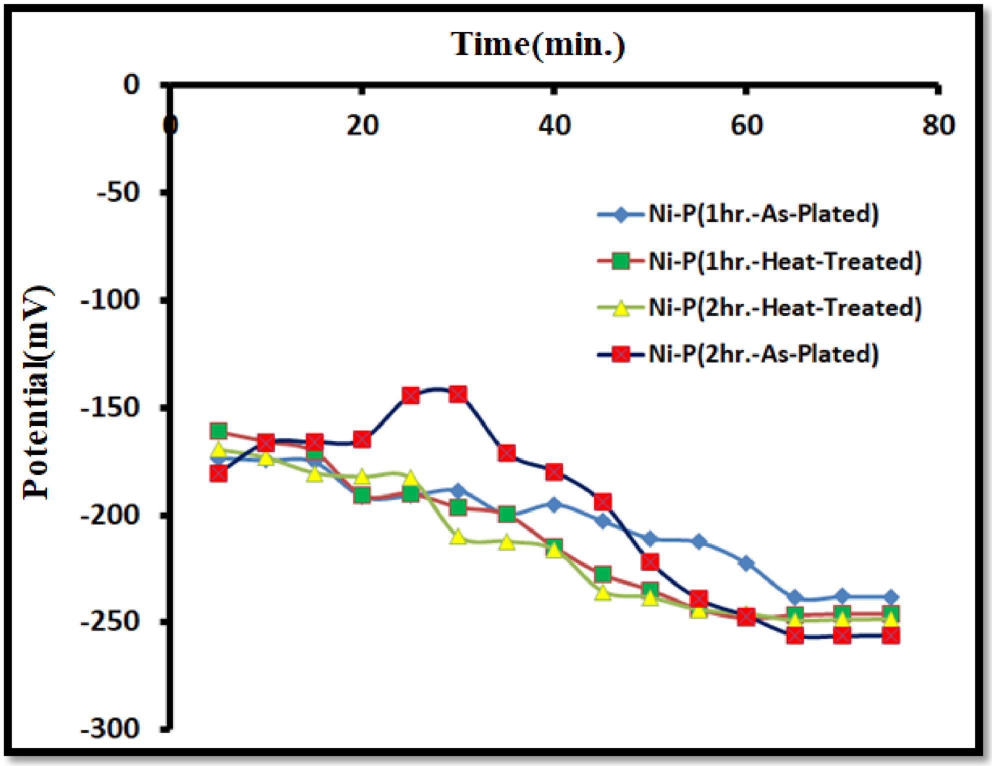

Figure (4.35): Open Circuit Potential Curves in 3.5%NaCl For Coated Specimen by Ni-P.

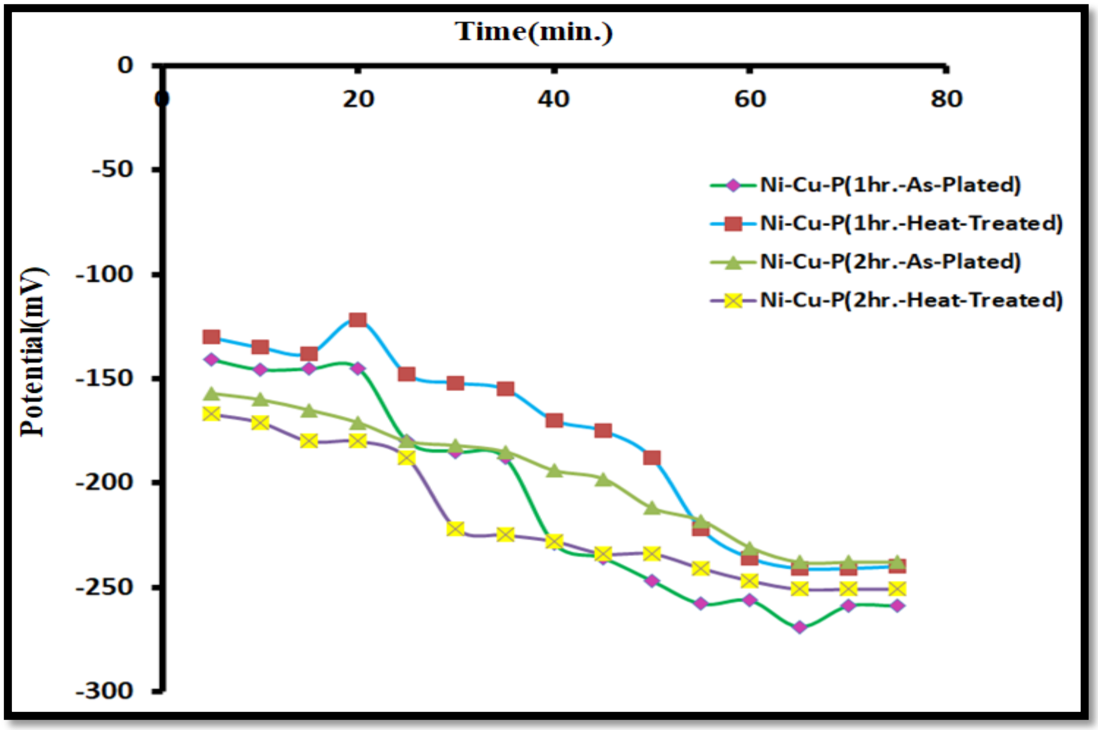

Figure (4.36): Open Circuit Potential Curves in 3.5%NaCl For Coated Specimen by Ni-Cu-P.

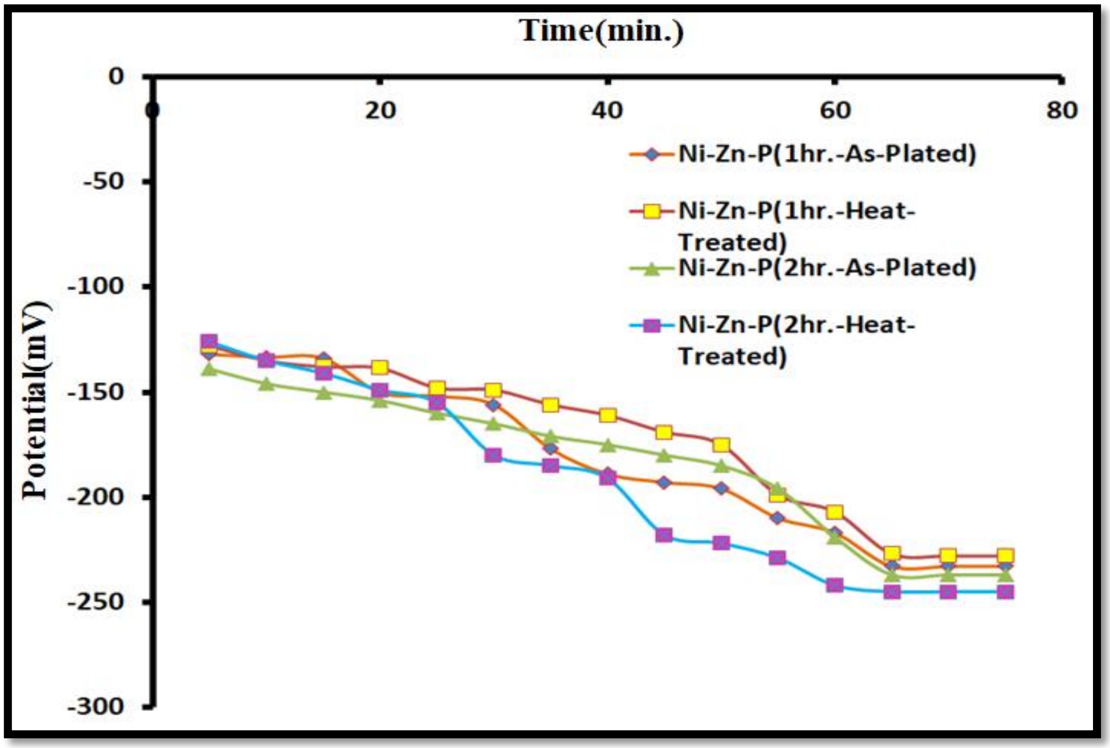

Figure (4.37): Open Circuit Potential Curves in 3.5%NaCl For Coated Specimen by Ni-Zn-P.

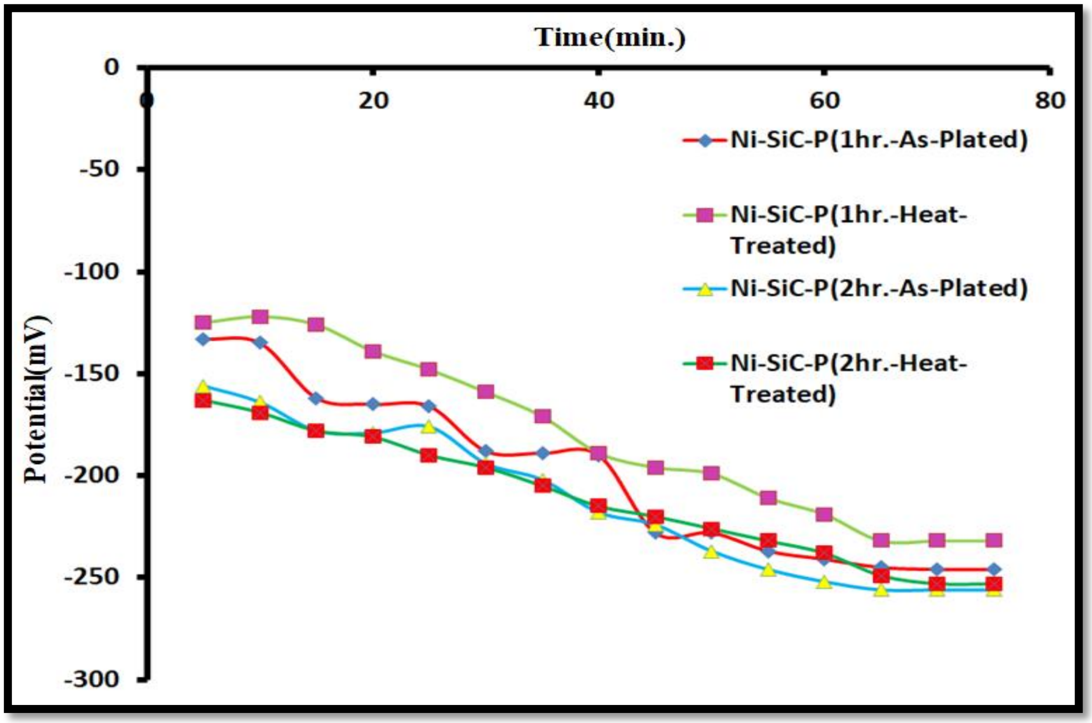

Figure (4.38): Open Circuit Potential Curves in 3.5%NaCl For Coated Specimen by Ni-SiC-P.

4.4.1.2. Polarization Evaluation

The behavior of corrosion to bare and coated SS316Lspecimens by Ni-P ,Ni-Cu-P, Ni-Zn-P and Ni-SiC-P at two different times has been identified by using curves of polarization technique. The tests of polarization are achieved in one active solution; 3.5%NaCl.

The measurements of open-circuit give good information around the potential range; starting potential and ending potential. The potential range of polarization advice is equal to (±250)according to ASTM G3-14(Standard Practice for Conventions Applicable to Electrochemical Measurements in Corrosion Testing). Corrosion potential (E_{corr}) refers to the point where the total rates of reduction and oxidation are equal, the density of corrosion current corresponding to this point is called the density of corrosion current i_{corr}.

The potential –Log of current density, gotten from polarization of bare specimen with one active solution is shown in Figure (4.39). The parameters values of polarization for bare and coated specimens in active solution is exposed in Table (4.8). The highest density of corrosion current happens in bare specimen is reached to (4.37μA/cm^2). Also the results show that the corrosion current density for specimens coated by ternary plating is less than the corrosion current density for specimens coated by Ni-P alone. The previous studies give good answer for the addition effect of ,zinc, silicon carbide and cupper content to Ni-P coating, where these three addition increases the compactness, uniformity and crystalline .On the other hand from the results in Table (4.7) the corrosion current density for coated specimens with two hours' times of coating are lower than the corrosion current of specimens which coated with one hour time of coating because they have high thickness of coating layer. All polarization curve for coated specimen are found in Appendix E.

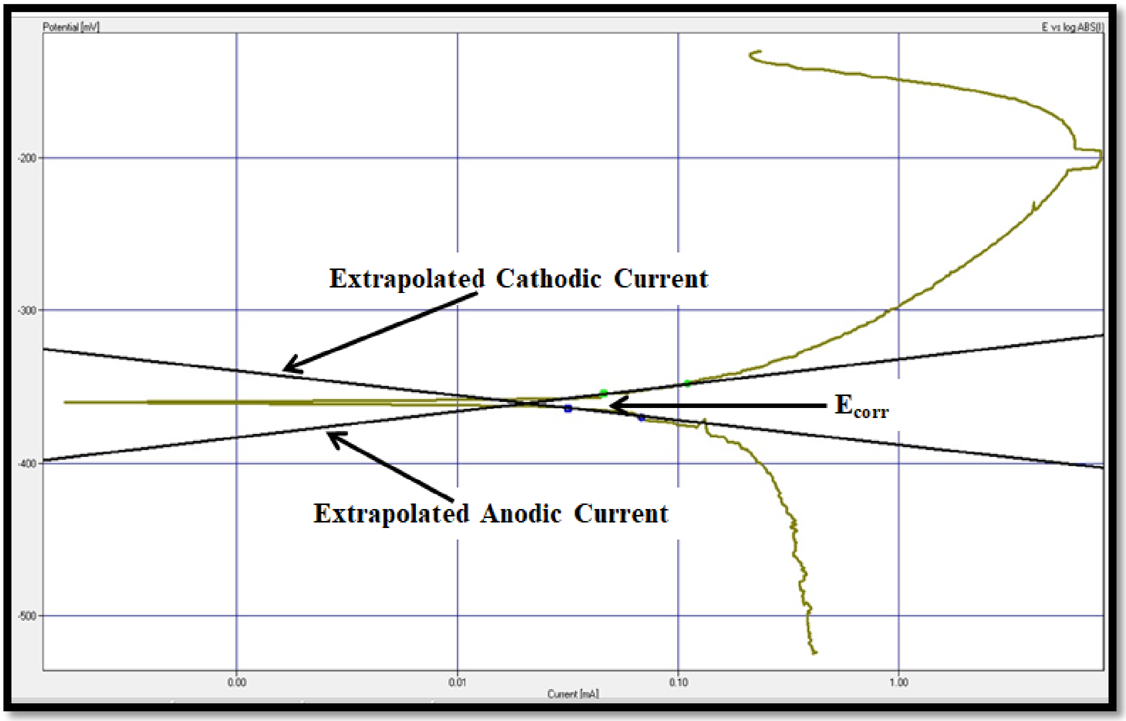

Figure (4.39): Polarization Curve for Bare Specimen in 3.5%NaCl.

Table (4.8): Parameters for Polarization of Bare and Heat Treated Coated Specimens.

Polarization Results in 3.5%NaCl Solution					
Specimens	**I_{corr} (µA)**	**E_{corr} (-mV)**	**i_{corr} (µA/cm^2)**	**Corrosion rate (mpy)**	**Inhibitive Efficiency (I.E.) %**
Bare Specimen	20.6	-360.7	4.37	1.81	-
Coated Specimen by Ni-P for 1-hrs.	6.32	-310.9	1.34	0.38	79
Coated Specimen by Ni-P for 2-hrs.	5.59	-245	1.18	0.34	81
Coated Specimen by Ni-Cu-P for 1-hrs.	4.4	-453.8	0.93	0.268	85
Coated Specimen by Ni-Cu-P for 2-hrs.	3.5	-456.5	0.7431	0.213	87.2
Coated Specimen by Ni-SiC-P for 1-hrs.	2.97	-426.1	0.63	0.18	90
Coated Specimen by Ni-SiC-P for 2-hrs.	2.88	-448.4	0.611	0.151	91.6
Coated Specimen by Ni-Zn-P for 1-hrs.	1.4	-277.7	0.3	0.073	96
Coated Specimen by Ni-Zn-P for 2-hrs.	1.22	-288.1	0.259	0.0642	96.5

4.4.1.3. Evaluation of Cyclic Polarization

In order to investigate the resistance of the samples to the localized corrosion, the cyclic polarization is carried out. Typically, the reading starts at the open circuit potential and scans upwards until breakdown is attained. Then the direction of scan is inverted after specific amount of localized corrosion is established and the passive scale is damaged. The potential at which stable pit formed is called breakdown potential (E_b) or pitting potential (E_p). Consequently, the E_p imply the potential over which the pits initiated and developed. If the E_p is high, the material has high resistance to the pitting corrosion. During the reverse scan, a negative hysteresis can be observed on the curves.The difference between E_p and E_{prot} (ΔE) will give an indication to the corrosion resistance of the samples, where the smaller ΔE value means the highest corrosion resistance, this clarification is agreed with **[133].** Figures (4.40 to 4.48) show the polarization curves for base metal and coated specimens by (Ni-P),(Ni-Cu-P),(Ni-Zn-P) and(Ni-SiC-P) in 3.5 NaCl solution at 38 °C. Significant differences were observed between the curves obtained for each specimen. For substrate specimen, has the largest ΔE=($E_{pit.}$-$E_{prot.}$) value compared to the susceptibility to other specimens after coating. The cyclic polarization curves obtained as noted in the Table (4.9), the extent of the hysteresis loop is highly reduced and therefore, the corrosion mechanism operating on the substrate surface is less active when coating. .

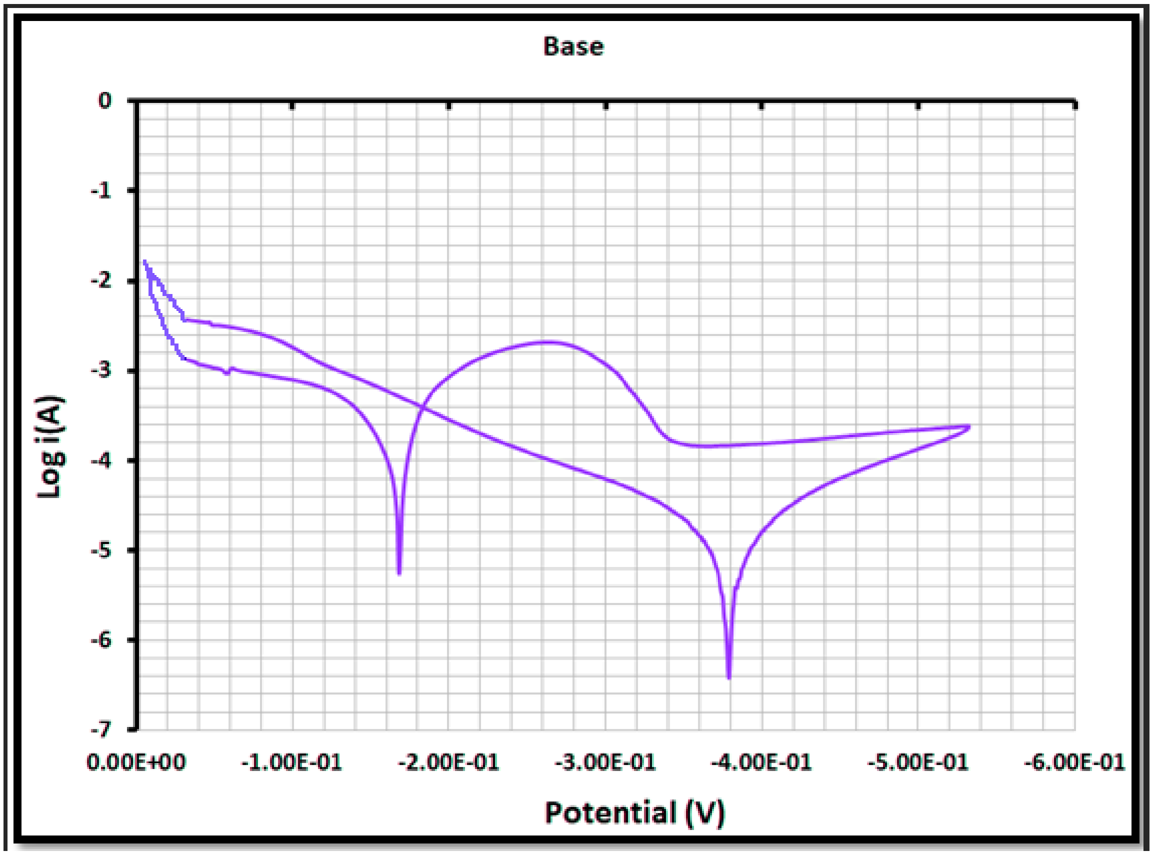

Figure (4.40): Cyclic Polarization Curve of Base Specimen in 3.5%NaCl.

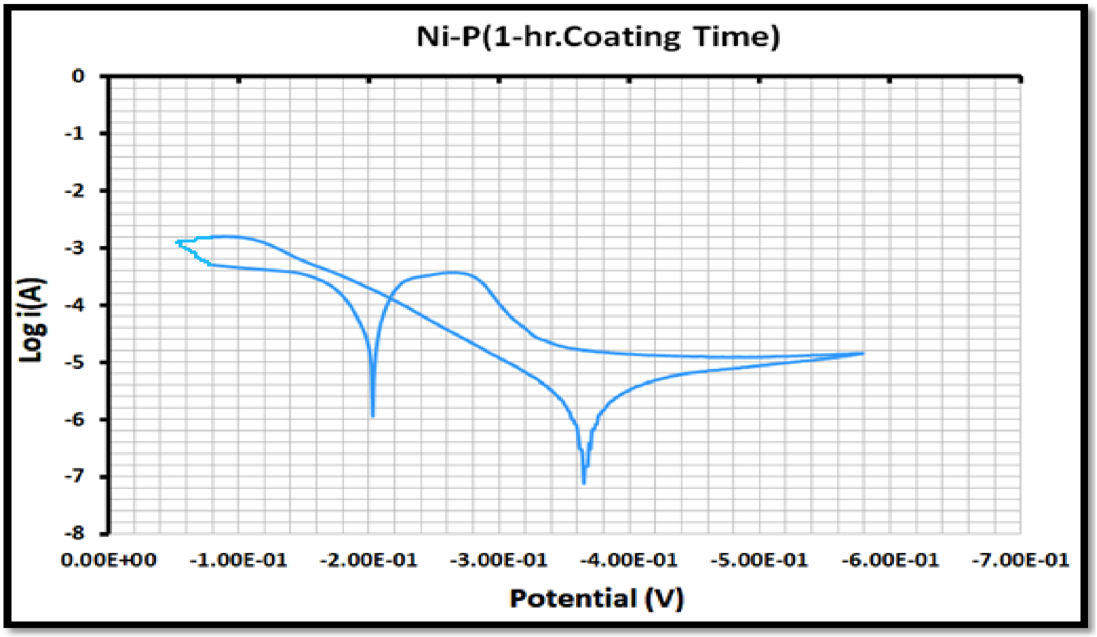

Figure (4.41): Cyclic Polarization Curve of Coated Specimen by Ni-P(1-hr.Coating Time) in 3.5%NaCl.

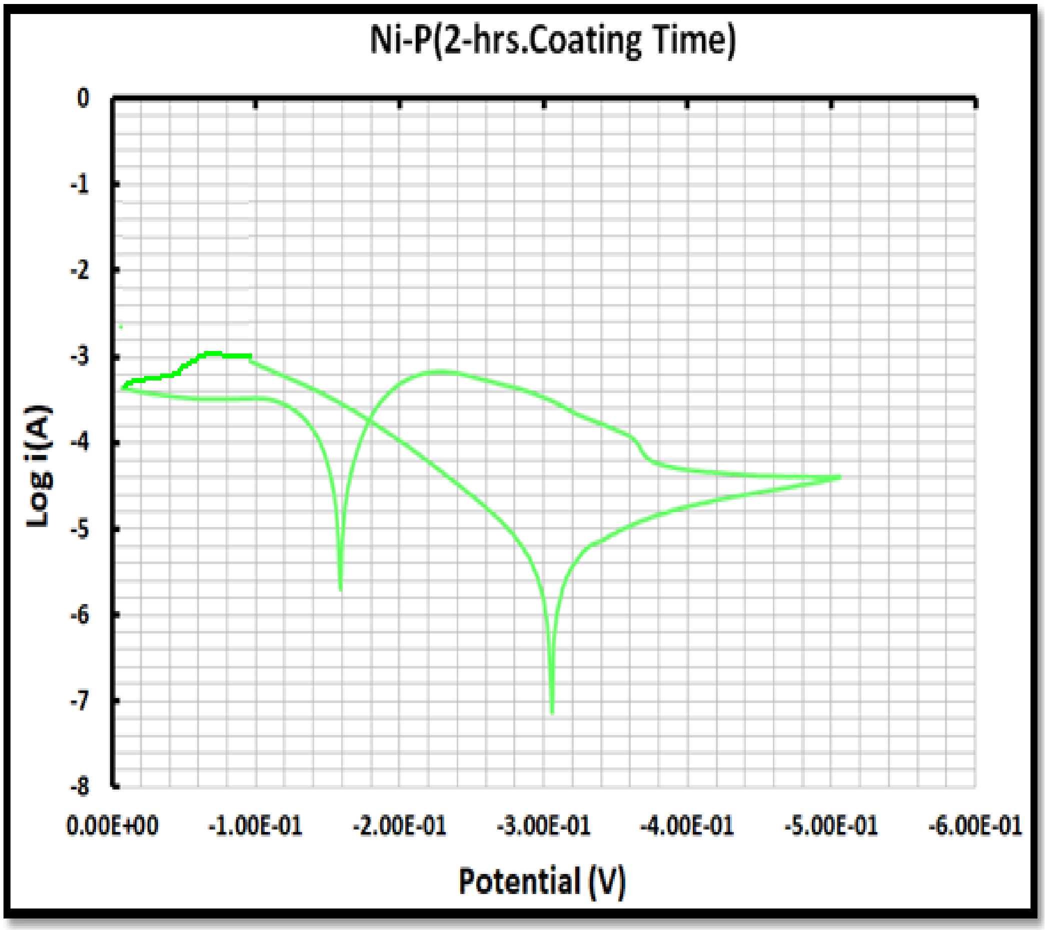

Figure (4.42): Cyclic Polarization Curve of Coated Specimen by Ni-P(2-hrs.Coating Time) in 3.5%NaCl.

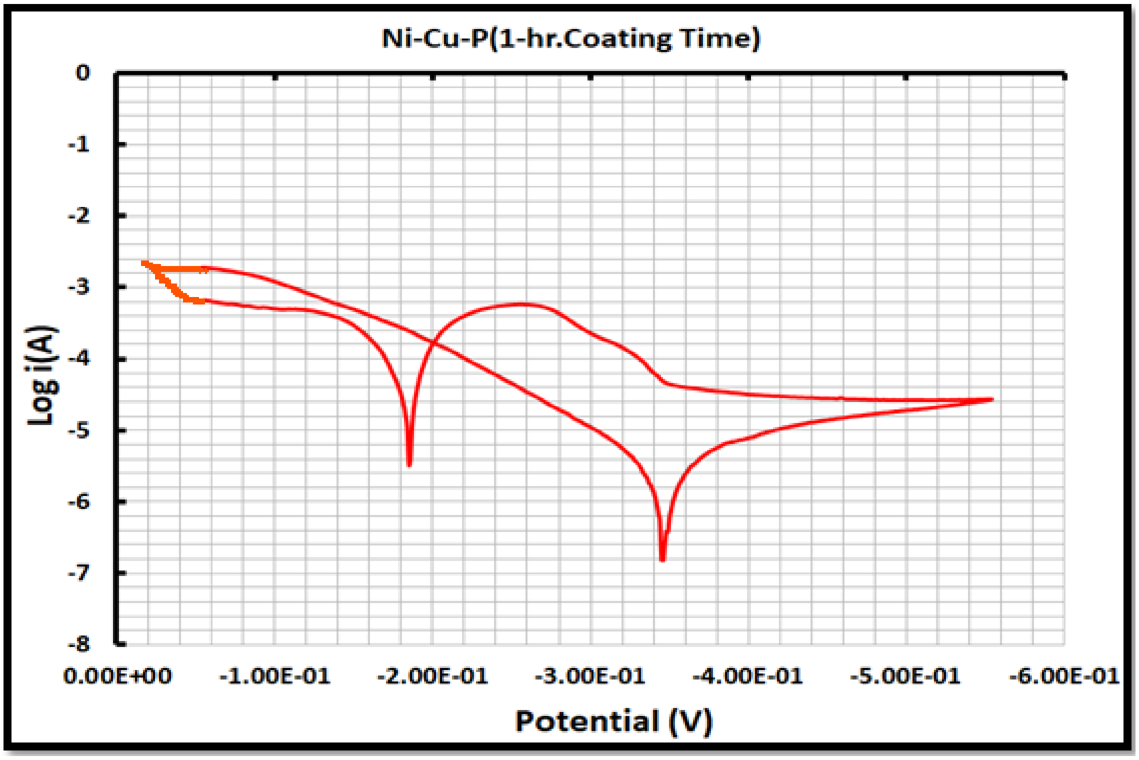

Figure (4.43): Cyclic Polarization Curve of Coated Specimen by Ni-Cu-P(1-hr.Coating Time) in 3.5%NaCl.

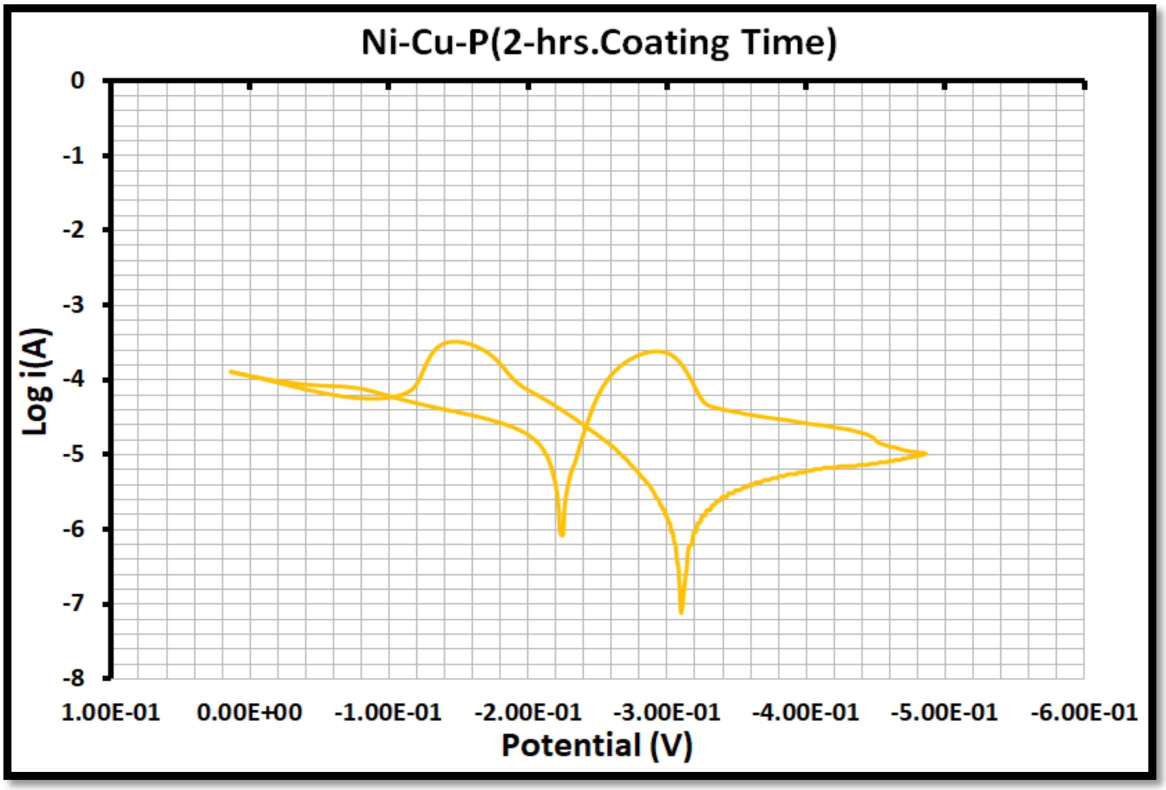

Figure (4.44): Cyclic Polarization Curve of Coated Specimen by Ni-Cu-P(2-hrs.Coating Time) in 3.5%NaCl.

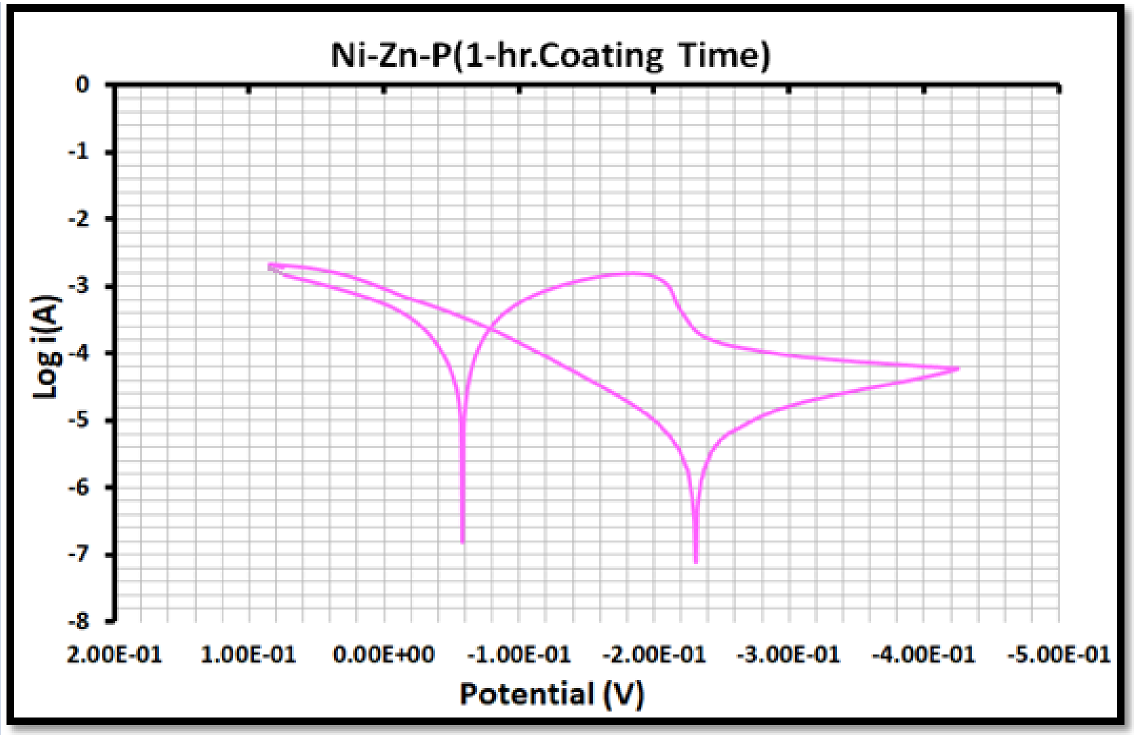

Figure (4.45): Cyclic Polarization Curve of Coated Specimen by Ni-Zn-P(1-hr.Coating Time) in 3.5%NaCl.

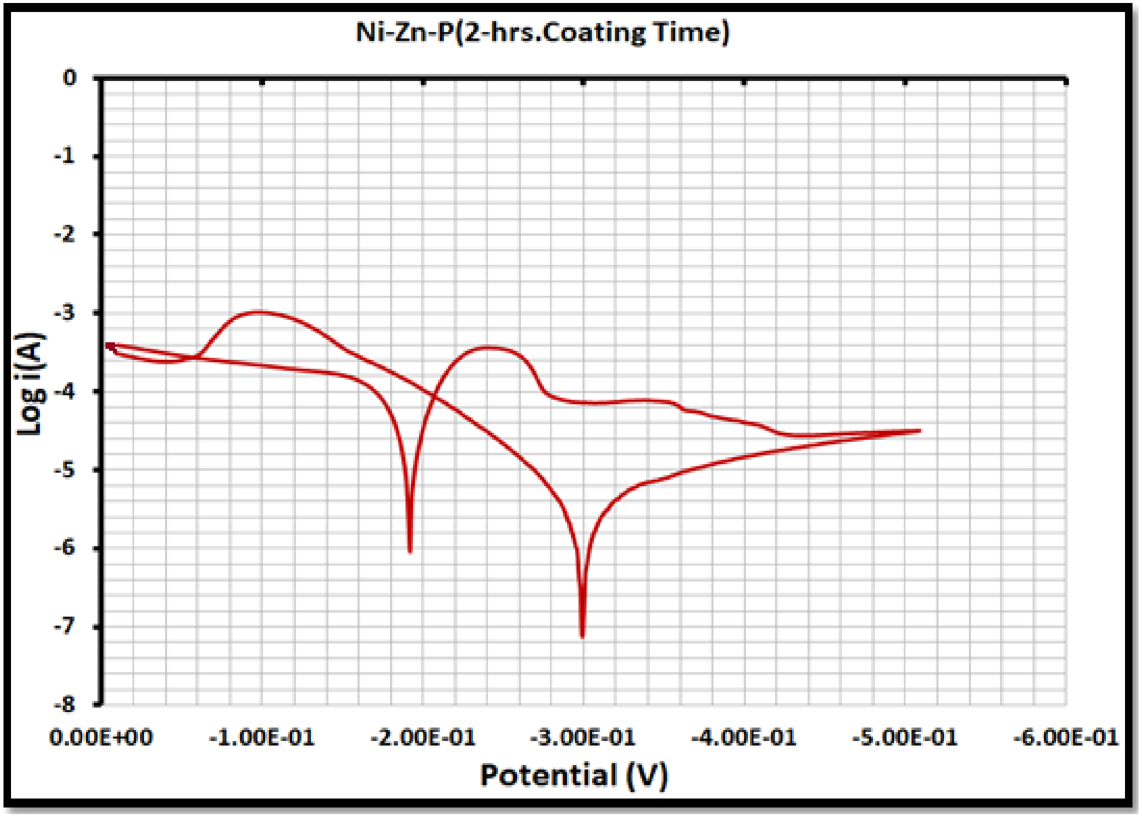

Figure (4.46): Cyclic Polarization Curve of Coated Specimen by Ni-Zn-P(2-hrs.Coating Time) in 3.5%NaCl.

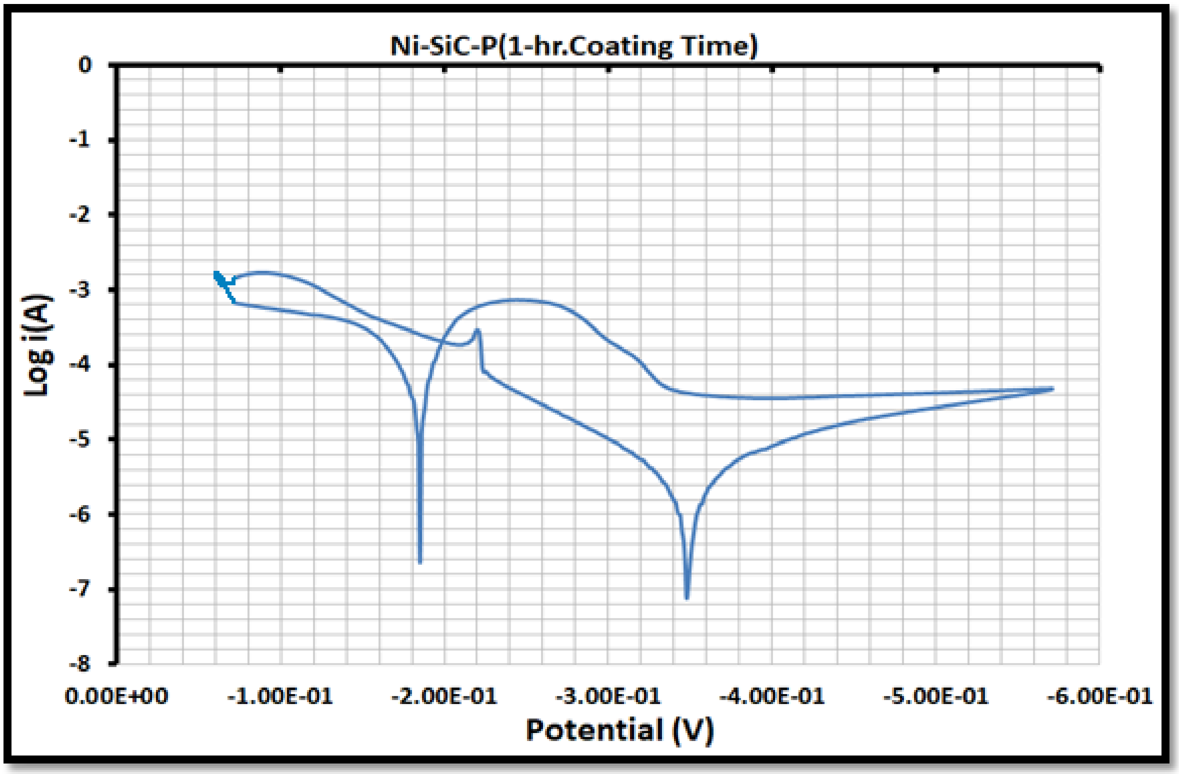

Figure (4.47): Cyclic Polarization Curve of Coated Specimen by Ni-SiC-P(1-hr.Coating Time) in 3.5%NaCl.

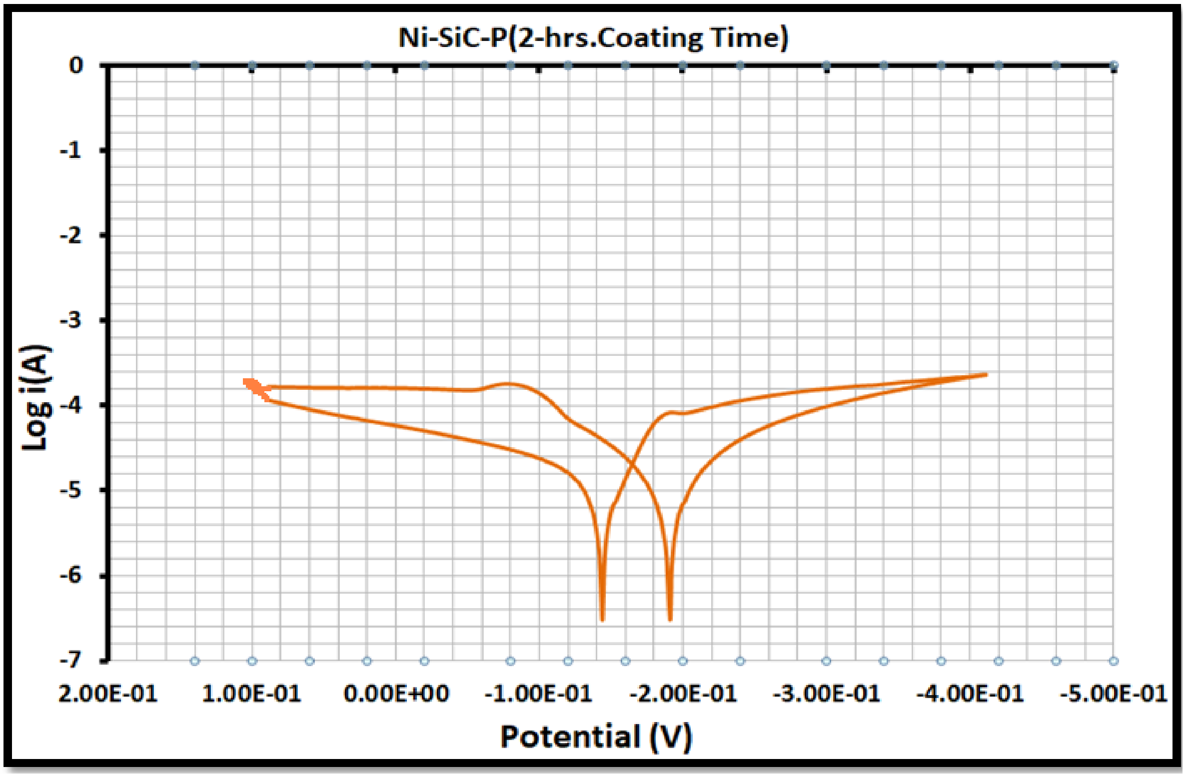

Figure (4.48): Cyclic Polarization Curve of Coated Specimen by Ni-SiC-P(2-hrs.Coating Time) in 3.5%NaCl.

Table (4.9):Cyclic Polarization Parameters for Bare and Coated Specimens in 3.5%NaCl Solution.

Cyclic Polarization Results in 3.5%NaCl Solution				
Specimens	**$E_{pit.}$ (mV)**	**$E_{prot.}$ (mV)**	**ΔE=($E_{pit.}$-$E_{prot.}$) (mV)**	**Improvement Efficiency (I.E.) %**
Bare Specimen	-415	-185	-230	-
Coated Specimen by Ni-P for 1-hrs.	-440	-225	-215	6.5
Coated Specimen by Ni-P for 2-hrs.	-360	-180	-180	21.7
Coated Specimen by Ni-Cu-P for 1-hrs.	-400	-200	-200	13
Coated Specimen by Ni-Cu-P for 2-hrs.	-380	-240	-140	39.1
Coated Specimen by Ni-SiC-P for 1-hrs.	-390	-200	-190	17.3
Coated Specimen by Ni-SiC-P for 2-hrs.	-260	-175	-85	63
Coated Specimen by Ni-Zn-P for 1-hrs.	-280	-75	-205	10.8
Coated Specimen by Ni-Zn-P for 2-hrs.	-360	-215	-145	36

4.4.2. Erosion Corrosion Evaluation

Figure (4.49) displays the results of erosion-corrosion rates with respect to time for bare specimens, coating specimens by (Ni -P) , (Ni-Cu-P), (Ni-Zn-P) and (Ni-SiC-P) at two different coating times(1hr. and 2hr.) in the state of as-plated and heat-treated specimens. The process is carried out in one high active solution; heavy crude oil at different nine intervals (15,30,45,60,75,90,105,120, and135) minutes respectively. The results show that behavior of bare metal or coated metal passes in four stage; incubation stage, acceleration stage, deceleration stage, and steady state. In incubation stage the change in weight is very low because high resistance of metal due to have high hardness. In the second stage the erosion rate increases due to the obtain reaction between the corrosive media which may be contained on NaCl solution and metal surface to form metal oxides and chlorine. These oxides play important role in erosion corrosion rate because it sticks with metal surface. In the third stage clearly decline appears in the erosion rate because most formation oxides and contamination on the surface metal may be removed due to high velocity of stream solution from jet of erosion advice. Also in this stage some of grooves may be appeared in the surface metal .The last stage which called the steady state stage, in this stage there is no significantly increasing or decreasing in weight of metal therefore the rate of erosion stays constant. In this last stage the little change in rate of erosion resulted from the ionic drawing as well as the ability of the metal to form protective strong oxides.

Figure (4.49) shows high different in the rate of erosion especially at the bare metal while the coating metal show less erosion rate. It is clear that heavy crude oil tends to form chlorine compound on the surface with exposure of time. This clear different is resulted from using different coating layer with respect to bare specimens. By comparing the results of the previous figure, the nickel-silicon carbide-phosphor coating shows a significant improvement in erosion resistance, especially when coating specimen at 2hrs. and heat treated. The low thickness of coating result from short period time that not enough to resistance erosion corrosion in active solutions. On the other hand, specimens with high coating thickness are useful because the high adhesion thickness give high resistance erosion.

From the heavy fuel analysis,chemical composition of corrosion product, the heavy fuel encourage for corrosion ,stress corrosion cracking and erosion to the strong surfaces such as stainless steel 316.

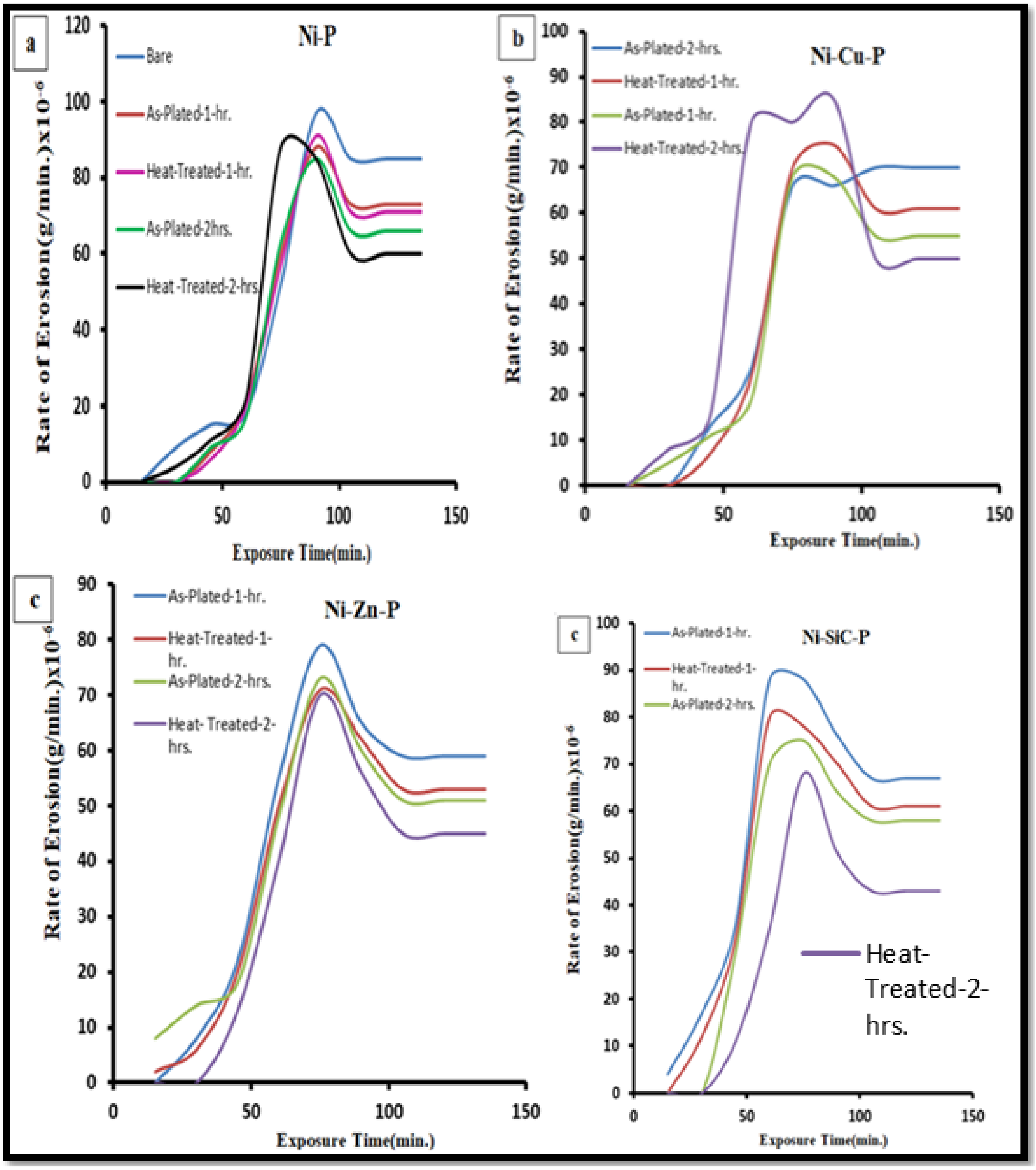

Figure (4.49): Rate of Erosion-Corrosion in Heavy Fuel for Bare &Coating Specimens.

Through the results of curves in Figure (4.49) which show that specimens coated by Ni-Cu-P especially the specimens which have 2-hours' time of coating have low rate of erosion in heavy crude oil than Ni-P alone. The presence of nano-particles of SiC, Zinc, and copper content in matrix of Ni-P creates more adhesion between the substrate and coating layer and increasing mobility and activity attempt to accelerate the crystalline and nucleation of crystalline phase during heat treatment. So that coating layer with these elemsnts has more corrosion resistance than Ni-P alone.This explaination is agreed with**[71].** After the completion of erosion-corrosion test, SEM is carried out in the bare and coated specimens to show the effect of erosion rate on surface of bare metal or on coating layer. Figure (4.50) shows the effect of erosion rate on bare specimen in one active media (heavy crude oil). SEM shows that the bare surface is more corroded than the coating surface where the rate of erosion in bare surface reach to 97×10^{-6} g/min at (90min.exposure time test). On the other hand the rate of erosion rate has high level drop in heat-treated coated specimens especially at plating of (Ni-SiC-P) where it reaches to 51.3×10^{-6} g/min.at 90min. exposure time.

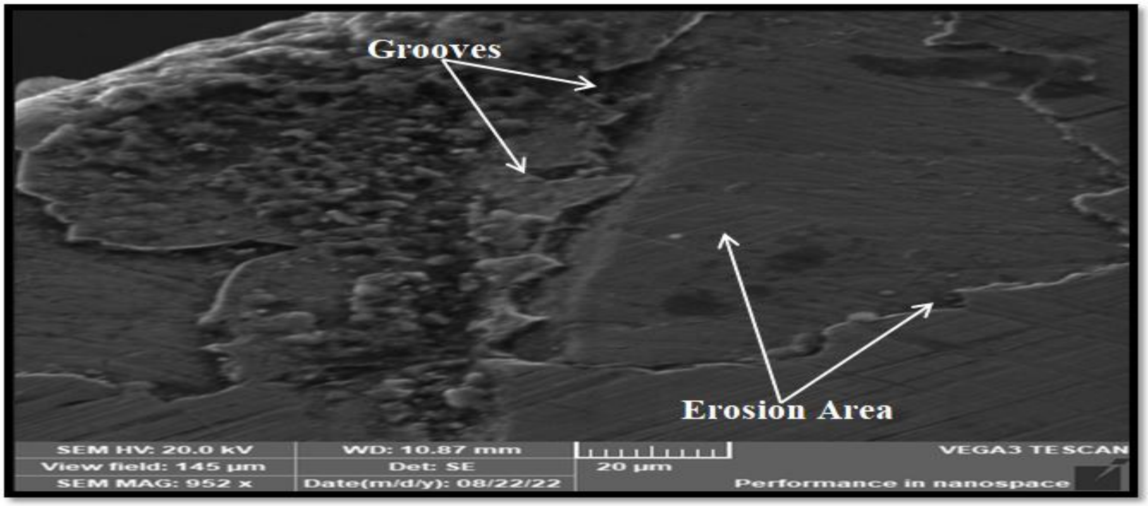

Figure (4.50): SEM Image of Erosion-Corrosion for Bare Specimen in heavy Crude Oil.

Figure(4.51) shows four different SEM images of four different coating layers which are exposed to high rate of erosion in active environment (heavy crude oil) at maximum time exposure time test 135min. The erosion-corrosion for coated specimen is characterized in appearance with grooves, waves, rounded holes, and/or shaped grooves. The rate of erosion Ni-P alone coating has high level when compared with other three coating layers at the same exposure time.This explanation is agreed with **[71].**

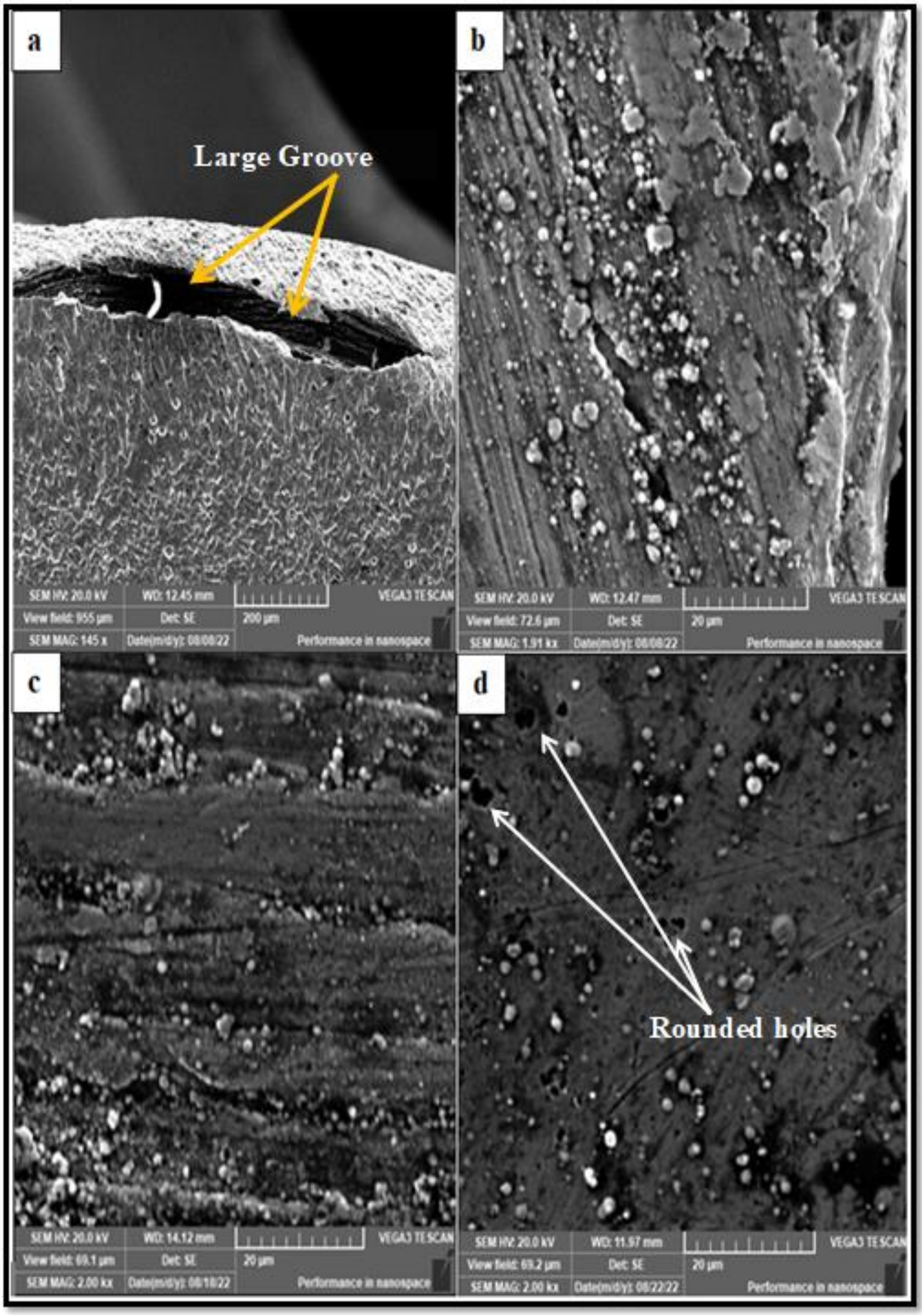

Figure (4.51): SEM Image of Erosion-Corrosion in Heavy Crude Oil For:(a)Ni-P (b)Ni-SiC-P(c)Ni-Zn-P(d)Ni-Cu-P.

4.4.3. Evaluation of Stress Corrosion Cracking(SCC)

At first; results of stress corrosion cracking for bare specimens are discussed, and then the results of stress corrosion cracking for coated specimens by four electroless plating are studied.

Stress corrosion cracking results are depended on the existence of micro-cracks due to expose the specimens to four different tension force from bending them according to (ASTM G30-97-2015) and putting them in heavy crude oil at three different exposure period time (480 ,960 and1440hrs.) At first in,480and 960 hrs. the presence of micro-cracks is impossible due to the short period time for testing but when the period time is increased over 960hrs.,the cracks may be occured.

The bending load and the sever corrosive media by crude oil for long period time encourage to obtain ductile cracks. At the macroscale, the ductile damage process is observable as a plastic flow, which can be increased by an extra consecutive loss of cohesion at the interfaces. The damage process is depicted in Figure(4.52) and its three stages are reviewed briefly.This explainable is agreed with**[134].**

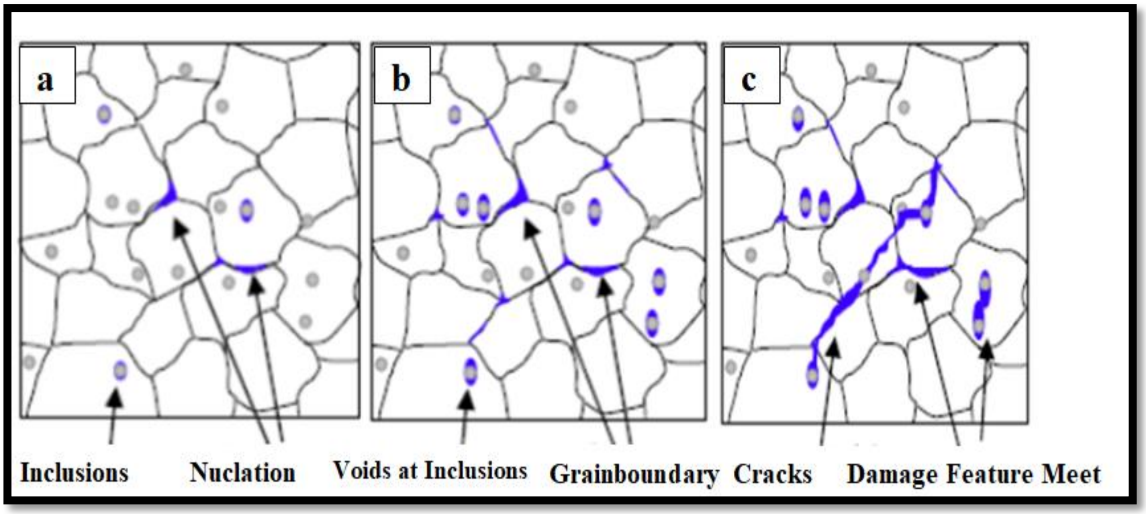

Figure(4.52): Simple Sketch of Initiation Crack Damage on Grain-Boundary in Three Stage:(a):Nucleation:(b)Growth(c):Coalescence**[135].**

In the first stage (nucleation) cavity initiation sites in metallic materials are typically associated with second phase particles or non-metallic inclusions. They can result from alloying procedures or as solidification impurities, such as gas pores (contained gas in the die cavity) or shrinkage pores. In the second stage(growth) the formation of voids is greatly influenced by strain and stress situations. In micromechanical analysis, two approaches can be distinguished: an uncoupled approach relying upon the Von Mises criteria as the flow criterion, and a coupled approach.At the last stage (Coalescence) cavity coalescence remains mostly unknown, necessitating extensive research. This event is influenced by geometrical characteristics (size of void, shape, spacing, and orientation), properties of material (sensitivity of strain rate, rate of work hardening), and stress state .

All the increasing in the length and depth of micro cracks at long period time in heavy crude oil is resulted from formation harmful compound which are adherent with the coating or bare metal. Stress corrosion cracking is accelerated especially at (1440hrs.) so the heavy crude oil consists of detrimental compounds and roots of halides such as (Cl). From Figure (4.53), the stress corrosion cracks are different according to the exposure force and time of test on coated or bare specimens. The stress corrosion cracking in this test usually is inter-granular fracture where the trans-granular fracture don’t appear. Figure (4.53.a)refers to the beginning of stress corrosion cracking to the specimen with code(A) which has tension force 55N and applied stress 9.24MPa. Figure (4.53.b)displays the propagation of cracking on grain-boundary for specimen with code(B) which has tension force543N and applied stress24.15MPa. Figure (4.53.c) that supporting the onset of formation cracking which is illustrated with code (C) which has tension force147N and applied stress 9.828MPA.

Specimen with code (D) has 1795N tension force and applied stress 63MPa where Figure(4.53.d) shows the increasing of cracks propagation on grain boundary.

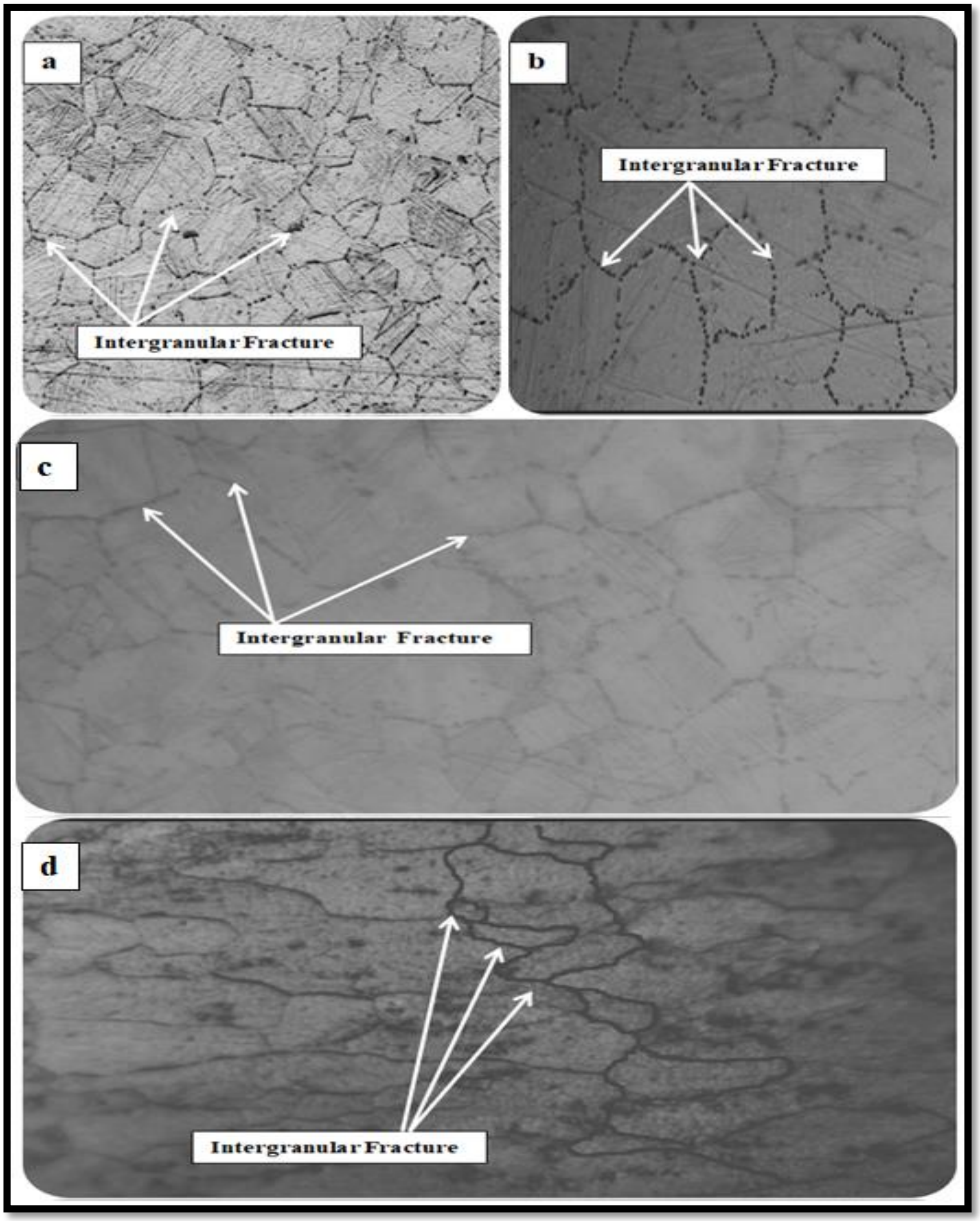

Figure (4.53): Optical Images(80X) of Stress Corrosion Cracking Test at 1440 hrs.for Bare Specimens(a):Specimen A(55N):(b) Specimen B(543N):(c): Specimen C(147N):(d) Specimen D(1795N).

Although the coated specimens in (1hr. time of coating) have good thickness but they have simple beginning of stress corrosion cracking rates, so the high thickness protect the bare metal. The results of stress corrosion cracking for coated specimens at 2-hrs.with some addition such as copper, zinc,carbide silicon show significantly change when they are compared with the obvious results of stress corrosion cracking for coated specimens by Ni-P alone.

It clears there is important role for copper ,zinc,silicon carbide content in improvement of corrosion resistance, this role clears in increasing the smoothness of specimens , the uniformity of coating and adhering of coating with substrate.

Scanning electron microscope (SEM) is used to identify the maximum effect of stress corrosion cracking on different coated specimens at 1440hrs. and different tension forces. Figure (4.54) shows SEM images of four coating layer which may be peeled or not effect due to expose for long period time in heavy crude oil . In Figure (4.54.a) the intergranular fracture after plating by Ni-P for 1hr. coating time begins by the presence also in Figure (4.54.b) the fracture was clear across grain boundary. On the other hand in Figures (4.54.c) and (4.54.d) the intergranular fracture across coating layer of Ni-Zn-P and Ni-SiC-P respectively was less extreme and beginning formation.

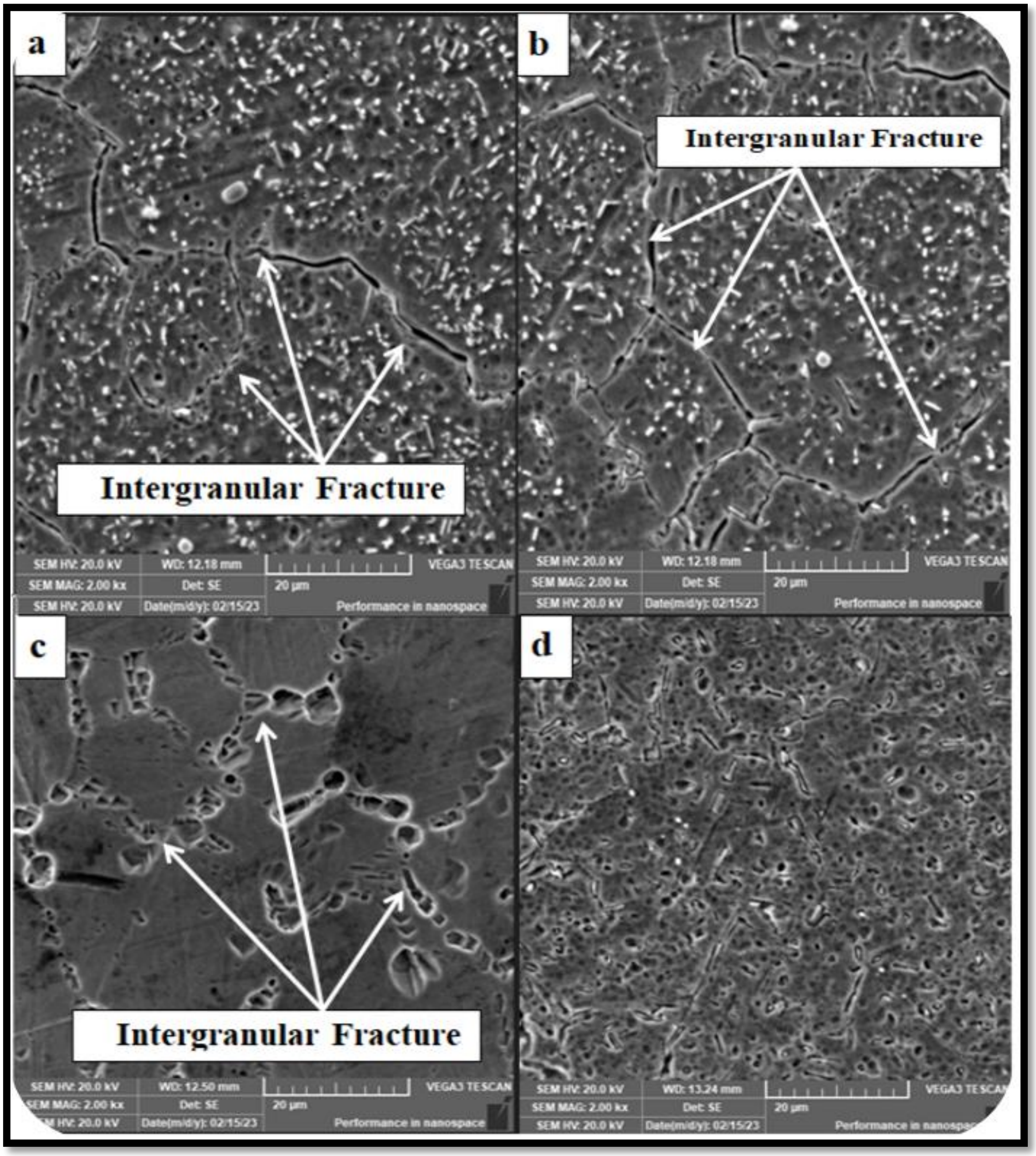

Figure (4.54): SEM Images of Stress Corrosion Cracking Test in 1440hrs. For Coated Specimens of sample D(1hr. Time of Coating)by: (a):Ni-P (b): Ni-Cu-P (c): Ni-Zn-P (d): Ni-SiC-P

The thickness of coating layer and the presence of some metal or non-metal addtives have high effect on the resistance of plating to more type of corosion, wear, erosion,erosion-corrsion and stress of corrosion cracking.

In this study four type of electrolessplatings are used to reduce erosion-corrosion and stress corrosion cracking(SCC).Cupper,zinc and silicon-carbide have good addition to the matrix Ni-P.Figure(4.55)displays the effect of stress corrosion cracking test after 1440 hrs.in heavy crude oil for four type of electrolessplatings which have good thickness.The suitable thickness gives high resistance to stress corrosion cracking.

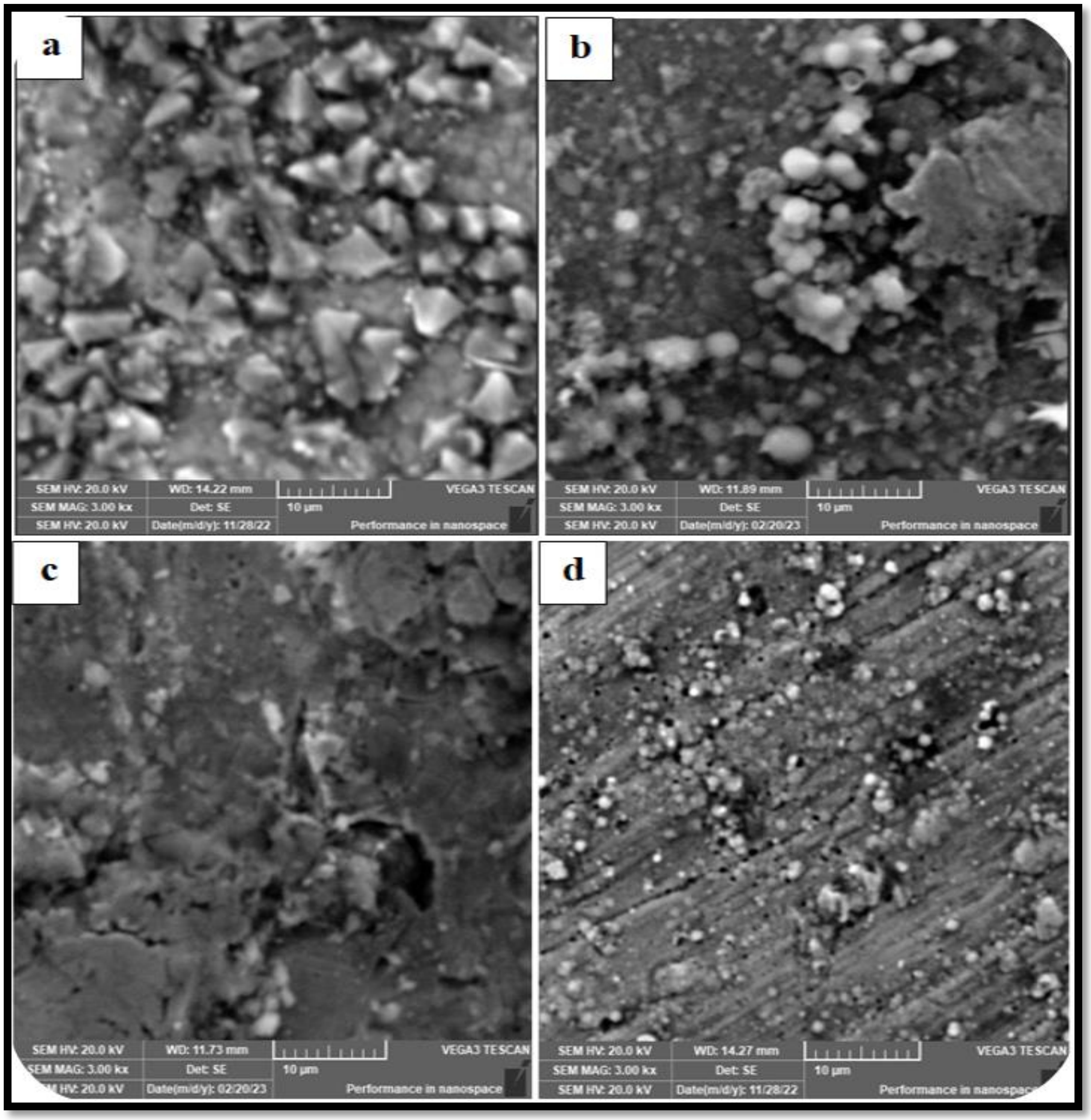

Figure (4.55): SEM Images of Stress Corrosion Cracking Test in 1440hrs. For Coated Specimens of Sample D(2hr. Time of Coating)by: (a):Ni-Zn-P (b): Ni-Cu-P (c): Ni -P (d): Ni-SiC-P.

4.5.Finite Elements Analysis Results

4.5.1. The Equivalent Stresses and Strain Analysis

Generally the equivalent stress criterion (Von-Mises stress) is valid for materials in the brittle or ductile state and that can be used to describe the beginning of yielding, loss of strength or damage in structural elements, granular materials, and so forth, that are subjected to multi axial stress states**[136]**.Figure(4.56) shows the equivalent stress and strain for sample(A) which subjected to resultant force equal 110.88N.The red color indicates the high levels of stress in the Figure (4.56) as well as the highest rates of strain. The high level of equivalent stress is 109.07Pa according to the Von-Miss theory. This high stress appears in the edge of U-bend region due to the stress is concentrated in edges .Also the high strain rate is 5.45×10^{-10}.On the other hand the blue color refers to low level of stress and strain.0.0310Pa and 2.5657×10^{-11} were the minimum of equivalent stress and strain respectively.

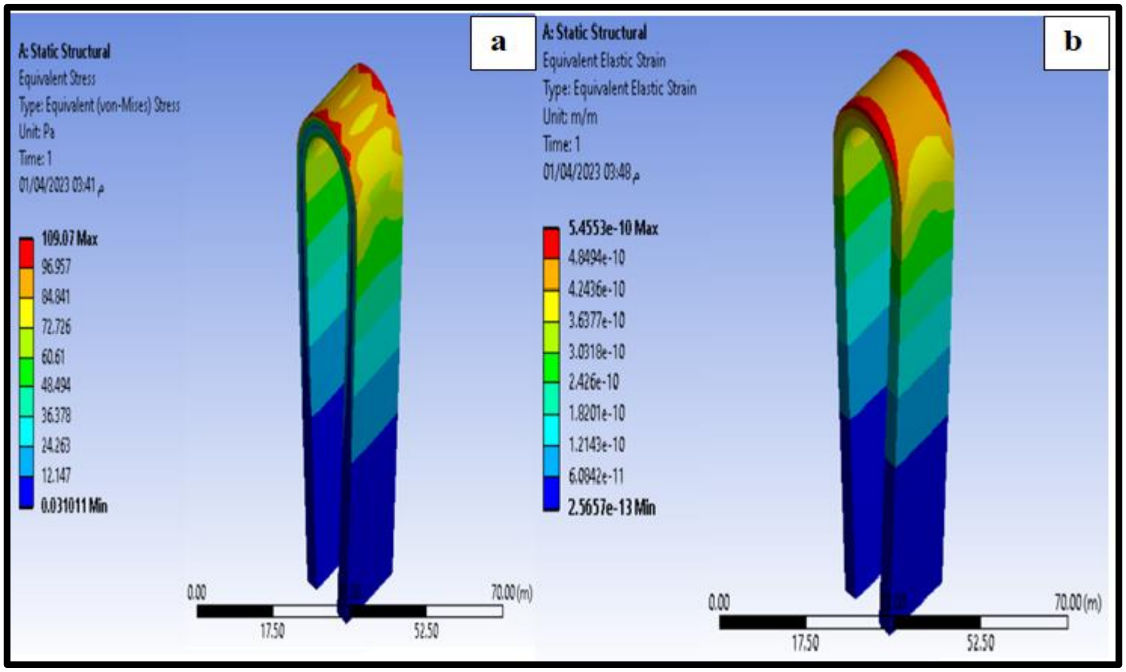

Figure(4.56):Sample (A):(a) Equivalent Stress(b) Equivalent Strain.

From Figure(4.56) and previous studies the equivalent elastic strain is a concept used in materials science and mechanics to quantify the amount of strain a material undergoes under an applied load. It is a scalar quantity that represents the total amount of elastic strain energy stored in the material. The concept of equivalent elastic strain is useful in analyzing the behavior of materials under complex stress states. Figure(4.57) shows the equivalent stress and strain for sample(B) which subjected to resultant force equal 1086.75N.The red color indicates the high levels of stress in the Figure (4.57) as well as the highest rates of strain. The high level of equivalent stress is 1009.4Pa according to the Von-Miss theory. This high stress appears in the edge of U-bend region due to the stress is concentrated in edges .Also the high strain rate is5.0469×10^{-9}.On the other hand the blue color refers to low level of stress and strain.0.405010Pa and 3.2429×10^{-12} were the minimum of equivalent stress and strain respectively.

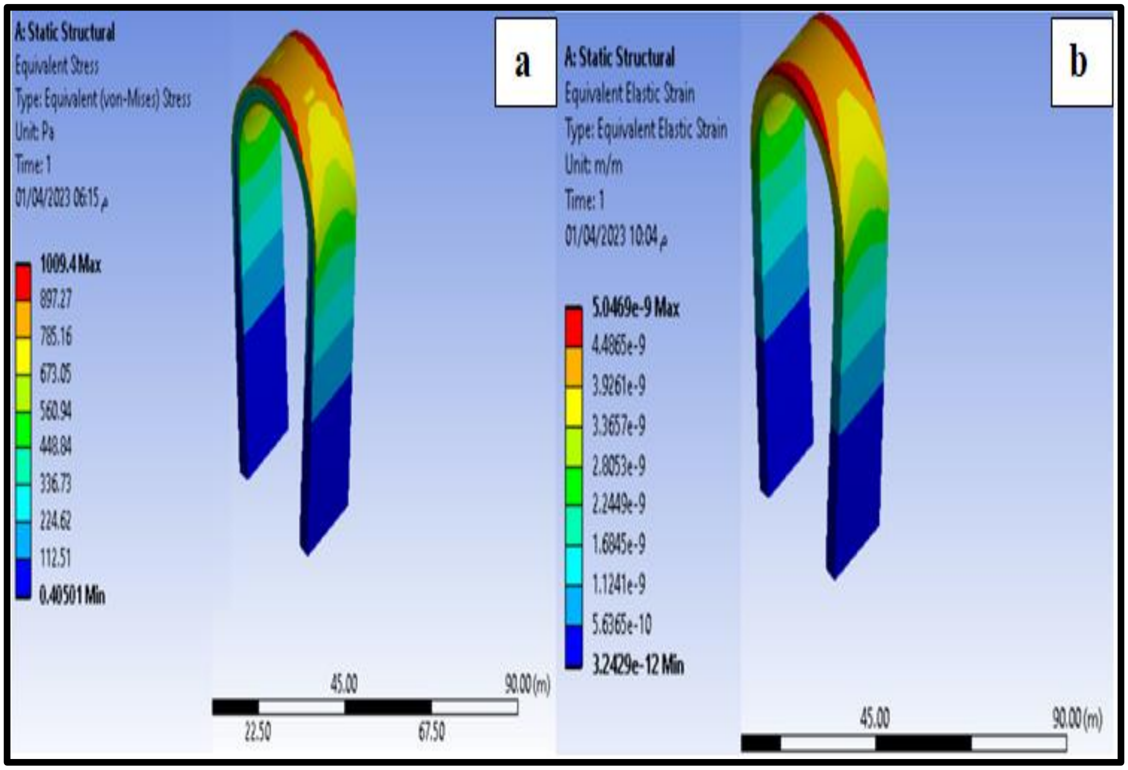

Figure(4.57):Sample (B):(a) Equivalent Stress(b) Equivalent Strain.

Figure(4.58) shows the equivalent stress and strain for sample(C) which subjected to resultant force equal 294.84N.The red color indicates the high levels of stress in the Figure (4.58) as well as the highest rates of strain. The high level of equivalent stress is 32946Pa according to the Von-Miss theory. This high stress appears in the edge of U-bend region due to the stress is concentrated in edges.Also the high strain rate is1.6473×10^{-7}.On the other hand the blue color refers to low level of stress and strain 7.6198Pa and 8.014×10^{-11} were the minimum of equivalent stress and strain respectively.

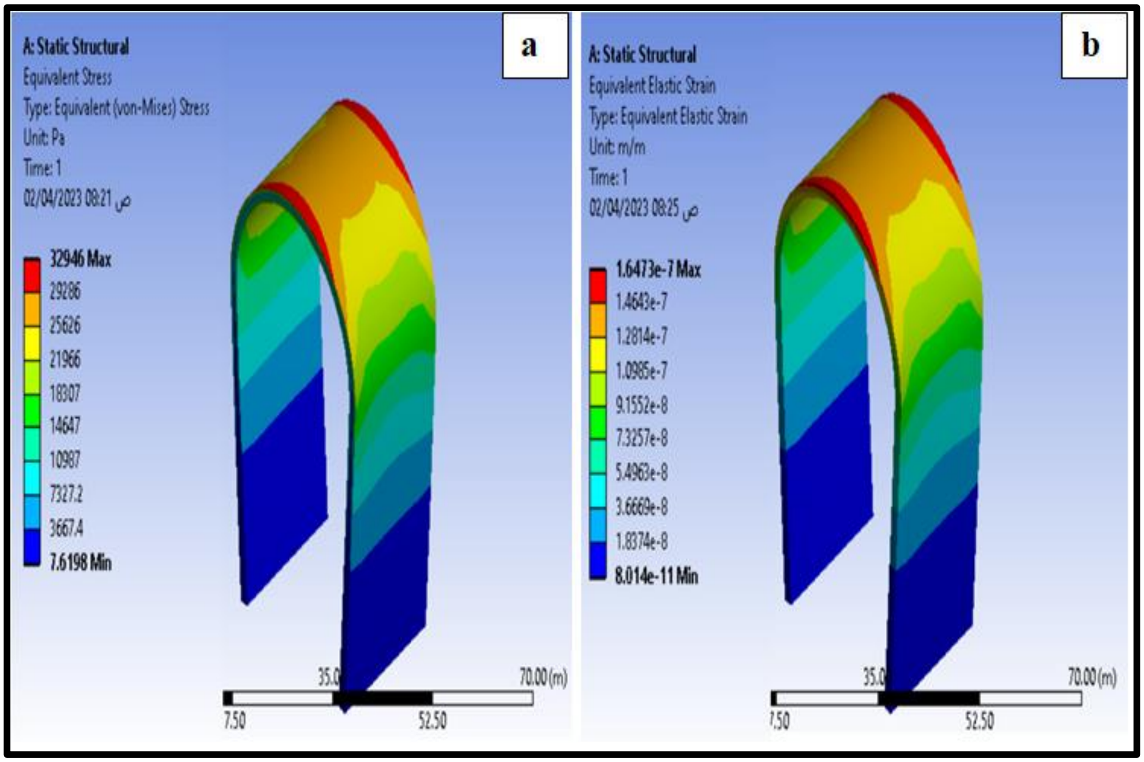

Figure(4.58):Sample (C):(a) Equivalent Stress(b) Equivalent Strain.

Figure(4.59) shows the equivalent stress and strain for sample(D) which subjected to resultant force equal 3591N.The red color indicates the high levels of stress in the Figure (4.59) as well as the highest rates of strain. The high level of equivalent stress is 1896.5Pa according to the Von-Miss theory. This high stress appears in the edge of U-bend region due to the stress is concentrated in edges . Also the high strain rate is 9.4829×10^{-9}.On the other hand the blue color refers to low level of stress and strain1.1228Pa and 6.06×10^{-12} were the minimum of equivalent stress and strain respectively.

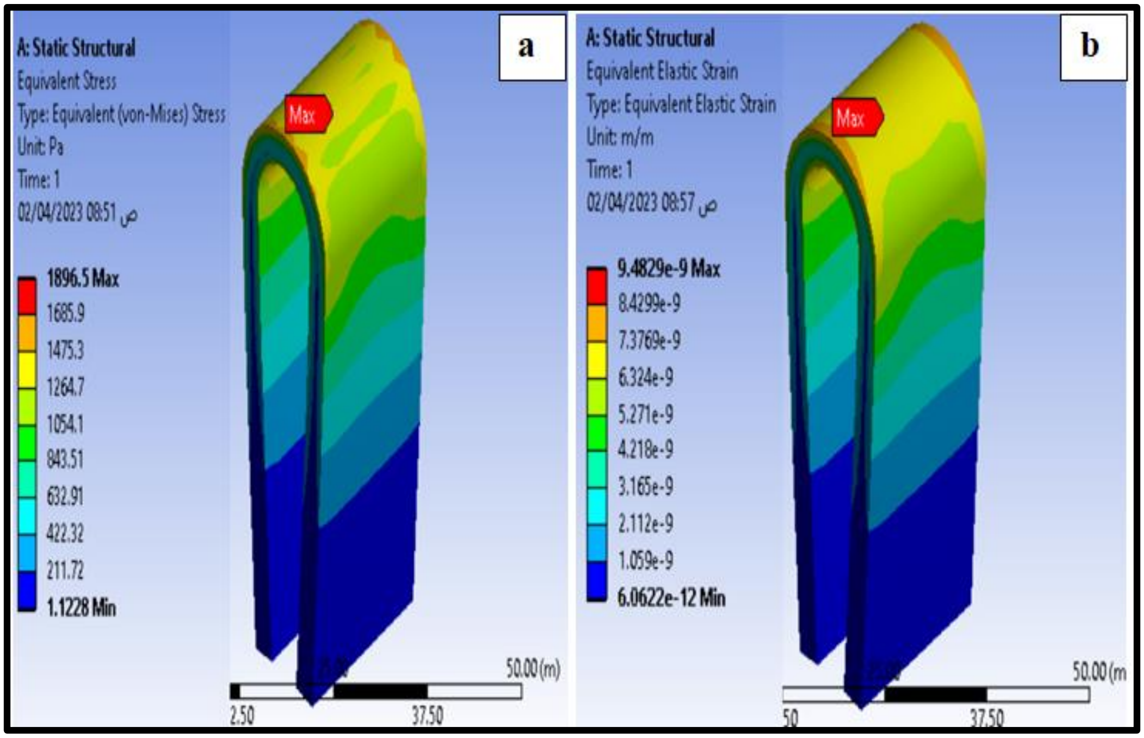

Figure(4.59):Sample (D):(a) Equivalent Stress(b) Equivalent Strain.

4.5.2.Total Deformation and Directional Deformation Analysis

Total deformation is the deformation that can be take place in all directions(XYZ)of body or specimens test. Directional deformation is the deformation that can be occurred within one direction X,Y or Z from body or specimens test **[137]**. Figure(4.60) shows the total deformation and directional deformation for sample(A) which subjected to equal opposite forces. These forces is 55.44N in each side.The red color indicates the high levels of total deformation as well as the highest rates of directional deformation. The high level of total deformation is 4.6835×10^{-7}m. This high total deformation appears in the end of two edges from U-bend region. Also the directional deformation is 4.6801×10^{-7}m.On the other hand the blue color refers to low level of total and directional deformation were 7.6458×10^{-9} m and -4.6801×10^{-7} m respectively.

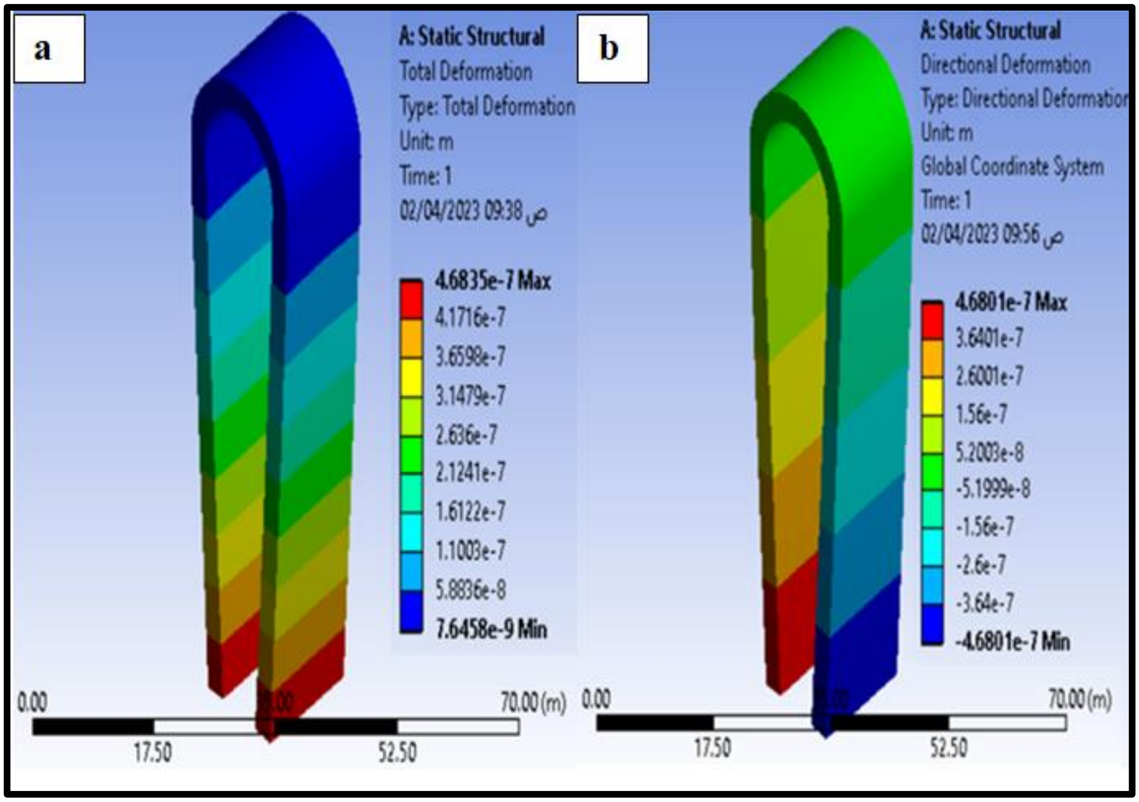

Figure(4.60):Deformation of Sample(A):(a): Total deformation (b): Directional deformation.

Figure(4.61) shows the total deformation and directional deformation for sample(B) which subjected to equal opposite forces. These forces is 543.375N in each side.The red color indicates the high levels of total deformation as well as the highest rates of directional deformation. The high level of total deformation is 4.0486×10^{-6}m. This high total deformation appears in the end of two edges from U-bend region. Also the directional deformation is 4.0458×10^{-6}m. On the other hand the blue color refers to low level of total and directional deformation were 1.2877×10^{-7} m and -4.0463×10^{-6} m respectively.

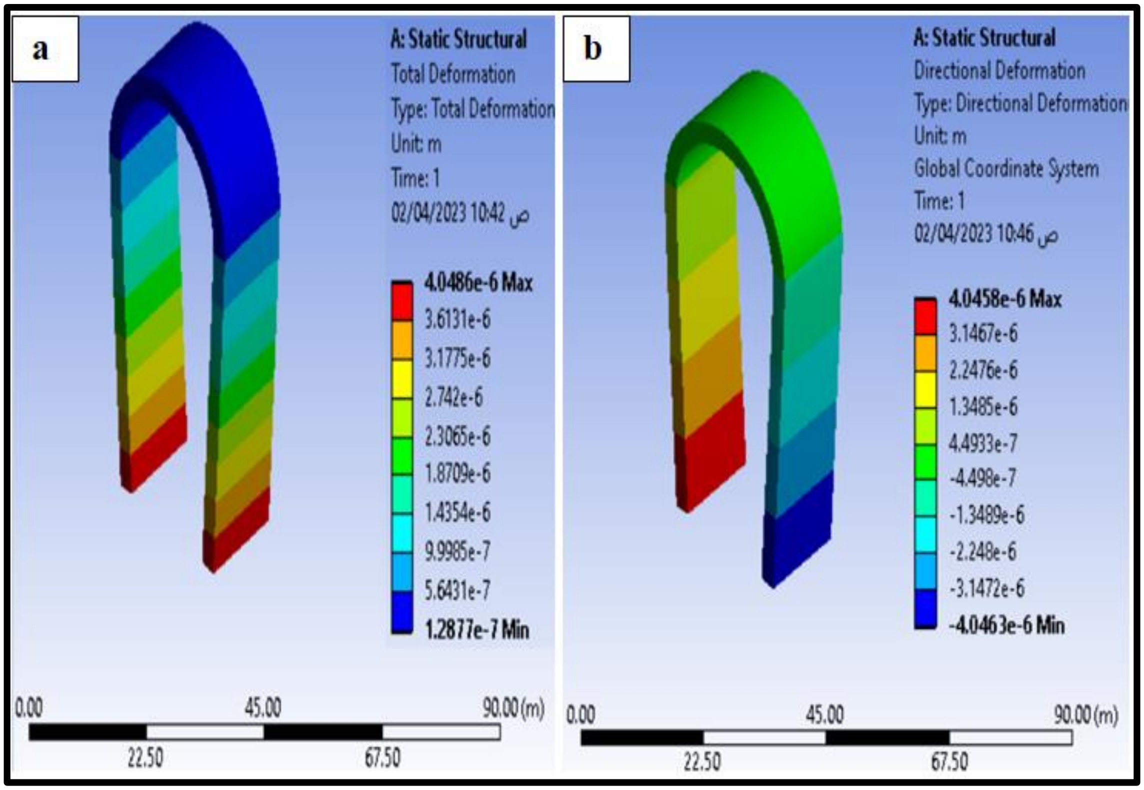

Figure(4.61):Deformation of Sample(B):(a): Total deformation (b): Directional deformation.

Figure(4.62) shows the total deformation and directional deformation for sample(C) which subjected to equal opposite forces. These forces is 147.42N in each side.The red color indicates the high levels of total deformation as well as the highest rates of directional deformation. The high level of total deformation is 0.0002039m. This high total deformation appears in the end of two edges from U-bend region. Also the directional deformation is0.00020345m.On the other hand ,the blue color refers to low level of total and directional deformation were 8.646×10^{-6} m and -0.002038 m respectively.

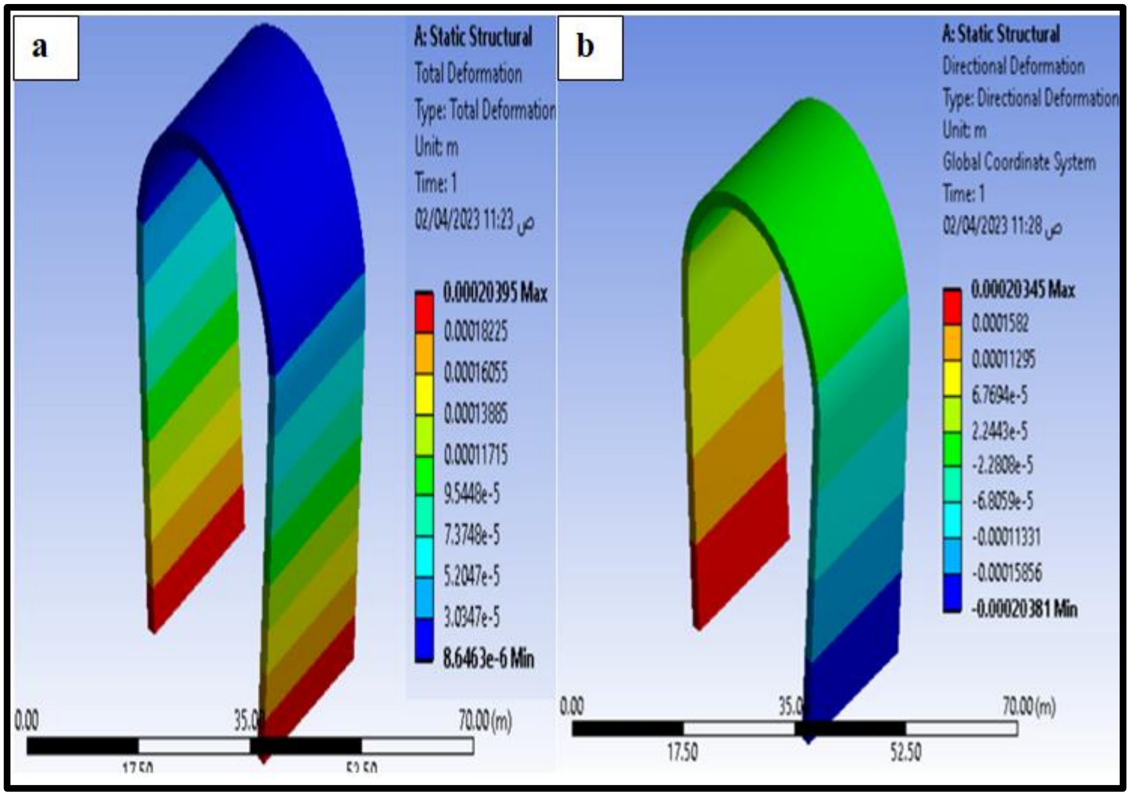

Figure(4.62):Deformation of Sample(C):(a): Total deformation (b): Directional deformation.

Figure(4.63) shows the total deformation and directional deformation for sample(D) which subjected to equal opposite forces. These forces is 1795.5N in each side.The red color indicates the high levels of total deformation as well as the highest rates of directional deformation. The high level of total deformation is 3.833×10^{-6}m. This high total deformation appears in the end of two edges from U-bend region. Also the directional deformation is 3.827×10^{6}m.On the other hand the blue color refers to low level of total and directional deformation were 6.678×10^{-8} m and -3.827×10^{-6} m respectively.

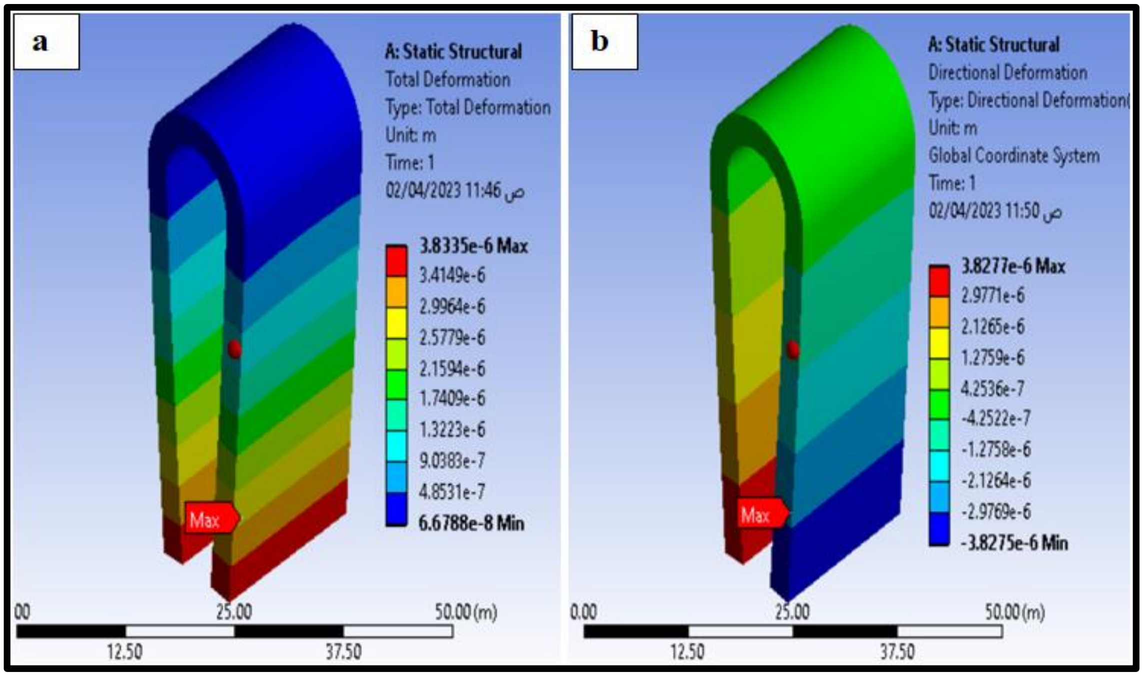

Figure(4.63):Deformation of Sample(D):(a): Total deformation (b): Directional deformation.

4.6. Comparison of Results for Four Electroless Plating Methods

The most prominent results obtained during this study were divided into two main parts. The first section witnessed analytical results on the causes of failure that occurred through visual examination, electron microscope examination(SEM),XRD,XRF,hardness measurement, chemical composition of materials used and analysis of heavy fuel oil.All available techniques also were used to determine and measure the damage . The second section viewed the suggestion's methods in this study to reduce the failure in disc separator. To recognize the best method of electroless plating (after 2-hrs.coating time) which were used to decrease the failure,so Table (4.10)depicted the important comparison results between four heat treated electroless platings in 2-hour coating time . Not only these results were obtained but also there were results didn't remember in this comparison about electroless plating which have one hour coating.

Table(4.10):Comparison Between Four Electroless Plating Results.

Type of Test	**Ni-P**	**Ni-Cu-P**	**Ni-Zn-P**	**Ni-SiC-P**
Coating Thickness(µm)	🟩 40-65	🟥 30-50	🟧 50-70	⬜ 18-30
Hardness (HV)	⬜ 928	🟩 941	🟧 937	🟥 1091
Coating Adhesion Strength(MPa)	🟧 50.11	🟩 58.8	⬜ 45.6	🟥 63.4
Roughness Average Sa(nm)	🟧 5.61	🟩 4.83	⬜ 5.64	🟥 4.69
Corrosion Rate (mpy)	⬜ 0.34	🟧 0.213	🟥 0.064	🟩 0.151
Erosion Corrosion g/min $\times 10^{-6}$(135min.)	⬜ 53	🟧 48	🟩 45	🟥 43
Stress Corrosion Cracking(SCC)	⬜ None Propagate	⬜ None Propagate	⬜ None Propagate	⬜ None Propagate

Excellent: 🟥 V.Good: 🟩 Good: 🟧 Normal ⬜

Chapter5

Conclusions & Recommendations

Chapter Five

Conclusions & Recommendations

5.1. Conclusions

In the following; conclusions of failure analysis process and the elctroless plating of four coating layers have been presented as:

5.1.1. Conclusions to Failure Analysis Process

According to the results of the first part in the present work, the catastrophic failure of separator disc has occurred as follows:

1- High percentage of contaminations such as V,S, Ca,Cl, and Na ,are presented in used fuel, so the stress corrosion cracking (SCC)and erosion- corrosion are developed due to the presence of these contaminations.

2- A typical failure mode in separators of heavy fuel oil is stress corrosion cracking. In this study, bowel separator 316 stainless steel discs were badly corroded by 3.5%NaCl and crude oil.

3- From SEM and L.O.P(light optical microscope) The fracture path can be integranular, depending on the alloy and corrosive media, with the latter being the more prevalent.

4- High drop in magnitude of hardness Vickers in surface of failed separator disc from330HV to218HV

5- The microstructure and the chemical composition of disc separator refer to high presence of Cr and Ni and the material is SS316.

5.1.2. Conclusions to Electroless Plating and Their Tests

According to the results of the second part in the present work, the suggested way to reduce the failure of separator disc has included the following conclusion:

1- Electroless plating by Ni-P as matrix is an effective method in coating of metal or alloys and can provide an acceptable homogenous distribution in most of metals and alloys substrates.

2- The additives elements metal or non-metal such as Cu, Zn, SiC nano particles in low percentage give good surface properties rather than without these elements.

3- Several different ranges of coating thickness that are obtained; (10-70), (7-50)and(7-30) µm. This difference depends on several parameters (time of coating, temperature of solution, type of bath, degree of agitations.

4- Surface and mechanical properties are significantly enhanced at 2-hrs.which reprecented time of coating and with using of copper, zinc, silicon carbide nano-particles content showed that (erosion-corrosion rate at heavy fuel media and 135 minutes)85×10^{-6}g/min in bare metal and 43×10^{-6}g/min in coated specimens by Ni-SiC-P(2hrs. coating time).

5- High increasing in hardness Vickers (HV) for coating specimens by Ni-SiC-P(2hrs.coating time-heat-treated) than coating specimens with Ni-P alone,where reached to 1091HV in the first coating while was 928HV in the last coating.

6- The average surface roughness(Sa) witnessed increasing in most magnitude for all four electroless-plating (with 2hrs. coating time)after heat treated than electroless plating(with 1hr. coating time)where it ranged between(4.69-5.64nm) in the first coating time but it was(1.57-3.58nm) in the last coating time.

7-Transgraular stress corrosion cracking can be appeared on bare specimens after 1440hrs. but don't appear especially on coating specimens with high thickness.

8-In finite element analysis by ANSYS(15.07) gives clear picture about the regions which subjected to high and low stresses and strains where the minimum equivalent stress and strain in all four samples were 0.0310Pa and 2.5657×10^{-10} respectively.

5.2. Recommendations for Future Work

For future works, the followings are suggested as:

1-High- fuel quality should be used through the decreasing potassium and sodium content .

2-Studying the direction solidification method to manufacturing separator disc.

3-Applying another ternary and nano composite coating such as TiC,ZrO_2,TiO,MgO andAl_2O_3 in surface of disc separators to protect it from corrosion , erosion corrosion and stress corrosion cracking.

4-Simulate corrosion-erosion behavior of stainless steel by using ANSYS software based on fluid-structural-thermal coupled field analysis.

References

Reference

[1] Golub, Ivana, Radovan Antonić, and Đorđe Dobrota. "Optimization of heavy fuel oil separator system by applying diagnostic inference methods." *Pomorstvo* 25, no. 1 (2011): 173-188.

[2] Başhan, Veysi, Hakan Demirel, and Erkan Celik. "Evaluation of critical problems of heavy fuel oil separators on ships by best-worst method." *Proceedings of the Institution of Mechanical Engineers, Part M: Journal of Engineering for the Maritime Environment* 236, no. 4 (2022): 868-876

[3] Fun-sang Cepeda, Maricruz A., Newton Narciso Pereira, Suzana Kahn, and Jean-David Caprace. "A review of the use of LNG versus HFO in maritime industry." *Marine Systems & Ocean Technology* 14, no. 2-3 (2019): 75-84.

[4] Zamiatina, Nadežda. "Comparative overview of marine fuel quality on diesel engine operation." *Procedia Engineering* 134 (2016): 157-164

[5] Kołakowski, Paweł, Mateusz Gil, Krzysztof Wróbel, and Yuh-Shan Ho. "State of play in technology and legal framework of alternative marine fuels and renewable energy systems: a bibliometric analysis." *Maritime Policy & Management* 49, no. 2 (2022): 236-260

[6] Karafyllias, George, Alexander Galloway, and Edward Humphries. "Erosion-corrosion assessment in strong acidic conditions for a white cast iron and UNS S31600 stainless steel." *Wear* 484 (2021): 203665.

[7] Qi, Hong, Yuhai Qian, Jingjun Xu, Jun Zuo, Meishuan Li, Zheng Zhang, Xiaobao Xie, and Qingshan Shi. "Fabrication of 60 wt% SiO2 filled hybrid nanocomposite and its application in erosion-corrosion and radiation resistance." *Vacuum* 189 (2021): 110228.

[8] Xu, Yunze, Qiliang Zhang, Shan Gao, Xiaona Wang, and Yi Huang. "Exploring the effects of sand impacts and anodic dissolution on localized erosion-corrosion in sand entraining electrolyte." *Wear* 478 (2021): 203907.

[9] Yang, Xiao-Lei, Jing-Lu Fei, Sheng-Hui Wang, Yi Gong, and Zhen-Guo Yang. "Failure analysis on synergistic effect of erosion and corrosion on failed fittings in specialty chemical plant. Part I: Elbows." *Materials and Corrosion* 70, no. 5 (2019): 906-920.

[10] Mattox, Donald M. *Handbook of physical vapor deposition (PVD) processing*. William Andrew, 2010.

[11] Nath, A. K., and S. Sarkar. "Laser transformation hardening of steel." In *Advances in laser materials processing*, pp. 257-298. Wood head Publishing, 2018.

[12] Bauri, Ranjit, and Devinder Yadav. *Metal matrix composites by friction stir processing*. Butterworth-Heinemann, 2017.

[13] Somers, Marcel AJ, and Thomas L. Christiansen. "Nitriding of Steels." In *Encyclopedia of Materials: Metals and Alloys*, pp. 173-189. Elsevier, 2022.

[14] Sharifalhoseini, Zahra, and Mohammad H. Entezari. "Enhancement of the corrosion protection of electroless Ni–P coating by deposition of sonosynthesized ZnO nanoparticles." *Applied Surface Science* 351 (2015): 1060-1068.

[15] Schweitzer, Philip A. *Corrosion and corrosion protection handbook*. Vol. 1. Crc Press, 1989.

[16] Schweitzer, Philip A. *Corrosion Engineering Handbook, -3 Volume Set*. CRC press, 1996.

[17] Kiran, K., Abhishek Arora, B. Ratna Sunil, and Ravikumar Dumpala. "Effect of heat treatment on the temperature dependent wear characteristics of electroless Ni–P–BN (h) composite coatings." *SN Applied Sciences* 2, no. 6 (2020): 1-12.

[18] Cissé, Mbouillé, Mohamed Abouchane, Tayeb Anik, Karima Himm, Rida Allah Belakhmima, Mohamed Ebn Touhami, Rachid Touir, and Abderrahmane Amiar. "Corrosion resistance of electroless Ni-Cu-P ternary alloy coatings in acidic and neutral corrosive mediums." *International Journal of Corrosion* 2010 (2010).

[19] Wang, Jie, Junpeng Liu, Nigel Neate, Mingwen Bai, Fang Xu, Tanvir Hussain, Colin Scotchford, and Xianghui Hou. "Investigation on time-dependent wetting behavior of Ni-Cu-P ternary coating." *Journal of Alloys and Compounds* 765 (2018): 221-228.

[20] Vasile, Marian Buradai and Dumitru Mitric." Electroless deposition process of Ni-Zn-P for anticorrosive applications" *Metallurgy and New Materials Researches* 2(2018):1221-5503.

[21] Ranganatha, S., T. V. Venkatesha, and K. Vathsala. "Development of electroless Ni–Zn–P/nano-TiO_2 composite coatings and their properties." *Applied Surface Science* 256, no. 24 (2010): 7377-7383.

[22] Popescu, Ana Maria, Virgil Constantin, Mircea Olteanu, Vasile Soare, Marian Burada, and Elena Ionela Neacsu. "Morphology and corrosion behavior of Zn-Ni-P thin films electrolessly deposited from chloride baths." *Chemistry Magazine* 64, no. 4 (2013): 417-424.

[23] Farzaneh, A., M. Ehteshamzadeh, Mustafa Can, Omer Mermer, and Salih Okur. "Effects of SiC particles size on electrochemical properties of electroless Ni-P-SiC nanocomposite coatings." *Protection of Metals and Physical Chemistry of Surfaces* 52, no. 4 (2016): 632-636.

[24] Ram, Munna, Moh Abdul Aleem Ansari, Sulaxna Sharma, Vipin Choudhary, and Awanish Kumar Sharma. "Microscale Hardness of Acidic Electroless Ni-P/Ni-P-SiC Nano Composite Depositions." *Journal of Graphic Era University* (2020): 71-77.

[25] Ram, Munna, Sulaxna Sharma, Aleem Ansari, and Awanish Kumar Sharma. "Surface modification of mild steel by electroless Ni-P-SiC nanocomposite coating and its corrosion and tribological resistance." In *AIP Conference Proceedings*, vol. 2335, no. 1, p. 080010. AIP Publishing LLC, 2021.

[26] William, T. BECKER, and J. S. Roch. "ASM Handbook Volume 11: Failure Analysis and Prevention." (2002): 827-1161.

[27] Callister Jr, William D., and David G. Rethwisch. *Fundamentals of materials science and engineering: an integrated approach*. John Wiley & Sons, 2020.

[28] Paredes, Marcelo, Vincent Grolleau, and Tomasz Wierzbicki. "On ductile fracture of 316L stainless steels at room and cryogenic temperature level: An engineering approach to determine material parameters." *Materialia* 10 (2020): 100624.

[29] Nani Babu, M., G. Sasikala, and K. Sadananda. "Analysis of fatigue crack growth behavior of SS 316 (N) welds using the unified approach." *Fatigue & Fracture of Engineering Materials & Structures* 43, no. 3 (2020): 527-538.

[30] Avanzini, Andrea. "Fatigue behavior of additively manufactured stainless steel 316L." *Materials* 16, no. 1 (2022): 65.

[31] Askeland, Donald R., Pradeep Prabhakar Phulé, Wendelin J. Wright, and D. K. Bhattacharya. "The science and engineering of materials." (2003): 357-374.

[32] Kassner, Michael E. *Fundamentals of creep in metals and alloys*. Butterworth-Heinemann, 2015

[33] Senhadji, F., Farid Belarifi, and François Robbe-Valloire. "Experimental investigation of friction coefficient and wear rate of brass and bronze under lubrication conditions." *Tribology in industry* 38, no. 1 (2016): 102-107.

[34] Collins, Jack A. *Failure of materials in mechanical design: analysis, prediction, prevention*. John Wiley & Sons, 1993.

[35] Sharma, Mala, Jeremy Schreiber, Timothy Eden, and Victor Champagne. "Stress corrosion cracking resistance of cold-sprayed Al 6061 deposits using a newly developed test fixture." *Coatings* 9, no. 7 (2019): 445.

[36] Ghiasi, Vahed, Husaini Omar, B. Zainuddin, Bujang K. Huat, Ratnasamy Muniandy, and Mohd Najmin Alias. "A New Model of Microcracks Propagation in Granite Rock." *Australian Journal of Basic and Applied Sciences* 1, no. 1 (2010): 1-23.

[37] Roberge, Pierre R. *Handbook of corrosion engineering*. McGraw-Hill Education, 2019. [38] Lee, Dong-Jun, You-Jin Kang, and Yong-Soo

Kima. "A Review on Stress Corrosion Cracking of Stainless Steel 316L in Oxygenated and Chlorinated Primary Water Chemistry." (2020).

[39] Stewart, Maurice. *Surface Production Operations: Volume 5: Pressure Vessels, Heat Exchangers, and Aboveground Storage Tanks: Design, Construction, Inspection, and Testing*. Gulf Professional Publishing, 2021.

[40] Fujii, Tomoyuki, Tatsuro Sawada, and Yoshinobu Shimamura. "Nucleation of stress corrosion cracking in aluminum alloy 6061 in sodium chloride solution: Mechanical and microstructural aspects." *Journal of Alloys and Compounds* (2022): 168583.

[41] Ahmad, Zaki. *Principles of corrosion engineering and corrosion control*. Elsevier, 2006.

[42] Rao, Sangeetha. "A Review of Chloride Stress Corrosion Cracking Factors for Austenitic Stainless Steel." *AMPP Annual Conference+ Expo* (2022).

[43] Cheng, Y. Frank. *Stress corrosion cracking of pipelines*. John Wiley & Sons, 2013.

[44] Loto, Cleophas Akintoye. "Stress corrosion cracking: characteristics, mechanisms and experimental study." *The International Journal of Advanced Manufacturing Technology* 93, no. 9 (2017): 3567-3582.

[45] Y. Frank Cheng (Author) " Stress Corrosion Cracking of Pipelines" 1st Edition (2020).

[46] James, M. N., D. G. Hattingh, and L. Matthews. "Embrittlement Failure of 51CrV4 Leaf Springs." *Engineering Failure Analysis* (2022): 106517.

[47] Hilti, A. G. "Corrosion Handbook." (2015).

[48] Revie, R. Winston. *Corrosion and corrosion control: an introduction to corrosion science and engineering*. John Wiley & Sons, 2008.

[49] Adamu, Mohammed, Lasisi Ejibunu Umoru, and Oladeji Oluremi Ige. "Effect of toluene and dioctylphthalate on the rebar corrosion of

medium carbon steel in seawater and cassava fluid." *Journal of Minerals and Materials Characterization and Engineering* 2, no. 1 (2014): 1-7.

[50] Muench, Falk. "Electroless plating of metal nanomaterials." *ChemElectroChem* 8, no. 16 (2021): 2993-3012.

[51] Campbell, Flake C., ed. *Elements of metallurgy and engineering alloys*. ASM International, 2008.

[52] Campbell, Flake C., ed. *Fatigue and fracture: understanding the basics*. ASM International, 2012.

[٥٣] حيدرحسن جابرجمال الدين (١٩٩٨م)"تحسين مقاومة التعرية لسبائك براص –الفا بواسطةالاضافات القليلة من بعض العناصر(Ge,Te,Al)"، رسالة ماجستير، الجامعة التكنولوجية

[54] Batchelor, Andrew W., Loh Nee Lam, and Margam Chandrasekaran. *Materials degradation and its control by surface engineering*. 3rd ed.London,World Scientific, 2011.

[55] Langill, Thomas J. "Corrosion Protection." *Basic corrosion theory and protection methods* (2006).

[56] Dillon, P. "Corrosion Handbook, No. 1: The Forms of Corrosion Recognition and Prevention." *NACE, Houston* (1982).

[57] Khalifeh, Alireza. "Stress corrosion cracking behavior of materials." *Eng. Fail. Anal* 10 (2020).

[58] Radhi, Nabaa S., Marwa Marza, and Zainab S. Al-Khafaji. "Modification of Nickel-phosphor Electroless Coatings by adding particles of Zirconia." *Solid State Technol* 63, no. 2 (2020).

[59] Parkinson, Ron. *Properties and applications of electroless nickel*. Vol. 37. Toronto: Nickel Development Institute, 1997.

[60] Kumar, Mayank, Tharra Bhavani, Sunil Rawal, and Ajay Sidpara. "Magnetorheological Finishing of Chemically Treated Electroless Nickel Plating." *Magnetochemistry* 8, no. 12 (2022): 184.

[61] Weil, Rolf, and Konrad Parker. "The properties of electroless nickel." *Electroless plating: fundamentals and applications* (1990): 111-137.

[62] Łosiewicz, B., Grzegorz Dercz, Magdalena Popczyk, Magdalena Szklarska, and Agnieszka Smołka. "Effect of Phosphorus on the Structure of Nickel Electrocoatings." In *Solid State Phenomena*, vol. 228, pp. 141-147. Trans Tech Publications Ltd, 2015.

[63] Alhaji, A., B. Sadeghi, and S. Kamali. "The effect of pre-heat and post-heat treatment on the hardness and blackening process of electroless NiP deposits on titanium alloy." *Surface Topography: Metrology and Properties* 8, no. 4 (2020): 045031.

[64] SESHADRI, KRISHNA RAM THOGULUVA. "Electroless Nickel Plating Formulation For Automotive And Mechanical Parts."

[65] Landolt, D. "Electrodeposition science and technology in the last quarter of the twentieth century." *Journal of the Electrochemical Society* 149, no. 3 (2002): S9.

[66] Sayyad, Farook, and Rohan Senanayake. "Experimental investigation on surface roughness of electroless Ni–B–TiO2 nanocomposite coatings." *Sādhanā* 46, no. 2 (2021): 1-5.

[67] Frontiers in Materials Science - Page 476 - Google Books B. Raj · 2005 · Materials

[68] Wu, Bo, Baizhao Tan, Guizhen Tan, Ming Zeng, Jinyi Luo, Guanghui Hu, Jiye Luo, Zhifeng Hao, Shaomei Lai, and Binyun Liu. "Electroless deposition of Ni–P/Au coating on Cu substrate with improved corrosion resistance from Au (iii)–DMH based cyanide-free plating bath using hypophosphite as a reducing agent." *RSC advances* 11, no. 62 (2021): 39153-39168.

[69] Sürdem, Sedat, Cihan Eseroğlu, and Ramazan Çitak. "A parametric study on the relationship between NaBH4 and tribological properties in the nickel-boron electroless depositions." *Materials Research Express* 6, no. 12 (2019): 125085.

[70] Mariani, F. “Electroless Deposition of NiP Alloys”, *School of Industrial and Information Engineering Master of Science in Materials Engineering and Nano-technology, Milano, Italy*(2017).

[71] Hassan, Kadhim and Abdulrheem " Investigation on corrosion and erosion -corrosion of nozzle ring in turbocharger heavy fuel engine"*MsC thes.,University of Babylon*,(2020).

[72] Taheri, Ray. "Evaluation of electroless nickel-phosphorus (EN) coatings." *Saskatoon: University of Saskatchewan Saskatoon* (2002).

[73] Delaunois, Fabienne, Veronique Vitry, and Luiza Bonin, eds. "*Electroless nickel plating: fundamentals to applications*." CRC Press,(2019).

[74] Shozib, Imtiaz Ahmed, Azlan Ahmad, Ahmad Majdi Abdul-Rani, and Mohammadali Beheshti. "A review on the corrosion resistance of electroless Ni-P based composite coatings and electrochemical corrosion testing methods." *Corrosion Reviews* 40, no. 1 (2022): 1-37.

[75] Tudela, Ignacio, Yi Zhang, Madan Pal, Ian Kerr, and Andrew J. Cobley. "Ultrasound-assisted electrodeposition of thin nickel-based composite coatings with lubricant particles." *Surface and Coatings Technology* 276 (2015): 89-105.

[76] Mallory, Glenn O., and Juan B. Hajdu, eds. *Electroless plating: fundamentals and applications*. William Andrew, 1990.

[77] Andersen, Simon I., and James G. Speight. "Petroleum resins: separation, character, and role in petroleum." *Petroleum science and technology* 19, no. 1-2 (2001): 1-34.

[78] Speight, James G. *Handbook of petrochemical Processes*. CRC Press, 2019.

[79] Davis, Joseph R., ed. *Alloy digest sourcebook: stainless steels*. ASM international, 2000.

[80] McGuire, Michael F. *Stainless steels for design engineers*. Asm International, 2008.

[81] Outokumpu Stainless, A. B. "Handbook of stainless steel." *Avesta Resarch Centre, Avesta, Sweden* (2013).

[82] Yang, Xiaojia, Menghao Liu, Zhiyong Liu, Cuiwei Du, and Xiaogang Li. "Failure analysis of a 304 stainless steel heat exchanger in

liquid sulfur recovery units." *Engineering Failure Analysis* 116 (2020): 104729.

[83] Zhou, Zhaoming, Dawen Gong, Zhong Zeng, and Tiejun Lin. "Failure analysis of a four-way flange erosioning in a KQ52 wellhead Christmas tree." *Engineering Failure Analysis* 129 (2021): 105641.

[84] Yan, Zhenxing, Lida Wang, Piji Zhang, Wen Sun, Zhengqing Yang, Bingyan Liu, Jisheng Tian, Xiangquan Shu, Yongpeng He, and Guichang Liu. "Failure analysis of Erosion-Corrosion of the bend pipe at sewage stripping units." *Engineering Failure Analysis* 129 (2021): 105675.

[85] Peng, Yi, Song Xue, Tao Yang, Xue Dong Liu, and Yi Ren. "Failure analysis of 316L stainless steel bellows serving in steam tube." *International Journal of Pressure Vessels and Piping* (2022): 104718.

[86] Rivaz, A., SH Mousavi Anijdan, M. Moazami-Goudarzi, A. Nazari Ghohroudi, and H. R. Jafarian. "Damage causes and failure analysis of a steam turbine blade made of martensitic stainless steel after 72,000 h of working." *Engineering Failure Analysis* 131 (2022): 105801.

[87] Wang, Haipeng, Yang Yang, Zhongna Yang, Zhigang Xu, Yuanyuan Chai, and Zhuwu Zhang. "Corrosion failure analysis of duplex stainless steel in marine environment." *Int. J. Electrochem. Sci* 17, no. 22055 (2022): 2.

[88] Mohapatra, J. N., Ravindra Kulkarni, D. Satish Kumar, and G. Balachandran. "Failure analysis of areal gas distribution skirt plate." *Engineering Failure Analysis* 131 (2022): 105885.

[89] Gokhale, Aditya, Anand Varma, Chetan Singh, Prahlad Halder, Jayant Jain, and Ravi Kumar Yadavalli. "Failure analysis of SS 304 HCu reheater tube of a supercritical power plant." *Engineering Failure Analysis* 137 (2022): 106244.

[90] Wang, Meng, Kai Guo, Yanhong Wei, Jicheng Chen, Chengming Cao, and Zhiwu Tong. "Failure analysis of cracking in the thin-walled pressure vessel of electric water heater." *Engineering Failure Analysis* 143 (2023): 106913.

[91] Smoljan, B., D. Iljkić, and M. Maretić. "Adhesivity of electroless Ni-P layer on austenitic stainless steel." *Archives of Materials Science* 54 (2016): 54.

[92] JEKLA, PODLAGI IZ AVSTENITNEGA NERJAVNEGA. "Heat treatment of electroless Ni-P layers on an austenitic stainless-steel substrate." *HEAT TREATMENT* 413 (2017): 417.

[93] Buchtík, Martin, Petr Kosár, Jaromír Wasserbauer, Jakub Tkacz, and Pavel Doležal. "Characterization of electroless Ni–P coating prepared on a wrought ZE10 magnesium alloy." *Coatings* 8, no. 3 (2018): 96.

[94] Fayyad, Eman M., Aboubakr M. Abdullah, Mohammad K. Hassan, Adel M. Mohamed, Chuhong Wang, George Jarjoura, and Zoheir Farhat. "Synthesis, characterization, and application of novel Ni-P-carbon nitride nanocomposites." *Coatings* 8, no. 1 (2018): 37.

[95] Kazimierczak, Honorata, Anna Wierzbicka-Miernik, Izabella Kwiecien, Maciej J. Szczerba, Anna Korneva, Michał Mosiałek, Krzysztof Miernik, and Joanna Wojewoda-Budka. "Electroless deposition of Ni–P and Ni–P–Re alloys from acidic hypophosphite baths." *Electrochimica Acta* 303 (2019): 157-166.

[96] Rajabalizadeh, Z., D. Seifzadeh, A. Khodayari, and Sh Sohrabnezhad. "Corrosion protection and mechanical properties of the electroless Ni-P-MOF nanocomposite coating on AM60B magnesium alloy." *Journal of Magnesium and Alloys* 10, no. 8 (2022): 2280-2295.

[97] Fu, Chenqi, Jinchun Sun, Ruijuan Guo, Lipeng Jiang, and Shun Xu. "Electroless Plating of Ni-P/Ni-Mo-P Duplex Coating on 16Mn Steel Weld Joint and its Corrosion Resistance in Natural Seawater." *Int. J. Electrochem. Sci* 17, no. 22078 (2022): 2.

[98] Kumar, Vikash, J. P. Singh, and Rabindra Kumar. "A Review on Hardness and Anti Corrosion Behavior of Steel Substrate By Electroless Coating of Ni-P and Ni-PB$_4$c." *Journal homepage: www. ijrpr. com ISSN* 2582: 7421(2022).

[99] Kumar, Kuldeep, Vakul Bansal, Sulaxna Sharma, Sanjeev Kimothi, and Awanish Sharma. "Microhardness and wear resistance of alkaline

electroless Ni-P/Ni-P-ZnO nanocomposite platings." *Materials Today: Proceedings* (2022).

[100] Fayyad, Eman M., Khouloud Jlassi, Mostafa H. Sliem, Fatma Nabhan, and Aboubakr M. Abdullah. "Design of highly anti-corrosive electroless plated Ni–P/modified halloysite nanotubes nanocomposite coating." *Journal of Materials Research and Technology* 24 (2023): 8014-8034.

[101] Li, Zhizhen, Chaoqun Bian, and Lingxia Hu. "Exploration of the Corrosion Behavior of Electroless Plated Ni-P Amorphous Alloys via X-ray Photoelectron Spectroscopy." *Molecules* 28, no. 1 (2023): 377.

[102] Khaira, Avinandan, Indrajit Shown, Satyanarayana Samireddi, Suman Mukhopadhyay, and Satyajit Chatterjee. "Mechanical and tribological characterization of deep eutectic solvent assisted electroless Ni–P-hBN coating." *Ceramics International* 49, no. 1 (2023): 461-473.

[103] Davoodi, Danial, Amir Hossein Emami, Sayed Mahmoud Monir Vaghefi, Mahdi Omidi, and Hamid Reza Bakhsheshi-Rad. "Deposition of electroless Ni–Cu–P coatings on L80 steel substrates and the effects of coatings thickness and heat treatment on the corrosion resistance." *International Journal of Pressure Vessels and Piping* 200 (2022): 104823.

[104] Biswas, Palash, Suman Kalyan Das, and Prasanta Sahoo. "Duplex electroless Ni-P/Ni-Cu-P coatings: Preparation, evaluation of microhardness, friction, wear, and corrosion performance." *Journal of Electrochemical Science and Engineering* 12, no. 6 (2022): 1261-1282.

[105] Biswas, Palash, Suman Kalyan Das, and Prasanta Sahoo. "Investigation of tribological and corrosion performance of duplex electroless Ni-P/Ni-Cu-P coatings." *Materials Today: Proceedings* (2022).

[106] Biswas, Palash, Suman Kalyan Das, and Prasanta Sahoo. "Role of heat treatment on the friction and wear behavior of duplex electroless nickel deposits." *Materials Today: Proceedings* 66 (2022): 3902-3909.

[107] Davoodi, Danial, Amir Hossein Emami, Sayed Mahmoud Monir Vaghefi, Mahdi Omidi, and Hamid Reza Bakhsheshi-Rad. "Investigation

of Microstructure and Mechanical Properties of Ni-Cu-P Coatings Deposited by the Electroless Method." *Journal of Advanced Materials and Processing* 10, no. 2 (2022): 3-10.

[108] Mukhopadhyay, Arkadeb, and Sarmila Sahoo. "A Grey-Fuzzy based approach for the optimization of corrosion resistance of rebars coated with ternary electroless nickel coatings." *Journal of Soft Computing in Civil Engineering* 6, no. 2 (2022): 107-127.

[109] Bhattacharyya, Suparna, Deviprasanna Mohanty, Prashant Kumar, Suman Kalyan Das, Prasanta Sahoo, Surya K. Pal, and Sudipto Chakraborty. "A corrosion and tribo-failure analysis of Ni-P-Cu coated mild steel (AISI-1040) at varied copper concentration." *Engineering Failure Analysis* 146 (2023): 107063.

[110] Zhang, Weizhi, Dandan Liao, Dezhi Tang, Enhou Han, and Jun Wang. "Study on corrosion behavior of Ni–P/Ni–Cu–P superhydrophobic composite coatings preparation on L360 steel by two-step method." *Journal of Materials Research and Technology* 23 (2023): 3035-3047

[111] Fayomi, Ojo Sunday Isaac, Adedamola Sode, Itopa Godwin Akande, Abimbola Patricia Idowu Popoola, and Oluranti Agboola. "Improving the structural properties and corrosion behaviour of electroless deposited Ni-P-Zn coatings on mild steel for advanced processes." *AIMS Materials Science* 7, no. 4 (2020): 441-452.

[112] Kilanko, O., O. S. I. Fayomi, and A. A. Sode. "Anticorrosion effect of silicon nitride and zirconium diboride composite on Ni–P–Zn electroless deposition on mild steel." *Journal of Bio-and Tribo-Corrosion* 6, no. 3 (2020): 1-9.

[113] Fu Chuan-qi,Huang Ya-zhong,Li. Sheng-jun,XiangYong-kuang."Study on Preparation and Corrosion Resistance of Ni-P/Ni-Zn-P Three-layer Composite Coating".*Surface Technology* 50,no.12(2021): 400-407

[114] Kao, Jin-Yih. "Optimization of Ni-Zn-P ternary alloy films fabricated using Grey-Taguchi design and control charts." *The International Journal of Advanced Manufacturing Technology* 122, no. 7 (2022): 3299-3310.

[115] Abdalla, K., H. Ibrahimb, Z. W. Sulaymanc, Y. A. Hamadd, and A. Khair-Aishae. "Effect of Process Time in the Deposition and Corrosion Resistance of Ni-Zn-P Coating Formed on Mild Steel Surface."(2022).

[116] Li, Po-Wei, Chung-Wei Hsu, Chong-Shen Yan, Chun-Yao Hsu, Ching-Hua Hung, and Jin-Yih Kao. "Structure and fatigue behavior of electroless plated Ni-Zn-P films using pretreatments, annealing and an applied magnetic field." *International Journal of Fatigue* 167 (2023): 107369.

[117] Dhakal, Dhani Ram, Gobinda Gyawali, Yuwaraj K. Kshetri, Jin-Hyuk Choi, and Soo Wohn Lee. "Influence of SiC and TiC nanoparticles reinforcement on the microstructure, tribological, and scratch resistance behavior of electroless Ni–P coatings." *Nanotechnology* 31, no. 10 (2019): 104001.

[118] Ram, Munna, Manoj Kumar, A. Ansari, Sulaxna Sharma, and Awanish Sharma. "Corrosion resistance of electroless Ni-P-SiC/Ni-P-TiO_2-ZrO_2 nano-coatings in paper mill bleach Plant." *Materials Today: Proceedings* 21 (2020): 1200-1212.

[119] Fu, Xiuqing, Feixiang Wang, Xinxin Chen, Jinran Lin, and Hongbing Cao. "Corrosion resistance of Ni–P/SiC and Ni–P composite coatings prepared by magnetic field-enhanced jet electrodeposition." *RSC advances* 10, no. 56 (2020): 34167-34176.

[120] Parthiban, K., Poovazhagan Lakshmanan, Sarangapani Palani, and Arun Arumugam. "Electroless deposition of SiC Nano Coating on Aluminium alloy and evaluation of wear resistance and electroless characteristics." *Materials Today: Proceedings* 46 (2021): 1096-1100.

[121] Chintada, Vinod Babu, Thirumala Rao Gurugubelli, and Ravindranadh Koutavarapu. "The impact of surfactants on the properties of electroless Ni–P–SiC coatings." *Materials Chemistry and Physics* 291 (2022): 126682.

[122] Uppada, Sudhakar, Ramji Koona, Vinod Babu Chintada, and Ravindranadh Koutavarapu. "Influence of heat treatment on crystal structure, microhardness and corrosion resistance of bilayer electroless Ni-P-SiC/Ni-P-Al_2O_3 Coatings." *Silicon* (2022): 1-11.

[123] Kumar, Santosh, Subrata Kumar Ghosh, Nitin Namdeo Pawar, Surendra Harichandra Rathod, Manoj Ashok Chaudhari, Raja Ram Bhagat, and Rohith Goli. "Design of Experiment with Tribological Performance Analysis of Electroless Nano-composite Ni-P-SiC Coating for Conveyors." *Tribology in Industry* 44, no. 4 (2022): 707.

[124] Jiaqiang, Gao, Liu Lei, Wu Yating, Shen Bin, and Hu Wenbin. "Electroless Ni–P–SiC composite coatings with superfine particles." *Surface and Coatings Technology* 200, no. 20-21 (2006): 5836-5842.

[125] ASTM.D4541-22" Standard Test Method for Pull-Off Strength of Coatings Using Portable Adhesion Testers". *ASTM*(2022).

[126] Astm, G. "Standard practice for calculation of corrosion rates and related information from electrochemical measurements." *G102-89* (2004).

[127] ASTM, ASTM. G73-10 "Standard Test Method for Liquid Impingement Erosion Using Rotating Apparatus". *ASTM: West Conshohocken, PA, USA* (2013).

[128]ASTM,ASTM. G30-97 "Standard Practice for Making and Using U-Bend Stress-Corrosion Test Specimens". *ASTM: PA, USA* (2015).

[129] Madenci, Erdogan, and Ibrahim Guven. *The finite element method and applications in engineering using ANSYS®*. Springer, 2015.

[130] Luis Hoyos. "Centrifugal Force Calculator" Hand book,Last updated: Jun 22, (2022).

[131] Arabani, M. R., and S. M. M. Vaghefi. "Effect of heat-treatment on hardness and adhesion of Ni–P coated 7075 aluminum alloys by electroless deposition process." In *15th IFHTSE–international federation for heat treatment and surface engineering congress*, pp. 457-61. 2006.

[132] Ma, Chunyang, Feifei Wu, Yumei Ning, Fafeng Xia, and Yongfu Liu. "Effect of heat treatment on structures and corrosion characteristics of electroless Ni–P–SiC nanocomposite coatings." *Ceramics International* 40, no. 7 (2014): 9279-9284.

[133] Esmailzadeh, Samaneh, Mahmood Aliofkhazraei, and Hossein Sarlak. "Interpretation of cyclic potentiodynamic polarization test results for study of corrosion behavior of metals: a review." *Protection of metals and physical chemistry of surfaces* 54 (2018): 976-989.

[134] Tasan, C. C., J. P. M. Hoefnagels, C. H. L. J. Ten Horn, and M. G. D. Geers. "Experimental analysis of strain path dependent ductile damage mechanics and forming limits." *Mechanics of materials* 41, no. 11 (2009): 1264-1276.

[135] Rodriguez-Ibabe, J. M., M. C. Revilla, N. Gonzalez, P. M. Lardizabal, D. C. J. Farrugia, Z. Husain, G. Claxton et al. "The prediction and avoidance of cracking in long products hot rolling (PACROLP Phase 2)." (2013).

[136] Jonas, John J., Chiradeep Ghosh, and Laszlo S. Toth. "The equivalent strain in high pressure torsion." *Materials Science and Engineering: A* 607 (2014): 530-535

[137] Kaur, Balwant, Parminder Kaur, and Ankush Kuamr Jain. "Analysis of deformation of RC beam with addition of fly ash: a Finite element based modeling." (2020).

Appendices

Appendix A

Chemical Composition for Base Alloy

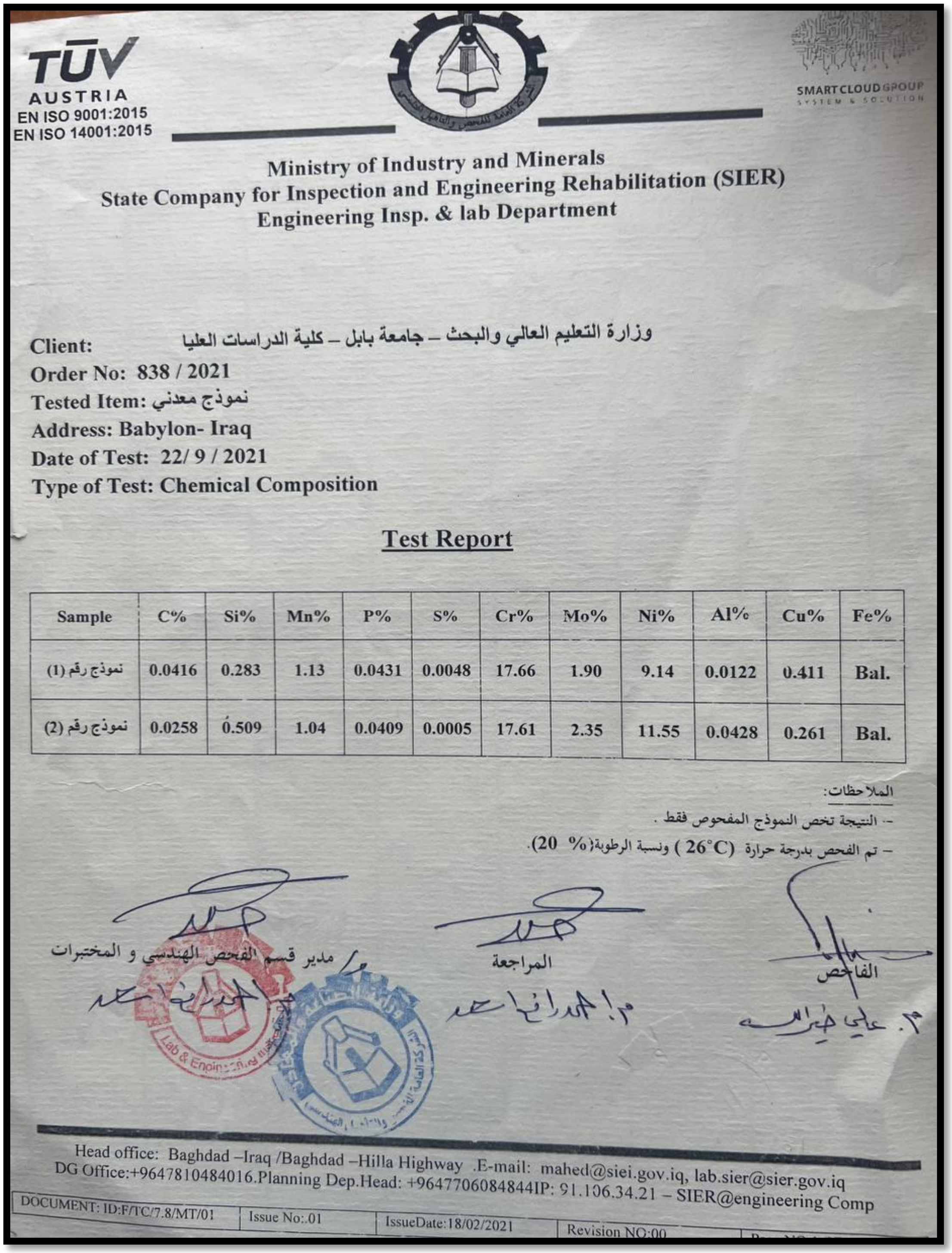

TÜV AUSTRIA
EN ISO 9001:2015
EN ISO 14001:2015

SMART CLOUD GROUP
SYSTEM & SOLUTION

Ministry of Industry and Minerals
State Company for Inspection and Engineering Rehabilitation (SIER)
Engineering Insp. & lab Department

Client: وزارة التعليم العالي والبحث – جامعة بابل – كلية الدراسات العليا
Order No: 838 / 2021
Tested Item: نموذج معدني
Address: Babylon- Iraq
Date of Test: 22/ 9 / 2021
Type of Test: Chemical Composition

Test Report

Sample	C%	Si%	Mn%	P%	S%	Cr%	Mo%	Ni%	Al%	Cu%	Fe%
نموذج رقم (1)	0.0416	0.283	1.13	0.0431	0.0048	17.66	1.90	9.14	0.0122	0.411	Bal.
نموذج رقم (2)	0.0258	0.509	1.04	0.0409	0.0005	17.61	2.35	11.55	0.0428	0.261	Bal.

الملاحظات:
- النتيجة تخص النموذج المفحوص فقط .
- تم الفحص بدرجة حرارة (26°C) ونسبة الرطوبة(% 20).

م/ مدير قسم الفحص الهندسي و المختبرات
م. أحمد رافع سعد

المراجعة
م. أحمد رافع سعد

الفاحص
م. علي خير الله

Head office: Baghdad –Iraq /Baghdad –Hilla Highway .E-mail: mahed@siei.gov.iq, lab.sier@sier.gov.iq
DG Office:+9647810484016.Planning Dep.Head: +9647706084844IP: 91.106.34.21 – SIER@engineering Comp

DOCUMENT: ID:F/TC/7.8/MT/01	Issue No:.01	IssueDate:18/02/2021	Revision NO:00

Appendix B

XRF for Corrosion Products

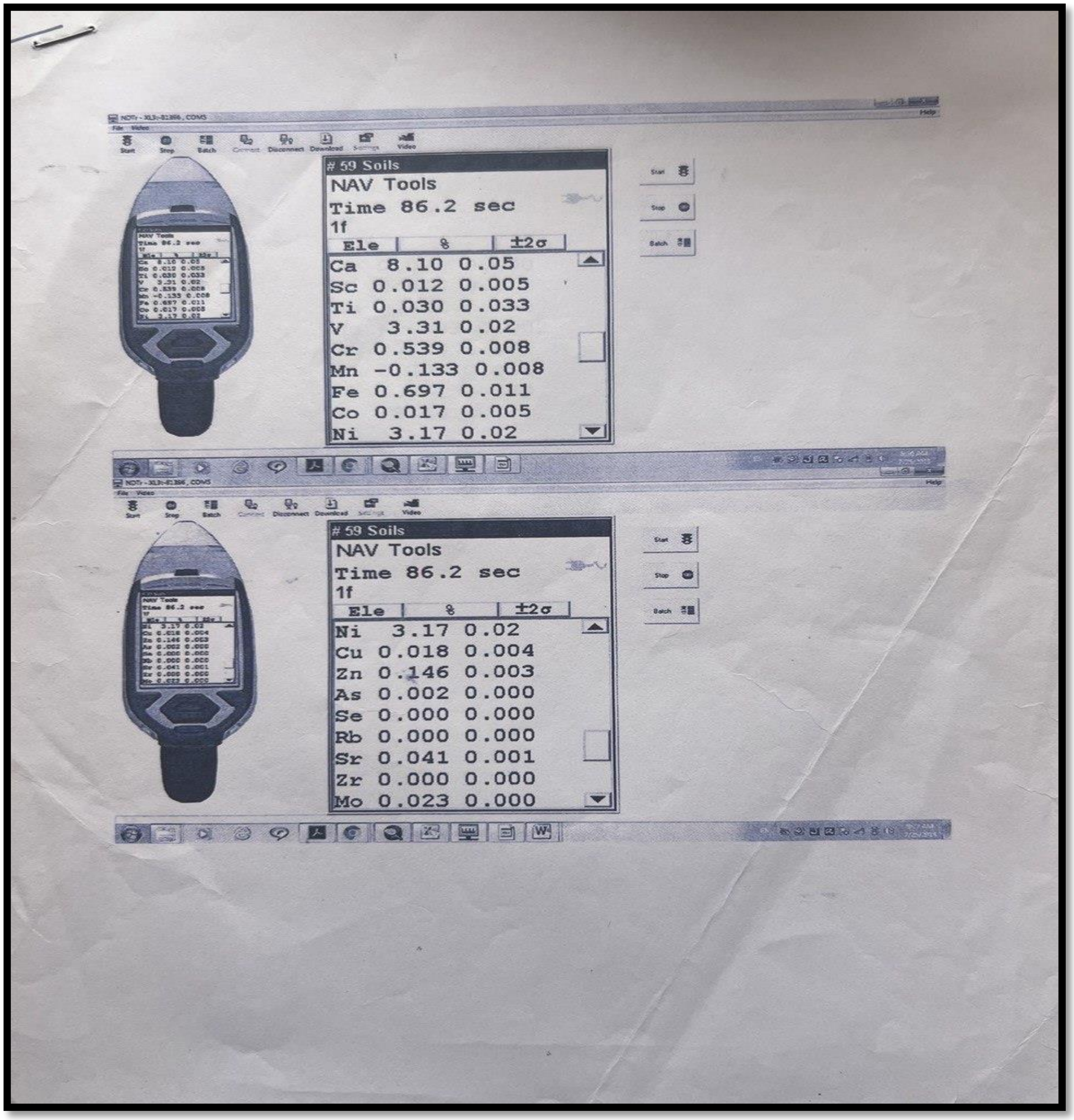

```
# 59 Soils
NAV Tools
Time 86.2 sec
1f
 Ele  |   %   | ±2σ
Ca   8.10 0.05
Sc 0.012 0.005
Ti 0.030 0.033
V    3.31 0.02
Cr 0.539 0.008
Mn -0.133 0.008
Fe 0.697 0.011
Co 0.017 0.005
Ni   3.17 0.02
```

```
# 59 Soils
NAV Tools
Time 86.2 sec
1f
 Ele  |   %   | ±2σ
Ni   3.17 0.02
Cu 0.018 0.004
Zn 0.146 0.003
As 0.002 0.000
Se 0.000 0.000
Rb 0.000 0.000
Sr 0.041 0.001
Zr 0.000 0.000
Mo 0.023 0.000
```

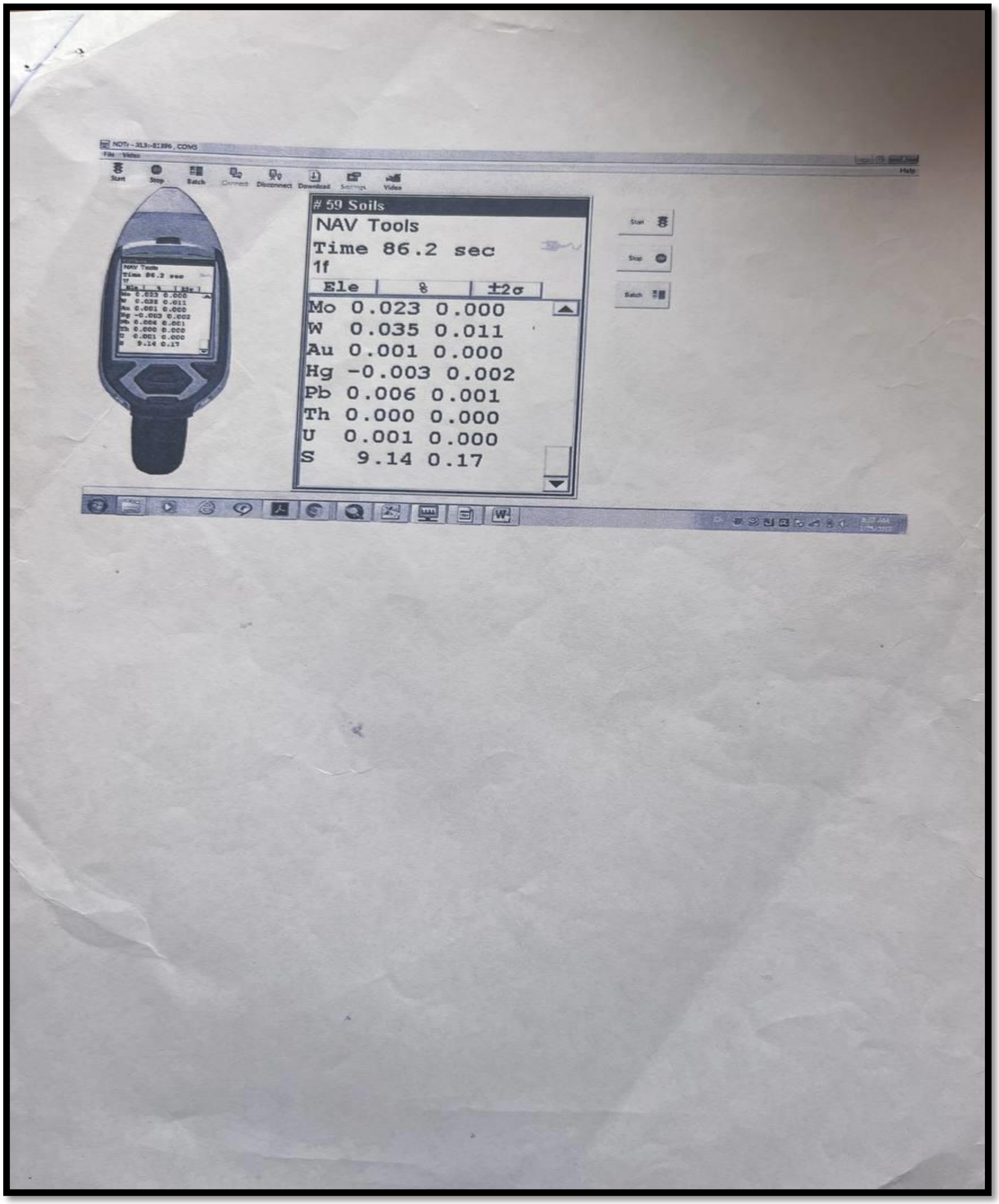

59 Soils

NAV Tools

Time 86.2 sec

1f

Ele	%	±2σ
Mo	0.023	0.000
W	0.035	0.011
Au	0.001	0.000
Hg	-0.003	0.002
Pb	0.006	0.001
Th	0.000	0.000
U	0.001	0.000
S	9.14	0.17

Appendix C

Heavy Fuel Analysis

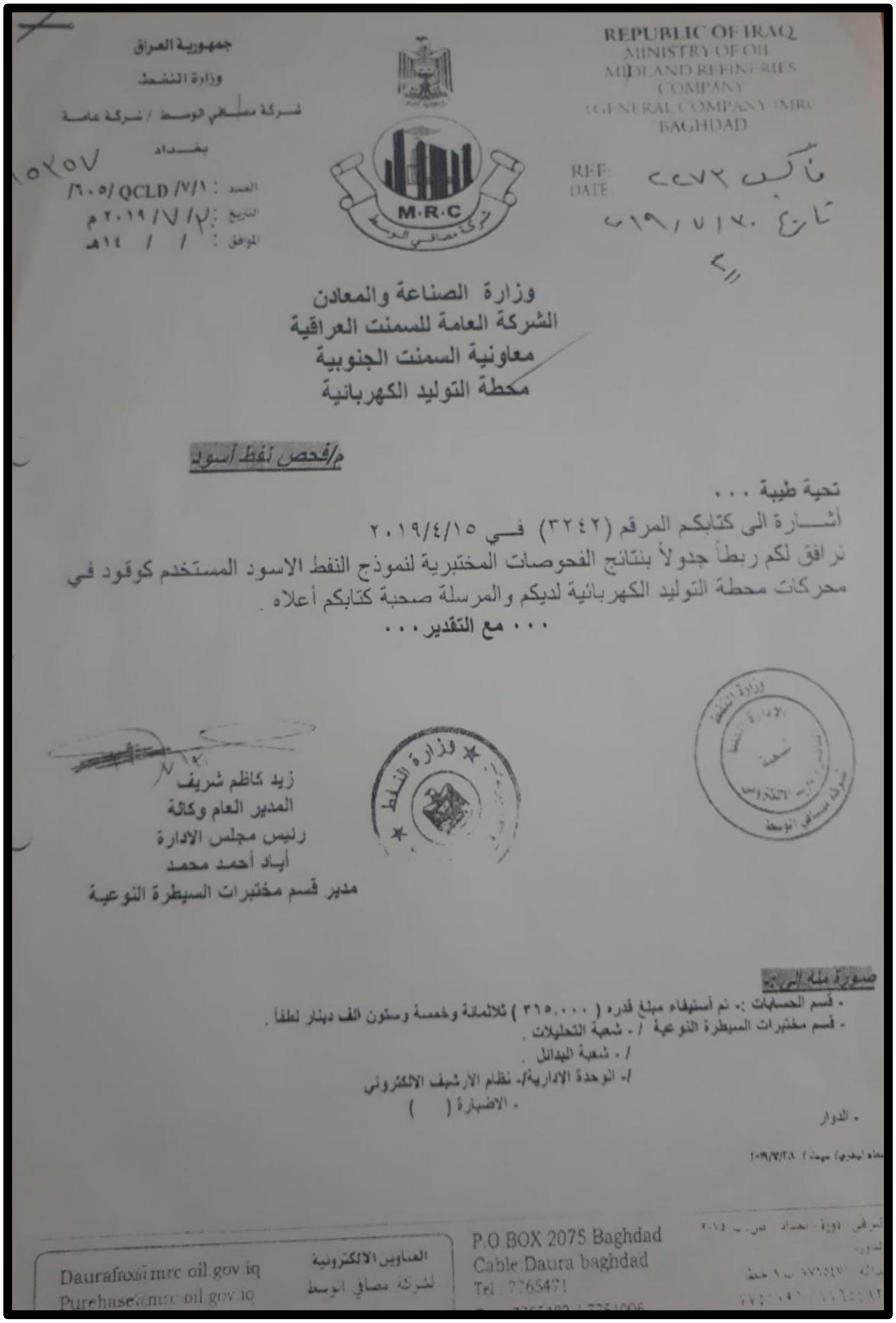

جمهورية العراق
وزارة النفط
شركة مصافي الوسط / شركة عامة
بغداد

REPUBLIC OF IRAQ
MINISTRY OF OIL
MIDLAND REFINERIES COMPANY
(GENERAL COMPANY) MRC
BAGHDAD

M·R·C
شركة مصافي الوسط

١٥٢٥٧
العدد : /٦٠٥/ QCLD /٧/١
التاريخ : ٢٠١٩/٧/٢ م
الموافق : / / ١٤ هـ

REF : ف/ كب ٢٢٧٢
DATE : تاريخ ٢٠١٩/٧/٢٠م

وزارة الصناعة والمعادن
الشركة العامة للسمنت العراقية
معاونية السمنت الجنوبية
محطة التوليد الكهربائية

م/فحص نفط أسود

تحية طيبة . . .

أشارة الى كتابكم المرقم (٣٢٤٢) في ٢٠١٩/٤/١٥
نرافق لكم ربطاً جدولاً بنتائج الفحوصات المختبرية لنموذج النفط الاسود المستخدم كوقود في محركات محطة التوليد الكهربائية لديكم والمرسلة صحبة كتابكم أعلاه .

. . . مع التقدير . . .

زيد كاظم شريف
المدير العام وكالة
رئيس مجلس الادارة

أياد أحمد محمد
مدير قسم مختبرات السيطرة النوعية

صورة منه الى :
- قسم الحسابات :- تم أستيفاء مبلغ قدره (٣٦٥,٠٠٠) ثلاثمائة وخمسة وستون الف دينار لطفاً .
- قسم مختبرات السيطرة النوعية / - شعبة التحليلات .
/ - شعبة البدائل .
/- الوحدة الادارية/- نظام الأرشيف الالكتروني
- الاضبارة ( )
- الدوار

[illegible] ٢٠١٩/٧/٢٨

العراق دورة بغداد ص.ب ٢٠٧٥
[illegible]

العناوين الالكترونية
لشركة مصافي الوسط
Daurafax@mrc.oil.gov.iq
Purchase@mrc.oil.gov.iq

P.O BOX 2075 Baghdad
Cable Daura baghdad
Tel : 7765471

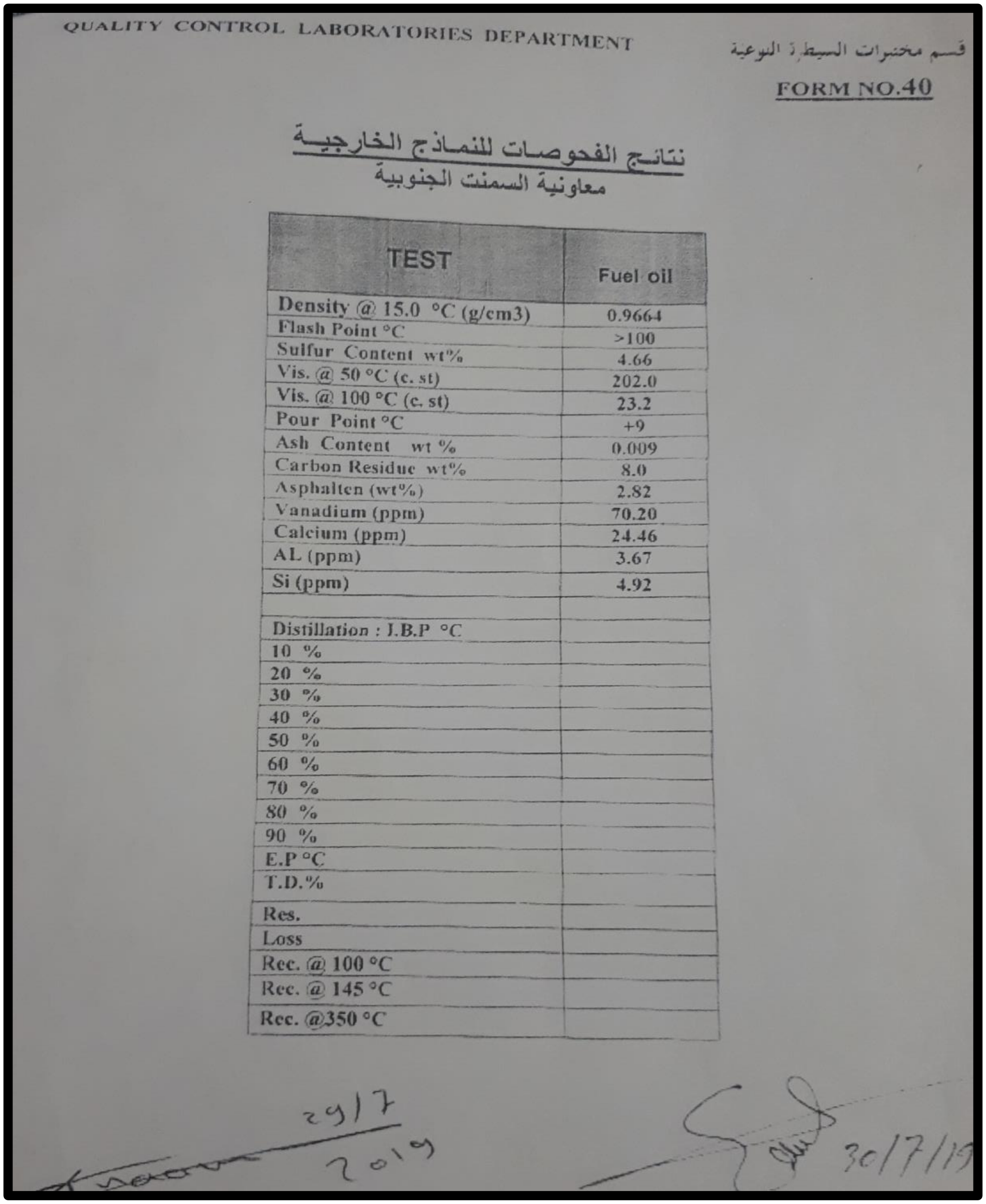

QUALITY CONTROL LABORATORIES DEPARTMENT

قسم مختبرات السيطرة النوعية

FORM NO.40

نتائج الفحوصات للنماذج الخارجية

معاونية السمنت الجنوبية

TEST	Fuel oil
Density @ 15.0 °C (g/cm3)	0.9664
Flash Point °C	>100
Sulfur Content wt%	4.66
Vis. @ 50 °C (c. st)	202.0
Vis. @ 100 °C (c. st)	23.2
Pour Point °C	+9
Ash Content wt %	0.009
Carbon Residue wt%	8.0
Asphalten (wt%)	2.82
Vanadium (ppm)	70.20
Calcium (ppm)	24.46
AL (ppm)	3.67
Si (ppm)	4.92
Distillation : I.B.P °C	
10 %	
20 %	
30 %	
40 %	
50 %	
60 %	
70 %	
80 %	
90 %	
E.P °C	
T.D.%	
Res.	
Loss	
Rec. @ 100 °C	
Rec. @ 145 °C	
Rec. @350 °C	

29/7
2019

30/7/19

Appendix D

Standard XRD Charts of Major Phases

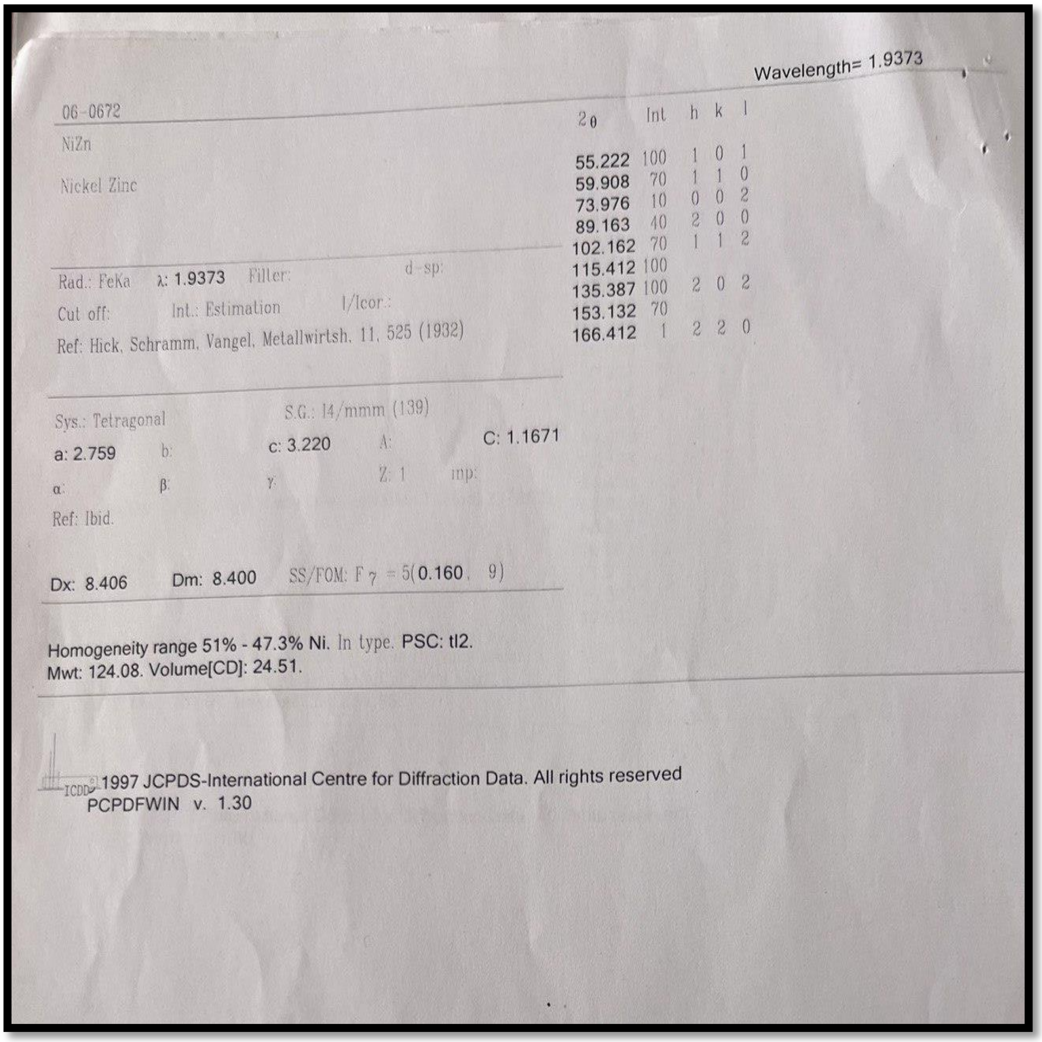

Wavelength= 1.9373

06-0672

NiZn

Nickel Zinc

Rad.: FeKa λ: 1.9373 Filter: d-sp:

Cut off: Int.: Estimation I/Icor.:

Ref: Hick, Schramm, Vangel, Metallwirtsh. 11, 525 (1932)

Sys.: Tetragonal S.G.: I4/mmm (139)

a: 2.759 b: c: 3.220 A: C: 1.1671

α: β: γ: Z: 1 mp:

Ref: Ibid.

Dx: 8.406 Dm: 8.400 SS/FOM: F_7 = 5(0.160, 9)

Homogeneity range 51% - 47.3% Ni. In type. PSC: tI2.
Mwt: 124.08. Volume[CD]: 24.51.

2θ	Int	h	k	l
55.222	100	1	0	1
59.908	70	1	1	0
73.976	10	0	0	2
89.163	40	2	0	0
102.162	70	1	1	2
115.412	100			
135.387	100	2	0	2
153.132	70			
166.412	1	2	2	0

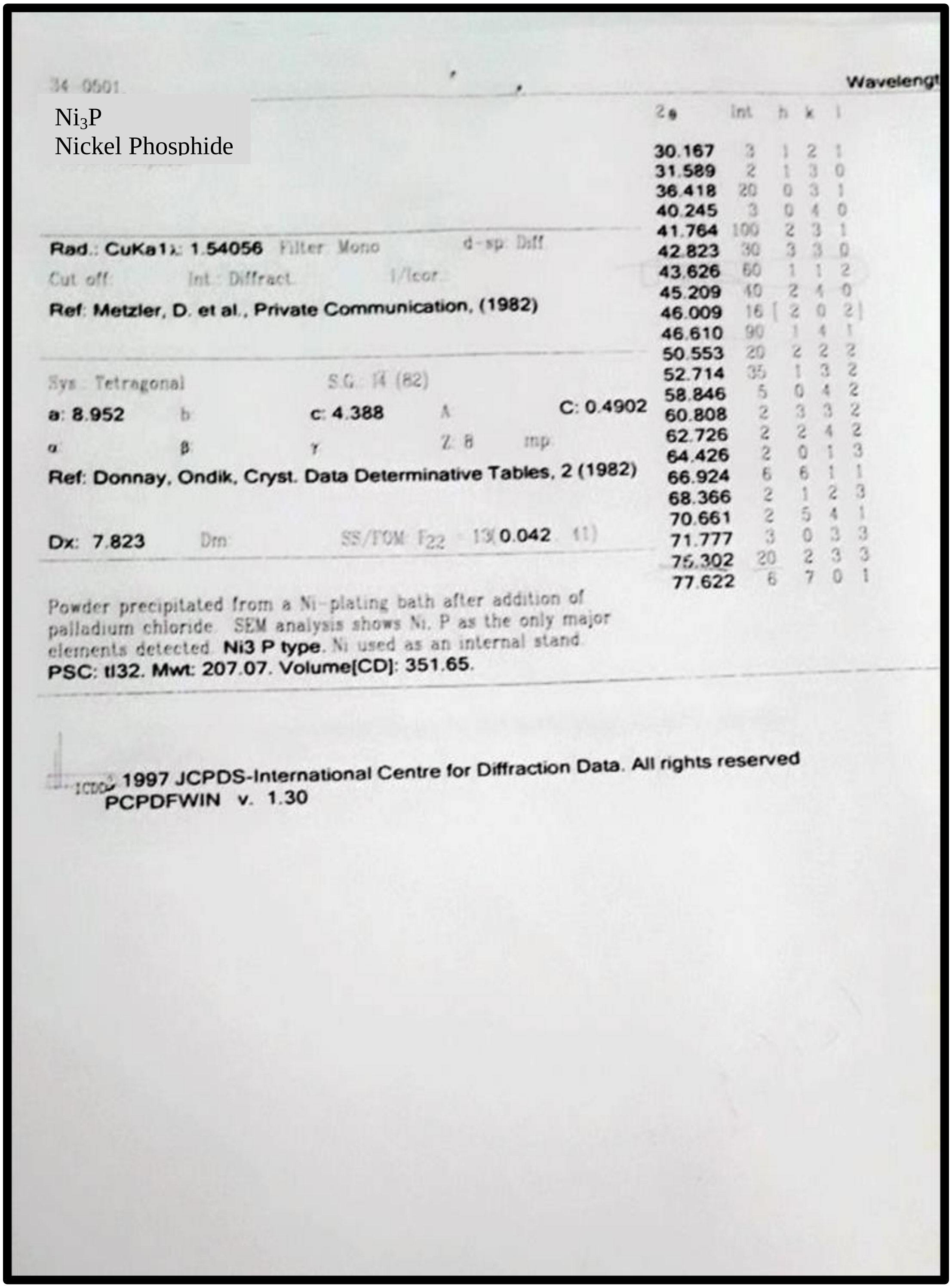

34-0501

Ni_3P
Nickel Phosphide

Wavelengt

Rad.: CuKa1λ: 1.54056 Filter: Mono d-sp: Diff
Cut off: Int.: Diffract. I/Icor.:
Ref: Metzler, D. et al., Private Communication, (1982)

Sys.: Tetragonal S.G.: I4 (82)
a: 8.952 b: c: 4.388 A: C: 0.4902
α: β: γ: Z: 8 mp:
Ref: Donnay, Ondik, Cryst. Data Determinative Tables, 2 (1982)

Dx: 7.823 Dm: SS/FOM: F_{22} = 13(0.042 , 41)

Powder precipitated from a Ni-plating bath after addition of palladium chloride. SEM analysis shows Ni, P as the only major elements detected. Ni3 P type. Ni used as an internal stand.
PSC: tI32. Mwt: 207.07. Volume[CD]: 351.65.

2θ	Int	h	k	l
30.167	3	1	2	1
31.589	2	1	3	0
36.418	20	0	3	1
40.245	3	0	4	0
41.764	100	2	3	1
42.823	30	3	3	0
43.626	60	1	1	2
45.209	40	2	4	0
46.009	16	2	0	2
46.610	90	1	4	1
50.553	20	2	2	2
52.714	35	1	3	2
58.846	5	0	4	2
60.808	2	3	3	2
62.726	2	2	4	2
64.426	2	0	1	3
66.924	6	6	1	1
68.366	2	1	2	3
70.661	2	5	4	1
71.777	3	0	3	3
75.302	20	2	3	3
77.622	6	7	0	1

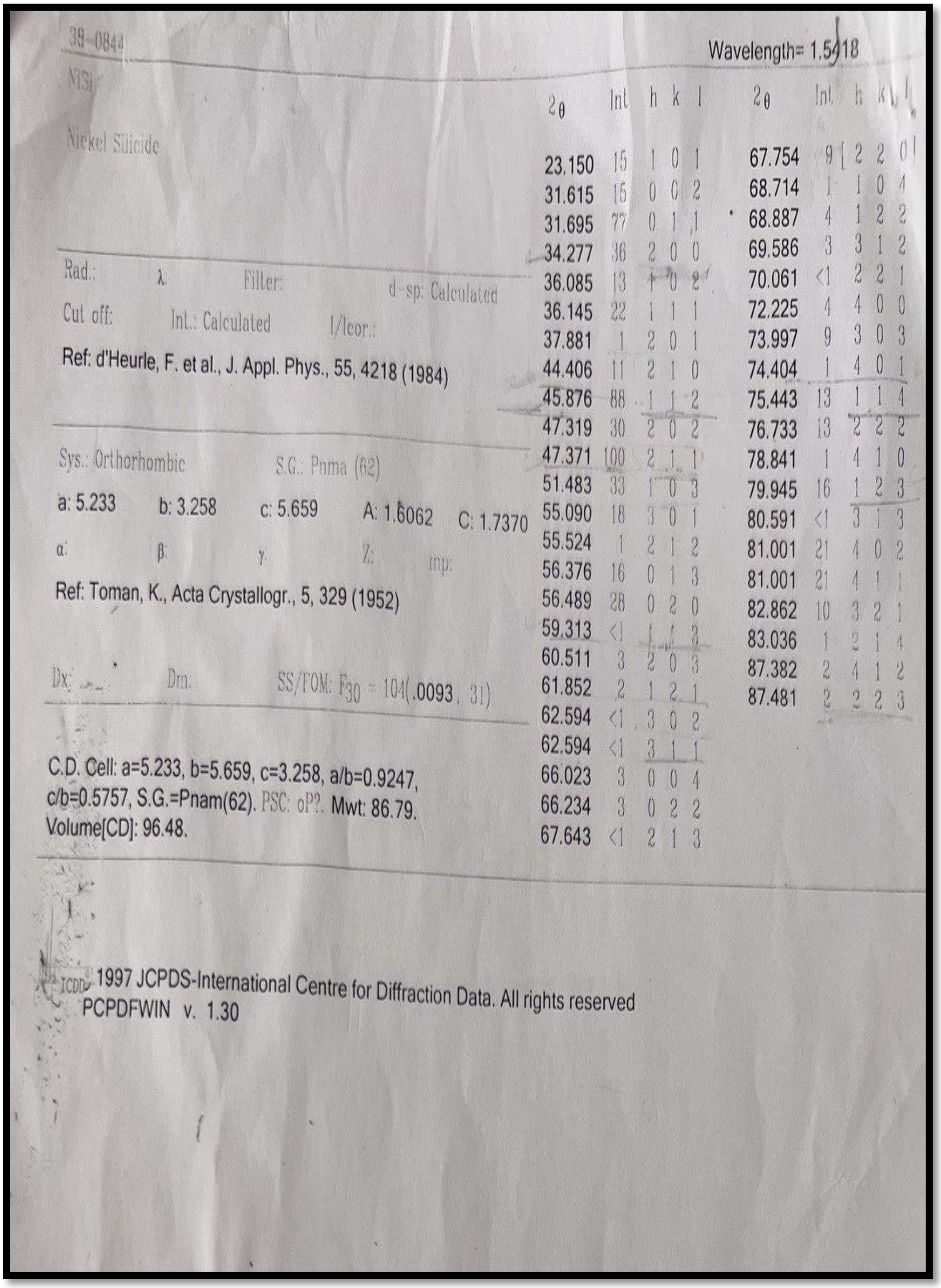

38-0844

NiSi

Nickel Silicide

Rad.: λ: Filter: d-sp: Calculated

Cut off: Int.: Calculated I/Icor.:

Ref: d'Heurle, F. et al., J. Appl. Phys., 55, 4218 (1984)

Sys.: Orthorhombic S.G.: Pnma (62)

a: 5.233 b: 3.258 c: 5.659 A: 1.6062 C: 1.7370

α: β: γ: Z: mp:

Ref: Toman, K., Acta Crystallogr., 5, 329 (1952)

Dx: Dm: SS/FOM: F_{30} = 104(.0093, 31)

C.D. Cell: a=5.233, b=5.659, c=3.258, a/b=0.9247, c/b=0.5757, S.G.=Pnam(62). PSC: oP?. Mwt: 86.79. Volume[CD]: 96.48.

Wavelength= 1.5418

2θ	Int	h	k	l
23.150	15	1	0	1
31.615	15	0	0	2
31.695	77	0	1	1
34.277	36	2	0	0
36.085	13	1	0	2
36.145	22	1	1	1
37.881	1	2	0	1
44.406	11	2	1	0
45.876	88	1	1	2
47.319	30	2	0	2
47.371	100	2	1	1
51.483	33	1	0	3
55.090	18	3	0	1
55.524	1	2	1	2
56.376	16	0	1	3
56.489	28	0	2	0
59.313	<1	1	1	3
60.511	3	2	0	3
61.852	2	1	2	1
62.594	<1	3	0	2
62.594	<1	3	1	1
66.023	3	0	0	4
66.234	3	0	2	2
67.643	<1	2	1	3
67.754	9	2	2	0
68.714	1	1	0	4
68.887	4	1	2	2
69.586	3	3	1	2
70.061	<1	2	2	1
72.225	4	4	0	0
73.997	9	3	0	3
74.404	1	4	0	1
75.443	13	1	1	4
76.733	13	2	2	2
78.841	1	4	1	0
79.945	16	1	2	3
80.591	<1	3	1	3
81.001	21	4	0	2
81.001	21	4	1	1
82.862	10	3	2	1
83.036	1	2	1	4
87.382	2	4	1	2
87.481	2	2	2	3

PCPDFWIN v. 1.30

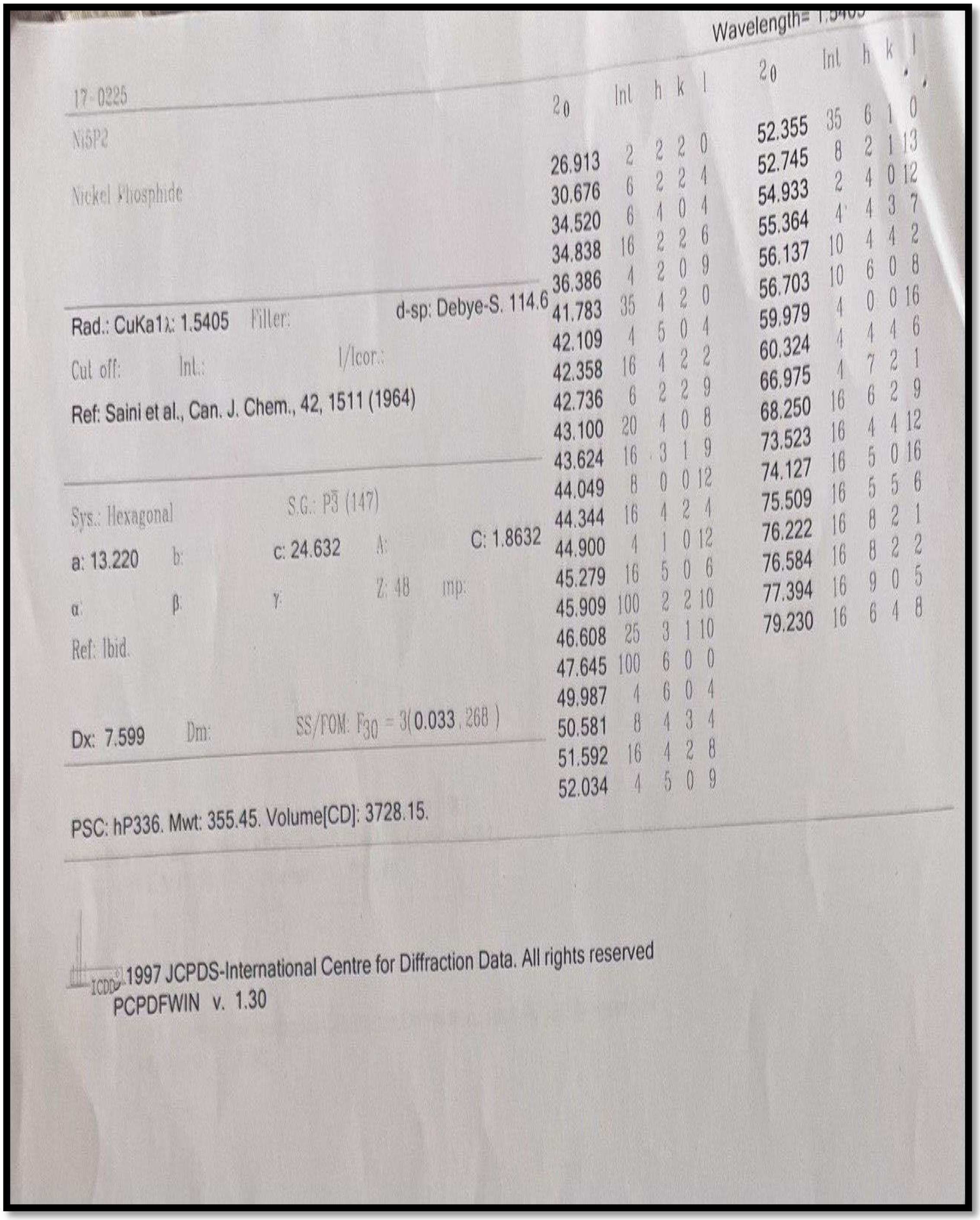

17-0225

Ni5P2

Nickel Phosphide

Wavelength= 1.5405

Rad.: CuKa1λ: 1.5405 Filter: d-sp: Debye-S. 114.6

Cut off: Int.: I/Icor.:

Ref: Saini et al., Can. J. Chem., 42, 1511 (1964)

Sys.: Hexagonal S.G.: P$\bar{3}$ (147)

a: 13.220 b: c: 24.632 A: C: 1.8632

α: β: γ: Z: 48 mp:

Ref: Ibid.

Dx: 7.599 Dm: SS/FOM: F_{30} = 3(0.033, 268)

PSC: hP336. Mwt: 355.45. Volume[CD]: 3728.15.

2θ	Int	h	k	l	2θ	Int	h	k	l
26.913	2	2	2	0	52.355	35	6	1	0
30.676	6	2	2	4	52.745	8	2	1	13
34.520	6	4	0	4	54.933	2	4	0	12
34.838	16	2	2	6	55.364	4	4	3	7
36.386	4	2	0	9	56.137	10	4	4	2
41.783	35	4	2	0	56.703	10	6	0	8
42.109	4	5	0	4	59.979	4	0	0	16
42.358	16	4	2	2	60.324	4	4	4	6
42.736	6	2	2	9	66.975	4	7	2	1
43.100	20	4	0	8	68.250	16	6	2	9
43.624	16	3	1	9	73.523	16	4	4	12
44.049	8	0	0	12	74.127	16	5	0	16
44.344	16	4	2	4	75.509	16	5	5	6
44.900	4	1	0	12	76.222	16	8	2	1
45.279	16	5	0	6	76.584	16	8	2	2
45.909	100	2	2	10	77.394	16	9	0	5
46.608	25	3	1	10	79.230	16	6	4	8
47.645	100	6	0	0					
49.987	4	6	0	4					
50.581	8	4	3	4					
51.592	16	4	2	8					
52.034	4	5	0	9					

ICDD ©1997 JCPDS-International Centre for Diffraction Data. All rights reserved
PCPDFWIN v. 1.30

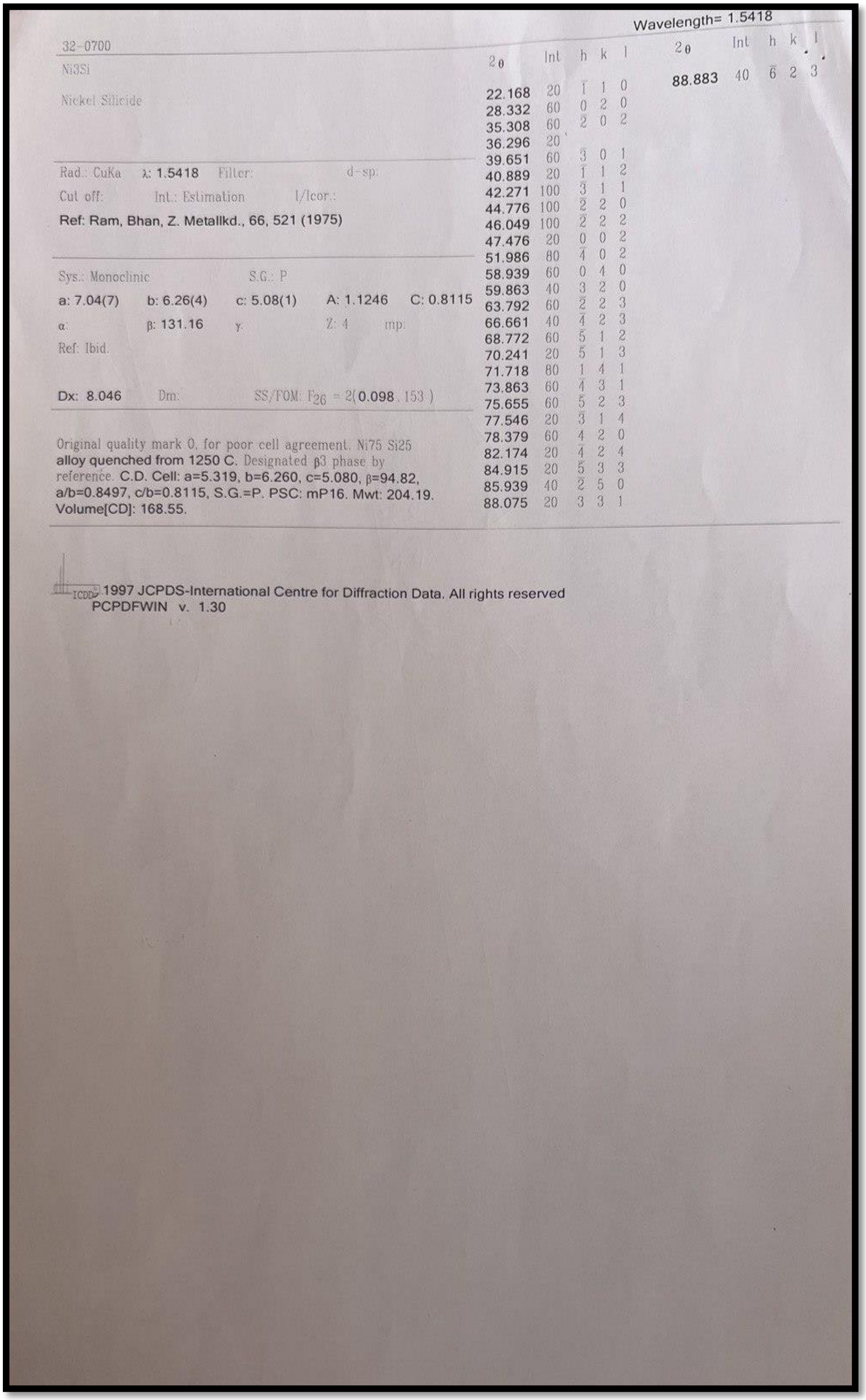

32-0700

Ni_3Si

Nickel Silicide

Rad.: CuKa λ: 1.5418 Filter: d-sp:

Cut off: Int.: Estimation I/Icor.:

Ref: Ram, Bhan, Z. Metallkd., 66, 521 (1975)

Sys.: Monoclinic S.G.: P

a: 7.04(7) b: 6.26(4) c: 5.08(1) A: 1.1246 C: 0.8115

α: β: 131.16 γ: Z: 4 mp:

Ref: Ibid.

Dx: 8.046 Dm: SS/FOM: F_{26} = 2(0.098 , 153)

Original quality mark 0, for poor cell agreement. Ni75 Si25 alloy quenched from 1250 C. Designated β3 phase by reference. C.D. Cell: a=5.319, b=6.260, c=5.080, β=94.82, a/b=0.8497, c/b=0.8115, S.G.=P. PSC: mP16. Mwt: 204.19. Volume[CD]: 168.55.

Wavelength= 1.5418

2θ	Int	h	k	l
22.168	20	$\bar{1}$	1	0
28.332	60	0	2	0
35.308	60	$\bar{2}$	0	2
36.296	20			
39.651	60	$\bar{3}$	0	1
40.889	20	$\bar{1}$	1	2
42.271	100	$\bar{3}$	1	1
44.776	100	$\bar{2}$	2	0
46.049	100	$\bar{2}$	2	2
47.476	20	0	0	2
51.986	80	$\bar{4}$	0	2
58.939	60	0	4	0
59.863	40	3	2	0
63.792	60	$\bar{2}$	2	3
66.661	40	$\bar{4}$	2	3
68.772	60	$\bar{5}$	1	2
70.241	20	$\bar{5}$	1	3
71.718	80	$\bar{1}$	4	1
73.863	60	$\bar{4}$	3	1
75.655	60	$\bar{5}$	2	3
77.546	20	$\bar{3}$	1	4
78.379	60	4	2	0
82.174	20	$\bar{4}$	2	4
84.915	20	5	3	3
85.939	40	$\bar{2}$	5	0
88.075	20	3	3	1
88.883	40	$\bar{6}$	2	3

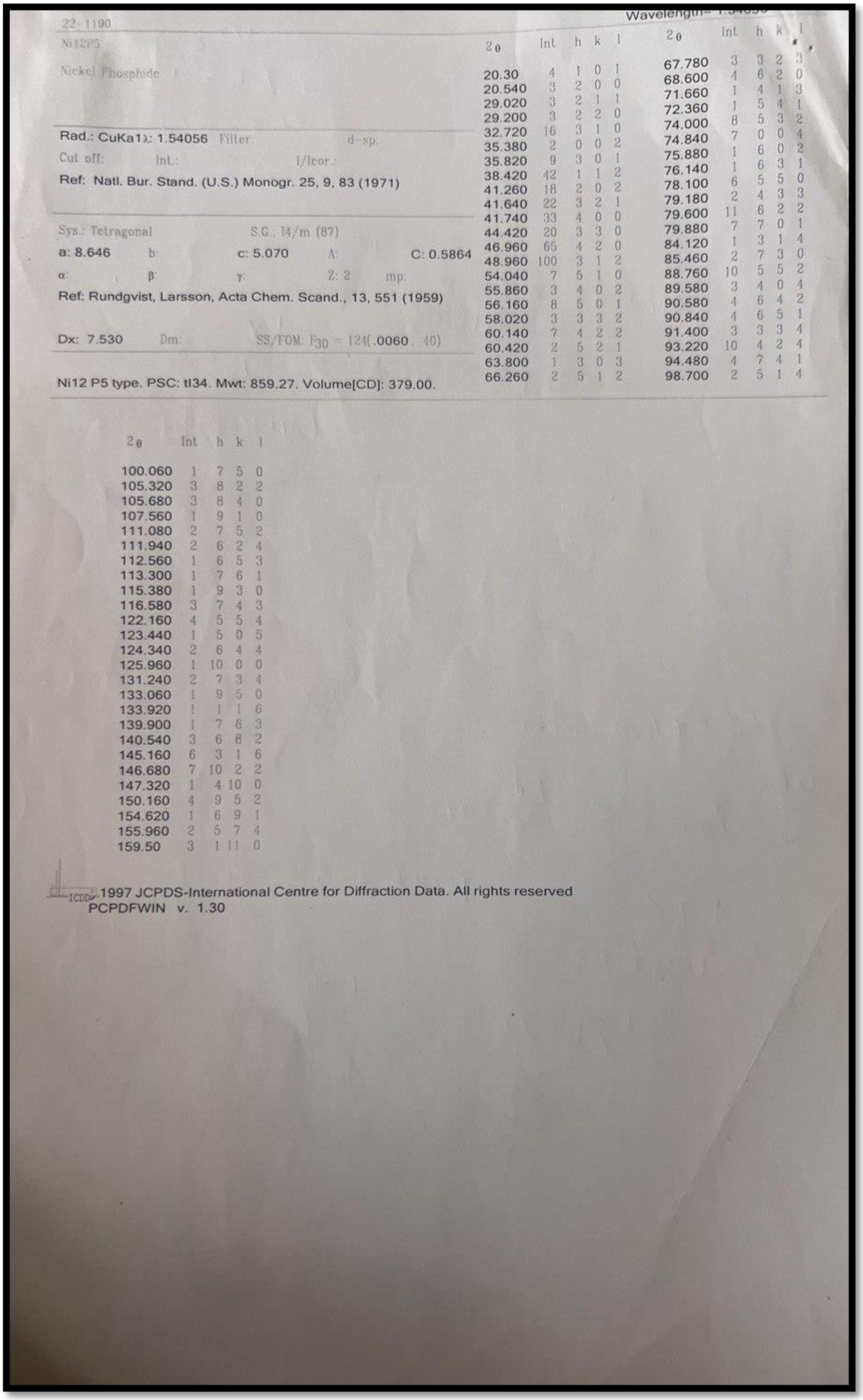

22-1190

$Ni_{12}P_5$

Nickel Phosphide

Wavelength=

Rad.: CuKa1λ: 1.54056 Filter: d-sp:

Cut off: Int.: I/Icor.:

Ref: Natl. Bur. Stand. (U.S.) Monogr. 25, 9, 83 (1971)

Sys.: Tetragonal S.G.: I4/m (87)

a: 8.646 b: c: 5.070 A: C: 0.5864

α: β: γ: Z: 2 mp:

Ref: Rundgvist, Larsson, Acta Chem. Scand., 13, 551 (1959)

Dx: 7.530 Dm: SS/FOM: F_{30} = 124(.0060, 40)

Ni12 P5 type. PSC: tI34. Mwt: 859.27. Volume[CD]: 379.00.

2θ	Int	h	k	l	2θ	Int	h	k	l
20.30	4	1	0	1	67.780	3	3	2	3
20.540	3	2	0	0	68.600	4	6	2	0
29.020	3	2	1	1	71.660	1	4	1	3
29.200	3	2	2	0	72.360	1	5	4	1
32.720	16	3	1	0	74.000	8	5	3	2
35.380	2	0	0	2	74.840	7	0	0	4
35.820	9	3	0	1	75.880	1	6	0	2
38.420	42	1	1	2	76.140	1	6	3	1
41.260	18	2	0	2	78.100	6	5	5	0
41.640	22	3	2	1	79.180	2	4	3	3
41.740	33	4	0	0	79.600	11	6	2	2
44.420	20	3	3	0	79.880	7	7	0	1
46.960	65	4	2	0	84.120	1	3	1	4
48.960	100	3	1	2	85.460	2	7	3	0
54.040	7	5	1	0	88.760	10	5	5	2
55.860	3	4	0	2	89.580	3	4	0	4
56.160	8	5	0	1	90.580	4	6	4	2
58.020	3	3	3	2	90.840	4	6	5	1
60.140	7	4	2	2	91.400	3	3	3	4
60.420	2	5	2	1	93.220	10	4	2	4
63.800	1	3	0	3	94.480	4	7	4	1
66.260	2	5	1	2	98.700	2	5	1	4

2θ	Int	h	k	l
100.060	1	7	5	0
105.320	3	8	2	2
105.680	3	8	4	0
107.560	1	9	1	0
111.080	2	7	5	2
111.940	2	6	2	4
112.560	1	6	5	3
113.300	1	7	6	1
115.380	1	9	3	0
116.580	3	7	4	3
122.160	4	5	5	4
123.440	1	5	0	5
124.340	2	6	4	4
125.960	1	10	0	0
131.240	2	7	3	4
133.060	1	9	5	0
133.920	1	1	1	6
139.900	1	7	6	3
140.540	3	6	8	2
145.160	6	3	1	6
146.680	7	10	2	2
147.320	1	4	10	0
150.160	4	9	5	2
154.620	1	6	9	1
155.960	2	5	7	4
159.50	3	1	11	0

Appendix E

Polarization Curves for Bare and Coated Specimens

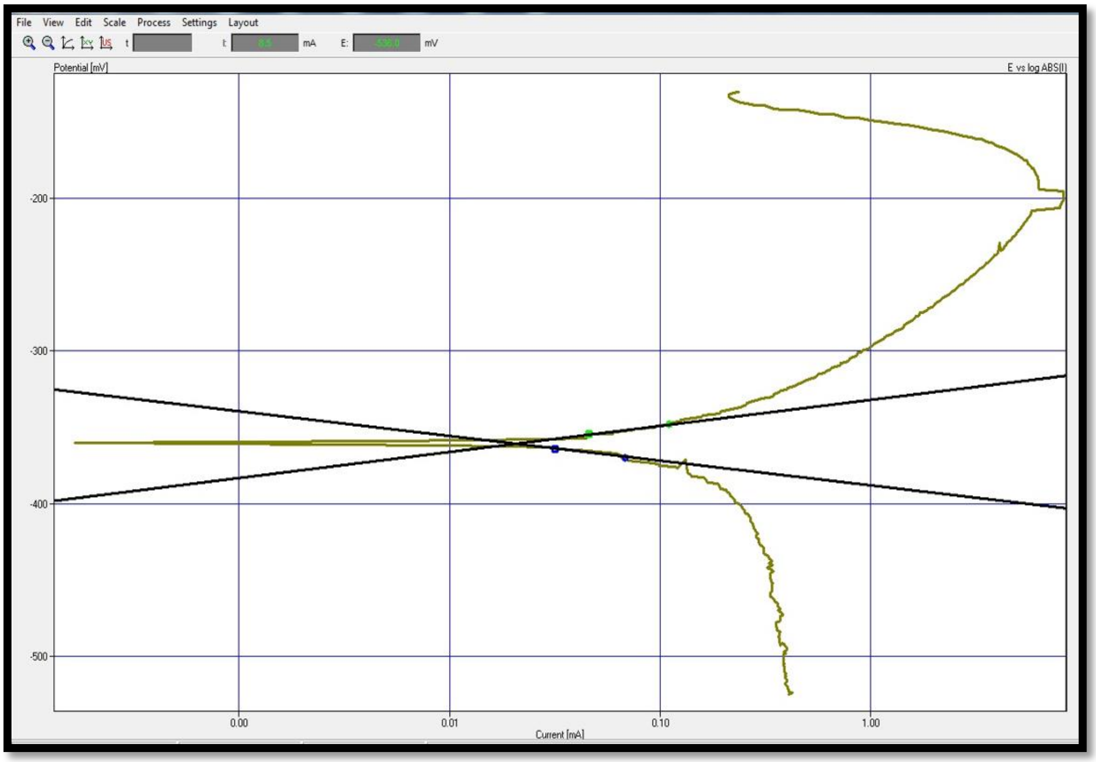

Figure 1: Polarization Curve for Bare Specimen

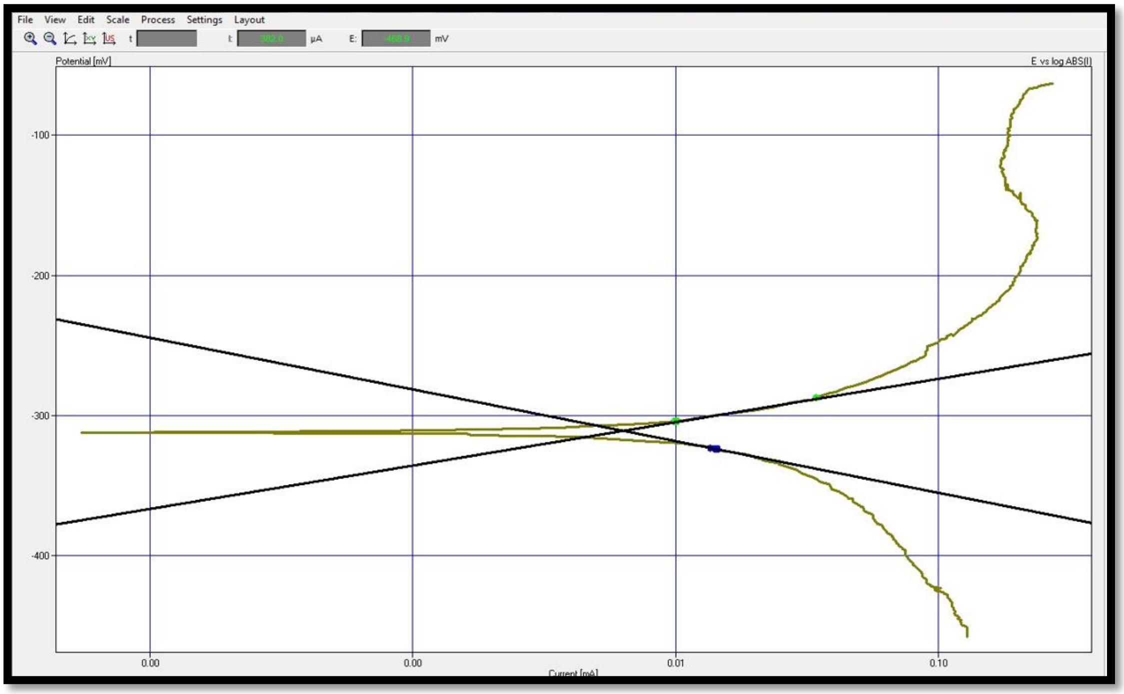

Figure 2: Polarization Curve for Coated Specimen by Ni-P (1-hr.Coating Time)

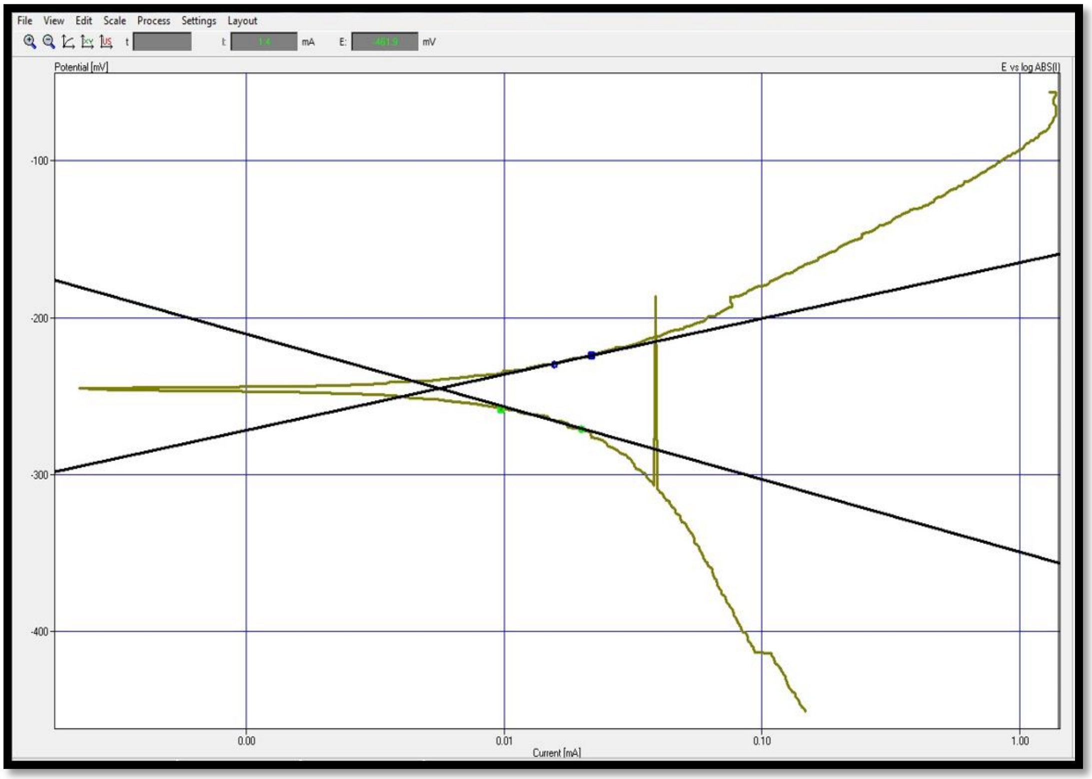

Figure 3: Polarization Curve for Coated Specimen by Ni-P(2-hrs.Coating Time)

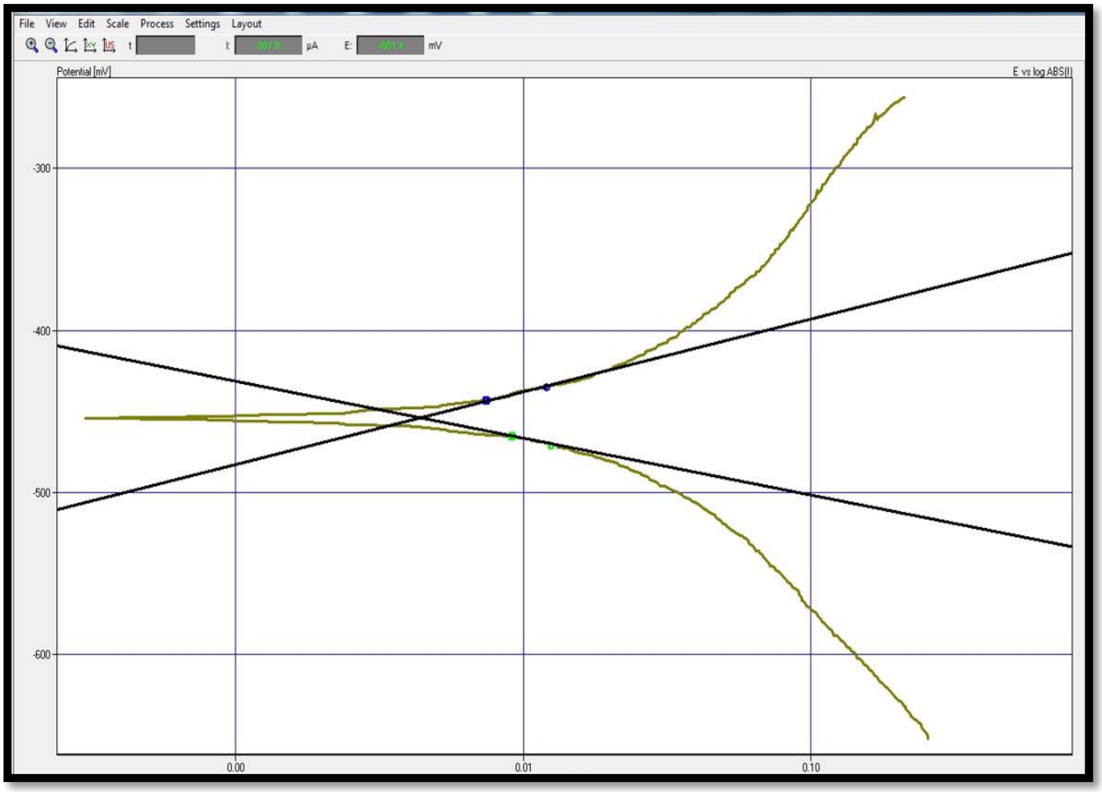

Figure 4: Polarization Curve for Coated Specimen by Ni-Cu-P(1-hr.Coating Time)

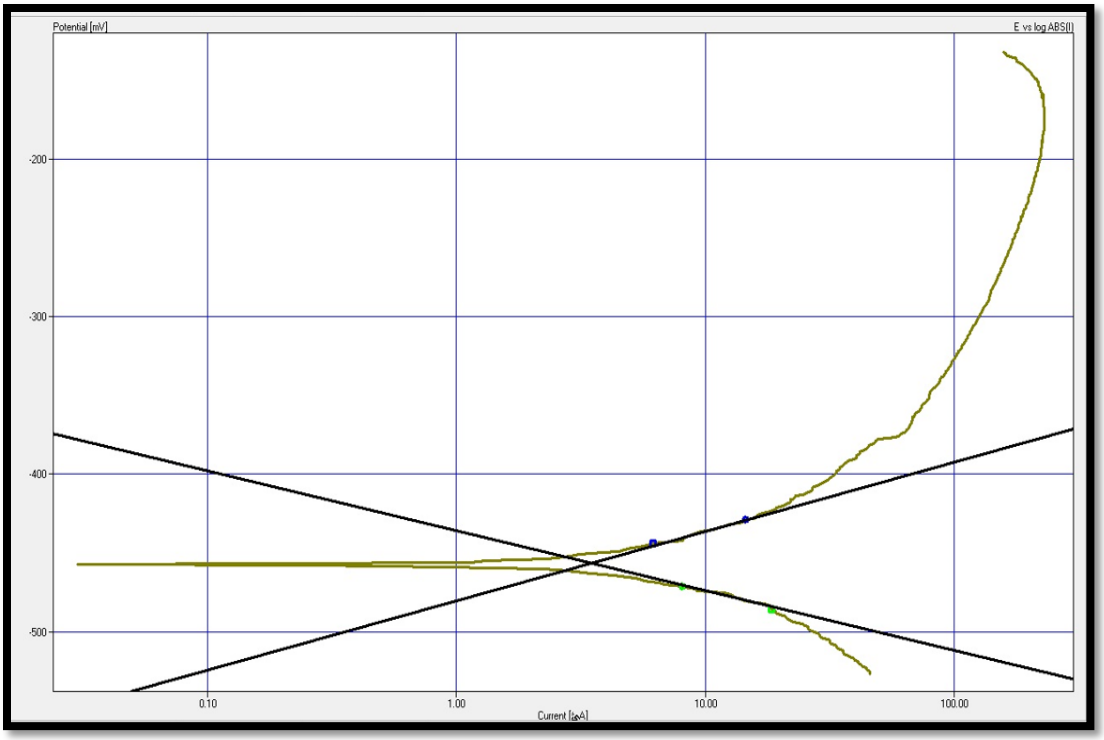

Figure 5: Polarization Curve for Coated Specimen by Ni-Cu-P (2-hrs.Coating Time)

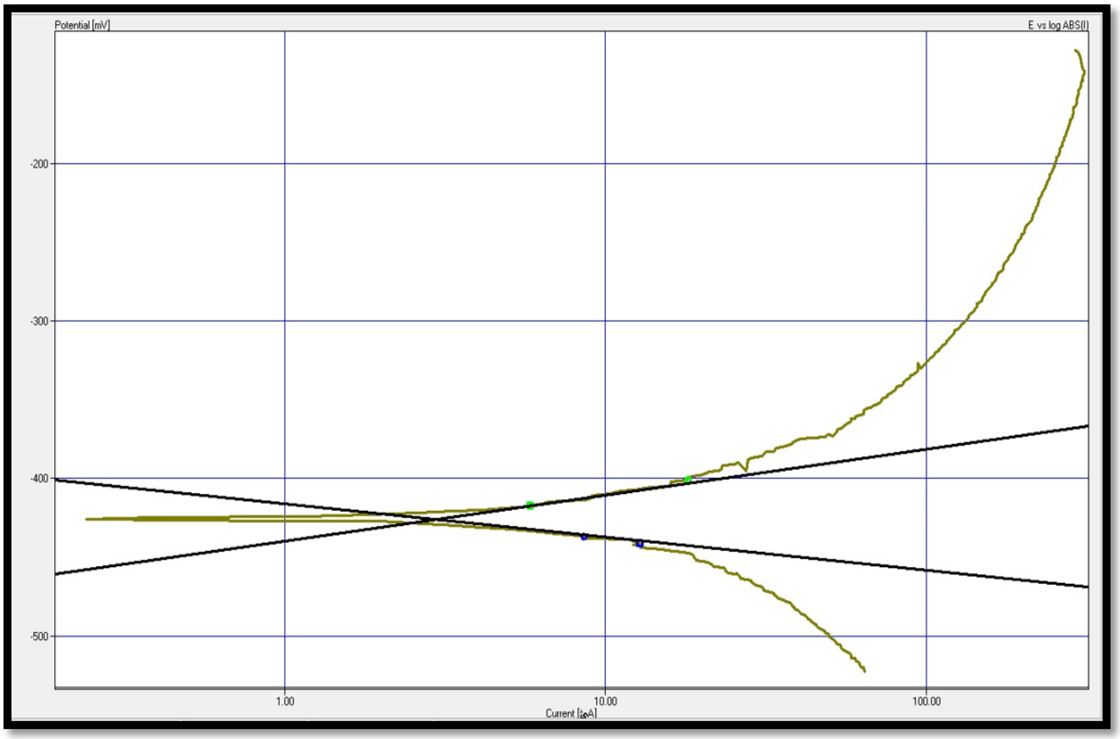

Figure 6: Polarization Curve for Coated Specimen by Ni-SiC-P(1-hr.Coating Time).

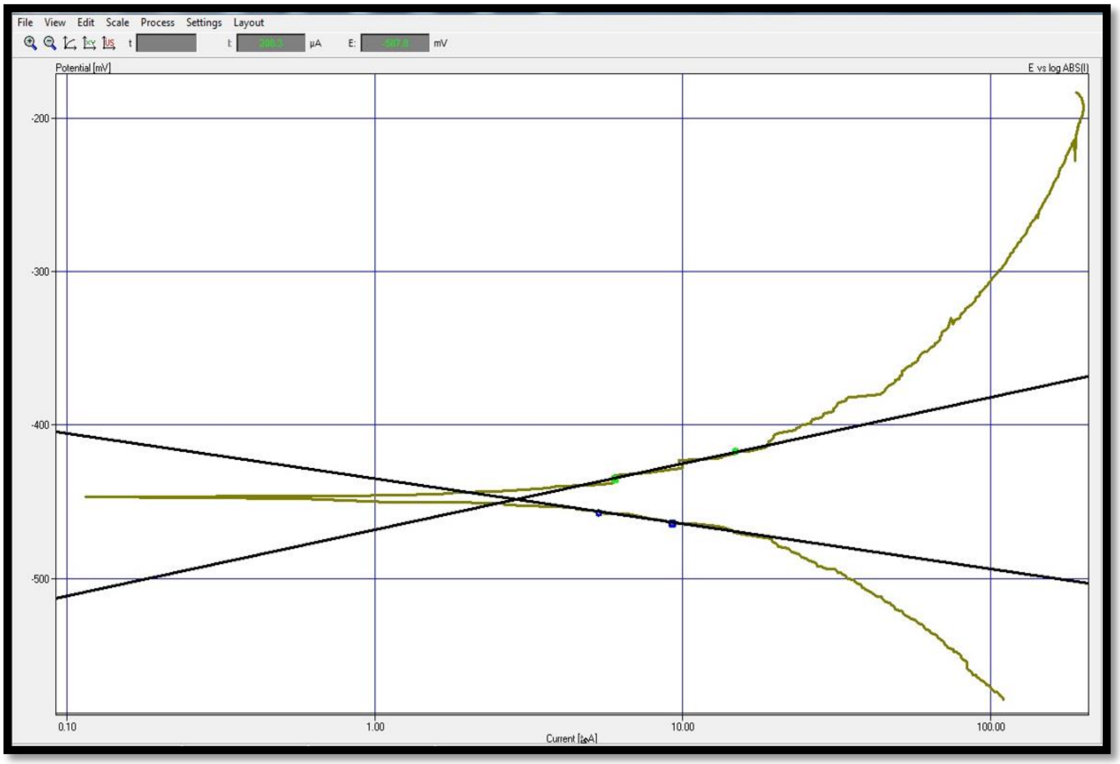

Figure 7: Polarization Curve for Coated Specimen by Ni-SiC-P(2-hrs.Coating Time)

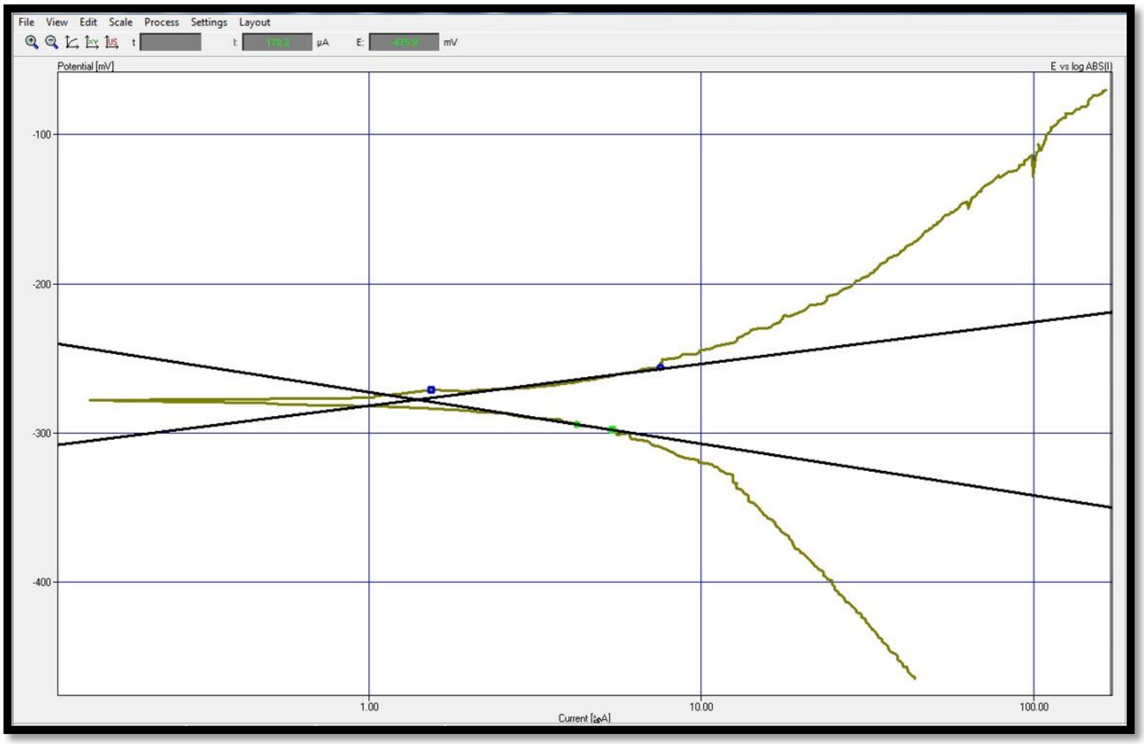

Figure 8: Polarization Curve for Coated Specimen by Ni-Zn-P(1-hr.Coating Time)

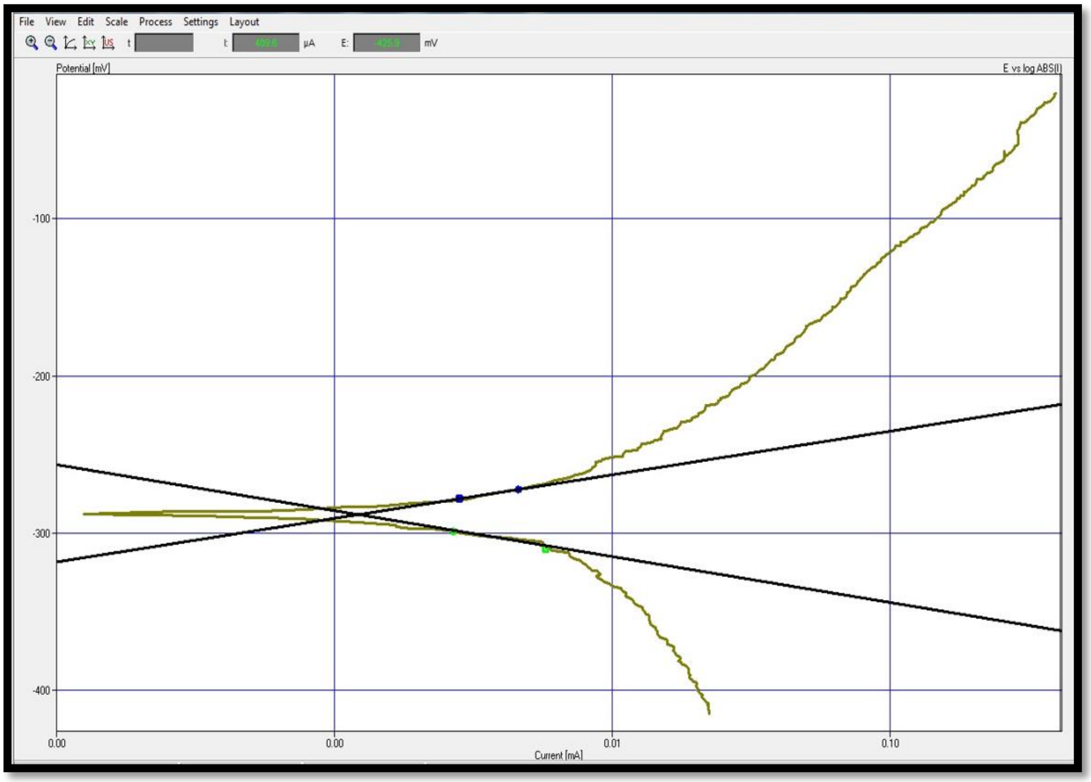

Figure 9: Polarization Curve for Coated Specimen by Ni-Zn-P(2-hrs.Coating Time)

Appendix F

Cyclic Polarization Curves for Bare and Coated Specimens

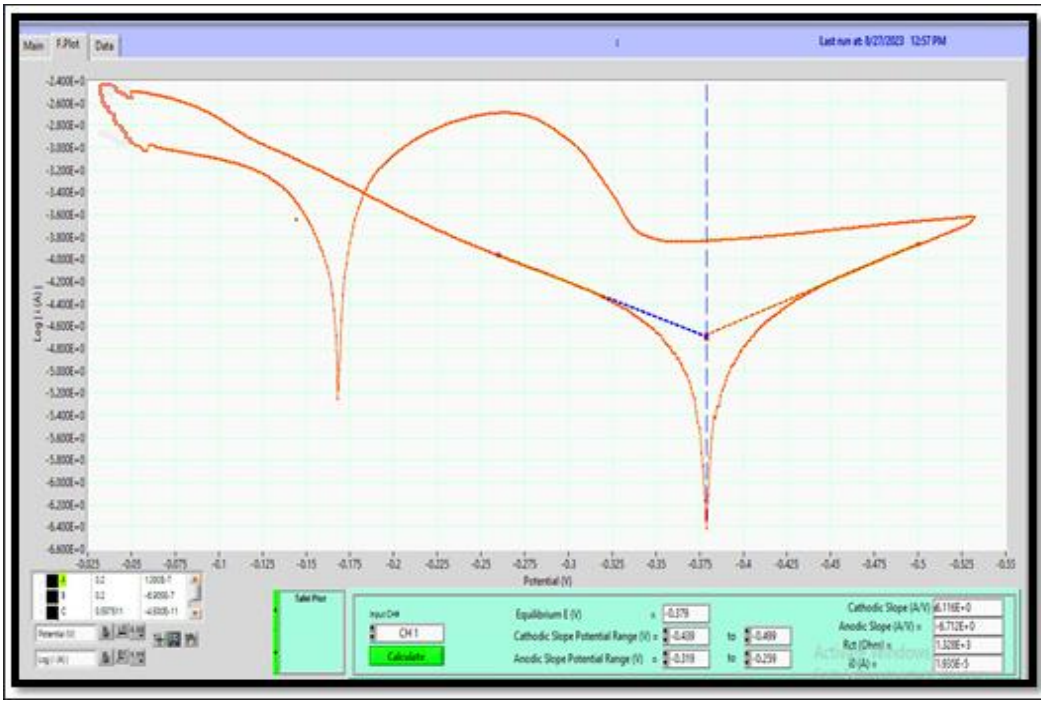

Input CH#: CH 1
Equilibrium E (V) = -0.379
Cathodic Slope Potential Range (V) = -0.439 to -0.499
Anodic Slope Potential Range (V) = -0.319 to -0.259
Cathodic Slope (A/V) 6.116E+0
Anodic Slope (A/V) = -8.712E+0
Rct (Ohm) = 1.328E+3
i0 (A) = 1.930E-5

Figure 1: Cyclic Polarization Curve for Bare Specimen.

Input CH#: CH 1
Equilibrium E (V) = -0.365
Cathodic Slope Potential Range (V) = -0.419 to -0.477
Anodic Slope Potential Range (V) = -0.321 to -0.309
Cathodic Slope (A/V) 1.232E+1
Anodic Slope (A/V) = -7.230E+0
Rct (Ohm) = 9.621E+3
i0 (A) = 2.671E-6

Figure 2:Cyclic Polarization Curve for Coated Specimen by Ni-P (1-hr.Coating Time).

Last run at: 8/27/2023 12:47 PM

Input CH#: CH 1

Equilibrium E (V) = -0.306

Cathodic Slope Potential Range (V) = -0.366 to -0.426

Anodic Slope Potential Range (V) = -0.250 to -0.213

Cathodic Slope (A/V) 1.238E+1

Anodic Slope (A/V) = -5.468E+0

Rct (Ohm) = 3.749E+3

i0 (A) = 6.854E-6

Figure 3:Cyclic Polarization Curve for Coated Specimen by Ni-P (2-hrs.Coating Time).

Last run at: 8/21/2023 10:24 AM

Input CH#: CH 1

Equilibrium E (V) = -0.347

Cathodic Slope Potential Range (V) = -0.387 to -0.475

Anodic Slope Potential Range (V) = -0.282 to -0.273

Cathodic Slope (A/V) 1.210E+1

Anodic Slope (A/V) = -5.660E+0

Rct (Ohm) = 5.232E+3

i0 (A) = 4.911E-6

Figure 4:Cyclic Polarization Curve for Coated Specimen by Ni-Cu-P(1-hr.Coating Time)

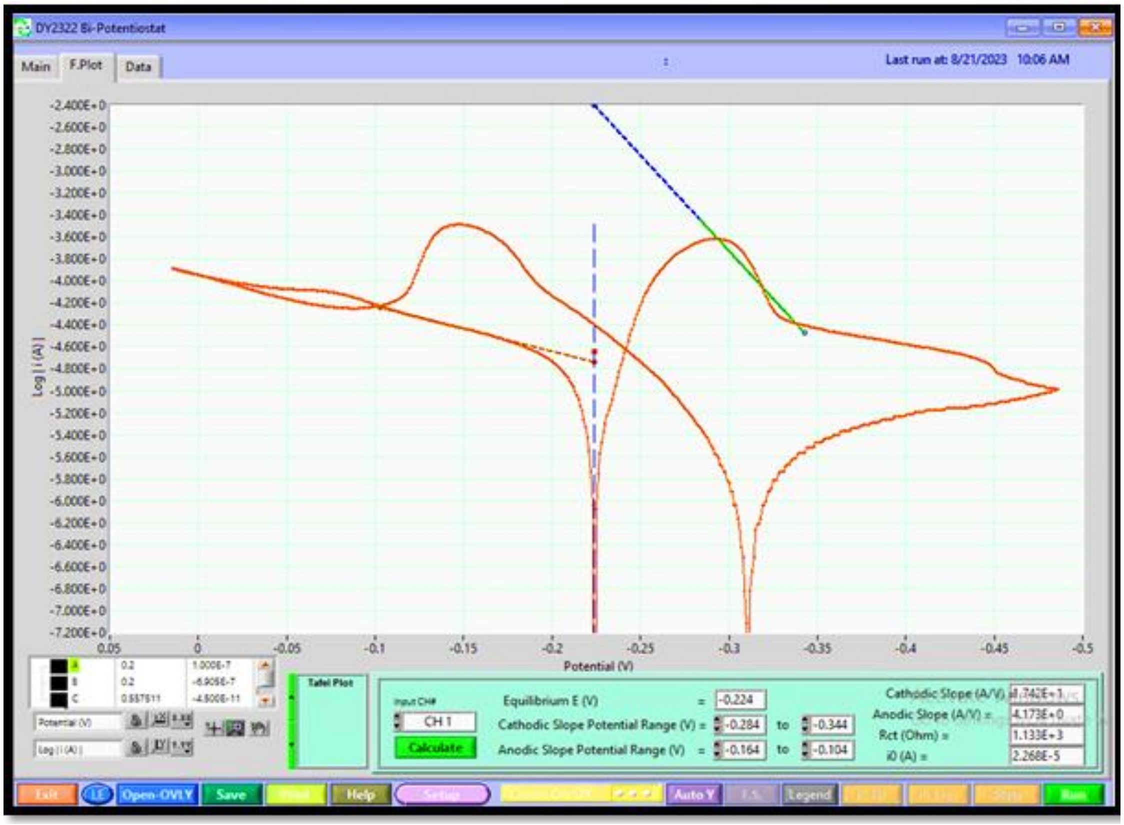

Last run at: 8/21/2023 10:06 AM

Input CH#: CH 1

Equilibrium E (V) = -0.224

Cathodic Slope Potential Range (V) = -0.284 to -0.344

Anodic Slope Potential Range (V) = -0.164 to -0.104

Cathodic Slope (A/V) 1.742E+1

Anodic Slope (A/V) = 4.173E+0

Rct (Ohm) = 1.133E+3

i0 (A) = 2.268E-5

Figure 5:Cyclic Polarization Curve for Coated Specimen by Ni-Cu-P (2-hr.Coating Time).

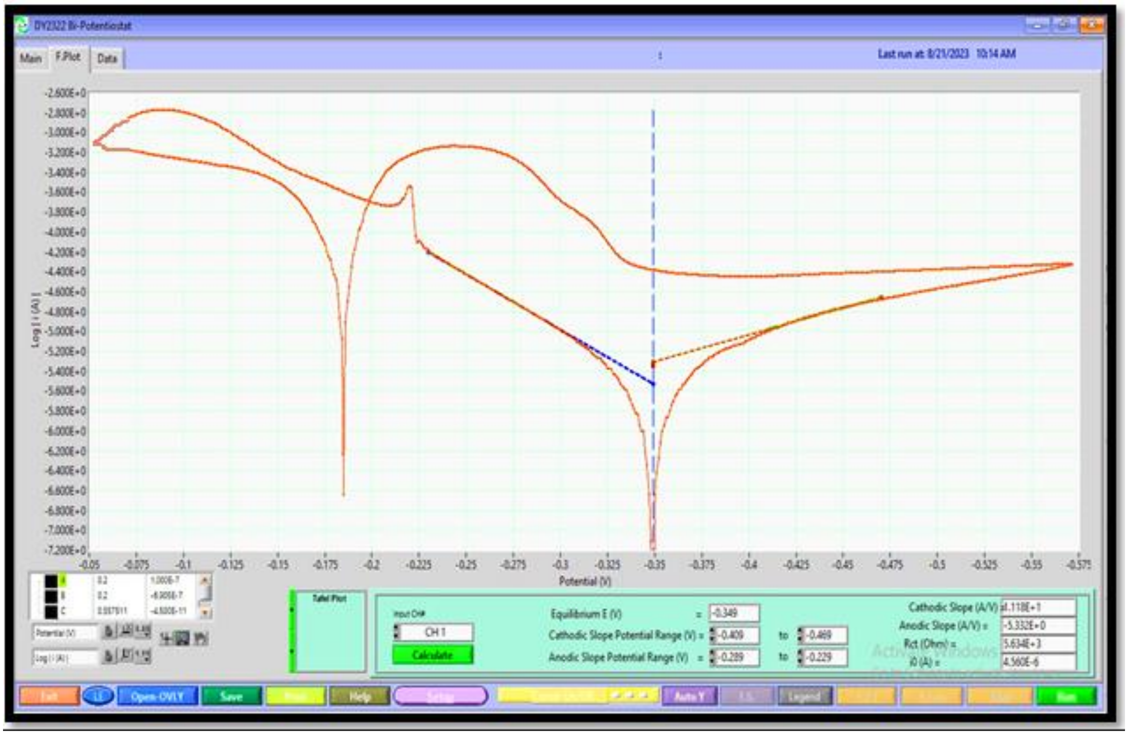

Last run at: 8/21/2023 10:14 AM

Input CH#: CH 1

Equilibrium E (V) = -0.349

Cathodic Slope Potential Range (V) = -0.409 to -0.469

Anodic Slope Potential Range (V) = -0.289 to -0.229

Cathodic Slope (A/V) 1.118E+1

Anodic Slope (A/V) = -5.332E+0

Rct (Ohm) = 5.634E+3

i0 (A) = 4.560E-6

Figure 6: Cyclic Polarization Curve for Coated Specimen by Ni-SiC-P (1-hr.Coating Time).

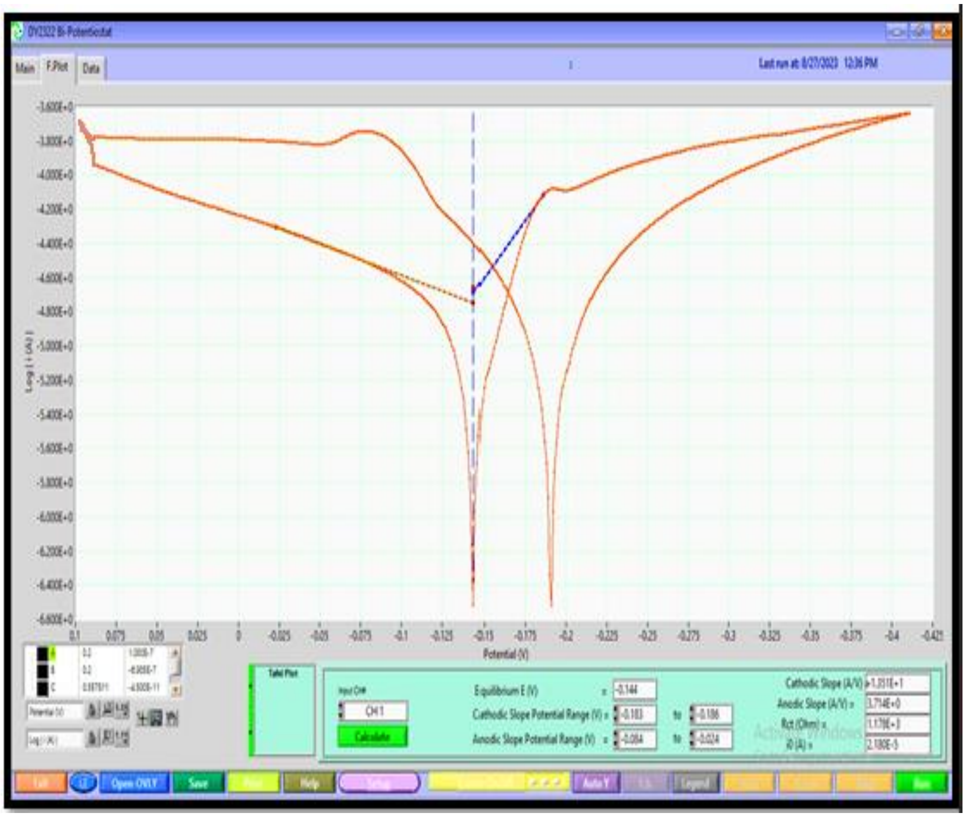

Last run at: 8/27/2023 12:36 PM

Input CH#: CH1

Equilibrium E (V) = -0.144

Cathodic Slope Potential Range (V) = -0.183 to -0.186

Anodic Slope Potential Range (V) = -0.084 to -0.024

Cathodic Slope (A/V) = 1.351E+1

Anodic Slope (A/V) = 3.714E+0

Rct (Ohm) = 1.179E+3

i0 (A) = 2.180E-5

Figure 7: Cyclic Polarization Curve for Coated Specimen by Ni-SiC-P (2-hr.Coating Time).

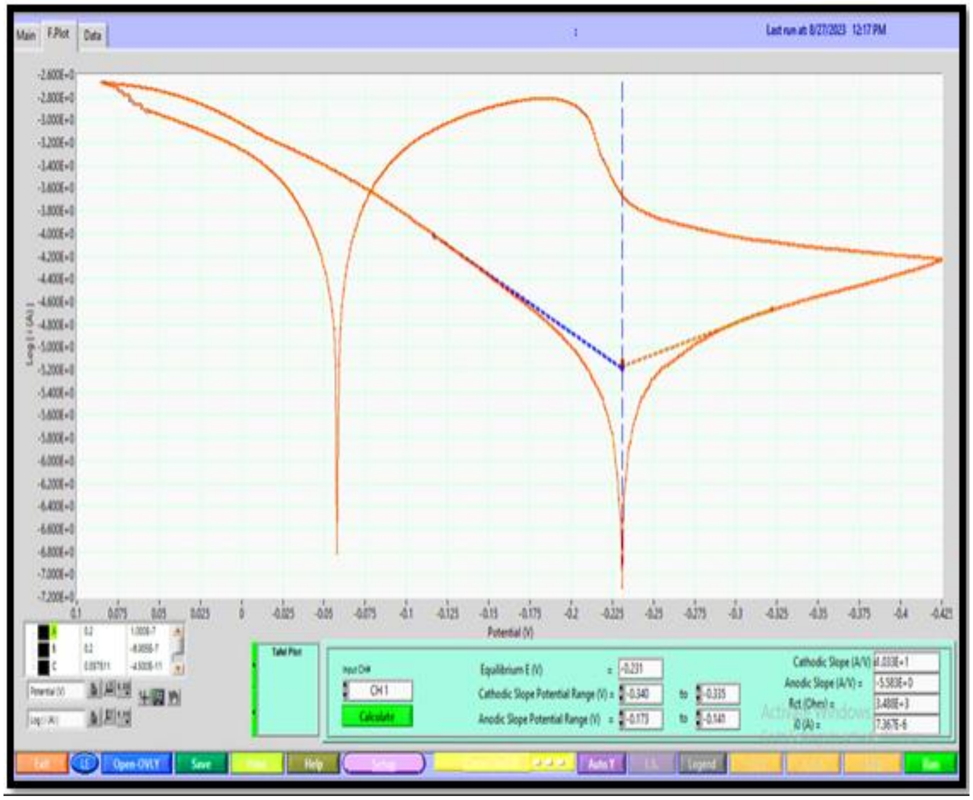

Last run at: 8/27/2023 12:17 PM

Input CH#: CH1

Equilibrium E (V) = -0.231

Cathodic Slope Potential Range (V) = -0.340 to -0.335

Anodic Slope Potential Range (V) = -0.173 to -0.141

Cathodic Slope (A/V) = 1.033E+1

Anodic Slope (A/V) = -5.583E+0

Rct (Ohm) = 3.480E+3

i0 (A) = 7.367E-6

Figure 8: Cyclic Polarization Curve for Coated Specimen by Ni-Zn-P (1-hr.Coating Time).

Input CH# CH 1

Calculate

Equilibrium E (V) = -0.299

Cathodic Slope Potential Range (V) = -0.159 to -0.419

Anodic Slope Potential Range (V) = -0.239 to -0.179

Cathodic Slope (A/V) 1.277E+1

Anodic Slope (A/V) = -4.659E+0

Rct (Ohm) = 4.266E+3

i0 (A) = 6.022E-6

Figure 9: Cyclic Polarization Curve for Coated Specimen by Ni-Zn-P (2-hr.Coating Time).

Appendix G

Advantage Endorsement of Current Study to Iraqi Cement State Company

Republic of Iraq
Ministry Of Industry and Minerals
Iraqi Cement State Company

الشركة العامة للسمنت العراقية
Iraqi Cement State Co.

جمهورية العراق
وزارة الصناعة والمعادن
الشركة العامة للسمنت العراقية
معاونية السمنت الجنوبية
معمل سمنت الكوفة

القسم الفني
شعبة البحث والتطوير

العدد / ج / ٢٥٠٥
التاريخ / ١١ / ٥ / ٢٠٢١م

الى / جامعة بابل – كلية هندسة المواد

م / بحث دكتوراه

السلام عليكم ...

نود إعلامكم بضرورة أن تكون الدراسة الخاصة ببحث الدكتوراه لمنسوبنا الباحث (حسن هادي مسلب) ضمن المشاكل الصناعية الموجودة في معملنا ومن أهمها :-

١- دراسة وتحديد الفشل الحاصل في منقيات الوقود الثقيل (Separators) في محطة التوليد الكهربائية.
٢- دراسة وتحليل الفشل في (Turbo charge) محركات الوقود الثقيل.

.... مع التقدير.

رئيس فيزياويين أقدم / جميل إبراهيم حسين
مدير معمل سمنت الكوفة

نسخة منه الى :-

- القسم الفني – شعبة البحث والتطوير / مع الاوليات.

Address: Al-Najaf Al-Ashraf / Al-kufa
E-Mail: kufa@icsc.gov.iq
E-Mail: kufa@southern-cement.com
Post Box: ٢٥ Al-kufa

العنوان : النجف الأشرف / الكوفة
البريد الالكتروني : kufa@icsc.gov.iq
البريد الالكتروني : : kufa@southern-cement.com
ص.ب : ٢٥ الكوفة

Appendix H

Silicon Carbides Particles from Two Sources

Appendix I

Particle Analysis

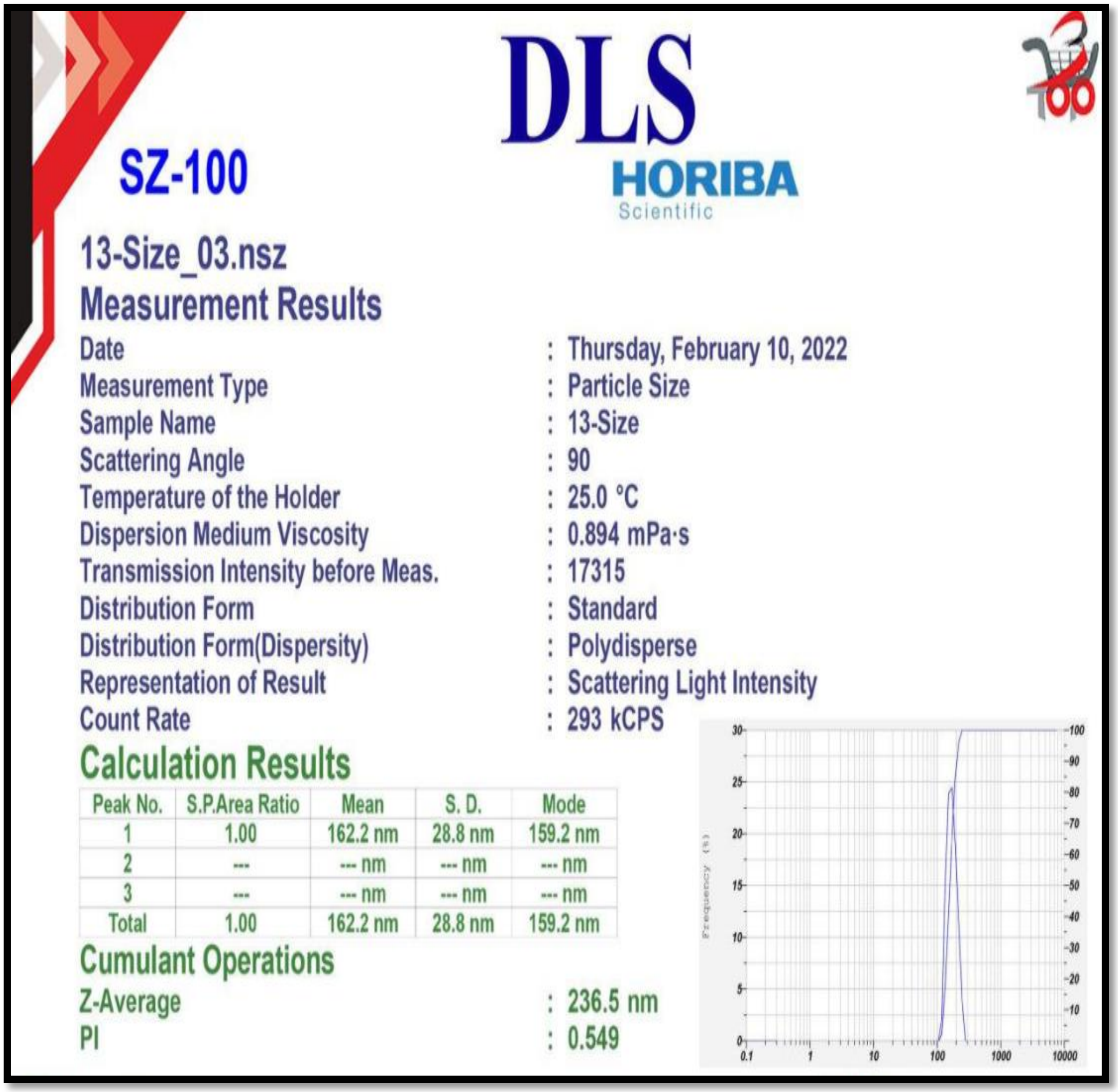

DLS

HORIBA
Scientific

SZ-100

13-Size_03.nsz

Measurement Results

Date : Thursday, February 10, 2022
Measurement Type : Particle Size
Sample Name : 13-Size
Scattering Angle : 90
Temperature of the Holder : 25.0 °C
Dispersion Medium Viscosity : 0.894 mPa·s
Transmission Intensity before Meas. : 17315
Distribution Form : Standard
Distribution Form(Dispersity) : Polydisperse
Representation of Result : Scattering Light Intensity
Count Rate : 293 kCPS

Calculation Results

Peak No.	S.P.Area Ratio	Mean	S. D.	Mode
1	1.00	162.2 nm	28.8 nm	159.2 nm
2	---	--- nm	--- nm	--- nm
3	---	--- nm	--- nm	--- nm
Total	1.00	162.2 nm	28.8 nm	159.2 nm

Cumulant Operations

Z-Average : 236.5 nm
PI : 0.549

الخلاصة

الفاصل هو اهم جزء في محطات الطاقة التي تستخدم الوقود الثقيل في نظام التشغيل. الفاصل يعمل على تنقية الوقود الثقيل (الخام)من الجسيمات، العناصر المعدنية، الماء، الاطيان والشوائب بواسطة قوى الطرد المركزي. في هذه الدراسة التحقق على اسباب الفشل لفواصل(منقيات)الوقود الثقيل واقتراح اربع حمامات من الطلاء اللاكهربائي لمنعه. ثلاثة انواع من العينات يتم استخدامها في هذه الدراسة. النوع الاول تمثل باخذ بضعة عينات من القرص المتضرر لتحليل الفشل. النوع الثاني هومجموعة عينات من شفت (الفولاذ المقاوم للصدا) ٣١٦باقطار ١٥ملم وسمك ١٠ملم للطلاء اللاكهربائي تم اخذها. النوع الاخير من العينات هو صفائح منحنية على شكل حرفUمن (الفولاذ المقاوم للصدا٣١٦ ايضا) مختلفة الابعاد استخدمت في فحص تشققات التاكل الاجهادي ونمذجة التحليلات العددية.

لتحليل الفشل ، خصائص المواد: التركيب الكيميائي، الصلادة، المجهر الضوئي، المجهر الالكتروني مكونات العناصر، حيود الاشعة السينية، والنمذجة العددية لتشققات التاكل الاجهادي بواسطة انسزز١٥,٠٧تم دراستها.

الطلاء اللاكهربائي تم اجراءه باربعة انواع مختلفة من الاوساط وهما(نيكل-فسفور) والاخر(نيكل- نحاس- فسفور)(نيكل –خارصين-فسفور)و(نيكل-جسيمات نانوية من كاربيد السليكون-فسفور)(وبفترتين مختلفيتين وهما (١و٢ساعة) على التوالي .فحص الصلادة ، خشونة السطوح، التاكل بفحص تافل والاستقطاب الدوري في محلول ٣,٥كلوريد الصوديوم تم انجازها. التاكل بالتعرية كذلك تم تنفيذها في وسط فعال(النفط الخام) وبفترات زمنية مختلفة(١٥-٣٠-٤٥-٦٠-٧٥-٩٠-١٠٥-١٢٠و١٣٥دقيقة)كذلك فحص تاكل التشققات الاجهادي لاربع عينات على شكل حرف Uالمنحنية من الفولاذ المقاوم للصدا في نفس الوسط السابق بثلاث فترات زمنية مختلفة(٤٨٠-٩٦٠و١٤٤٠ساعة) تم اخذها.

من نتائج تحليل الفشل التي تم الحصول عليها هي معرفة التركيب الكيميائي للسبيكة المستخدمة في صناعة قرص الفاصل حيث تبين انها مطابقة لسبيكة (الفولاذ المقاوم للصدا٣١٦) وان الصلادة للقرص المتضررانخفضت من ٣٣١فيكرز في مناطق بعيدة عن موقع الفشل وتحت حمل ٣٠٠غم\مايكرومتر الى ٢٢٠فيكرزفي مناطق قرب الضرر.

من الفحص البصري وصور المجهر الالكتروني و انخفاض الصلادة وفقدان وزن القرص وقلة متانة القرص ووجود تشققات مايكروية يتبين ان اهم اسباب الفشل هو التاكل بالتعري وتاكل التشققات الاجهادي. تشققات التاكل الاجهادي عبر الحدود الحبيبية يمكن مشاهدتها بصور المجهر الالكتروني.

من اهم نتائج الطلاء اللاكهربائي للعينات المطلية والمعاملة حراريا لطلاء(نيكل-كاربيد السليكون-فسفور)، (نيكل-خارصين-فسفور)، (نيكل-نحاس-فسفور) و(نيكل-فسفور)بزمن طلاء ساعتين هو (معدل التاكل بالتعري في وسط النفط الخام وبزمن ٩٠دقيقه)انخفضت بنسبة (٤٧,٥، ٤٢,٤%، ١٣%و١٢,٥%) على التوالي. في الجانب المقابل بعد المعاملة الحرارية صلادة فيكرز ازدادت بنسبة(٧٠,٥، ٦٤,٧%، ٦٥%و٦٤%) للعينات المطلية(نيكل-كاربيد السليكون-فسفور)، (نيكل-خارصين-فسفور)، (نيكل-نحاس-فسفور) و(نيكل-فسفور)وبزمن طلاء ساعتين على التوالي .

من اهم نتائج اختبارات الاستقطاب ان معدل التاكل للعينات المطلية بعد المعاملة الحرارية(نيكل-كاربيد السليكون-فسفور)، (نيكل-خارصين-فسفور)، (نيكل-نحاس-فسفور) و(نيكل-فسفور)انخفضت بنسبة(٩١,٦، ٩٦%، ٨٧%و٨١%) على التوالي. في فحوصات الاستقطاب الدوري تبين ان الاختلاف في فرق جهد التنقر وفرق جهد الحماية لطلاءات (نيكل-كاربيد السليكون-فسفور)، (نيكل-نحاس-فسفور)، (نيكل-خارصين-فسفور) و(نيكل- فسفور) تحسنت بنسبة (٦٣%، ٣٩.١%، ٣٦%و٢١.٧%) على التوالي.

على اي حال معدل خشونة السطوح لكل طبقات الطلاء الاربعة لزمن طلاء ساعتين ازدادت بعد المعاملة الحرارية عن نفس الطبقات لكن بزمن ١-ساعة فقط بنسبة (٧٣%، ٣٦,٥%، ٦٠%و٦٥%)على التوالي.

نتائج صور المجهر الالكتروني لاختبار تشققات التاكل الاجهادي لعينات Uالمنحنية في النفط الخام كوسط فعال عند زمن (٤٨٠و١٤٤٠، ٩٦٠ساعة)بينت ان تشققات التاكل الاجهادي كانت من نوع التشققات عبر الحدود الحبيبية خصوصا للعينات العارية. تشققات التاكل الاجهادي لم تظهر في كل العينات المطلية وتمتلك سمك طلاء عالي. اخيرا نتائج تحليل العناصر تعطي صورة واضحة عن المناطق التي تعرضت لإجهادات وانفعالات عالية ومنخفضة. وكان الحد الأدنى للإجهاد والانفعال المكافئ في العينات الأربعة ٠,٠٣١٠ باسكال ٢,٥٦٥*١٠$^{-١٠}$على التوالي.